2D NANOSHEETS AS FUNCTIONAL BUILDING BLOCKS FOR 1D PHOTONIC CRYSTAL SENSORS

Katalin Szendrei-Temesi (geb. Szendrei)

aus

Budapest, Ungarn

2018

ERKLÄRUNG

Diese Dissertation wurde im Sinne von §7 der Promotionsordnung vom 28. November 2011 von Frau Prof. Dr. Bettina V. Lotsch betreut.

EIDESSTATTLICHE VERSICHERUNG

Diese Dissertation wurde eigenständig und ohne unerlaubte Hilfe erarbeitet.

München, 20.06.2018

Katalin Szendrei-Temesi

Dissertation eingereicht am: 20.04.2018

Erstgutachterin: Prof. Dr. Bettina V. Lotsch

Zweitgutachter: Prof. Dr. Achim Hartschuh

Mündliche Prüfung am: 28.05.2018

Apukámnak

"Just because something doesn't do what you planned it to do doesn't mean it's useless."

Thomas Alva Edison

KÖSZÖNÖM! DANKE! THANK YOU!

Ich möchte meinen Praktikanten ganz herzlich für die spannenden Ergebnisse und Diskussionen danken, und ich hoffe, dass ihr Spaß hattet mit meinen bunten Forschungsthemen: Bernhard Illes danke ich für die Messungen am „H1-Selektivität"-Projekt, Andre Mähringer für das unveröffentlichte MOF/nanosheet Bragg stack Projekt, Jakob Blahusch und Katharina Durner für das „all-nanosheet" Projekt, Denis Hartmann und Carola Lampe für das „Transfer" Projekt, und Dimitra Chatzitheodoridou für das „Diffusion und Aminprojekt".

Ich möchte mich bei dem kompletten AK Lotsch für diese schönen 3,5 Jahre bedanken, für die lustige Zeit sowohl in München, also auch in Stuttgart. Einen besonderen Dank geht an die direkten Münchner Kollegen für die Gruppenveranstaltungen, die wissenschaftlichen Diskussionen und für das Zuhören in guten und in schlechten Zeiten: Albi, Kerstin, Claudi, Sascha, Anna, Leo, Charlotte, Hendrik, Stefan, Lars, Dimitra, Annick, Verena, Natalie – Danke!

Für die organisatorische Hilfe im Laufe der Doktorarbeit möchte ich mich bei diversen Leuten ganz herzlich bedanken – ihr habt meinen Alltag erleichtert. Vielen Dank an Claudia Kamella, die sich um alle Stuttgarter Angelegenheiten gekümmert hat und wenn sie nicht selber helfen konnte, wusste sie sofort, an wen man sich wenden soll und an Sigrid Fuhrmann, die sich um die Verwaltungssachen gekümmert hat. Mein besonderes Dankeschön oder besser gesagt „Köszönöm" geht an Olga Lorenz, die mit den Münchner organisatorischen Angelegenheiten behilflich war. Bei Wolfgang Wünschheim möchte ich mich für die Lösung aller IT-Probleme und bei Thomas Miller für seine technische Hilfe bedanken.

Für das NIM (Peter Sonntag, Christoph Hohmann, Birgit Ziller, Isabella Almstätter und Silke Mayerl-Kink) und CeNS team (Susanne Hennig, Claudia Leonhard und Marilena Pinto) möchte ich mich neben dem „travel award" und „research visit funding" für die tollen Veranstaltungen für die schöne Zeit im Student board, für die Pressemeldungen (Birgit Ziller und Isabella Almstätter) und für das Cover Bild und für die Grundlagen im 3D image design (Christoph Hohmann) bedanken.

Köszönöm a családomnak a támogatást így a távolból is! Köszönöm, Lacinak, Attilának, Csabinak, Dórinak és Áginak (Bros&Partners), Anyának, Mamának, Papának, Gábornak a támogatást, illetve Apukámnak, aki ezt ugyan nem láthatja, de a matematika és a természettudományok iránti szeretét kellő mértékben átadta, hogy idáig eljussak.

Végül, de nem utolsó sorban köszönöm férjemnek, Gábornak a támogatást és a biztatást nem csak ez alatt a 3,5 év alatt, hanem mindig. Köszi mindenek előtt a türelmedet, a sok szeretetet, a tanácsaidat, a mindig diplomatikus megoldási javaslatokat, illetve egyszerűen, hogy vagy.

TABLE OF CONTENTS

SUMMARY

One-dimensional (1D) Photonic Crystals (1DPCs) have emerged in recent years as a novel functional platform for optical sensing applications. These bioinspired periodic multilayered structures exhibit a pronounced structural color originating from interference phenomena, which can be dynamically varied by external stimuli. Changes in the refractive index or the layer thickness of the individual layers of the multilayered structure caused by an external stimulus can be translated into spectral shifts and, hence, into structural color changes, which renders these structures label-free colorimetric sensors. Although in the last three decades, several research approaches were proposed in order to improve the optical quality of such photonic sensors, their structural properties and sensing performance, there are still challenges remaining, which impact the applicability of these platforms. These include the sensor´s (long-term) stability, the signal reproducibility, the sensitivity, selectivity, and the improvement of the optical quality and the readout schemes.

This thesis proposes functional material-based solutions to these above mentioned challenges. In order to improve the sensor's stability and signal reproducibility, robust and at the same time stimuli-responsive inorganic materials, namely two-dimensional (2D) nanosheets, were integrated into 1DPC architectures for the first time. 2D antimony phosphate nanosheets were exfoliated and afterwards optimized for solution processed 1DPC fabrication schemes. This class of 2D materials exhibits the capability to intercalate analyte molecules and, as a consequence, to change the layer thickness significantly. This phenomenon could be exploited in 1DPC architectures and translated into full-spectrum color shifts, which are among the largest color changes induced by volatile analytes (humidity or organic vapors) reported to date. These large color changes induce larger sensitivity, i.e. color change per analyte concentration, which also allowed us to explore novel sensing applications. One example is the touchless motion tracking of a human finger, whereby the humidity sheath of a finger can be detected optically in real time and true color, without touching the sensor surface.

Further, these nanosheets were also able to differentiate optically between chemically similar analytes, such that even the optical separation of isomers, e.g. 1-propanol and 2-propanol, became possible. Hereby, optical differentiation between analytes could be traced back to molecular features such as the molecule size and size-related properties, including acidity or polarity, which determine the optical response of the 1DPCs to analytes.

Additionally, 2D lithium tin sulfide nanosheets were identified as solution processable ultrahigh-refractive-index materials, which are advantageous in the field of 1DPC based sensors, as the optical contrast within the multilayer structure can be further increased. On the one hand, this

leads to better optical properties, such as higher reflectance intensity and a more pronounced structural color; on the other hand, the number of layers and, thus, the entire device thickness and material costs can be reduced. Additionally, lithium tin sulfide nanosheets showed a great potential in accumulating water molecules in their interlayer space, similar to the antimony phosphates. Besides improving the optical properties, this leads to a high sensitivity to ambient humidity. By combining the two nanosheet materials – antimony phosphate and lithium tin sulfide - in a single 1DPC, an ultrahigh humidity sensitivity could be observed based on the swelling behavior of both stimuli-responsive materials.

The swelling of the antimony phosphate nanosheets was further exploited to identify alternative readout schemes besides reflectometry and spectroscopy. Hereby, in collaboration with the group of Prof. Hernán Miguez, ICMSE-CSIC, in Sevilla, Spain, a carefully designed optical resonator was constructed based on two porous 1DPCs and a nanosheet "defect" layer. The coupling of the photonic modes with the emissive properties of dye molecules embedded in the nanosheet layer was used to modify the photoluminescence of the dyes by swelling of the nanosheet cavity, induced by humidity changes. In extreme cases, we could even suppress the emission completely, triggered exclusively by reaching a certain external humidity value. Photoemission as a sensing signal, compared to the typical photonic readout scheme, offers a more direct way to couple the sensor to electrical readout schemes.

Finally, for the first time we performed experimental and theoretical studies on molecular diffusion in 1DPC structures. For this, we designed a 1DPC structure, which was capable of resolving the layer-by-layer diffusion of analyte molecules within the structure. Hereby, we used antimony phosphate nanosheet based 1DPCs as a model system, where the intercalation of primary amine molecules was measured by optical methods. Owing to the acid-base properties of the host layers, these analytes are trapped in the interlayer space, enabling the spatio-temporal resolved study of analyte uptake. The experimental measurements were completed with theoretical calculations, carried out by Alberto Jiménez-Solano, MPI for Solid State Research, Stuttgart, Germany, which allowed us to extract information about the time dependent layer thickness changes and their correlation with molecular diffusion.

In summary, this thesis introduces novel material-based solutions for next-generation sensor devices and sensing applications. Further, due to the high chemical variety and the potential for covalent and non-covalent post-synthetic modifications of 2D nanosheet materials, these photonic devices offer a versatile platform for different sensing applications in the future.

1. INTRODUCTION

Only in the period of this PhD thesis (2014-2018), an enormous increase in the usage of gas sensors in consumer applications from 1.2 million units to 110 million sensor units was observed and predicted. According to an analysis and forecast of the company Yole Développement in 2016 (Figure 1.1),[1] the growing demand for compact and easy-to-integrate gas sensors will continue for the next years. This is mainly connected with two important application fields entering the gas sensor market: wearable technologies and smartphones, where the impact of the latter is more decisive.
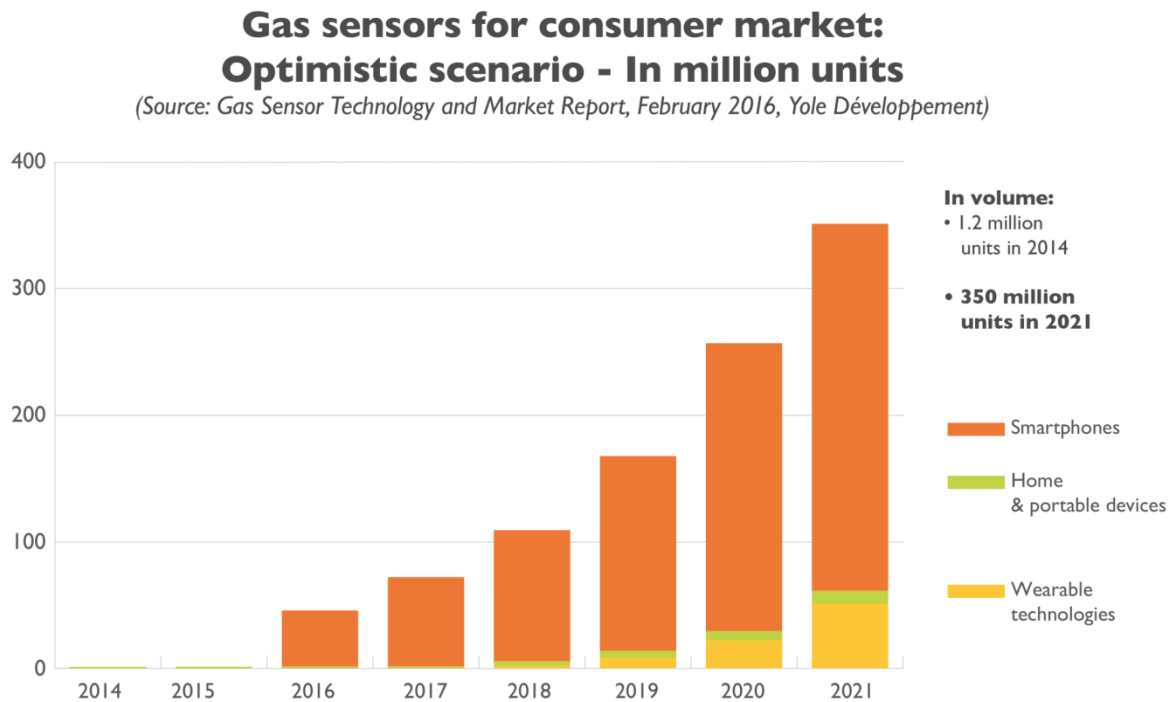
Figure 1.1: Optimistic scenario forecast about gas sensors for consumer applications. The image is adapted with permission.[1]

These novel application fields generate new technological and economical requirements, including selectivity, long lifetime, small packaging size, low power consumption, wireless communication,

multiple gas detection, high sensitivity, fast response time and low price.[2] The next value proposition for smartphones lies in the integrity and connectivity of a high variety of sensors and actuators for internet of things (IoT) applications.[3, 4] For this, multiple sensor units will be integrated increasingly into one device and connected online for diverse applications, such as enhanced security (face/eye recognition, fingerprint sensor), motion tracking (accelerometer, gyroscope), sound-related applications (microphones), optical applications (autofocus, cameras), communication (antenna, filters) and finally environmental applications (particle, gas, temperature and humidity sensors).[5, 6] The increasingly complicated sensing cases require not only the integration and connection of these sensors into one single device but also the development of the sensors themselves in terms of sensing materials, connectivity and sensing performance.

For gas sensors in particular, depending on the specific application and integration needs, different readout and detection principles are applied.[7] Metal Oxide Semiconductor (MOS) based or electrochemical sensors present the most important sensing platforms by measuring either resistance, capacitance or current intensity changes.[8] Other categories include acoustic sensors measuring the gas velocity, the rather expensive chromatography based detection methods, or calorimetric elements, which measure temperature or resistance shifts upon gas adsorption. For this thesis, the most relevant detection scheme is the optical detection, which ranges from wavelength shifts upon light absorption of the analyte to photoluminescence changes or color changes induced by a chemical reaction or gas adsorption.[9] Optical sensors are particularly interesting, as they provide a readout also in an electricity-free environment, as color changes can be detected qualitatively also by the naked eye.

Although the demand for novel sensing concepts and sensing targets is high, the bottleneck of the development is often the sensing material itself.[10] The sensor material usually defines many sensing descriptors, such as sensitivity, selectivity, response time, stability, reproducibility and accuracy, and hence, the entire sensor characteristics and applicability. The main focus of this thesis lies on identifying novel functional materials and integrating them into 1D Photonic Crystal (1DPC) architectures in order to achieve better sensing performance and to identify novel sensing concepts.

1.1 PHOTONIC CRYSTALS

Photonic Crystals (PCs) are periodic nanostructures exhibiting a periodic arrangement of two materials with different refractive indices (RI), which influence the motion of light. In 1887, Lord Rayleigh published his work on the optical properties of materials exhibiting periodicity in their dielectric properties in one spatial dimension and postulated the existence of an optical bandgap, a forbidden energy range for photons.[11] Although this was a significant discovery, it took 100 years until this concept was generalized and reduced to practice and the bandgap was realized experimentally for 2-dimensional (2D) and 3-dimensional (3D) systems. In 1987, Yablonovich[12] and John[13] published independently from each other with just a month time difference the two milestone papers describing novel periodic materials, which can control and manipulate the motion of light. The motivation of the two researchers was quite different:[14] while Yablonovitch worked for Bell Communication research on more applied topics and wanted to make the telecommunication lasers more efficient – by using a laser without threshold,[15] – John was motivated by pure academic research goals and wanted to propose the bandgap for means of light localization.[16] The terms "Photonic Crystal" and "photonic bandgap" were suggested by Yablonovitch in 1989 and have been used ever since.[14]

In the last three decades, the developments in this field, including the physical theories[17] and the fabrication and material development[18] converted these structures into a multifunctional optical system and a functional material platform on the landscape of optical sensing.[19] Inspired by natural structures, such as butterfly wings,[20] opals,[21] peacock feathers[22] or the skin of the chameleons,[23] nowadays a large variety of synthetic PC is known.[18, 24] Three different classes of Photonic Crystals can be distinguished: 1D, 2D and 3D PCs, referring to structures with a periodicity of the refractive RIs in one, two or three spatial dimensions (Figure 1.2).[17]
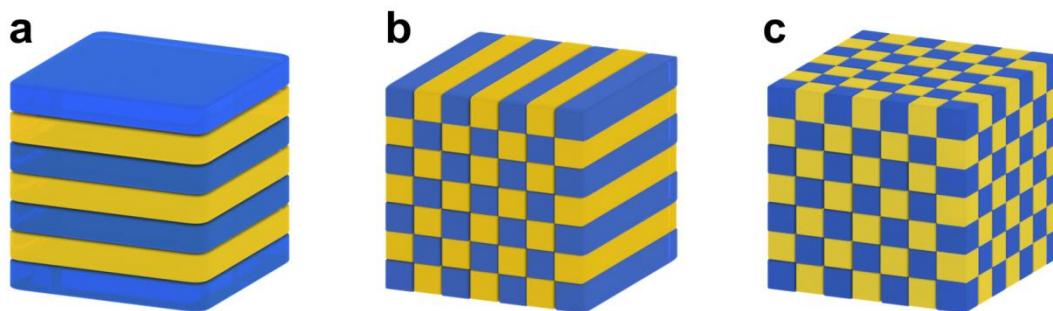
Figure 1.2: Schemes of (a) 1D, (b) 2D and (c) 3D photonic crystals. The different colors represent materials (or air) with different refractive index.

In the focus of this thesis are 1DPCs and optical resonator structures, thus the basic concepts underlying the optical properties and the sensing mechanisms of these systems will be discussed in detail. Additionally, integrated functional materials will be introduced, as these are the key components for the optical sensing performance and the sensing characteristics of these proposed new platforms.

1.2 ONE-DIMENSIONAL PHOTONIC CRYSTALS

1DPCs, also referred to as Bragg stacks (BS), distributed Bragg reflectors (DBR) or interference filters, are periodic nanostructures exhibiting a periodicity in the RI in one spatial dimension and, hence, are composed of two types of thin films deposited on top of each other in an alternating fashion.[17] In order to achieve an interaction with visible light, the periodicity, e.g. the optical thicknesses τ equation (1.1)

$$\tau = n \cdot d \qquad (1.1)$$

must be in the same range as the wavelength of the visible spectral range (400-800 nm), whereby n is the RI and d the physical thickness of the layer.[25]

1.2.1 OPTICAL PROPERTIES OF 1D PHOTONIC CRYSTALS

Upon propagation of white light through this periodic arrangement of dielectric films, the incident light beam is partially diffracted and reflected at each interface of two layers with differing RIs (Figure 1.3), depending on the optical thickness τ equation (1.1) of the two adjacent layers.
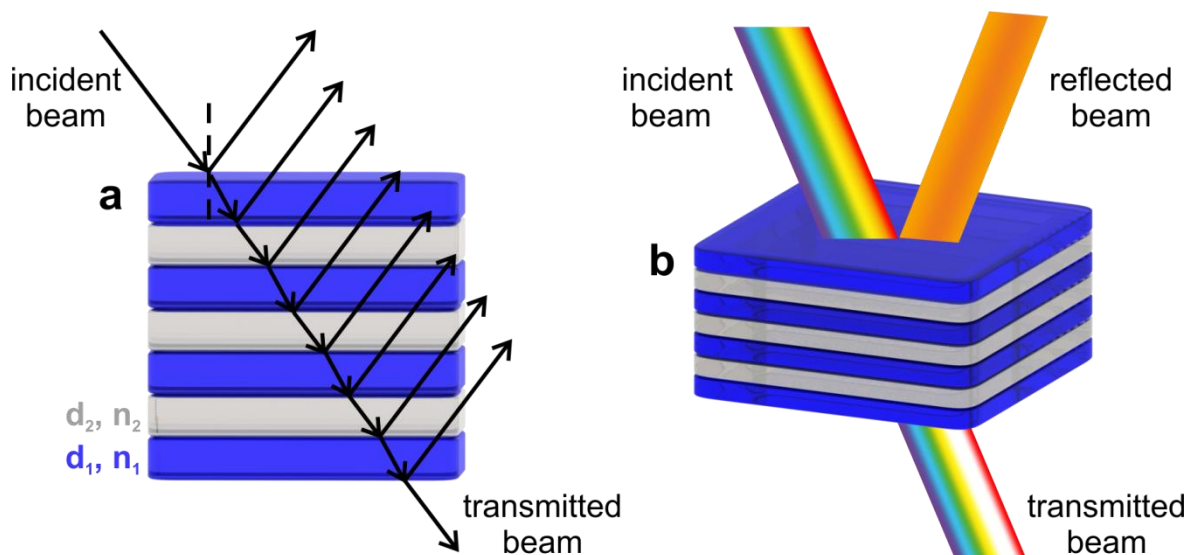
Figure 1.3: Interaction of light with a 1DPC. (a) The beam path of light within the multilayered structure, (b) the interaction of white light with the 1DPC resulting in a partially reflected and transmitted beam exhibiting complementary colors.

The constructive interference of the reflected light beams results in a strong reflection in a well-defined wavelength regime, the *photonic stopband*,[14] which is a forbidden energy range, in which no propagating waves through the structure in the direction of periodicity exist. In this spectral range, a maximum of reflection is observed, while beyond the stopband region, in which energy range the photons are not forbidden to propagate the structure, a maximum of transmission arises (Figure 1.4a). If the photonic bandgap lies in the visible range, a strong color, a *structural color* is observed, as the result of the periodic arrangement of inherently transparent materials. Beyond the stopband, the transmitted color occurs, which is the complementary color to the reflected structural color. Hence, 1DPCs exhibit the unique property to act as wavelength-selective filters for light, since they reflect light with a certain energy, while keeping the transparency in the rest of the spectrum. Further, as a consequence of the interaction of light with the multilayered structure, the electromagnetic (EM) field intensity distribution within the 1DPC shows an inhomogeneous behavior (Figure 1.4b).[26, 27] In Figure 1.4 the optical (Figure 1.4a-d) and structural properties (Figure 1.4e) of a 1DPC are shown. In the scanning electron microscope (SEM) cross section image (Figure 1.3e), the periodic arrangement of the two different materials showing a material contrast is depicted.
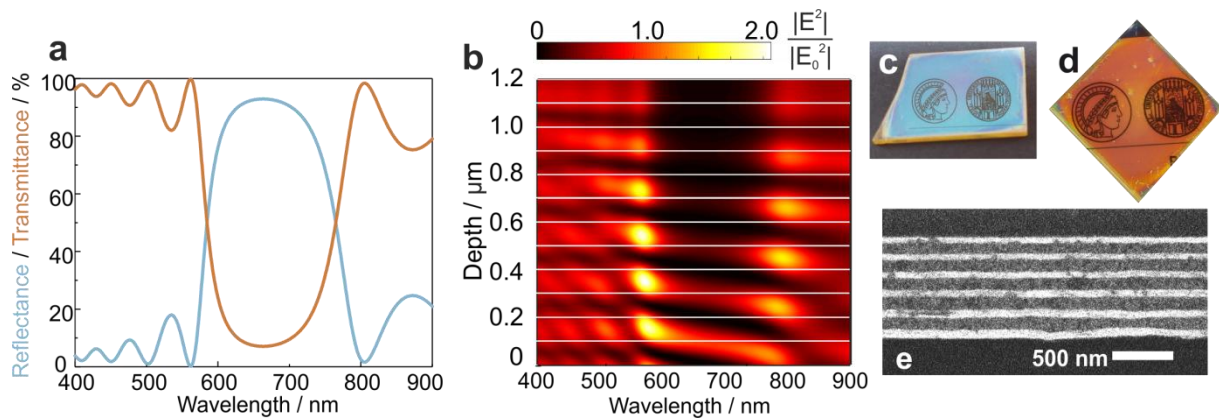
Figure 1.4: Structural and optical properties of 1DPCs. (a) Reflectance (blue) and transmittance (red) spectra of a 1DPC made of $H_3Sb_3P_2O_{14}$ nanosheets and TiO_2 nanoparticles. (b) EM field intensity distribution within the 1DPC described in (a), the horizontal white lines correspond to the layer interfaces within the structure. (c) Photograph of a 1DPC showing high reflectance. Note that the emblems were kept above the sample and the photograph was taken in reflection mode. (d) Photograph of a 1DPC sample demonstrating the transparency in the complementary spectral range of the bandgap. Note that the emblems were placed below the sample and the photograph was taken in transmission mode. (e) Secondary electron scanning electron microscopy image of a 1DPC made of $H_3Sb_3P_2O_{14}$ nanosheets and TiO_2 nanoparticles.

The interaction of light with this periodic multilayered structure can be described by Maxwell`s equations (1.2).[28]

$$\nabla \cdot \boldsymbol{D} = \rho$$
$$\nabla \cdot \boldsymbol{B} = 0$$
$$\nabla \times \boldsymbol{E} = -\frac{\partial \boldsymbol{B}}{\partial t} \qquad (1.2)$$
$$\nabla \times \boldsymbol{H} = J + \frac{\partial \boldsymbol{D}}{\partial t}$$

whereby $\boldsymbol{D}$ is the electric displacement, $\boldsymbol{B}$ the magnetic induction, $\boldsymbol{E}$ the electric field, $\boldsymbol{H}$ the magnetic field, ρ the charge density, J the free current density.

After approximations for homogenous, linear, isotropic, non-dispersive and transparent media, a "master equation", - similar to the Schrödinger equation for the propagation of electrons in a periodic potential - which contains all information about the photonic band structure, can be written as:[24]

$$\nabla \times \left(\frac{1}{\varepsilon(\boldsymbol{r})} \nabla \times \boldsymbol{H}(\boldsymbol{r}) \right) = \left(\frac{\omega}{c} \right)^2 \boldsymbol{H}(\boldsymbol{r}) \qquad (1.3)$$

whereby ε is the electric permittivity, ω the frequency and c the speed of light.

In this eigenvalue problem for a perfectly periodic medium, such as a perfect photonic crystal, *H(r)* can be solved using the Bloch theorem[29] and the entire photonic bandgap can be calculated. For a 1-dimensional case, a 1DPC, with some approximations, important features of the Bragg peak can be extracted from equation (1.3). One of the important features which can be derived from the Maxwell equations is the central position of the photonic stopband. This can be formulated according to the Bragg-Snell law,[30] which states that the position of the photonic stopband depends on the unit cell thickness (periodicity), effective RI and the angle of incidence equation (1.4).

$$m\lambda_0 = 2D\sqrt{n_{eff}^2 - sin^2\theta} \qquad (1.4)$$

whereby m is the diffraction order, λ_0 the central position of the stopband, D the unit cell ($D = d_1 + d_2$), θ the incidence angle, n_{eff} the effective RI of a bilayer, which is defined as $n_{eff} = \frac{n_1 d_1 + n_2 d_2}{d_1 + d_2}$, with d_1 and d_2 being the layer thicknesses and n_1, n_2 the RIs of the single layers in the multilayered structure.

For normal incidence angle, this equation simplifies to equation (1.5)

$$m\,\lambda_0 = 2d\,n_{eff} \tag{1.5}$$

Further, the reflectance intensity and the bandwidth of the stopband can be estimated by the equations (1.6) and (1.7), respectively:

$$R = \left[\frac{n_0 - n_s \left(n_l / n_h \right)^{2N}}{n_0 + n_s \left(n_l / n_h \right)^{2N}} \right]^2 \tag{1.6}$$

and

$$\Delta\lambda_0 = \frac{4\lambda_0}{\pi} arcsin\left(\frac{n_h - n_l}{n_h + n_l} \right) \tag{1.7}$$

whereby n_0 is the RI of the surrounding medium, n_s the RI of the substrate, n_l the RI of the low RI material, n_h the RI of the high RI material, and N the number of bilayers.[19]

In Figure 1.5, the practical impact of these two equations (1.6), (1.7) shown above is demonstrated: the influence of the number of bilayers (Figure 1.5a) and the RI contrast (Figure 1.5b; the low RI is fixed and the high RI is changed among the spectra).
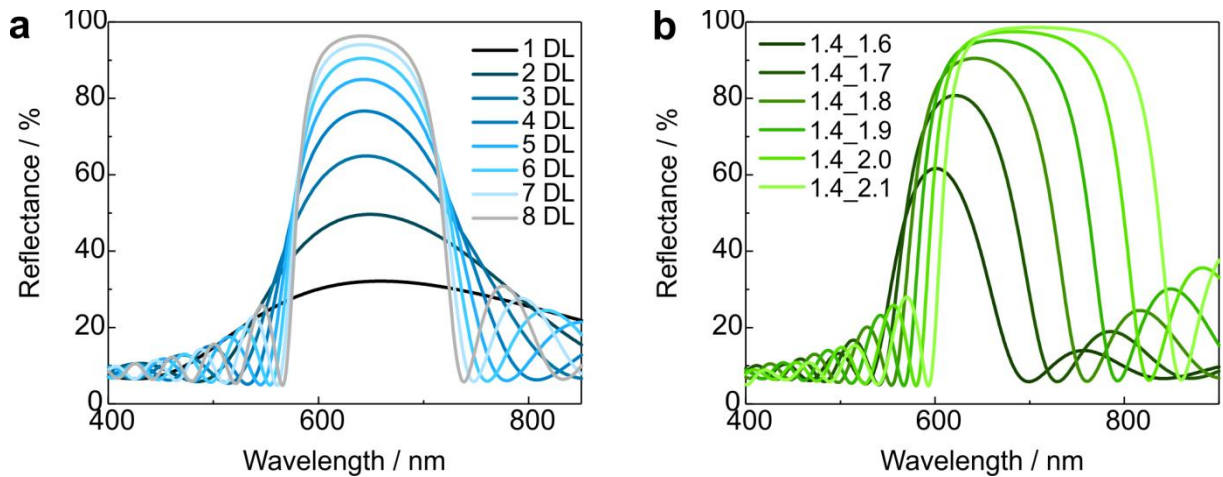
Figure 1.5: Theoretical reflectance spectra demonstrating the spectral changes with increasing number of bilayers (a) and increasing RI contrast (b). Both systems were calculated with a glass substrate (n = 1.55) and a low RI of n_l = 1.4. In (a) the high RI was fixed to n_h = 1.8, and the number of bilayers was varied from 1 to 8. In (b) the number of bilayers was fixed to six, and the high RI was varied from n = 1.6 to n = 2.1 in steps of 0.1.

On the one hand, according to Figure 1.5, the number of bilayers has a high impact on the reflectance intensity, which increases significantly and the stopband becomes more defined and narrower with increasing number of bilayers. On the other hand, changing the RI contrast induces a change in the reflectance intensity, as well as in the bandwidth of the stopband. For these reasons,

the design before the fabrication and the reverse engineering after the fabrication has an important role to achieve tailor-made optical properties of these multilayered structures.

1.2.2 OPTICAL PROPERTIES OF RESONATORS

PCs are also called "semiconductors for light"[15] as they exhibit a characteristic bandgap for photons arising from the periodicity in their dielectric properties, similar to "electronic semiconductors" whose band gap arises from their periodic crystal structure and the resulting periodic potential for electrons. Analogously to semiconductors, 1DPCs can be doped by introducing defects, e.g. a layer with a differing optical thickness, as illustrated in Figure 1.6a,[17, 25] which breaks the periodicity and generates allowed states in the stopband region. A controlled inclusion of defects in all types of PCs (1D, 2D and 3D) is an important feature to control light in the stopband range.[31-34] In 1DPCs, upon introduction of the defect layer, a well-defined dip in the reflectance spectrum occurs within the photonic stopband (Figure 1.6c) The position and the intensity of this transmission maximum depend on the optical thickness of the defect layer.[17] This configuration leads to very accurate changes in the spectrum upon optical thickness changes, i.e. by analyte infiltration in porous structures for instance, resulting in an accurate optical sensor readout, as the sharp dip in reflectance serves as a well-defined probe.[35]
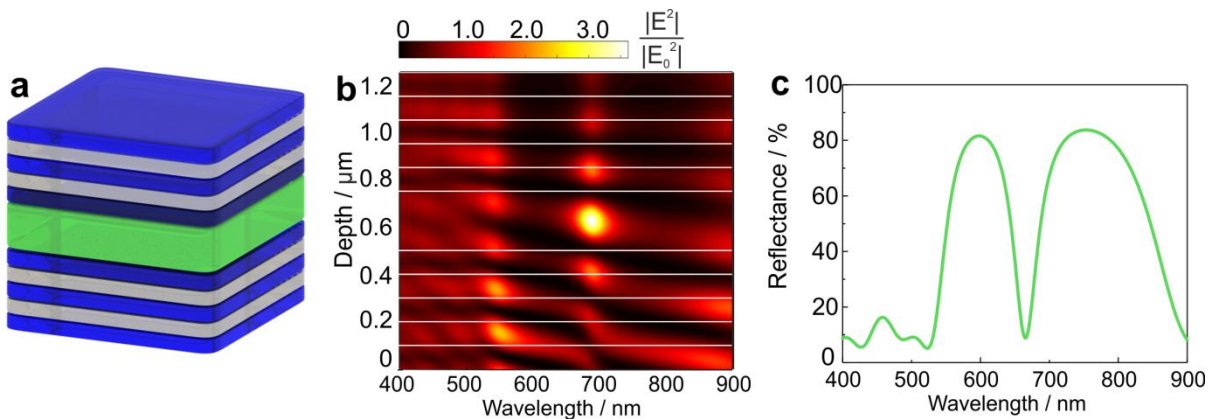
Figure 1.6: Structural and optical properties of an optical resonator structure. (a) Schematic illustration of a resonator. (b) Calculated EM field intensity distribution within the optical resonator. The white lines refer to the interfaces in the structure. (c) Theoretical reflectance spectrum of an optical resonator structure. The structure of the resonator for (b) and (c) is based on the optical thicknesses d_1 = 100 nm, n_1 = 1.40, d_2 = 100 nm, n_2 = 1.90 and d_{def} = 225 nm, n_{def} = 1.40.

The integrated defect layer serves also as a cavity, i.e. one can obtain a strong localization of light in the defect layer, and the strong enhancement in EM field intensity. The calculated EM field intensity distribution of a structure with the layer thicknesses d_1 = 100 nm, n_1 = 1.40, d_2 = 100 nm, n_2 = 1.90 and d_{def} = 225 nm, n_{def} = 1.40 is depicted in Figure 1.6b. The EM field intensity enhancement in the

cavity can lead to a strong modification of absorption[36] and emission[37] properties of an integrated component and offers a possibility to utilize these in sensing applications.[32]

1.3 OPTICAL SENSING *VIA* PHOTONIC CRYSTALS

One of the application fields, which developed dynamically since the discovery of photonic crystals, is the sensing field.[19, 38, 39] According to the Bragg-Snell law equation (1.5), the position of the photonic stopband and with it, the structural color can be determined from the optical thicknesses of the constituent layers. This not only means that the reflectance properties can be designed with the careful fabrication of the structure, but thus also the structural color can be modified dynamically. Once the optical thickness, e.g. the physical layer thickness or the RI, changes in response to external stimuli, photonic stopband changes occur, as illustrated in Figure 1.7.
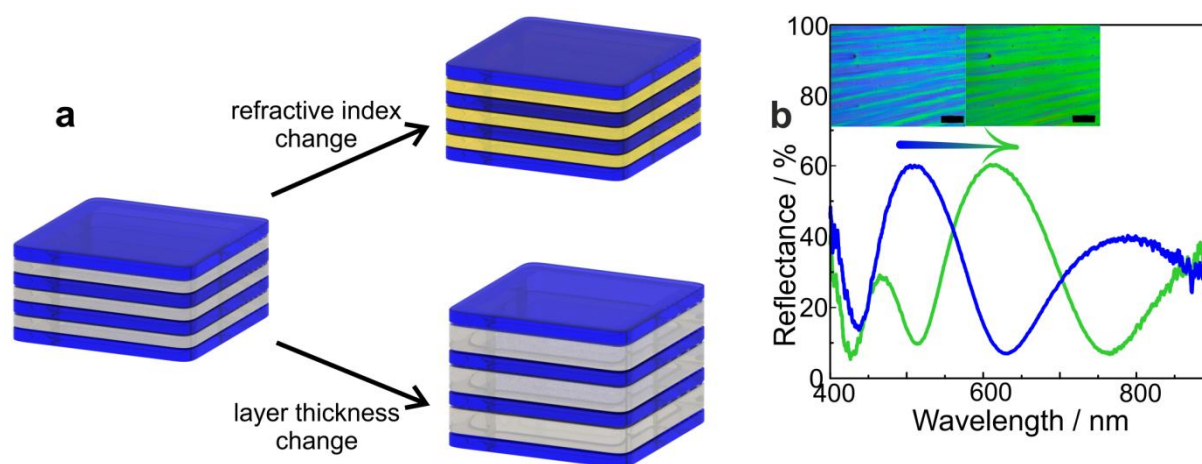
Figure 1.7: Schematic illustration of the sensing mechanism of 1DPC optical sensors based on RI or layer thickness changes of the integrated layers. (a) Scheme of the two possible sensing mechanisms: the RI change (top) and the layer thickness change (bottom). (b) Reflectance spectra of a 1DPC before (blue) and after (green) exposure to water vapor showing a stopband shift, inset: microscope images demonstrating different structural colors cause by humidity level changes. Scale bar: 200 μm.

Consequently, PCs exhibit a great potential to translate external stimuli changes into structural color changes, and thus serving as colorimetric physical, chemical and biological sensors.[19] One of the main advantages is that the sensing principle also works without labeling (in contrast to e.g. a fluorescent tag in a fluorescence sensor) and that the color change can be read out, in principle, qualitatively also by the naked eye. The well-defined optical properties accompanied by a simple structure make these colorimetric sensors competitive with other optical sensors.

– Introduction –

In the last three decades, numerous PC based optical sensors were reported for various sensing applications and sensing analytes. Just to name some of the representative systems, various chemical sensors for metal ions (Cu^{2+},[40] Pb^{2+},[41, 42] Ca^{2+},[43] Ba^{2+}, K^+, Zn^{2+}[44]), for ionic strength and pH,[45] other chemically and biologically relevant analytes, such as glucose,[40, 46] volatile organic compounds (VOC),[47-52] organic solvents,[53, 54] humidity,[55-57] for physical stimuli such as temperature[58, 59] or pressure,[60, 61] and also various biological sensors[54, 62-64] were presented.

In the main focus of this thesis are functional material based 1DPCs and resonator structures for vapor sensing applications, hence in the next chapter an overview of state-of-the-art VOC and humidity sensors is presented.

1.3.1 FUNCTIONAL MATERIAL BASED SOLUTION PROCESSED 1D PHOTONIC CRYSTALS FOR CHEMICAL SENSING APPLICATIONS

According to the Bragg-Snell law, equation (1.5), 1DPC based optical sensing relies on two main mechanisms, first on the changes in RI upon analyte infiltration, and secondly on the changes in the physical layer thickness. 1DPCs for which the sensing mechanism is based on the swelling or shrinking of the layers operate on intercalation or inclusion of analyte molecules into the layered structure. In Figure 1.8, one of the possible mechanisms for layer thickness increase is shown, namely the intercalation of the analyte molecules into the sensing material.
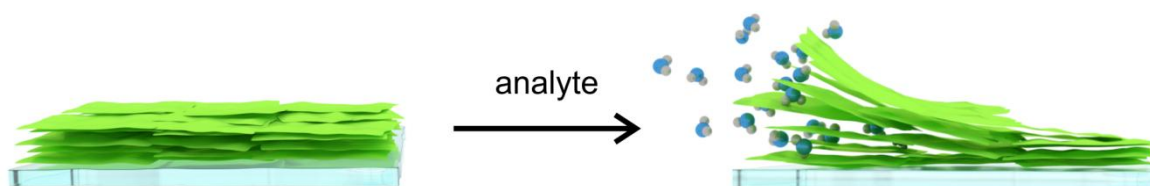
Figure 1.8: Schematic illustration of the intercalation mechanism of an analyte into a thin film created of 2D nanosheets.

The other possibility to manipulate the photonic stopband and to utilize it for sensing applications is by changing the RI of the layers. Devices which are designed for sensing applications *via* RI changes usually possess high porosity, which is either given by template-induced porosity or by the inherent structural porosity of the materials, or by textural porosity, if the layer is composed of dense nanoparticles. The RI of such porous layers can be estimated by the effective medium approximation (EMA), whereby for different systems different models apply, such as parallel or series model, the Maxwell-Garnet equation or the Bruggeman model.[65, 66] In all models, the effective RI of the entire dielectric layer is determined as an interplay of the layer material and the pores using different approximations. In the models, no information about pore size or arrangement can be obtained or is

24

included. The most commonly used EMA, which was also used in this thesis, is the parallel model, which can be written for the real part of the RI according to equation (1.8)

$$n_{eff} = (1-x)n_1 + xn_2 \qquad\qquad (1.8)$$

whereby n_1 and n_2 are the RIs of the layer material and the pores, respectively, and x is the porosity. The parallel model gives the effective RI as a linear function of the RIs of the continuous and dispersed phases. By calculating porous structures and sorption procedures, n_2 will be modified according to the filling fraction of the pores.
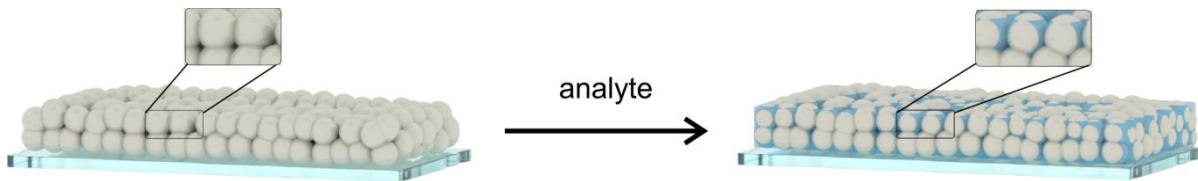
Figure 1.9: Schematic illustration of the sensing principle based on RI changes of a nanoparticle based thin film. The image shows the condensation of the analyte in the textural pores.

These two mechanisms – sensing based on thickness changes and sensing based on RI changes – are naturally not completely independent of each other, but in most of the cases one of the two dominates the sensing mechanism. In this chapter, functional material based 1DPC sensors will be discussed, which either rely mainly on RI changes or mainly on layer thickness changes. Hereby, the 1DPCs are categorized by the effect that has the largest impact on the sensing behavior.

1.3.1.1 SENSING PLATFORMS BASED ON RI CHANGES – POROUS 1D PHOTONIC CRYSTALS

The history of sensing *via* 1DPCs started with the utilization of RI changes in porous layers, with templated mesoporous silicon dioxide (SiO_2) and titanium dioxide (TiO_2) layers (Figure 1.10, 1), reported by Choi *et al.* in 2006.[53] Upon immersion of the 1DPC into different organic solvents (Figure 1.10, 2), the structural color changes due to the filling of the mesopores of the structure and a stopband shift occurs (Figure 1.10, 3). These proof-of-concept experiments show that porous 1DPCs can be utilized as RI sensors, as they change the structural color depending on the RI of the analytes.
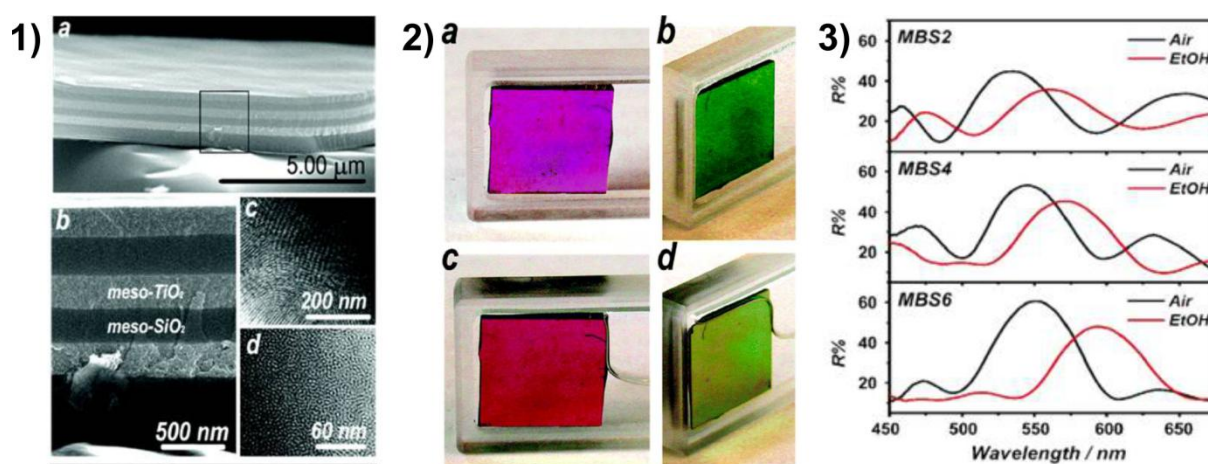
Figure 1.10: The first 1DPCs for sensing applications. (1) SEM images of templated mesoporous SiO_2 and TiO_2 based 1DPCs showing (a-b) the cross section images and (c-d) the mesoporous character of the layers. (2) Structural color changes of the created 1DPCs upon infiltration with solvents, (a-b) show the 1DPCs without a solvent at normal incidence and at a higher viewing angle, demonstrating the angle dependency of the structural color and (c-d) show the infiltrated samples with changed structural color also at normal incidence and higher incident angle. (3) Reflectance spectra of three 1DPCs before and after infiltration with ethanol. Image adapted with permission.[53] Copyright of the American Chemical Society.

Later, Míguez and co-workers reported highly porous 1DPCs and optical resonator structures, which are built of SiO_2 and TiO_2 NPs (Figure 1.11, 1). The structural and optical properties and the response of these novel highly porous systems was reported extensively, including the behavior of the optical properties to changes in the number of bilayers, the thickness of the layers and the cavity.[67] In this system, the porosity is formed by textural pores, which are created by the interparticle voids showing mesoporous behavior.[35, 68, 69] Instead of liquid analytes, it was shown that VOCs can be detected and optical isotherms based on the stopband shifts can be measured (Figure 1.11, 2). These systems posses no chemical sensitivity; instead, they act as a RI sensor, i.e. depending on the RI of the analyte vapors, the optical response of the 1DPCs or the resonator differs (Figure 1.11, 3).
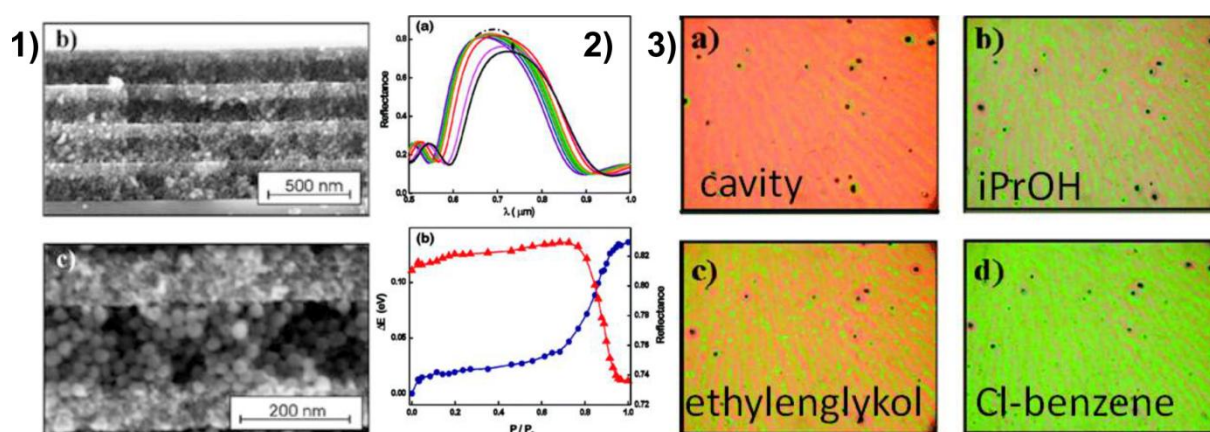
Figure 1.11: The first NP based 1DPC for vapor sensing applications. 1) SEM cross section images of the fabricated 1DPCs demonstrating the highly porous behavior of the layers, as they are containing SiO_2 and TiO_2 nanoparticles. 2) Reflectance spectra and stopband shifts at different ethanol vapor pressure. 3) Optical microscope images of the NP based 1DPCs after infiltration with different organic solvents. Image adapted with permission. [35, 68] Copyright of the American Chemical Society.

Such NP based 1DPCs are nowadays commonly used in the research field as standard porous platforms. In the sensing field, Bonifacio *et al.*[41, 70] reported in 2010 and 2011 two examples for applications of such platforms for biologically relevant sensing problems, for food and water quality control. Hereby, they modified the NPs covalently with trialkoxysilanes and created an array of differently modified 1DPCs. The differentiation of the analytes was performed based on a statistical method, namely principal component analysis (PCA) of the color changes of the single 1DPCs in the array.

To illustrate the diversity of these NP based 1DPC platforms, other approaches were demonstrated in the literature, such as for visualization of chemical mass transport, e.g. diffusion of solvents in the porous matrix.[54] Additionally, an electronic detection scheme was also coupled to the optical readout *via* a narrow-band light source and a photodiode. Due to changes in the stopband position, the intensity of light source is modified, which can be detected with a photodiode and converted into electric current changes.[54, 71]

Other metal oxide NPs were utilized in vapor sensing experiments in 1DPCs with diverse aims. To increase the RI contrast within the stack, WO_3 nanoparticles were applied in periodic,[72] tandem and gradient structures.[73] With this, the RI contrast can be increased compared the commonly used titania based systems. To avoid the UV absorbing properties of titania, and to create a radiation shielding device purely based on reflection, high RI ZrO_2 NPs were combined with the commonly used low RI silica nanoparticles.[74, 75] Further, SnO_2, Sb- and In-doped tin oxide particles[76] were applied in 1DPCs for vapor and gas sensing applications. The integration of these conductive

materials into such platforms is of interest, as an electric signal, such as the conductance change, could be combined with the readout based on color changes.[25]

To achieve a higher molecular sensitivity, functional nanoparticles, such as metal-organic framework (MOF, Figure 1.12),[48, 49, 77] and zeolite NPs[78, 79] were developed and integrated into 1DPC devices. MOFs provide a chemical platform with the possibility for covalent and non-covalent functionalization and with this, an inherent chemical selectivity (Figure 1.12). Further, these structures exhibit structural microporosity, which can serve as molecular sieve providing size-selectivity, while keeping the highly porous character within the entire structure provided by the textural pores. Ranft *et al.*[77] demonstrated an optical differentiation of chemically similar analytes, ethanol and methanol, with an array of three different MOF NP (ZIF-8, CAU-1, HKUST-1) based 1DPCs (Figure 1.12). To achieve more defined adsorption sites, a controlled growth of MOFs (HKUST) was applied in the 1DPC fabrication, and the vapor sensing capability was demonstrated.[76] Further, mesoporous silica particles were combined with titania layers to achieve an additional chemically tunable porosity in the 1DPCs.[80]
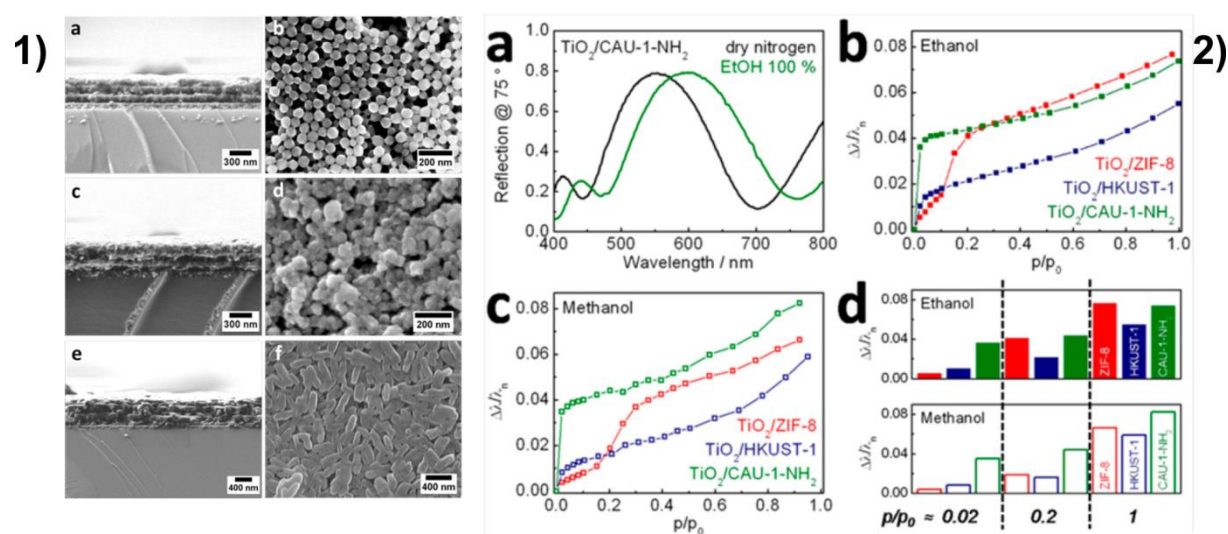
Figure 1.12: MOF NP based 1DPCs. (1) SEM images demonstrating the structural properties of the MOF NP based 1DPCs showing the morphology of the different particles and the cross sections of the 1DPCs: (a-b) ZIF-8 NP, (c-d) HKUST-1 NP, (e-f) CAU-1 NP based 1DPCs. (2) Optical response of the three different MOF NP based 1DPCs towards solvent vapors: (a) the stopband shift of the CAU-1 NP based 1DPC upon ethanol infiltration, (b-c) the optical isotherms of the three different systems upon ethanol and methanol adsorption, (d) comparison of the relative stopband shifts of the three systems at different ethanol and methanol vapor pressures. Image adapted with permission.[77] Copyright of the American Chemical Society.

Although by today, a big pool of functional colloidal NPs were developed for sensing applications in 1DPCs with a high molecular selectivity, the main disadvantage of these RI based detection schemes is their low sensitivity. The extent of the stopband change is limited through the moderate changes in

the optical thickness of the layers, caused by the RI change, which translates only into rather small stopband shifts, according to the Bragg-Snell law (1.5). To avoid this, 1DPCs with a swelling component were developed to achieve larger stopband shifts.

1.3.1.2 SENSING PLATFORMS BASED ON LAYER THICKNESS CHANGES

In order to overcome the drawbacks of the RI change based detection principles and to enhance the resolution due to larger optical thickness changes of the individual layers, devices were developed where the physical layer thickness is modulated as a response to the presence of a vapor. This has a higher impact on the optical thickness and with this also on the resolution and the sensitivity.[25]

In 2007, shortly after the publication of the first solvent-responsive 1DPCs,[53] the first swelling 1DPCs were reported (Figure 1.13).[81] In this work, polymer layers were used as the stimuli-responsive material in a 1DPC, and upon infiltration with a liquid analyte, an enormous, full-spectral stopband change was observed. Following this principle, many other polymer based 1DPCs were reported in the last few years. One of the largest stopband changes was obtained by Tian *et al.*[57] applying a hydrogel based 1DPC with a stopband shift of around 300 nm. Further, a plethora of hybrid inorganic-organic polymer based structures were created for chemical vapor and solvent sensing and detection approaches.[55, 82-85] Although the chemical selectivity can be fine-tuned through the polymer composition, and the high sensitivity is given by the swelling mechanism, the chemical and long-term stability of the organic layers and the slow response time in the range of several hours present severe drawbacks of these systems.
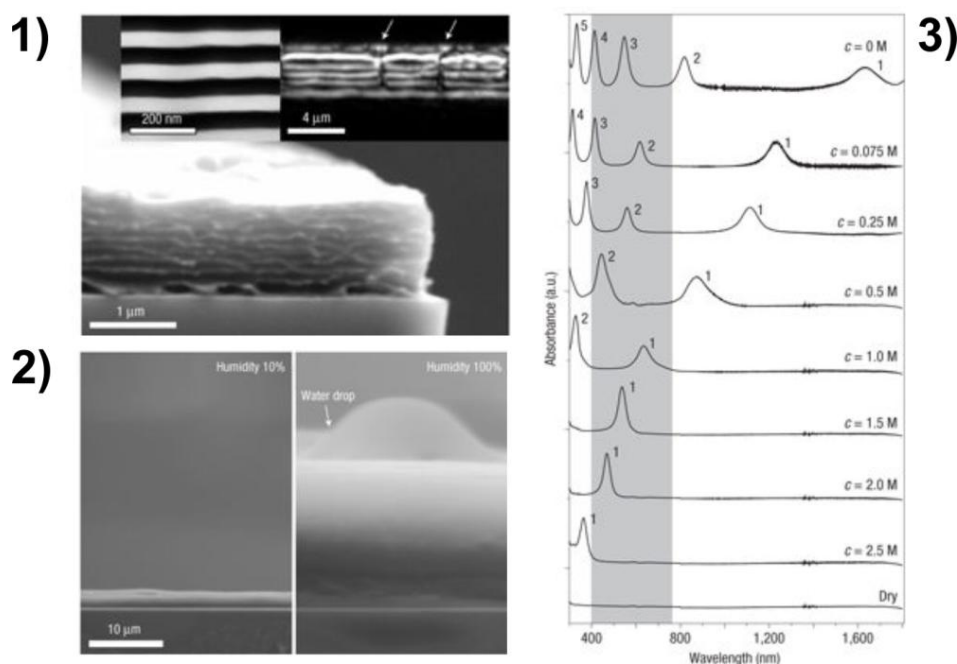
Figure 1.13: The first responsive polymer based 1DPC. (1) SEM cross section images of the polymer-TiO$_2$ based hybrid 1DPC showing the homogenous stacking of the two materials. (2) Environmental SEM image of the polymer layer at 10% and 100% humidity, showing a swelling behavior of the polymer layer. (3) Changes in the absorbance spectrum of the 1DPC upon infiltration with water with a different ionic strengths. Image adapted with permission. [81] Copyright of the Nature Publishing Group.

In order to circumvent the disadvantages of the organic polymer based 1DPCs, inorganic swelling materials were developed and integrated into the multilayered structure. Clays[86-88] are prominent candidates, which show a pronounced swelling in the presence of surfactant molecules, such as CTAB or polyelectrolytes, such as poly(diallyldimethylammonium chloride), PDDA (Figure 1.14, 1). In these examples, porous clay layers were combined with porous titania as an optical contrast material, and the time-dependent stopband changes upon analyte intercalation was reported. Further, layered double hydroxides (LDH, Figure 1.14, 2), were also presented as a functional material in 1DPCs. Upon hydratation-calcinantion cycles, the changes of water amount in the LDH layer lead to layer thickness changes, which translate into reversible structural color changes in the 1DPC. On these LDH based 1DPCs, no comprehensive sensing studies were performed, but the switching of the structural color upon hydratation and calcination was demonstrated.
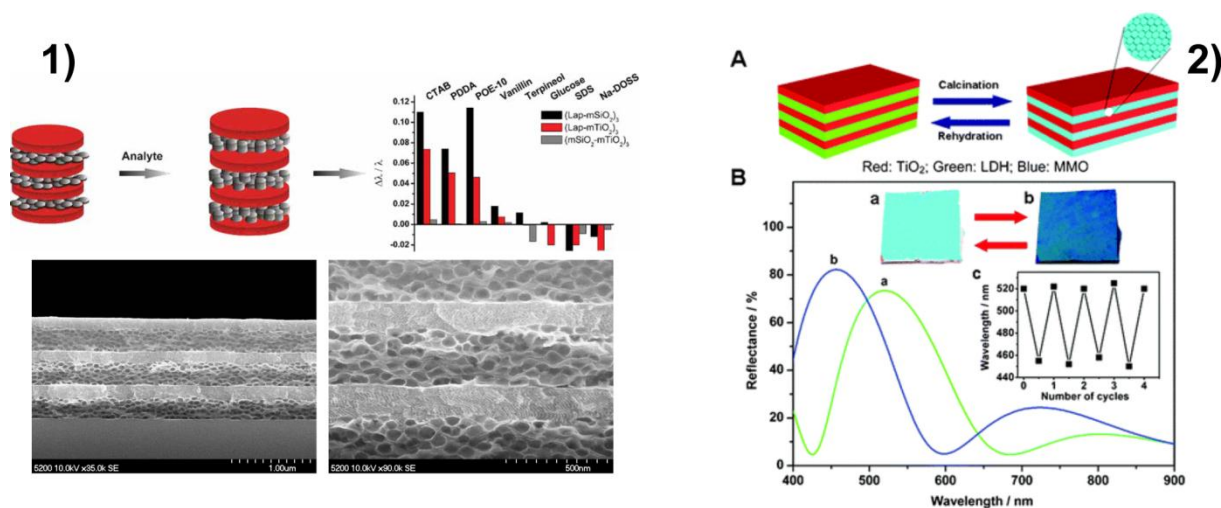
Figure 1.14: Structural and optical properties of 1DPCs with inorganic layered materials as the stimuli-responsive component. (1) Laponite clay and TiO_2 NP based Bragg stacks. Top: the porous clay shows a pronounced swelling in the presence of different surfactants, as these are capable of intercalating into the structure.[87] Bottom: SEM cross section images of the TiO_2-clay 1DPC showing the homogenous stacking order and the porous appearance of the clay, which was templated upon the synthesis with nanospheres to obtain a porous structure.[86] Images were adapted with permission. [86, 87] Copyright of of WILEY-VCH[87] and the American Chemical Society.[86] (2) Optical and sensing properties of the LDH based 1DPCs: (A) schematic illustration of the sensing principle based on the layer thickness changes of the LDH layer upon hydratation, (B) optical response of the LDH based 1DPCs to hydratation and calcination processes. Image was adapted with permission. [89] Copyright of the the Royal Society of Chemistry.

Using a combinatorial approach connecting the large stopband shifts and the chemical selectivity of MOFs, Hu *et al*.[90] reported a 1DPC based sensing platform, which relies on the breathing effect of the integrated MIL-88 MOF nanoparticles. The flexible MOF structure is capable of swelling in a different extent upon adsorption of different VOCs.

In this thesis, 2D nanosheet materials were studied and integrated into 1DPCs in order to combine the advantages of the robust inorganic materials with the layer thickness changing capability upon analyte intercalation. The sensing performance along with the structural and optical properties was studied in depth.

1.3.2 CURRENT CHALLENGES IN PHOTONIC CRYSTAL SENSING

Although since the last two decades, many groups working in the field of 1DPC sensing apply different approaches, architectures, materials and techniques, there are still remaining challenges in this research field, which emerge partly from challenges in the sensing field in general, and are partly related specifically to 1DPCs. The main challenges are related with the sensitivity, selectivity, stability, readout schemes and material improvement, as will be discussed in the following.[91]

- The sensitivity of 1DPCs is mainly limited by small stopband shifts, as the majority of 1DPC optical sensors are based on RI changes due to analyte infiltration. Usually, the filling of the porous matrix translates into stopband shifts of some tens of nanometers at best. With increasing stopband changes, the sensitivity (signal change per analyte concentration) and the resolution can be increased, leading to possible naked-eye-readout or a detection scheme based on a previous color calibration. This development would pave the way towards photonic test stripes or other easy-to-use probe methods.

- Based on the issue of low sensitivity and small signal changes, the readout schemes are usually limited to reflectometry or interferometry, but these techniques are impracticable for commercially used devices. In the last few years, several other approaches were developed to bypass this technique. The electro-photonic nose was presented, whereby the stopband shifts change the intensity of a narrow light source by changing the reflectance regime upon analyte uptake. These light intensity variations could be translated by means of a photodiode into electric current changes. Further, photoluminescence [92-94] and optical absorption due to plasmonic effects[95] were combined with photonic structures and were also presented as an attractive readout scheme.

- Another aspect, the stability, is restricted in two different ways: the stability of the sensor itself and the signal stability. On the one hand, upon storage, the sensing performance can be altered, giving rise to the need for more frequent calibrations. On the other hand, the sensor itself can be damaged or poisoned during the sensing event, which is highly unfavorable and impractical for practical applications.

- Finally, one of the largest issues in the sensing field in general is the selectivity and the cross sensitivity to other chemically similar analytes. Many sensors in this field that do not rely on molecular recognition or labeling schemes (biological sensors), are usually not chemically selective and distinguish the analytes often only by RI or solvent polarity.[53, 69] In other approaches, the selectivity issue is solved with complicated statistical data evaluation, such as principal component analysis (PCA),[41, 70, 77] or with the application of complex hierarchical structures.[52]

For these challenges, the development of novel sensing materials, which compensate for the above shortcomings by featuring for example inherent chemical selectivity or a pronounced swelling capability, is highly desired. Further, the optimization of existing materials in terms of monodispersity, homogeneity and crystallinity can also be crucial to establish more efficient devices.

1.4 2D MATERIALS

2D materials are crystalline materials with a thickness of a single layer of atoms or one crystallographic unit cell, having a thickness in the range between 1 Å and 1 nm and lateral dimensions of several hundreds of nanometers up to the micron range. Although the first crystalline 2D material, graphene, had already been studied theoretically by Wallace[96] and isolated and imaged already in 1962 by Boehm *et al.*,[97] its "re-discovery", followed by extensive experimental work and characterization by Andre Geim and Konstantin Novoselov[98] tackled renewed research interest in this carbon modification in the material science community. In 2010, Geim and Novoselov were awarded with the Nobel Prize "for groundbreaking experiments regarding the two-dimensional material graphene".[99] The exceptional electronic, mechanical, thermal and optical properties differ significantly from graphite, the three-dimensional (3D) bulk material, which can be lead back to the unusual electronic and optical properties as well as the high anisotropy and size confinement effects of the single layered hexagonal lattice of carbon atoms in graphene. After this first revolutionary discovery, new ways were paved towards other classes of 2D materials, with an even wider scope of physical and chemical properties.[100] The 2D materials discovered as of today show a rather broad chemical variety, which gives the possibility for diverse applications as single nanosheets and also rationally designed nanodevices[101] or hybrid artificial solids.[102-104]

1.4.1 EXFOLIATION

The synthesis methods of these single-layered nanosheets can be performed by different exfoliation methods:[100] mechanical exfoliation or solution assisted exfoliation into stable colloidal suspensions. Exfoliation is in general defined as a method, in which larger aggregates are decomposed into smaller particles or nanosheets, whereby more specifically, if the bulk material is decomposed into single nanosheets, the process is called delamination. The exfoliation method is mostly dependent on the type of the bulk material. In the following, some general exfoliation routes will be presented.

The mechanical exfoliation includes methods such as the scotch tape method or rubbing the surface of a layered crystalline material to another surface to obtain single or multilayered flakes.[98] Besides graphene,[105] several inorganic van der Waals solids were isolated with this method, such as MoS_2[106, 107] or $NbSe_2$.[108] Although this fabrication method is very straightforward and fast, single layered nanosheets are produced only in the minority, compared to multilayered flakes, which limits the scalability to larger scale production. For this reason, solvent assisted exfoliation methods are more preferred for a sufficient nanosheet fabrication.

Solvent-mediated exfoliation methods were reported in the literature for manifold nanosheet compositions,[109-119] which can result in lateral sizes of several microns. Further, the separation of single layered sheets from multilayered flakes is very straightforward by means of sedimentation or centrifugation. Groundbreaking works on solution processed exfoliation were reported already in the 1990s by Sasaki et al.,[120-121] whereby the exfoliation of single nanosheets was proved by diverse methods. Only one decade later, with the rediscovery of graphene and the increasing research interest for 2D materials, these exfoliation methods gain in importance as they make a broad palette of nanosheet materials accessible.[122-123] Since these developments, several solution based exfoliation methods, aiming at the disruption of the attractive interlayer forces, were developed and adapted for the materials to be exfoliated. In the following the exfoliation methods for the two main types: van der Waals solids and layered ionic materials, are presented.

Van der Waals solids are layered bulk materials, which consist of neutral (i.e. non-charged) layers of atoms with rather weak van der Waals interlayer bonding. For van der Waals solids, besides the straightforward but less efficient scotch tape method, different solvent mediated exfoliation routes were presented. The most straightforward method is the mechanical exfoliation of the layered structure by ultrasound treatment of the bulk material in an appropriate solvent.[117] The choice of the solvent depends on the chemical properties and the surface tension of the bulk material, whereby for a sufficient exfoliation, the solvent molecules intercalate the van der Waals solid, weaken the interlayer interactions and upon sonication, the bulk material is exfoliated. The drawback of this method is that not only single layer nanosheets are observed, but also multilayered flakes. Another method, which circumvents this disadvantage, is the reductive or oxidative intercalation with a subsequent exfoliation. One example is the intercalation of lithium *via* electrochemical routes or chemical methods. By a subsequent sonication step, single layered nanosheets are observed with a large lateral size. In this process, most probably lithium reduces the bulk material (metal center) in the first step. Upon contact with water, the metal center is oxidized again and caused by hydrogen production, the bulk material delaminates into single nanosheets.[110, 124, 125] Further, the chemical oxidation of the bulk material can lead to the introduction of repulsive forces, such as the oxidation of graphite to graphene oxide, which significantly facilitates its subsequent exfoliation in polar solvents such as water.[126] For the reductive and oxidative intercalation methods, a subsequent stabilization by electrostatic forces[118] or surfactants[127] is needed to prevent agglomeration.

Layered ionic solids are bulk materials consisting of negatively or positively charged crystallographic layers, whereby charge compensating anions or cations are located in the interlayer space. For layered ionic materials, different solvent-mediated exfoliation routes are available. The simplest method, which only applies for specific bulk materials, is the spontaneous exfoliation by stirring,

shaking or sonicating the bulk material in a solvent.[128, 129] Hereby the driving force for the exfoliation is the hydratation of the charge compensating ions in the interlayer gallery. Usually, anionic and cationic layered materials are exfoliated *via* ionic exchange reactions (Figure 1.15). In the first step, the initial charge compensating ions between the layers in the bulk material are exchanged against larger ions (Figure 1.15, step 1).[130] This increases the interlayer distance and weakens the attractive forces between the layers, which favors the exfoliation. Secondly, an optional ion exchange and the addition of bulky chemical intercalating agents (usually TBA or TMA)[104, 131] can weaken the attractive forces between the nanosheets further (Figure 1.15, step 2). After the ionic exchange reactions, mechanical forces, such as stirring or shaking, can lead to the delamination of the bulk material. Hereby, the intercalating agents also inhibit the reassembly by repulsive forces after exfoliation.
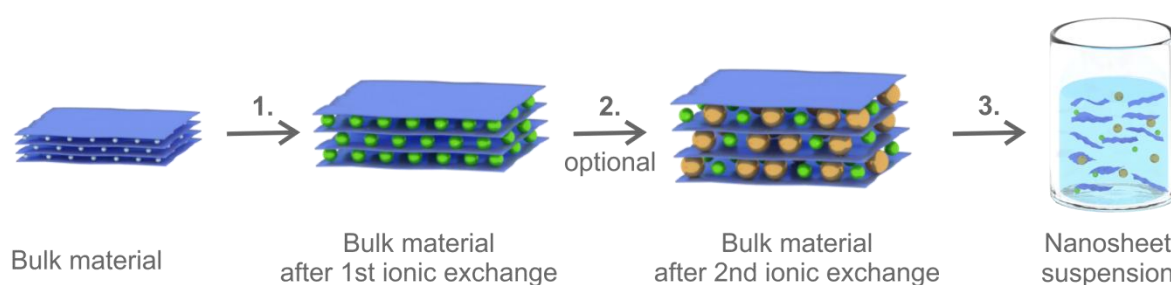
Figure 1.15: Schematic illustration of a typical exfoliation procedure for 2D nanosheets. In the first step, an ionic exchange reaction of the layered bulk material is performed. Hereby the ions in the interlayer space are exchanged against other ions, which weaken the attractive forces between the layers. Secondly, as an optional step, a chemical intercalator (TBA^+, TMA^+) can be introduced into the interlayer space, to weaken the attractive interactions further. Finally, by applying mechanical forces, e.g. by stirring the bulk material in a solvent, exfoliation can be achieved and a stable colloidal suspension obtained.

In the last decade, plenty of 2D materials were synthesized, characterized and numerous application fields were opened up, including transistors,[132-134] optoelectronic devices,[135] memory devices,[132, 136, 137] capacitors,[138, 139] magneto-optical nanostructures,[140, 141] photocatalytic applications,[142, 143] and photo-conductive cells.[144, 145] However, as the main focus of this thesis lies on sensing devices, some examples of sensing schemes using 2D materials as active components will be given.

1.4.2 2D MATERIALS FOR GAS AND VAPOR SENSING

With the development of the diversity of 2D materials, several applications could be revolutionized, miniaturized and brought into a lab-on-a-chip fashion by using these nanoscale materials. One of these applications is gas and vapor sensing, whereby the miniaturization is an important factor for commercial and industrial applications.

Most of the presented 2D material based sensor devices rely on electronic changes of the sample. Upon adsorption, the sensing material can act as an electron donor or acceptor to the adsorbed gas molecules, and the electric properties, such as resistivity or conductivity can change and be measured. Many examples based on different readout schemes were presented in the last few years; here a selection of the most important principles and examples is presented.

Chemiresistive sensors are capable of changing the resistivity upon analyte adsorption. Using this technique, a broad palette of chemical analytes, such as humidity,[146-150] mercury vapor,[151] triethylamine,[152, 153] methane,[154] ammonia[155] or VOCs[156] could be reliably detected by MoS_2, functionalized MoS_2, SnS_2 or VS_2 nanosheet based devices. MoS_2 and graphene based devices were further used in field effect transistor (FET) based sensors for environmental monitoring, such as ethanol,[157] hydrogen,[158] NO,[159] NO_2[160] or ammonia[161] detection. FETs have some advantages, such as portability, the capability for miniaturization and their high sensitivity, which makes these types of sensors important candidates in this group. In FETs, a semiconductor channel, the sensing material, connects the metal electrodes, the source and the drain. Upon analyte adsorption, the drain current flowing from the source to the drain, is modulated, which gives the sensing signal.[162]

Further, 2D nanosheet material based Fabry-Pérot devices were fabricated for humidity and VOC sensing applications, whereby all fabricated thin film devices act as optical sensors and the interference color change based on the layer thickness changes can be detected. The layer thickness changes, in turn, were induced by intercalation of the analyte molecules in the interlayer space of the randomly restacked nanosheet based thin films.[163]

1.5 OBJECTIVES

The main goal of this thesis was to tackle salient challenges (such as sensor and signal stability, selectivity, sensitivity, the development of simple readout schemes, higher optical quality and the exploration of new sensing materials) in 1DPC based optical sensors. These challenges were addressed through the integration of environmentally responsive functional materials into 1DPCs. Specifically, inorganic 2D nanosheets were synthesized, exfoliated into stable colloidal suspensions and integrated into 1DPCs, which were then characterized in terms of their structure, morphology, and sensing characteristics.

The first objective was to increase the stopband shifts by using swellable materials, which results in larger sensing signals and higher sensitivity and signal resolution. The aim of the first project was to integrate 2D antimony phosphate ($H_3Sb_3P_2O_{14}$) nanosheets into 1DPCs, as these are known to swell in their bulk form in the presence of ambient water. By utilizing the enhanced sensitivity of the

exfoliated nanosheets towards water vapor, a further goal of this project was to realize other sensing approaches additionally to conventional humidity sensors. Inspired by the high sensitivity, one attempt hereby was to realize touchless positioning devices, which are able to track very small humidity changes in a very short time, such as the humidity gradient of the human finger (Chapter 3) and characterizing these novel sensors (Chapter 4).

The second aim was to realize high selectivity towards a certain analyte whilst enabling the sensor to identify also other analytes or vapor mixtures, similar to photonic nose applications. For this project, another member of the antimony phosphate family, $HSbP_2O_8$, was integrated into 1DPCs, and the optical response based on the intercalation of analyte molecules was tested for several VOCs and VOC mixtures (Chapter 5). Furthermore, simple sensing descriptors, such as saturation time and stopband shift, were analyzed.

A further goal of this thesis was to improve the optical properties of these functional 1DPCs whilst maintaining good sensing performance. For this goal, another type of nanosheets, namely ultrahigh RI lithium tin sulfides, were integrated into 1DPCs. In these systems the optical contrast increases due to the high RI of the nanosheets, which leads to a better optical quality, e.g. higher reflectance intensities with less deposited layers and, hence, decreased material costs. As these structures are still highly receptive for ambient water molecules, the sensitivity towards water vapor is still present. A further goal was to demonstrate the variability of this system, i.e. to combine the nanosheets with different types of NPs or other nanosheet materials and thus to create hybrid structures with enhanced or novel optical and sensing properties (Chapter 6).

In chapter 7, we aimed to address alternative readout schemes besides reflectometry or spectrophotometry. Hereby, we combined the photonic environment with photoluminescent dyes, whose emissive properties are changed depending on the local photonic environment. In order to obtain tailor-made optical properties, a careful theoretical design of the hierarchical photonic structures was necessary, which was done in collaboration with the group of Prof. Hernán Míguez, ICMSE-CSIC, Sevilla, Spain.

Finally, a target of this thesis was to monitor the time-dependent infiltration and propagation of analytes within the photonic structure in order to understand the intercalation mechanism and the molecular diffusion within hybrid nanosheet – nanoparticle 1DPCs. To this end, an experimental set-up was designed which enables the tracking of analytes through the structure. Further, theoretical analysis of the optical measurements by fitting the reflectance spectra and analyzing the time-dependent evolution and diffusion of the analyte molecules into the multilayered structure was

the main focus (Chapter 8). With these studies, information about molecular diffusion, the sensing mechanism, saturation states and sensing kinetics was obtained.
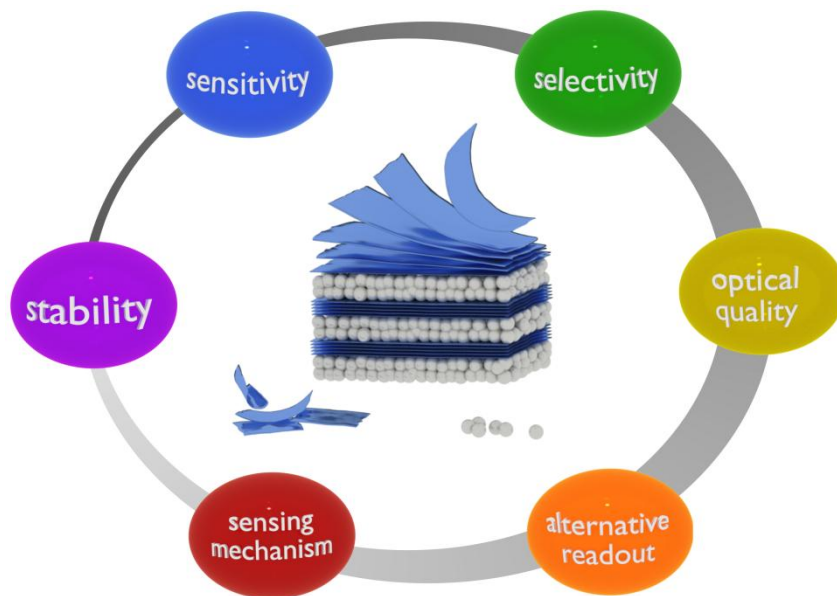
Figure 1.16: Objectives of this thesis showing important sensing characteristics and the materials platform under study, which is a hybrid 1DPC composed of nanoparticle and nanosheet layers.

1.6 REFERENCES

[1] E. Mounier, Y. Développement, *Gas sensor report,* **2018**.

[2] R. A. Potyrailo, *Chem. Soc. Rev.* **2017**, *46*, 5311-5346.

[3] V. Haasz, K. Madani, *Advanced Data Acquisition and Intelligent Data Processing*, River Publishers, **2014**.

[4] M. M. Cruz-Cunha, *Handbook of Research on Mobility and Computing: Evolving Technologies and Ubiquitous Impacts: Evolving Technologies and Ubiquitous Impacts*, Information Science Reference, **2011**.

[5] https://developer.android.com/guide/topics/sensors/sensors_overview.html, accessed: 06.03.2018.

[6] https://www.kachwanya.com/2017/05/29/smartphone-sensors/, accessed: 06.03.2018.

[7] K. Arshak, E. Moore, G. M. Lyons, J. Harris, S. Clifford, *Sensor Rev.* **2004**, *24*, 181-198.

[8] B. Robert, *Sensor Rev.* **2007**, *27*, 7-13.

[9] S. Capone, Forleo, A., Francioso, L., Rella, R., Siciliano, P., Spadavecchia, J., Presicce, D. S., Taurino, A. M., *J. Optoelectron. Adv. M.* **2003**, *5*, 1335-1348.

[10] S. Ishihara, J. M. Azzarelli, M. Krikorian, T. M. Swager, *J. Am. Chem. Soc.* **2016**, *138*, 8221-8227.

[11] L. Rayleigh, *The London, Edinburgh, and Dublin Philosophical Magazine and Journal of Science* **1887**, *24*, 145-159.

[12] E. Yablonovitch, *Phys. Rev. Lett.* **1987**, *58*, 2059-2062.

[13] S. John, *Phys. Rev. Lett.* **1987**, *58*, 2486-2489.

[14] K. Tsakmakidis, *Nat. Mater.* **2012**, *11*, 1000.

[15] E. Yablonovitch, *Scientific American* **2001**, *285*, 47-55.

[16] S. John, *Nat. Mater.* **2012**, *11*, 997.

[17] J. D. Joannopoulos, S. G. Johnson, J. N. Winn, R. D. Meade, *Photonic crystals: molding the flow of light*, Princeton university press, **2011**.

[18] C. López, *Adv. Mater.* **2003**, *15*, 1679-1704.

[19] J. Ge, Y. Yin, *Angew. Chem. Int. Ed.* **2011**, *50*, 1492-1522.

[20] W. Keiichiro, H. Takayuki, K. Kazuhiro, H. Yuichi, M. Shinji, *Jpn. J. Appl. Phys.* **2005**, *44*, L48.

[21] C. I. Aguirre, E. Reguera, A. Stein, *Adv. Funct. Mater.* **2010**, *20*, 2565-2578.

[22] J. Zi, X. Yu, Y. Li, X. Hu, C. Xu, X. Wang, X. Liu, R. Fu, *P. Natl. A. Sci.* **2003**, *100*, 12576-12578.

[23] J. Teyssier, S. V. Saenko, D. van der Marel, M. C. Milinkovitch, *Nat. Commun.* **2015**, *6*, 6368.

[24] G. von Freymann, V. Kitaev, B. V. Lotsch, G. A. Ozin, *Chem. Soc. Rev.* **2013**, *42*, 2528-2554.

[25] L. D. Bonifacio, B. V. Lotsch, D. P. Puzzo, F. Scotognella, G. A. Ozin, *Adv. Mater.* **2009**, *21*, 1641-1646.

[26] P. Yeh, *Optical Waves in Layered Media*, John Wiley & Sons, New York, **1988**.

[27] L. Novotny, B. Hecht., *Principles of Nano-Optics*, Cambridge University Press, **2012**.

[28] J. C. Maxwell, *Philos. T. R. Soc. Lond.* **1865**, *155*, 459-512.

[29] F. Bloch, *Z. Physik* **1929**, *52*, 555-600.

[30] G. A. Ozin, A. C. Arsenault, L. Cademartiri, R. S. o. Chemistry, *Nanochemistry: A Chemical Approach to Nanomaterials*, Royal Society of Chemistry, **2009**.

[31] M. E. Calvo, S. Colodrero, N. Hidalgo, G. Lozano, C. Lopez-Lopez, O. Sanchez-Sobrado, H. Miguez, *Energ. Environ. Sci.* **2011**, *4*, 4800-4812.

[32] Y.-n. Zhang, Y. Zhao, R.-q. Lv, *Sensor Actuat. A: Phys.* **2015**, *233*, 374-389.

[33] P. V. Braun, S. A. Rinne, F. García-Santamaría, *Adv. Mater.* **2006**, *18*, 2665-2678.

[34] J. D. Joannopoulos, P. R. Villeneuve, S. Fan, *Nature* **1997**, *386*, 143-149.

[35] S. Colodrero, M. Ocana, A. R. Gonzalez-Elipe, H. Miguez, *Langmuir* **2008**, *24*, 9135-9139.

[36] O. Sánchez-Sobrado, G. Lozano, M. E. Calvo, A. Sánchez-Iglesias, L. M. Liz-Marzán, H. Míguez, *Adv. Mater.* **2011**, *23*, 2108-2112.

[37] A. Jiménez-Solano, J. F. Galisteo-López, H. Míguez, *Small* **2015**, *11*, 2727-2732.

[38] R. V. Nair, R. Vijaya, *Prog. Quant. Electron.* **2010**, *34*, 89-134.

[39] H. Xu, P. Wu, C. Zhu, A. Elbaz, Z. Z. Gu, *J. Mater. Chem. C* **2013**, *1*, 6087-6098.

[40] J. H. Holtz, S. A. Asher, *Nature* **1997**, *389*, 829-832.

[41] L. D. Bonifacio, G. A. Ozin, A. C. Arsenault, *Small* **2011**, *7*, 3153-3157.

[42] M. M. W. Muscatello, S. A. Asher, *Adv. Funct. Mater.* **2008**, *18*, 1186-1193.

[43] S. Chakravarty, J. Topol'ancik, P. Bhattacharya, S. Chakrabarti, Y. Kang, M. E. Meyerhoff, *Opt. Lett.* **2005**, *30*, 2578-2580.

[44] S. A. Asher, A. C. Sharma, A. V. Goponenko, M. M. Ward, *Anal. Chem.* **2003**, *75*, 1676-1683.

[45] K. Lee, S. A. Asher, *J. Am. Chem. Soc.* **2000**, *122*, 9534-9537.

[46] Y.-J. Lee, S. A. Pruzinsky, P. V. Braun, *Langmuir* **2004**, *20*, 3096-3106.

[47] P. A. Snow, E. K. Squire, P. S. J. Russell, L. T. Canham, *J. Appl. Phys.* **1999**, *86*, 1781-1784.

[48] F. M. Hinterholzinger, A. Ranft, J. M. Feckl, B. Ruhle, T. Bein, B. V. Lotsch, *J. Mater. Chem.* **2012**, *22*, 10356-10362.

[49] A. Ranft, I. Pavlichenko, K. Szendrei, P. M. Zehetmaier, Y. Hu, A. von Mankowski, B. V. Lotsch, *Microporous Mesoporous Mater.* **2015**, *216*, 216-224.

[50] C. McDonagh, C. S. Burke, B. D. MacCraith, *Chem. Rev.* **2008**, *108*, 400-422.

[51] H. Yang, P. Jiang, B. Jiang, *J. Colloid Interface Sci.* **2012**, *370*, 11-18.

[52] T. L. Kelly, A. Garcia Sega, M. J. Sailor, *Nano Lett.* **2011**, *11*, 3169-3173.

[53] S. Y. Choi, M. Mamak, G. von Freymann, N. Chopra, G. A. Ozin, *Nano Lett.* **2006**, *6*, 2456-2461.

[54] I. Pavlichenko, E. Broda, Y. Fukuda, K. Szendrei, A. K. Hatz, G. Scarpa, P. Lugli, C. Brauchle, B. V. Lotsch, *Mater. Horiz.* **2015**, *2*, 299-308.

[55] Z. Wang, J. Zhang, J. Xie, C. Li, Y. Li, S. Liang, Z. Tian, T. Wang, H. Zhang, H. Li, W. Xu, B. Yang, *Adv. Funct. Mater.* **2010**, *20*, 3784-3790.

[56] R. A. Barry, P. Wiltzius, *Langmuir* **2005**, *22*, 1369-1374.

[57] E. Tian, J. Wang, Y. Zheng, Y. Song, L. Jiang, D. Zhu, *J. Mater. Chem.* **2008**, *18*, 1116-1122.

[58] I. Pavlichenko, A. T. Exner, M. Guehl, P. Lugli, G. Scarpa, B. V. Lotsch, *J. Phys. Chem. C* **2011**, *116*, 298-305.

[59] I. Pavlichenko, A. T. Exner, M. Guehl, P. Lugli, G. Scarpa, B. V. Lotsch, *J. Phys. Chem. C* **2011**, *116*, 298-305.

[60] A. C. Arsenault, T. J. Clark, G. von Freymann, L. Cademartiri, R. Sapienza, J. Bertolotti, E. Vekris, S. Wong, V. Kitaev, I. Manners, R. Z. Wang, S. John, D. Wiersma, G. A. Ozin, *Nat. Mater.* **2006**, *5*, 179-184.

[61] F. Castles, S. M. Morris, J. M. C. Hung, M. M. Qasim, A. D. Wright, S. Nosheen, S. S. Choi, B. I. Outram, S. J. Elston, C. Burgess, L. Hill, T. D. Wilkinson, H. J. Coles, *Nat. Mater.* **2014**, *13*, 817-821.

[62] V. N. Konopsky, E. V. Alieva, *Anal. Chem.* **2007**, *79*, 4729-4735.

[63] M. R. Lee, P. M. Fauchet, *Opt. Express* **2007**, *15*, 4530-4535.

[64]   N. Skivesen, A. Têtu, M. Kristensen, J. Kjems, L. H. Frandsen, P. I. Borel, *Opt. Express* **2007**, *15*, 3169-3176.

[65]   M. M. Braun, L. Pilon, *Thin Solid Films* **2006**, *496*, 505-514.

[66]   N. Nagy, Deak, A., Horvölgyi, Z., Fried, M., Agod, A., Barsony, I., *Langmuir* **2006**, *26*, 8416-8423.

[67]   M. E. Calvo, O. Sánchez-Sobrado, S. Colodrero, H. Míguez, *Langmuir* **2009**, *25*, 2443-2448.

[68]   S. Colodrero, M. Ocaña, H. Míguez, *Langmuir* **2008**, *24*, 4430-4434.

[69]   M. C. Fuertes, S. Colodrero, G. Lozano, A. R. González-Elipe, D. Grosso, C. Boissière, C. Sánchez, G. J. d. A. A. Soler-Illia, H. Míguez, *J. Phys. Chem. C* **2008**, *112*, 3157-3163.

[70]   L. D. Bonifacio, D. P. Puzzo, S. Breslav, B. M. Willey, A. McGeer, G. A. Ozin, *Adv. Mater.* **2010**, *22*, 1351-1354.

[71]   A. T. Exner, I. Pavlichenko, D. Baierl, M. Schmidt, G. Derondeau, B. V. Lotsch, P. Lugli, G. Scarpa, *Laser Photonics Rev.* **2014**, *5*, 726-733.

[72]   E. Redel, P. Mirtchev, C. Huai, S. Petrov, G. A. Ozin, *ACS Nano* **2011**, *5*, 2861-2869.

[73]   E. Redel, C. Huai, M. Renner, G. von Freymann, G. A. Ozin, *Small* **2011**, *7*, 3465-3471.

[74]   M. E. Calvo, J. R. Castro Smirnov, H. Míguez, *J. Polym. Sci., Part B: Polym. Phys.* **2012**, *50*, 945-956.

[75]   J. R. C. Smirnov, M. Ito, M. E. Calvo, C. López-López, A. Jiménez-Solano, J. F. Galisteo-López, P. Zavala-Rivera, K. Tanaka, E. Sivaniah, H. Míguez, *Adv. Opt. Mater.* **2015**, *3*, 1633-1639.

[76]   J. Liu, E. Redel, S. Walheim, Z. Wang, V. Oberst, J. Liu, S. Heissler, A. Welle, M. Moosmann, T. Scherer, M. Bruns, H. Gliemann, C. Wöll, *Chem. Mater.* **2015**, *27*, 1991-1996.

[77]   A. Ranft, F. Niekiel, I. Pavlichenko, N. Stock, B. V. Lotsch, *Chem. Mater.* **2015**, *27*, 1961–1970.

[78]   B. V. Lotsch, F. Scotognella, K. Moeller, T. Bein, G. A. Ozin, *Proc. SPIE*, *7713*, **2010**, 7713V.

[79]   K. Lazarova, H. Awala, S. Thomas, M. Vasileva, S. Mintova, T. Babeva, *Sensors* **2014**, *14*, 12207.

[80]   J. Kobler, B. V. Lotsch, G. A. Ozin, T. Bein, *ACS Nano* **2009**, *3*, 1669-1676.

[81]   Y. Kang, J. J. Walish, T. Gorishnyy, E. L. Thomas, *Nat. Mater.* **2007**, *6*, 957-960.

[82]   R. Xuan, Q. Wu, Y. Yin, J. Ge, *J. Mater. Chem.* **2011**, *21*, 3672-3676.

[83]   Z. Wang, J. Zhang, J. Li, J. Xie, Y. Li, S. Liang, Z. Tian, C. Li, Z. Wang, T. Wang, H. Zhang, B. Yang, *J. Mater. Chem.* **2011**, *21*, 1264-1270.

[84]   Z. Wang, J. Zhang, Z. Wang, H. Shen, J. Xie, Y. Li, L. Lin, B. Yang, *J. Mater. Chem. C* **2013**, *1*, 977-983.

[85]   K. G. Lazarova, R.; Vasileva, M.; Georgieva, B.; Spassova, M.; Malinowski, N.; Babeva, T., *Opt. Quantum Electron.* **2016**, *6*.

[86]   B. V. Lotsch, G. A. Ozin, *ACS Nano* **2008**, *2*, 2065-2074.

[87]   B. V. Lotsch, G. A. Ozin, *Adv. Mater.* **2008**, *20*, 4079-4084.

[88]   B. V. Lotsch, G. A. Ozin, *J. Am. Chem. Soc.* **2008**, *130*, 15252-15253.

[89] J. Han, Y. Dou, M. Wei, D. G. Evans, X. Duan, *RSC Adv.* **2012**, *2*, 10488-10491.

[90] Z. Hu, C.-a. Tao, F. Wang, X. Zou, J. Wang, *J. Mater. Chem. C* **2015**, *3*, 211-216.

[91] C. Fenzl, T. Hirsch, O. S. Wolfbeis, *Angew. Chem. Int. Ed.* **2014**, *53*, 3318-3335.

[92] O. Sanchez-Sobrado, M. E. Calvo, N. Nunez, M. Ocana, G. Lozano, H. Miguez, *Nanoscale* **2010**, *2*, 936-941.

[93] M. Li, F. He, Q. Liao, J. Liu, L. Xu, L. Jiang, Y. Song, S. Wang, D. Zhu, *Angew. Chem. Int. Ed.* **2008**, *120*, 7368-7372.

[94] X. Zhao, Y. Cao, F. Ito, H.-H. Chen, K. Nagai, Y.-H. Zhao, Z.-Z. Gu, *Angew. Chem. Int. Ed.* **2006**, *118*, 6989-6992.

[95] M. Shaban, A. M. Ahmed, E. Abdel-Rahman, H. Hamdy, *Sci. Rep.* **2017**, *7*, 41983.

[96] P. R. Wallace, *Phys. Rev.* **1947**, *71*, 622-634.

[97] H. P. Boehm, A. Clauss, G. O. Fischer, U. Hofmann, *Z. anorg. Allg. Chem.* **1962**, *316*, 119-127.

[98] K. S. Novoselov, A. K. Geim, S. V. Morozov, D. Jiang, Y. Zhang, S. V. Dubonos, I. V. Grigorieva, A. A. Firsov, *Science* **2004**, *306*, 666-669.

[99] https://www.nobelprize.org/nobel_prizes/physics/laureates/2010/, accessed 02.03.2018.

[100] R. Mas-Balleste, C. Gomez-Navarro, J. Gomez-Herrero, F. Zamora, *Nanoscale* **2011**, *3*, 20-30.

[101] K. J. Koski, Y. Cui, *ACS Nano* **2013**, *7*, 3739-3743.

[102] B. V. Lotsch, *Annu. Rev. Mater. Res.* **2015**, *45*, 85-109.

[103] L. Li, R. Ma, Y. Ebina, K. Fukuda, K. Takada, T. Sasaki, *J. Am. Chem. Soc.* **2007**, *129*, 8000-8007.

[104] C. Ziegler, S. Werner, M. Bugnet, M. Wörsching, V. Duppel, G. A. Botton, C. Scheu, B. V. Lotsch, *Chem. Mater.* **2013**, *25*, 4892-4900.

[105] A. K. Geim, K. S. Novoselov, *Nat. Mater.* **2007**, *6*, 183-191.

[106] B. Radisavljevic, A. Radenovic, J. Brivio, V. Giacometti, A. Kis, *Nat. Nanotechnol.* **2011**, *6*, 147-150.

[107] S. Ghatak, A. N. Pal, A. Ghosh, *ACS Nano* **2011**, *5*, 7707-7712.

[108] K. S. Novoselov, D. Jiang, F. Schedin, T. J. Booth, V. V. Khotkevich, S. V. Morozov, A. K. Geim, *Proc. Natl. Acad. Sci. U.S.A.* **2005**, *102*, 10451-10453.

[109] P. May, U. Khan, J. M. Hughes, J. N. Coleman, *J. Phys. Chem. C* **2012**, *116*, 11393-11400.

[110] Z. Zeng, Z. Yin, X. Huang, H. Li, Q. He, G. Lu, F. Boey, H. Zhang, *Angew. Chem. Int. Ed.* **2011**, *50*, 11093-11097.

[111] K.-G. Zhou, N.-N. Mao, H.-X. Wang, Y. Peng, H.-L. Zhang, *Angew. Chem. Int. Ed.* **2011**, *50*, 10839-10842.

[112] G. Cunningham, M. Lotya, C. S. Cucinotta, S. Sanvito, S. D. Bergin, R. Menzel, M. S. P. Shaffer, J. N. Coleman, *ACS Nano* **2012**, *6*, 3468-3480.

[113] F. Leroux, M. Adachi-Pagano, M. Intissar, S. Chauviere, C. Forano, J.-P. Besse, *J. Mater. Chem.* **2001**, *11*, 105-112.

[114] R. J. Smith, P. J. King, M. Lotya, C. Wirtz, U. Khan, S. De, A. O'Neill, G. S. Duesberg, J. C. Grunlan, G. Moriarty, J. Chen, J. Wang, A. I. Minett, V. Nicolosi, J. N. Coleman, *Adv. Mater.* **2011**, *23*, 3944-3948.

[115] Z. Zeng, T. Sun, J. Zhu, X. Huang, Z. Yin, G. Lu, Z. Fan, Q. Yan, H. H. Hng, H. Zhang, *Angew. Chem. Int. Ed.* **2012**, *51*, 9052-9056.

[116] M. B. Dines, *Mater. Res. Bull.* **1975**, *10*, 287-291.

[117] J. N. Coleman, M. Lotya, A. O'Neill, S. D. Bergin, P. J. King, U. Khan, K. Young, A. Gaucher, S. De, R. J. Smith, I. V. Shvets, S. K. Arora, G. Stanton, H.-Y. Kim, K. Lee, G. T. Kim, G. S. Duesberg, T. Hallam, J. J. Boland, J. J. Wang, J. F. Donegan, J. C. Grunlan, G. Moriarty, A. Shmeliov, R. J. Nicholls, J. M. Perkins, E. M. Grieveson, K. Theuwissen, D. W. McComb, P. D. Nellist, V. Nicolosi, *Science* **2011**, *331*, 568-571.

[118] P. Joensen, R. F. Frindt, S. R. Morrison, *Mater. Res. Bull.* **1986**, *21*, 457-461.

[119] G. Eda, H. Yamaguchi, D. Voiry, T. Fujita, M. Chen, M. Chhowalla, *Nano Lett.* **2011**, *11*, 5111-5116.

[120] T. Sasaki, M. Watanabe, H. Hashizume, H. Yamada, H. Nakazawa, *J. Am. Chem. Soc.* **1996**, *118*, 8329-8335.

[121] T. Sasaki, M. Watanabe, H. Hashizume, H. Yamada, H. Nakazawa, *Chem. Commun.* **1996**, 229-230.

[122] H. Nakano, M. Ishii, H. Nakamura, *Chem. Commun.* **2005**, 2945-2947.

[123] R. Ma, Z. Liu, L. Li, N. Iyi, T. Sasaki, *J. Mater. Chem.* **2006**, *16*, 3809-3813.

[124] V. Nicolosi, M. Chhowalla, M. G. Kanatzidis, M. S. Strano, J. N. Coleman, *Science* **2013**, *340*.

[125] S. Z. Butler, S. M. Hollen, L. Cao, Y. Cui, J. A. Gupta, H. R. Gutierrez, T. F. Heinz, S. S. Hong, J. Huang, A. F. Ismach, E. Johnston-Halperin, M. Kuno, V. V. Plashnitsa, R. D. Robinson, R. S. Ruoff, S. Salahuddin, J. Shan, L. Shi, M. G. Spencer, M. Terrones, W. Windl, J. E. Goldberger, *ACS Nano* **2013**, *7*, 2898-2926.

[126] B. Vedhanarayanan, B. Babu, M. M. Shaijumon, A. Ajayaghosh, *ACS Appl. Mater. Interfaces* **2017**, *9*, 19417-19426.

[127] C.-J. Shih, A. Vijayaraghavan, R. Krishnan, R. Sharma, J.-H. Han, M.-H. Ham, Z. Jin, S. Lin, G. L. C. Paulus, N. F. Reuel, Q. H. Wang, D. Blankschtein, M. S. Strano, *Nat. Nanotechnol.* **2011**, *6*, 439.

[128] A. Kuhn, T. Holzmann, J. Nuss, B. V. Lotsch, *J. Mater. Chem. A* **2014**, *2*, 6100-6106.

[129] T. Holzmann, L. M. Schoop, M. N. Ali, I. Moudrakovski, G. Gregori, J. Maier, R. J. Cava, B. V. Lotsch, *Energy Environ. Sci.* **2016**, *9*, 2578-2585.

[130] M. A. Jobbágy, A. E. Regazzoni, *J. Colloid Interface Sci.* **2004**, *275*, 345-348.

[131] L. Chang, M. A. Holmes, M. Waller, F. E. Osterloh, A. J. Moule, *J. Mater. Chem.* **2012**, *22*, 20443-20450.

[132] L. Britnell, R. V. Gorbachev, R. Jalil, B. D. Belle, F. Schedin, A. Mishchenko, T. Georgiou, M. I. Katsnelson, L. Eaves, S. V. Morozov, N. M. R. Peres, J. Leist, A. K. Geim, K. S. Novoselov, L. A. Ponomarenko, *Science* **2012**, *335*, 947-950.

[133] U. Zschieschang, T. Holzmann, A. Kuhn, M. Aghamohammadi, B. V. Lotsch, H. Klauk, *J. Appl. Phys.* **2015**, *117*, 104509.

[134] W. J. Yu, Z. Li, H. Zhou, Y. Chen, Y. Wang, Y. Huang, X. Duan, *Nat. Mater.* **2012**, *12*, 246.

[135] Z.-G. Chen, J. Zou, G. Liu, F. Li, Y. Wang, L. Wang, X.-L. Yuan, T. Sekiguchi, H.-M. Cheng, G. Q. Lu, *ACS Nano* **2008**, *2*, 2183-2191.

[136] G. Appala Naidu, N. A. Husam, S. Udo, *J. Phys.: Condens. Matter* **2017**, *29*, 035504.

[137] J. Lee, J.-H. Shin, G.-H. Lee, C.-H. Lee, *Nanomaterials* **2016**, *6*, 193.

[138] E. G. da Silveira Firmiano, A. C. Rabelo, C. J. Dalmaschio, A. N. Pinheiro, E. C. Pereira, W. H. Schreiner, E. R. Leite, *Adv. Energy Mater.* **2014**, *4*, 1301380.

[139] L. Peng, X. Peng, B. Liu, C. Wu, Y. Xie, G. Yu, *Nano Lett.* **2013**, *13*, 2151-2157.

[140] Z. Liu, R. Ma, M. Osada, N. Iyi, Y. Ebina, K. Takada, T. Sasaki, *J. Am. Chem. Soc.* **2006**, *128*, 4872-4880.

[141] M. Osada, M. Itose, Y. Ebina, K. Ono, S. Ueda, K. Kobayashi, T. Sasaki, *Appl. Phys. Lett.* **2008**, *92*, 253110.

[142] B. Lin, P. Sun, Y. Zhou, S. Jiang, B. Gao, Y. Chen, *J. Hazard. Mater.* **2014**, *280*, 156-163.

[143] J. L. Gunjakar, T. W. Kim, H. N. Kim, I. Y. Kim, S.-J. Hwang, *J. Am. Chem. Soc.* **2011**, *133*, 14998-15007.

[144] N. Miyamoto, Y. Yamada, S. Koizumi, T. Nakato, *Angew. Chem. Int. Ed.* **2007**, *46*, 4123-4127.

[145] T. Yui, Y. Kobayashi, Y. Yamada, T. Tsuchino, K. Yano, T. Kajino, Y. Fukushima, T. Torimoto, H. Inoue, K. Takagi, *Phys. Chem. Chem. Phys.* **2006**, *8*, 4585-4590.

[146] J. Feng, L. Peng, C. Wu, X. Sun, S. Hu, C. Lin, J. Dai, J. Yang, Y. Xie, *Adv. Mater.* **2012**, *24*, 1969-1974.

[147] S.-L. Zhang, H.-H. Choi, H.-Y. Yue, W.-C. Yang, *Curr. Appl. Phys.* **2014**, *14*, 264-268.

[148] W. M. R. Divigalpitiya, R. F. Frindt, S. R. Morrison, *J. Phys. D: Appl. Phys.* **1990**, *23*, 966.

[149] S. Borini, R. White, D. Wei, M. Astley, S. Haque, E. Spigone, N. Harris, J. Kivioja, T. Ryhänen, *ACS Nano* **2013**, *7*, 11166-11173.

[150] B.-H. Wee, W.-H. Khoh, A. K. Sarker, C.-H. Lee, J.-D. Hong, *Nanoscale* **2015**, *7*, 17805-17811.

[151] D. Wang, K. Zhou, M. Sun, Z. Fang, X. Liu, X. Sun, *Anal. Methods* **2013**, *5*, 6576-6578.

[152] F. K. Perkins, A. L. Friedman, E. Cobas, P. M. Campbell, G. G. Jernigan, B. T. Jonker, *Nano Lett.* **2013**, *13*, 668-673.

[153] R. Gatensby, N. McEvoy, K. Lee, T. Hallam, N. C. Berner, E. Rezvani, S. Winters, M. O'Brien, G. S. Duesberg, *Appl. Surf. Sci.* **2014**, *297*, 139-146.

[154] M. Sajjad, P. Feng, *Mater. Res. Bull.* **2014**, *49*, 35-38.

[155] S. Weidong, H. Lihua, W. Haishui, Z. Hongjie, Y. Jianhui, W. Pinghui, *Nanotechnology* **2006**, *17*, 2918.

[156] J.-S. Kim, H.-W. Yoo, H. O. Choi, H.-T. Jung, *Nano Lett.* **2014**, *14*, 5941-5947.

[157] B. Chen, H. Liu, X. Li, C. Lu, Y. Ding, B. Lu, *Appl. Surf. Sci.* **2012**, *258*, 1971-1975.

[158] J. L. Johnson, A. Behnam, S. J. Pearton, A. Ural, *Adv. Mater.* **2010**, *22*, 4877-4880.

[159] Q. He, Z. Zeng, Z. Yin, H. Li, S. Wu, X. Huang, H. Zhang, *Small* **2012**, *8*, 2994-2999.

[160] D. J. Late, Y.-K. Huang, B. Liu, J. Acharya, S. N. Shirodkar, J. Luo, A. Yan, D. Charles, U. V. Waghmare, V. P. Dravid, C. N. R. Rao, *ACS Nano* **2013**, *7*, 4879-4891.

[161] A. L. Friedman, F. Keith Perkins, E. Cobas, G. G. Jernigan, P. M. Campbell, A. T. Hanbicki, B. T. Jonker, *Solid-State Electron.* **2014**, *101*, 2-7.

[162] S. Yang, C. Jiang, S.-h. Wei, *Appl. Phys. Rev.* **2017**, *4*, 021304.

[163] P. Ganter, L. M. Schoop, B. V. Lotsch, *Adv. Mater.* **2017**, *29*, 1604884.

2. METHODS

Every one-dimensional photonic crystal (1DPC) presented in this thesis was carefully designed, and after the fabrication analyzed with various methods in order to determine and adjust the optical and structural properties to the different application needs. For this, diverse theoretical calculation tools, fabrication techniques and a large spectrum of analytical methods were applied, in order to control and characterize the structural and optical properties. In this section, these methods will be introduced: first the fabrication methods, secondly the characterization techniques and finally the theoretical calculations.

2.1 FABRICATION METHODS

In order to create tailor-made 1DPCs and optical resonators, a solution processed fabrication technique with a very high variability and tunability had to be applied. The method of choice was spin-coating, which is shown in this section shortly, including its advantages, disadvantages, limits and possibilities.

2.1.1 SPIN-COATING

Spin-coating was first applied in the 1950s by Emslie *et al*.[1] and since then it is considered as one of the simplest solution processed, bottom-up method for thin film and multilayer fabrication for various systems and applications.[2] For spin-coating, a homogenous and stable colloidal suspension with a known concentration is needed, which in the first step is deposited on top of a substrate. Preferably, the suspension is formed in a solvent, which evaporates fast, e.g. an alcoholic medium. The substrate starts to rotate with the suspension on top of it. In the acceleration step, the majority of the excess material is removed by centrifugal forces from the substrate and from the residual substance, the thin film starts to form. Upon rotation, the volatile solvent of the suspension evaporates, which causes a viscosity increase of the suspension and the thinning of the film. Once the solvent evaporated completely, the thin film formation is completed. Eventually, a heating step

can be applied afterwards, in order to densify and stabilize the coating by removing the residual solvent out of the created thin film.

In order to create multilayers, such as 1DPCs or optical resonators, sequential spin-coating was applied, meaning the deposition of thin films successively on top of each other (Figure 2.1). To create multilayered structures with the desired and pre-designed optical properties, it is crucial to achieve high thin film homogeneity and a high variability of the film thicknesses. The thin film thickness can be easily tuned by changing the acceleration speed, the final rotation speed, the colloidal concentration or the number of applied deposition steps.
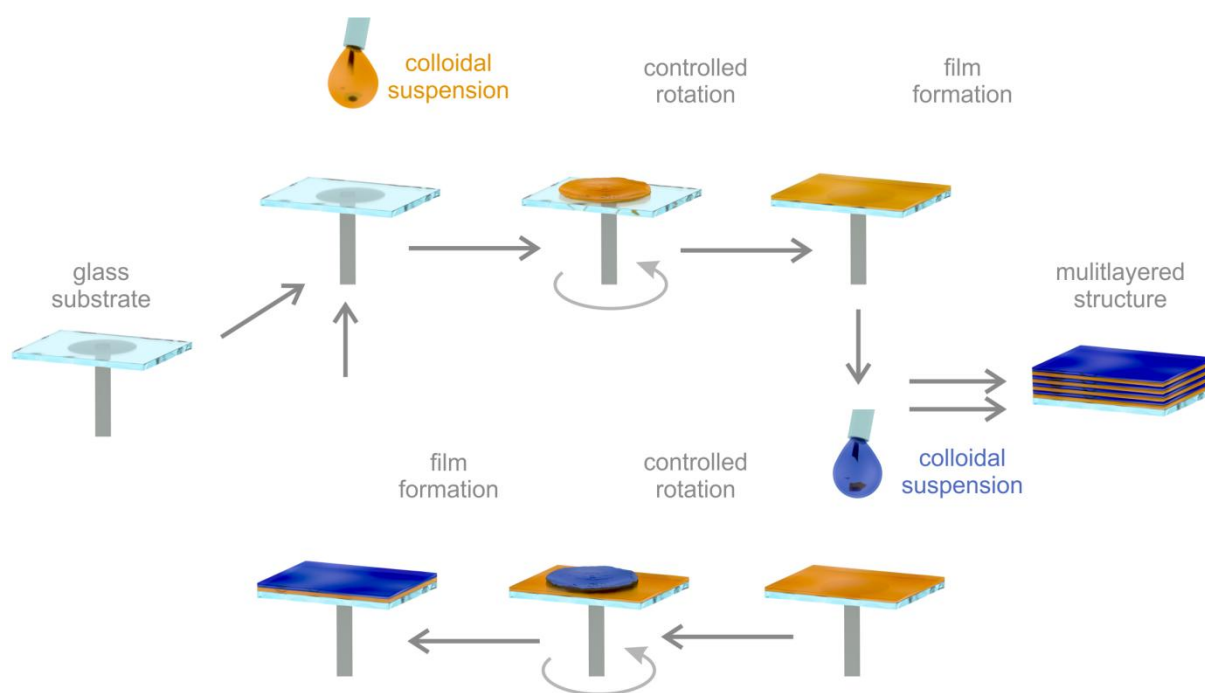
Figure 2.1: Schematic illustration of the spin-coating procedure.

In this work, SiO_2 and TiO_2 nanoparticles (NPs), dye doped polystyrene (PS) nanospheres and $H_3Sb_3P_2O$, $HSbP_2O_8$ and $Li_2Sn_2S_5$ nanosheets were spin-coated using stable colloidal suspensions. The nanoparticle suspensions were dispersed in methanol, in order to achieve a high evaporation rate and a homogenous thin film formation. The dyed nanospheres were spin-coated as purchased, without a further treatment or dilution, starting from an aqueous suspension. The nanosheets were dispersed in a mixture of water : ethanol = 40 : 60 vol%, which was a compromise between the fast evaporation rate of the solvent (ethanol) and the exfoliation and suspension stability (water) of the nanosheets. After each deposited layer, a heating treatment was applied for 10 min at 80°C to stabilize the previously deposited layer. It is important to note that the nanosheets cannot be heated above 100°C, as they lose the capability to intercalate water once the crystal water was removed

completely. The spin-coating experiments were performed on a LAURELL – WS-650MZ-23NPP spin-coater.

2.2 CHARACTERIZATION TECHNIQUES

In this section the analytical methods are introduced, which were applied to characterize the optical and structural properties, the phase purity, the elemental composition or the particle size of the samples.

2.2.1 ULTRAVIOLET-VISIBLE SPECTROPHOTOMETRY

Ultraviolet-Visible (UV-Vis) spectroscopy is one of the oldest spectroscopy methods, which has its origin in the 17th century.[3] Sir Isaac Newton was the first scientist, who studied colors in nature and splitted white light into its spectral components, marking the birth date of spectroscopy.[4] Later in the middle of the 19th century, Joseph von Fraunhofer characterized the solar spectrum and discovered instead of a continuous spectrum, well-defined spectral lines, the later called Fraunhofer-lines.[5] Upon his experiments, he constructed the first spectrometer. The theoretical explanation of the Fraunhofer-lines was delivered by Kirchhoff in his theory of absorption and emission.[6, 7] The new development era in Vis-spectroscopy arose in the 19th century with the proposal of Niels Bohr for an atomic model, and linking the Fraunhofer-lines to quantum states and transitions.[8, 9] The first prototype of a colorimeter or a spectrophotometer was built in 1930[10] and finally after the discovery of ultraviolet (UV) radiation,[11] the first UV-Vis spectrophotometer was built in 1947 by Varian.[12]

Upon the parallel evolution of the theory and the detectors to measure light intensities quantitatively together with the development of quantum chemistry, UV-Vis spectroscopy became by today a powerful method in material characterization. This narrow range of the electromagnetic spectrum (200-900 nm) is of great importance, as atoms and molecules undergo electronic transition and the interaction of light with matter results in a, for the naked eye, visible color.[13] UV-Vis spectroscopy allows the optical characterization of materials or (nano)structures in three different modes: by measuring the transmittance (T) or the reflectance (R) and absorptance (A) of the sample.[14]

For the optical characterization of the 1DPCs in this thesis, we attach to a wide-field optical microscope an UV-Vis spectrophotometer. Hereby, the objective of the microscope is coupled through an optical fiber to the spectrophotometer in order to collect light normal to the sample and simultaneously an image of it by a CMOS (Complementary Metal-Oxide Semiconductor) camera

(Figure 2.2a). A typical output including the microscope image with the corresponding reflectance spectrum is shown in Figure 2.2b-c.
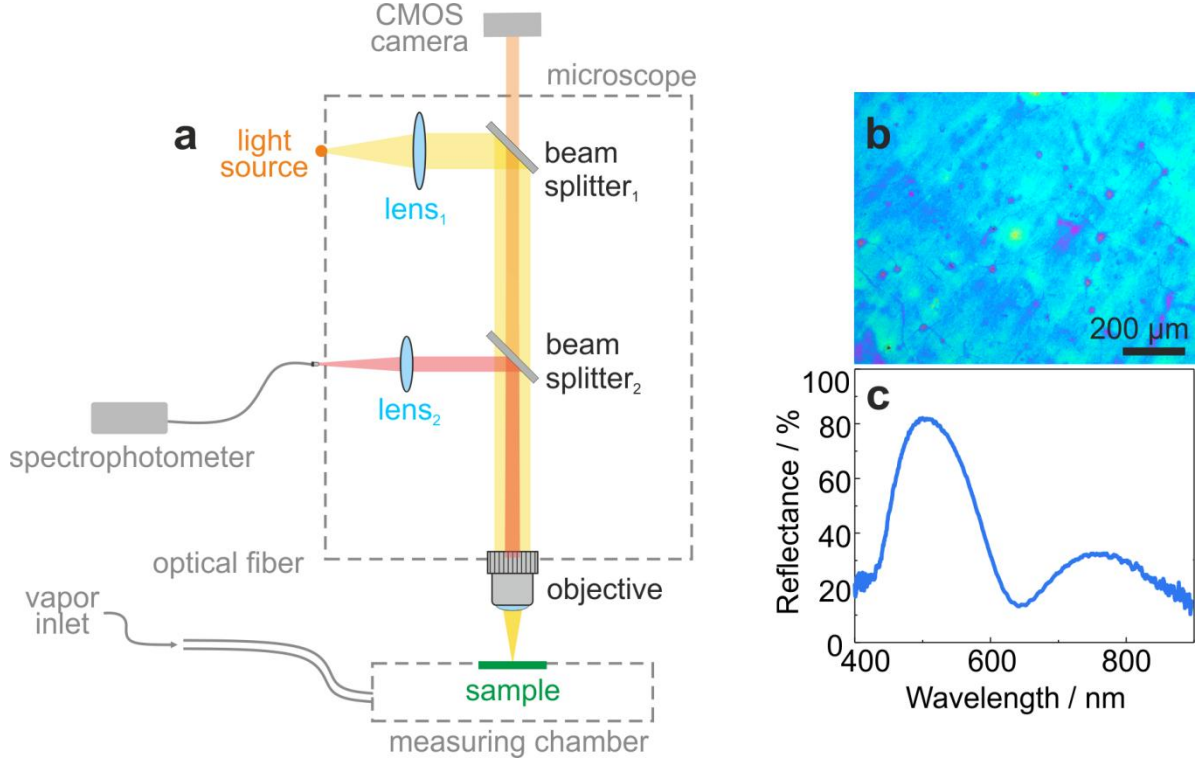
Figure 2.2: Schematic illustration of the optical measurements performed in this thesis. (a) Structure and beam path of the optical microscope attached to the spectrophotometer and CMOS camera. (b) CMOS camera microscope image from a 1DPC surface. (c) Reflectance spectrum corresponding to the sample shown in (b).

Using this microscope spectrophotometer set-up, the reflectance relative to a reference sample (calibrated reflecting mirror, Ocean Optics STAN-SSH) of the sample is given by following expression:

$$R(\lambda) = \frac{I(\lambda) - I_{\mathrm{d}}(\lambda)}{I_{\mathrm{ref}}(\lambda) - I_{\mathrm{d}}(\lambda)} \tag{2.1}$$

whereby $I(\lambda)$ is the reflected intensity through the sample at wavelength λ, $I_{\mathrm{d}}(\lambda)$ the dark intensity, i.e. without any excitation, at wavelength λ and $I_{\mathrm{ref}}(\lambda)$ the reflectance intensity of the reference at λ. Using air as a reference, the transmittance can be expressed similarly.

The advantage of this set-up is the possibility to correlate the information from the image (color, RGB values, surface characteristics, homogeneity) with the acquired reflectance/transmittance spectra from the same spot at the same time (Figure 2.2b-c). Another benefit offered by this set-up is the capability of creating optical characterization maps of the samples obtaining microscopic features.

In this thesis, optical properties, such as intensity, shape and spectral position of the photonic stopband, and its changes with analyte adsorption were measured in real-time *via* UV-Vis

spectroscopy coupled to the optical microscope. All measurements were performed on a Leica M2500 optical microscope equipped with a CMOS camera (Leica DMS54510), which was connected to an Ocean optics USB4000-XR1-ES spectrophotometer in order to acquire the images and the spectra simultaneously.

2.2.2 MASS FLOW CONTROL OF VAPORS

In order to measure the material based sensor`s response to diverse analytes, the fabricated samples were placed into a closed chamber with a transparent quartz window, which was placed in the path of the light under the objective. The chamber was connected *via* a teflon tube to the vapor source. By a stable, adjustable dosing of the vaporous analyte, a real-time optical response of the sensor can be characterized.

In order to ensure a precise and adjustable vapor flow, a system of mass flow controllers from Bronkhorst High-Tech[15] was used. The equipment as indicated in Figure 2.3 is based on a Controlled Evaporator Mixer (CEM), which connects a Mass Flow Controller (MFC) for the carrier gas and the Liquid Flow Controller (LFC) for the analyte.[16]
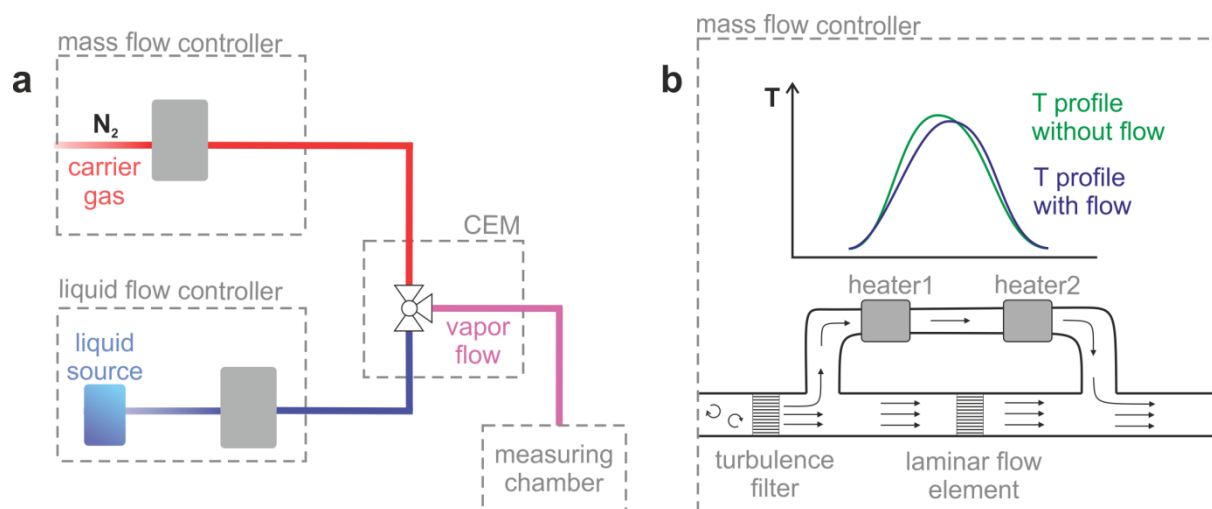
Figure 2.3: Schematic operation principle of the controlled evaporation mixer and the mass flow controller. Images reproduced with permission.[15] (a) Scheme of the applied MFC-LFC-CEM combined setup for vapor dosing applications. (b) Schematic structure and working principle of a MFC.

The applied thermal MFC is a closed system,[17] which doses, adjusts and measures the flow of a gas of interest. The gas entering the system flows through a turbulence filter, which ensures a laminar flow in the entire system. The flow can be measured and controlled using a bypass sensor tube, as indicated in Figure 2.3. The sensor tube is heated at two different points (heater 1 and heater 2) and also the temperature gradient between the two heaters is monitored at the same time (T1 and T2 at the position of heater 1 and heater 2). If there is no gas flow, the temperature profile of the sensor

tube shows a Gaussian shape (green curve), and T1 and T2 are equal. By applying a gas flow, the gas molecules are heated by heater 1 and the temperature gradient within the sensor tube is shifted (blue curve), the two measured temperatures drift apart. The temperature profile shift and *ΔT* is constant to the mass flow in the tube. The mass flow is controlled *via* a PID (proportional-integral-derivative) controller and a valve at the end of the flow tube.

The LFC operates similarly to the MFC, using a sensor tube with a generated temperature difference. However, hereby the main challenge is to design the components in a way that bubble formation and retention is avoided. The third component, the CEM evaporates the liquid dosed by the LFC and mixes it homogenously with the carrier gas, coming from the MFC.

In this thesis, the correct and stable dosing of diverse solvent vapors was crucial to determine the sensor characteristics, most importantly the selectivity towards the main target, humidity, and to prove the cross-selectivity to other analytes, such as alcohols, n-heptane, toluene or acetonitrile. The set-up used in this thesis was calibrated for nitrogen with a maximum flow rate of 200 mL min^{-1} as a carrier gas and water with a flow rate of maximum 2 g h^{-1} as an analyte. By applying different analytes, the calculation tool of FLUIDAT on the Net software[18] was used. The CEM heater could provide temperatures between ambient and 200°C.

2.2.3 SPECTROSCOPIC ELLIPSOMETRY

Ellipsometry has its roots in the end of the 19th century, as Paul Drude not only carried out the first experimental studies on absorbing and transparent solids[19] but also derived the equations and with this created the theoretical background of ellipsometry.[20] Later, Aspnes and Studna[21] performed the first spectroscopic ellipsometry measurement by increasing the accuracy of the ellipsometric measurements, after which wavelength-dependent measurements were possible. The first *in situ* measurements were performed in 1984, as Muller and Farmer[22] succeeded to measure the entire spectrum within a few seconds and with this allow following processes by this technique in real time.

Spectroscopic ellipsometry is a contactless, non-destructive method to determine thin film properties, such as thickness, complex refractive index, roughness, composition or doping concentration. Ellipsometry presents a fast and sensitive method, which is based on the measurement of the changes of light polarization after reflection from the material.[23]
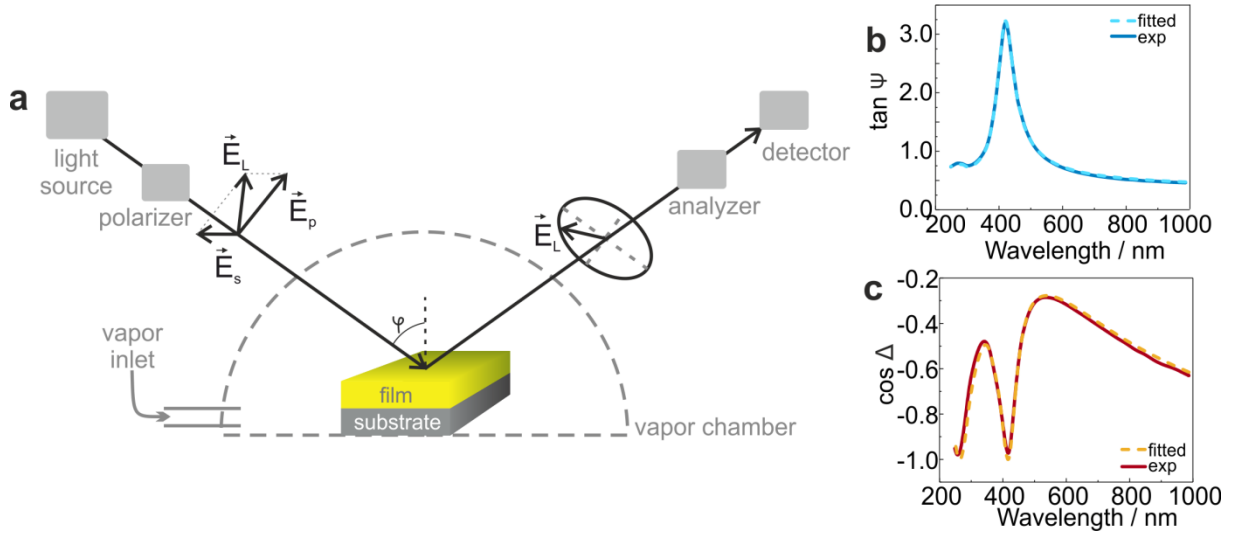
Figure 2.4: Scheme of the working principle of spectroscopic ellipsometry. (a) Schematic set-up of a spectroscopic ellipsometer combined with a porosimetry tool. (b-c) Direct output spectra (tan Ψ (b) and cos Δ (c)) of a spectroscopic ellipsometry measurement showing the phase changes and the corresponding fittings.

The working principle is schematically illustrated in Figure 2.4. From the light source, which is usually a lamp with a wide spectral range (140-1700 nm), after passing a polarizer, the circularly polarized light beam is reflected by the investigated sample. Upon interaction with the sample, the polarization changes, and elliptically polarized light is generated. After passing the analyzer, the elliptically polarized light hits the detector. An ellipsometry measurement can be expressed by following equation, whereby the amplitude ratio Ψ and the phase shift Δ (Figure 2.4b-c) are measured:[24]

$$\rho = \frac{r_p}{r_s} = \tan \Psi \cdot e^{i\Delta} \tag{2.2}$$

where ρ is the Fresnel coefficient of r_p and r_s for p- (parallel) and s-polarized (perpendicular to the plain of incidence) electric field components.

In order to extract actual physical information from the sample, such as the thickness, the complex refractive index or surface roughness, a theoretical model has to be constructed and fitted with regression analysis. Usually, for transparent dielectric thin films, the Cauchy dispersion model is used:

$$n(\lambda) = A + \frac{B}{\lambda^2} + \frac{C}{\lambda^4} \tag{2.3}$$

whereby A, B and C are the optimization parameters and λ the wavelength. Upon fitting materials with absorption, the Cauchy with Urbach tail[25] model is applied, whereby a dispersion term is added to the classical Cauchy expression:

$$k(\lambda) = \alpha \cdot e^{\beta\left(\frac{K}{\lambda}-E_g\right)} \tag{2.4}$$

whereby α is the amplitude of the extinction coefficient, β the exponent decay factor, E_g the optical band gap and K the conversion constant between wavelength and energy units.

2.2.3.1 ELLIPSOMETRIC POROSIMETRY

Since the instrumental developments by Muller and Farmer[22] and later Kim, Collins and Verdam[26] at the end of the 80s, ellipsometry is considered as a fast analytical method, which is capable of process monitoring *in situ* and in real time. One example for such measurements is the monitoring of vapor sorption in real-time on porous thin films.[27] In this thesis, a spectroscopic ellipsometer was used, which was equipped with a vapor chamber (Figure 2.4), whereby different solvent vapors could be dosed and injected to the chamber and the changes of the thin film materials are measured instantaneously. Hereby again, the phase shift and the amplitude changes were measured successively and with an automated model, optical isotherms monitoring the thickness and the refractive index evolution with changing vapor pressure are created.

In this thesis, two different types of materials were investigated *via* spectroscopic ellipsometry: thin films of porous materials (Figure 2.5a-b) and of two dimensional (2D) nanosheets (Figure 2.5c-d). Both are capable of adsorbing vaporous analytes, such as water vapor or volatile organic compounds (VOCs).
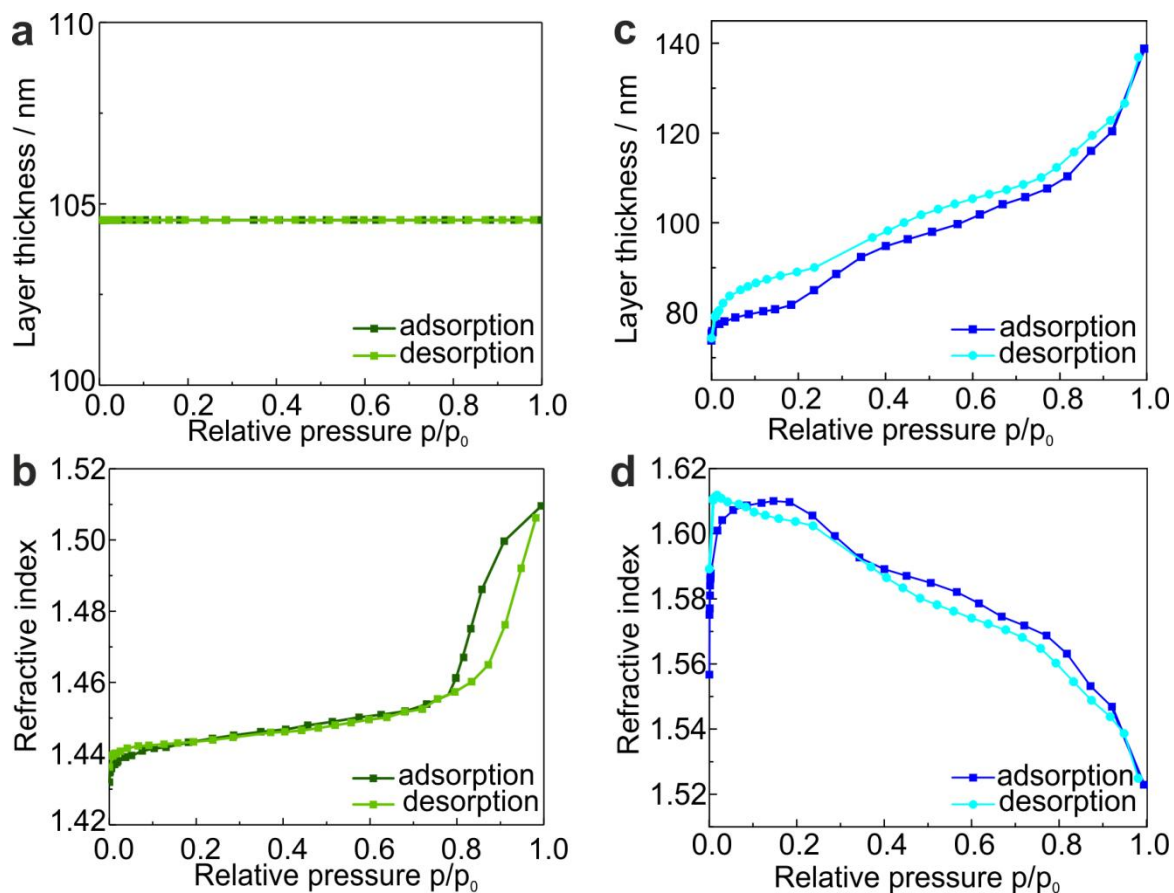
Figure 2.5: Optical isotherms resulting from porosimetry measurements with ethanol and water vapor as analyte. (a) Layer thickness changes of a SiO_2 nanoparticle based thin film, the thickness is assumed to be constant with changing relative pressure of ethanol vapor. (b) Refractive index changes of the SiO_2 nanoparticle based thin film with changing ethanol relative pressure, giving rise to a mesoporous behavior. (c) Layer thickness changes of a $H_3Sb_3P_2O_{14}$ nanosheet based layer showing a strong swelling with increasing relative pressure of water vapor. (d) Refractive index changes of the $H_3Sb_3P_2O_{14}$ nanosheet based thin film as a function of the relative pressure of water vapor.

As porous thin films, SiO_2 and TiO_2 nanoparticle based films were fabricated. In Figure 2.5a-b, the optical isotherm of SiO_2 nanoparticles is shown, the TiO_2 based thin films behave very similarly. Hereby, the particles themselves are dense but upon deposition as a thin film, a porous structure is created by the textural pores and the analyte uptake is favored. According to the definition of the International Union of Pure and Applied Chemistry (IUPAC),[28] for porous materials, six types of isotherms can be distinguished. The sorption behavior of mesoporous materials, such as these nanoparticle based thin films is described by type IV and V, exhibiting the characteristic hysteresis in the higher relative pressure region, which indicates the capillary condensation of the analyte in the mesopores. Upon fitting with the sorption fitting tool, the thickness of the layers is assumed to be constant and only the refractive index is fitted with changing relative pressure range, resulting in the type IV isotherm. Different fitting parameters were applied for nanosheet based thin films (Figure

2.5c-d), which build the core of this thesis. All types of the applied nanosheets (antimony phosphates and lithium tin sulfides) are known for their swelling properties in the bulk material with increasing water vapor pressure,[29] thus also for the thin films we have to assume a swelling upon analyte (water) uptake. For this reason, for the nanosheet based samples, the layer thickness (Figure 2.5c) and the refractive index (Figure 2.5d) are fitted simultaneously with changing analyte relative pressures. For all types of nanosheet films, we observe a similar behavior: a layer thickness increase accompanied by a refractive index decrease with increasing relative vapor pressure of the analyte. These effects point towards an intercalative behavior, the analyte molecules accumulate between the single nanosheets of the thin film, the effective layer thickness increases and the effective refractive index decreases as it is a combination of pure nanosheets and the intercalated analytes.[30, 31]

In this thesis, ellipsometry measurements were performed on thin films of all applied materials, such as antimony phosphate nanosheets, lithium tin sulfide nanosheets, silica and titania nanoparticles. For all thin films, the layer thickness and the tunability of the thickness was determined along with the optical properties, i.e. the wavelength dependent refractive index and extinction coefficient. Further, for all thin films, also the water and VOC sorption capability was tested and from the optical isotherms, the sorption mechanism was derived. The ellipsometry and porosimetry measurements were not only helpful to characterize the materials optically, but these measured constants were also important input parameters for the theoretical calculations. The ellipsometry measurements were performed on a Semilab Sopra PS1000 spectroscopic ellipsometer, which was equipped with a vapor chamber. The data analysis was performed by the SEA tool of Sopra.

2.2.4 PHOTOLUMINESCENCE

Although there are reports on "glow-in-the-dark" materials from the ancient Greeks and later from the middle age,[32] the first scientific experiments on photoluminescence were performed by G. G. Stokes,[33] who also used the word fluorescence[34] for the first time and constructed the first theory in this topic. Parallel, Edmond Becquerel was a pioneering scientist in the instrumental development of photoluminescence,[35] he built the first "phosphoroscope" and was able to measure the time-dependent decay. The deeper understanding of photoluminescence – similar to UV-Vis spectroscopy – was possible after the theoretical development by Max Planck and Albert Einstein.[36]

Photoluminescence (PL) describes light-induced phenomena resulting in emission of photons, such as fluorescence or phosphorescence.[37] The analysis of PL is important for i.e. biological samples, where the dye molecules act as fluorescence markers and can be tracked in fluorescence microscopy for

analysis[38] or chemical for samples, where information about the doping concentrations or phase purity can be gained based on the PL signal.[39]

In PL, a photon with a certain energy is absorbed by the material in study, thereby an electron is excited to a higher energy level, creating an electron-hole pair, an exciton. Upon relaxation, two processes can occur: a radiative and a non-radiative recombination of the exciton. By a radiative recombination, the electron relaxes into the ground state, light is emitted, as the energy gap between the excited and ground state corresponds to the energy of the visible spectral range. The excited electron usually loses energy by relaxation or thermal oscillations, thus the emission spectrum is always red-shifted compared to the excitation wavelength (Figure 2.6b). In phosphorescence, after the excitation, an intersystem crossing takes place, which increases the lifetime of the emission, whereby fluorescence refers to a fast process without the intersystem crossing. Upon a non-radiative process, the recombination energy creates phenomena in the sample, which imply a temperature increase of the system.

According to Figure 2.6a, in our experimental PL set-up, first white light passes through the excitation monochromator, and the light with a desired energy is selected. This monochromatic light interacts with the sample and the emitted photons are detected. After the sample-light interaction, the emitted light enters the detector monochromator and a spectral range with a certain width is detected. One can measure the maximal emission intensity by using monochromatic excitation and tuning the emission wavelength. Further, the excitation optimum can be found by varying the excitation wavelength and measuring the emission and tracking the spectral changes.
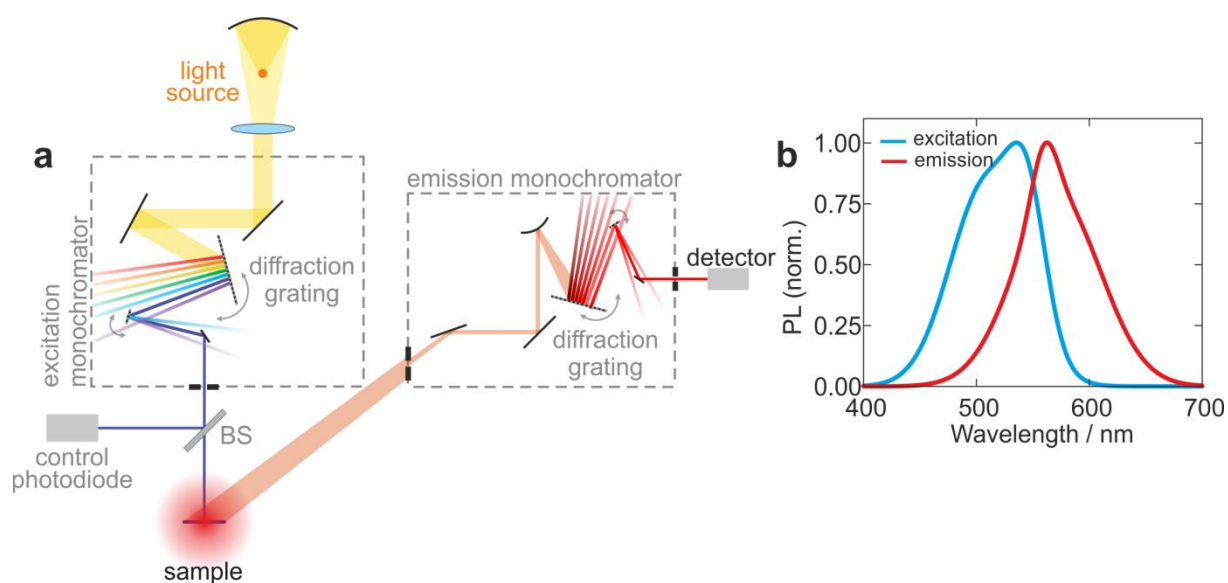
Figure 2.6: (a) Schematic illustration of the photoluminescence measurements, spectrofluorometer Horiba Jobin-Ybon, Fluorolog-3. The image was reproduced with permission.[40] (b) Excitation and emission spectra of the utilized Fluoromax R, Red dyes.

In this thesis, commercial polystyrene nanospheres doped with organic dye (Fluoromax R, Red Thermo Scientific, d ≈ 25 nm) were used as nanosized light sources (Figure 2.6b), which due to the nanometric appearance were suitable to be integrated into photonic resonator structures without introducing any remarkable change in their optical response. The variation of the emission within a carefully designed photonic resonator was monitored with changing humidity values. Hereby, the correlation between changes in the photonic structure and the emission could be investigated.[41] It is important to note the high angle-dependency of the optical properties of the Bragg stacks, which required a careful instrumental design and a PL measurement near to normal incidence. In order to minimize the angular influence, equal excitation and emission angles of 11.25° were applied. To change the humidity levels, the sample was placed into a quartz cuvette, in which the relative humidity value could be defined. The sample was fixed to the chamber in order to preserve constant measurement conditions including the measurement angle. The PL measurements were performed on a spectrofluorometer Horiba Jobin-Ybon, Fluorolog-3, during a research stay at the Multifunctional Optical Materials Group, Institute of Materials Science of Seville, Spanish National Research Council (ICMSE-CSIC).

2.2.5 SCANNING ELECTRON MICROSCOPY

Scanning electron microscopy (SEM) is a powerful and versatile tool to analyze sample morphologies and chemical composition with high resolution. Although the first SEM image was recorded by Max Knoll[42] in 1935 and sample-electron interactions were studied by Manfred von Ardenne in 1937,[43]

[44] the development of SEM was "overshadowed" by the development of transmission techniques, e.g. transmission electron microscopy (TEM). One decade after Ardenne`s development, the first SEM was built and operated by Zworykin and co-workers in 1942,[45] who could reach an image resolution of 50 nm. The SEM as we know it today was built by Charles Oatley[46] and his co-workers in 1948, whereby the resolution was similar to Zworykin`s microscope, but they achieved the 3D image formation and they additionally defined possible application fields of this method.[47]

In contrast to optical methods where the resolution is limited by diffraction,[48] SEM offers high spatial resolution down to 1-10 nm. As indicated in Figure 2.7a, in the SEM, an electron beam is created by an electron gun (usually field emission gun) and is focused by condenser lenses on the sample surface with a spot size of 0.5-5 nm. Passing the scanning coils, the electron beam scans over the sample surface line by line.
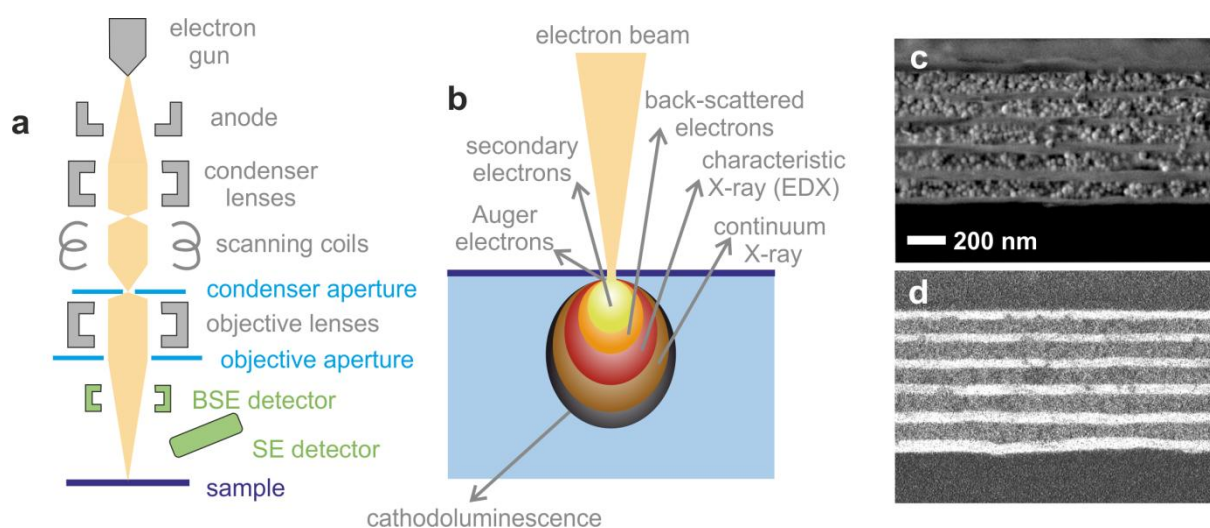
Figure 2.7: (a-b) Scheme of SEM. The illustration of the electron beam path in the SEM (a) and the interaction volume in a SEM measurement and the corresponding signals (b). Secondary electron (c) image and back scattered electron image (d) of a cross section of a SiO_2 nanoparticle and $H_3Sb_3P_2O_{14}$ nanosheet based 1DPC.

Upon hitting the sample surface, different signals generated by different types of interactions of the electron beam with the sample surface are detected and converted into gray scale values on the computer image (Figure 2.7c-d). To obtain an SEM image, secondary electrons and back scattered electrons are detected. Secondary electrons are generated by interactions of the primary beam with the weakly bound outer electrons of the atoms in the sample. The primary electrons transfer energy to the valence electron of the sample, which are ejected by this procedure and can be detected. As these electrons originate from areas near the sample surface, secondary electrons are suitable to visualize the topology of the samples (Figure 2.7c), such as the sheet-like and the nanoparticle morphology in the 1DPC in Figure 2.7c. Back scattered electrons are reflected electrons of the primary beam by elastic scattering. The intensity of this reflection depends on the atomic number (*Z*)

of the elements the samples is made of, which fact leads to a direct correlation of the atomic number of the sample and the image brightness in the back scattered image (Figure 2.7d). With this type of signal, chemical compositions of the sample can be analyzed, for example in Figure 2.7d, the $H_3Sb_3P_2O_{14}$ nanosheet layers appear brighter compared to the SiO_2 caused by the higher average Z and a larger probability of back scattered electrons to arise from this area.

In this thesis, SEM measurements were performed in order to visualize the morphology of the exfoliated nanosheet materials and to obtain the cross section images of the 1DPCs and resonator structures. Analyzing the latter, the stacking homogeneity, the stacking order, the quality of the interfaces and the different material morphologies can be obtained. The cross sections of the 1DPCs and optical resonators were investigated with a Zeiss Merlin FE-SEM, the images were recorded by Viola Duppel, MPI for Solid State Research. SEM images of the exfoliated nanosheets and the bulk materials were performed by Claudia Kamella, MPI for Solid State Research, on a Vega TS 5130 MM (Tescan) electron microscope.

2.2.5.1 ENERGY DISPERSIVE X-RAY SPECTROSCOPY

To analyze the local chemical composition of the materials, energy dispersive X-ray analysis can be performed in combination with SEM. Once the primary electron beam hits the sample, an electron from an inner shell can be emitted by the transferred energy, and the created hole is filled by an electron from an outer shell (Figure 2.8). The energy difference of both shells is emitted in the form of characteristic X-rays. The spectrum can be analyzed with the internal software of the SEM-EDX and the distribution of elements can be determined, thus the elemental composition can be derived. As these X-rays are emitted from areas near the surface, this technique gives information about the local material composition at or near the surface.
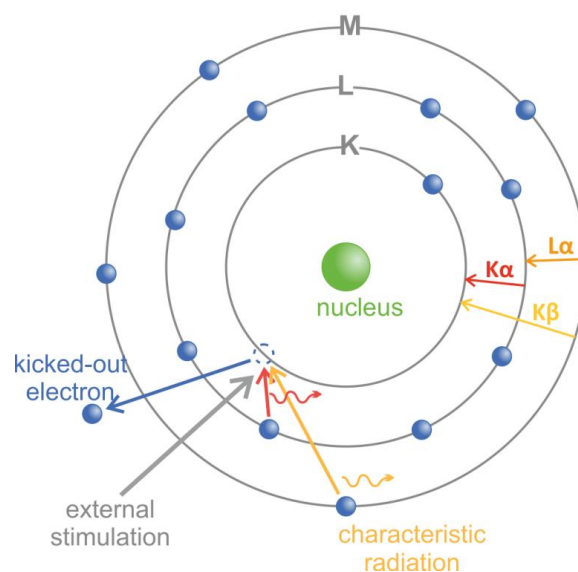
Figure 2.8: Schematic illustration of the signal generation in EDX analysis in a SEM.

In this thesis, the SEM-EDX measurements were performed in order to prove the composition of the exfoliated nanosheet materials. SEM-EDX measurements were performed by Claudia Kamella, MPI for Solid State Research, on a Vega TS 5130 MM (Tescan) electron microscope equipped with Si/Li detector (Oxford).

2.2.6 TRANSMISSION ELECTRON MICROSCOPY

While the resolution in SEM is limited by the focused spot diameter and the interaction volume, in transmission electron microscopy (TEM), parallel illumination (Figure 2.9) is used to create the image and resolutions down to the Angstrom range can be reached.[49] Transmission electron microscopy (TEM) is the original form of electron microscopy and was invented by Ernst Ruska in 1933 – a PhD student of Max Knoll, who recorded the first SEM image. Many years later in 1986, Ruska was awarded the Nobel Prize in Physics for the invention of the TEM.[50]

The electron beam is generated by an electron gun, and is accelerated by the anode at typically about 300 kV.[51] The electron beam passed through the ultrathin sample (typically maximum 100 nm thick), which due to interaction with the sample is modified, e.g. is elastically scattered or diffracted. After the interaction, the beam passes the objective, the intermediate and the projective lenses and after magnification, the imprint of the sample is detected on the image plane, usually by fluorescence, complementary metal oxide (CMOS) or a CCD (charge-coupled device) camera (Figure 2.9a). For TEM, the sample preparation is a crucial point, otherwise the electrons are absorbed or scattered to a large extent and cannot be transmitted through the sample.
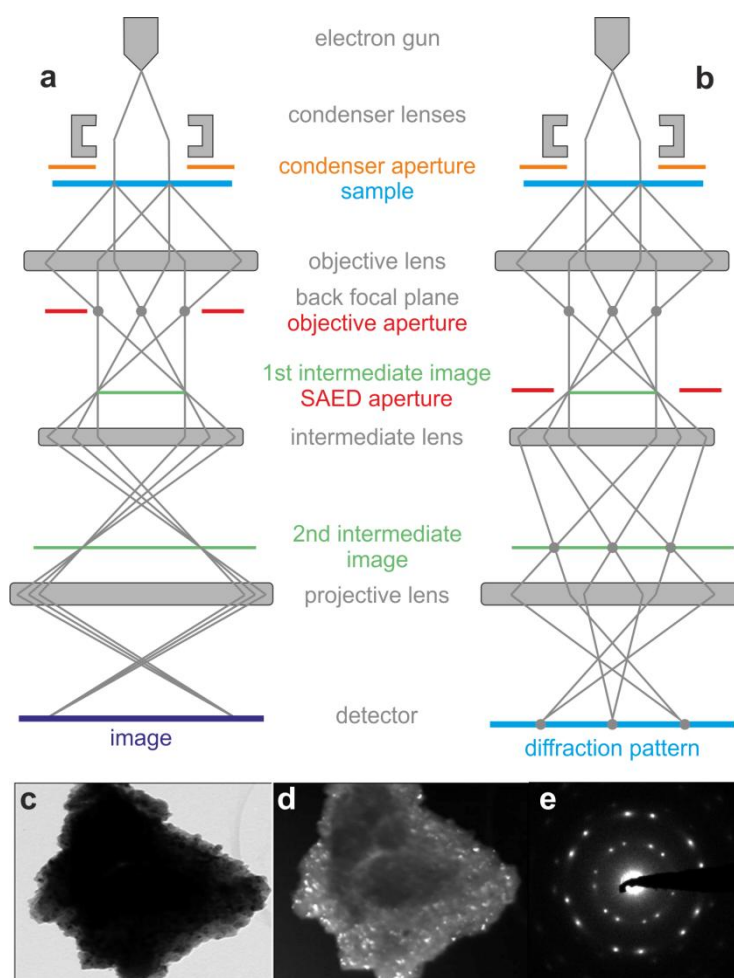
Figure 2.9: (a-b) Scheme of the working principle of TEM. Schematic illustration of the beam path in the imaging mode (a) and in the diffraction mode (b). An exemplary bright field image (c) and dark field image (d) of an aluminium-copper-alumina nanocomposite.[52] (e) An electron diffraction pattern of two single lithium tin sulfide nanosheets after exfoliation.[53]

In TEM, different imaging techniques are possible: the direct image detection and the detection of the diffraction pattern (Figure 2.9). These two imaging modes work with the two different types of generated electrons after the interaction with the sample, the unscattered electrons and the scattered electrons.

IMAGING IN TRANSMISSION ELECTRON MICROSCOPY

In imaging mode, the objective aperture is applied in the back focal plane to create the bright field (BF) image (Figure 2.9c), the central transmitted electrons (unscattered electrons) are selected, the rest is blocked by the aperture. The image is created by the mass-thickness-contrast; sample areas with a higher atomic number (Z) or thickness appear darker in the image, as these scatter the electron beam more strongly and the scattered electrons are blocked by the aperture. Thin areas with a low Z appear brighter in these images, as more unscattered electrons are transmitted through

the sample and reach the detector. By blocking the unscattered electrons and using the scattered electrons in the imaging mode, the dark field (DF) image (Figure 2.9d) is created. Hereby sample areas with a higher *Z* appear brighter (e.g. clusters in the composite with a larger *Z*, embedded in a lower *Z* matrix), as more electrons from these areas are detected, as only the scattered electrons are used for the image formation.

ELECTRON DIFFRACTION IN TRANSMISSION ELECTRON MICROSCOPY

Another powerful tool of TEM in the analysis of crystalline samples is the selected area electron diffraction (SAED) analysis. The thin crystalline sample in TEM acts to the incident electron beam as a diffraction grating, and the electrons get diffracted by the atoms of the sample. In this technique, the SAED aperture is inserted and the back focal plane is projected, and as a result, a diffraction pattern arises (Figure 2.9e). The SAED aperture gives additionally the possibility to select the sample area and record the diffraction pattern from this region. From the diffraction pattern, information on the crystal structure, composition or phase purity can be gained.

SCANNING TRANSMISSION ELECTRON MICROSCOPY

TEM can be modified with the application of a scanning coil and additional lenses to a scanning TEM (STEM). In contrary to parallel illumination of the sample, the electron beam is focused and scanned above the sample surface. In STEM, the image is formed by detecting the counts, the amount of detected electrons arising from the different points of the sample.

2.2.6.1 ELECTRON ENERGY LOSS SPECTROSCOPY

In combination with STEM, in addition to the visualization of the sample with high resolution, the local composition and the chemical properties can also be analyzed with Electron Energy Loss Spectroscopy (EELS).[54, 55] Upon passing the specimen, the electron beam interacts with the sample and the electrons are scattered elastically or inelastically. Inelastic scattering refers to electrons which lose from their original energy upon, while the energy of elastically scattered ones remains constant. These scattered electrons can be split up by a magnetic prism (Figure 2.10a), which deflects the electron beam depending on its energy. With this, the exact energy losses can be determined and the material composition can be analyzed. In the EEL spectrum, three different regions can be distinguished. The zero loss peak (ZLP) appears at 0 eV energy loss, and refers to electrons which do not undergo inelastic scattering, but are only scattered elastically and do not lose energy. The ZLP is usually used for the sample calibration. Secondly, the low loss range (energy loss 2-50 eV) represents the excitation of plasmons, inter- or intraband transitions. This region can be used for phase identification, or the analysis of bandgaps. The third and for this thesis the most important range is

the core loss region (>50 eV). A core excitation occurs, when an incident electron promotes a core electron to higher, free energy states. In the core loss region, characteristic edges in the spectrum can be observed, as in this process the incident electron loses a characteristic energy, as the electrons can be promoted only by defined energy levels. For the analyses in this thesis, this core-loss region was used (Figure 2.10c), as the element edges are very characteristic for the particular element (and oxidation state) and this allows a very specific elemental composition analysis. The notation of the different electron excitations are depicted in Figure 2.10b.
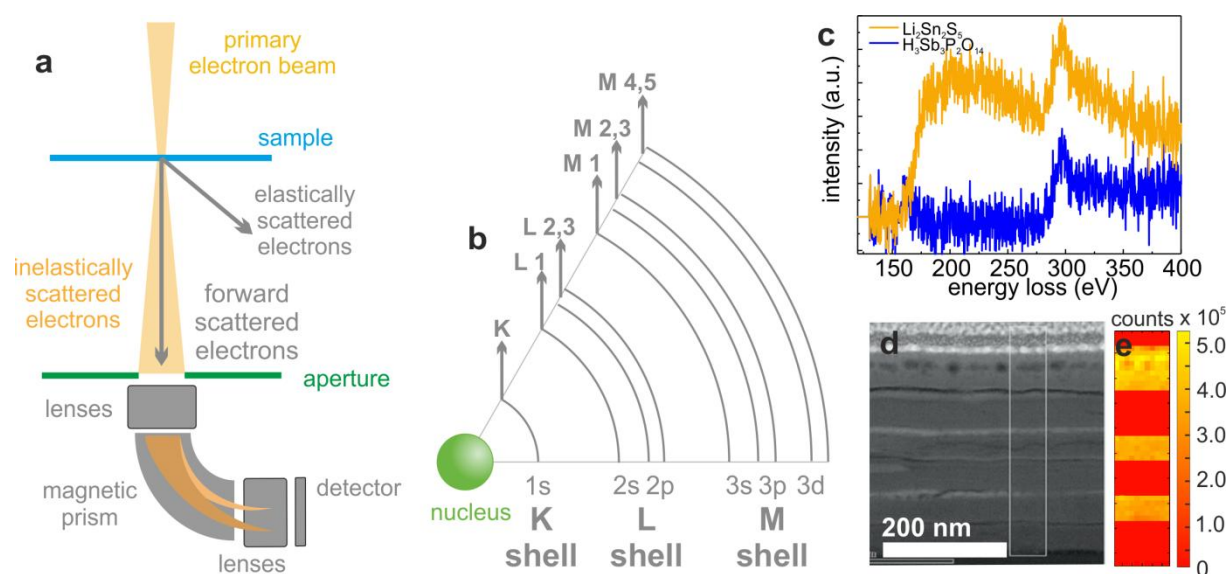
Figure 2.10: Schematic illustration of EELS. (a) The detection principle of EELS. (b) The notation of the different signals arising from the core loss region signal. (c) An exemplary EEL spectrum of the core loss region showing $Li_2Sn_2S_5$ (yellow) and $H_3Sb_3P_2O_{14}$ (blue). (d) A STEM image of a cross section of a $Li_2Sn_2S_5$/$H_3Sb_3P_2O_{14}$ nanosheet based 1DPC. (e) An element map of $Li_2Sn_2S_5$ in the 1DPC showing the periodic layer structure of this material.[53]

Upon combining EELS with STEM, element maps across the sample can be created and the local elemental composition can be analyzed. Hereby, the intensities of the different characteristic element edges are detected in the STEM mode (Figure 2.10d) and the intensity plots give rise to the appearance of the specific elements at the specific sample position (Figure 2.10e).

TEM-EELS measurements in this thesis were performed on 1DPC cross sections as the SEM reached its spatial resolution limits. Using the secondary electron images from the SEM (chapter 2.2.5) the two different nanosheet materials ($H_3Sb_3P_2O_{14}$ and $Li_2Sn_2S_5$ nanosheets) could not be distinguished based on the similar morphology, and further the back scattered electron image in SEM gave only a weak material contrast, as the atomic numbers of these two materials are very similar. However, EELS provided a suitable analytical method to distinguish the two different materials also locally by

performing the elemental mapping. Further, in this thesis TEM-SAED patterns were recorded in order to prove the turbostratically disordered morphology (rotated along the z-direction) of the nanosheets after the exfoliation of the bulk material.

TEM and EELS measurements were performed by Dr. Sophia Betzler, LMU München and MPI for Solid State Research, on a FEI Titan Themis microscope (60–300 kV) equipped with a Cs corrector. TEM measurements with SAED patterns were measured by Viola Duppel, MPI for Solid State Research, on a Phillips CM30 ST TEM (300 kV, LaB$_6$ cathode) equipped with a Gatan CCD camera.

2.2.7 X-RAY DIFFRACTION

X-ray diffraction (XRD) is a powerful and non-destructive method to analyze and identify crystalline samples regarding their crystal structure, crystallinity, phase purity and particle size. X-rays, also called Röntgen-rays, were discovered by Wilhelm Röntgen in 1895, for which he was awarded with the first Nobel Prize in Physics in 1901.[56] Long time ago it was debated by the physical society, whether X-rays are electromagnetic waves. The final prove was delivered by Max von Laue by his diffraction experiment of X-rays on a copper sulfide crystal in 1912 at the University of Munich, for which he was awarded with the Nobel Prize in 1914.[57] This ultimately proved the wave-nature of X-rays and simultaneously delivered important contributions to crystal structure analysis via X-rays. After Laue`s discovery, many scientists were involved in the theoretical and instrumental development of X-ray crystallography, whereby the most important contribution was provided by William Henry Bragg and his son William Lawrence Bragg, who were awarded for "their services in the analysis of crystal structure by means of X-rays", including the Bragg law, with the Nobel Prize in 1915.[58]

Similar to other analytical techniques, also in XRD analysis the probe beam must have a wavelength comparable to the range of the analyzed specimen features, i.e. the atomic spacings in the crystal structure. For this, X-rays are generated when targets, such as Cu or Mo, are irradiated by high-energy electrons under vacuum. Thereby, core electrons are promoted to higher levels of outer shells, and by the relaxation back to the ground state, they emit X-rays with a characteristic wavelength (λ (Cu-K$_\alpha$) = 1.541 Å, λ (Mo-K$_\alpha$) = 0.710 Å). The created X-ray beam passes through a monochromator and a collimator before interacting with the crystalline sample. The incident monochromatic X-ray beam is diffracted at the lattice planes of the sample (Figure 2.11a) and intensity maxima arise from constructive interferences, when the Bragg equation (2.5) is fulfilled:
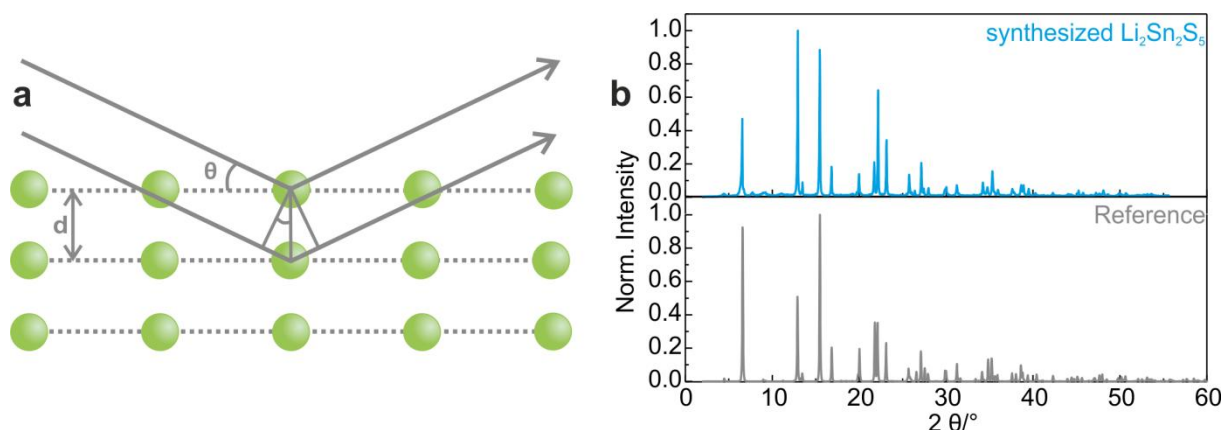
Figure 2.11: Schematic illustration of X-ray diffraction on a crystalline sample. (a) The beam path of X-rays interacting with the sample. (b) An exemplary powder diffraction pattern of $Li_2Sn_2S_5$ with the calculated reference.

$$n\lambda = 2d\,sin\,\theta \qquad\qquad (2.5)$$

where the order of diffraction *n* is an integer, λ is the wavelength, *d* the plane-spacing in the crystalline lattice and θ the incident angle of the X-ray beam. The created intensity pattern is recorded by the detector and a powder diffraction pattern is created (Figure 2.11b).

In this thesis, X-ray diffraction analysis was used to analyze the synthesized solid-state samples and identify their compositions and crystal structures. Further, bulk cation-proton exchanges were detected by monitoring the shift of the stacking reflection, and further the exfoliation of the bulk material into single nanosheets was followed. Hereby, the intensity of the stacking reflection significantly decreases upon exfoliation and reflections of the diffraction pattern of the nanosheet sample exhibits an asymmetric Warren-type peak.[59, 60] X-ray diffractograms were analyzed with the help of the software WINXPOW[61, 62] and compared with the International Centre of Diffraction Data (ICDD) database.[63]

In this thesis, a STOE Stadi P powder diffractometer in Debye-Scherrer-geometry (STOE & Cie GmbH, Darmstadt) Cu $K_{\alpha 1}$ (λ (Cu-K_α) = 1.541 Å) or Mo K_α radiation λ (Mo-K_α) = 0.710 Å, Ge(111)-monochromator, with a Mython 1k detector was used to perform the measurements.

2.2.8 DYNAMIC LIGHT SCATTERING

Dynamic Light Scattering (DLS) is a non-destructive tool to analyze the particle size and distribution of nanoparticles in a colloidal suspension.[64] The roots of the DLS technique point back to Lord Rayleigh and his studies on light scattering on particles smaller than the wavelength of light,[65, 66] and to Albert Einstein and his studies on Brownian motion.[67] The instrumental development began with the development of lasers, and with the pioneering studies of Pecora *et al.*[68] on time dependent light

scattering. At that time, DLS was used to measure the diffusion of macromolecules and to calculate the hydrodynamic radius. With the development of information technology, for today, DLS became a fast method to analyze particle size and size distribution in solution.

In a DLS measurement, a monochromatic laser beam travels through the measured suspension. The sample is thermally stabilized, in order to keep the thermal motion constant, which influences the Brownian motion in the suspension, as it has an important impact on the particle size determination. Upon illuminating the sample, the suspended particles scatter the laser light. The intensity variations caused by interference of the scattered light by the moving particles give rise to the diffusion coefficient and hence the size of the suspended particles, according to the Einstein-Stokes equation (2.6):

$$D = \frac{k_B T}{3\pi\eta d} \qquad (2.6)$$

where D is the diffusion coefficient, k_B the Boltzmann constant, T the temperature, η the viscosity and d the hydrodynamic diameter of the particles. For the exact determination of the particle size in DLS, requirement is that the particles are in a size range approx. below 1 micron.

In this thesis, DLS measurements were performed in order to measure the particle size of the applied TiO_2 and SiO_2 nanoparticles after the synthesis. The measurements were performed with a Malvern Zetasizer Nano-ZS with a 4 mW He-Ne laser (λ = 633 nm).

2.2.9 ATOMIC FORCE MICROSCOPY

Atomic Force Microscopy (AFM) is a type of Scanning Probe Microscopy (SPM),[69] which is capable of investigating the surface of nanostructured samples with a high resolution. Scanning Tunneling Microscopy (STM), as a predecessor of AFM, was invented by Gerd Binnig and Heinrich Rohrer in the early 1980s, and the two inventors were awarded with the Nobel Prize for Physics in 1986 (together with Ernst Ruska for the development of TEM).[70] Few years later, AFM and its first implementations were developed by Gerd Binning and co-workers.[71, 72]

AFM can be used in three modes: for force measurement, for manipulation or for imaging. In this thesis, only the latter, the imaging mode was used and, hence, will be discussed here in detail. In AFM, a sharp probe tip, fixed on a flexible cantilever, is brought in contact with the sample and scans through the sample surface.[73] By experiencing the sample`s height variations, the cantilever is deflected in order to follow the sample surface with the tip. Further, a laser beam is reflected on the back side of the cantilever and hits a photodiode, which can read out the position of the laser beam.

By the deflection of the cantilever, the laser beam is also deflected and its position on the photodiode is changed. After scanning the sample surface line by line, a 3D image can be created, which corresponds to the topology of the sample. To avoid damages of the surface, often the tapping mode is used, whereby the tip is continuously oscillating and does not touch the sample. By monitoring the changes in this oscillation, a height profile can be reconstructed similar to the contact mode. AFM is a very sensitive technique to surface variations and shows a height resolution below 1 nm.[74]

In this work, this technique was used to determine, if the exfoliation of the bulk material into nanosheets was successful and if single or multilayered nanosheets were achieved by the delamination. The measurements were conducted by Pirmin Ganter, MPI for Solid State Research, on a Veeco CP II system.

2.2.10 IMPEDANCE SPECTROSCOPY

Impedance spectroscopy or dielectric spectroscopy is a method to analyze the dielectric properties of samples as a function of the frequency. An alternating current (AC) flows through the sample and interacts with the dipole moments. At different AC frequencies, various dielectric processes are generated and measured. The following processes can occur with decreasing AC frequency ranges: electronic polarization, atomic polarization, dipole relaxation, ionic relaxation or dielectric relaxation. Depending on the nature of the measured sample, different processes dominate, but the sum of all processes is measured as the impedance. The characteristic features can be analyzed indirectly by fitting the electric response of a model circuit with different components, such as capacitors or resistance in parallel or series connection. With the combination of the basic circuit elements, even complex structures can be described, such as ionic conductors as a capacitor and a resistance connected in parallel.

In this thesis, the conductance change of the nanosheet thin films at various relative humidity levels was measured in a two-point measurement geometry. An AC voltage of 500 mV was applied to the sample and the frequency range of 1 Hz to 1 MHz measured, however for time-dependent measurements, the frequency was fixed to 300 Hz and the conductance was measured. The measurements were performed by Pirmin Ganter, MPI for Solid State Research, on a Princeton Applied Research, Versa STAT MC impedance bridge.

2.3 THEORETICAL CALCULATIONS

Theoretical calculations were performed in order to design the photonic structures prior to fabrication, to understand the optical properties (reflectance, transmittance, field intensity

distribution, emission) and their behavior under environmental conditions changes. In this section, the applied transfer matrix method and genetic algorithm formalisms are introduced.

2.3.1 TRANSFER MATRIX METHOD

In order to design 1DPCs showing a desired optical response and understand the different phenomena related with their structure, analytical calculations were performed. Hereby, the reflectance and transmittance spectra as well as the spatial and spectral field intensity distributions were calculated for 1DPCs as well as for optical resonator structures.

The Transfer Matrix Method (TMM) was applied in order to calculate these properties of the applied systems, as it is a commonly used method to describe the propagation of electromagnetic waves in a layered medium in one spatial direction.[75, 76] The reflection and transmission at a single interface between two media is described by the Fresnel equations. However, when the studied system is composed of several layers, at every interface, a partial reflection and transmission occurs (Figure 2.12). Depending on the path lengths, which in turn depend on the refractive indices and the layer thicknesses, the light beams can interfere constructively or destructively. The total reflection/transmission is the sum of an infinite number of reflections/transmissions arising from the multilayer. According to Maxwell`s equations, the conditions of continuity for the electric field propagating the interface between two optically different media are defined, which is utilized by the TMM. This means, that if the field is known at the beginning of the layer, the field at the end of the layer, before entering the next interface, can be derived from simple matrix operations. As a result, a multilayer system can be described as the product of the matrices, which describe the layers and the interfaces. Finally, the physical measures, such as the reflectance and the transmittance can be extracted from the matrices and additionally, the field intensity distribution can be calculated at each spatial point of the multilayer at each wavelength giving rise to an intensity map.
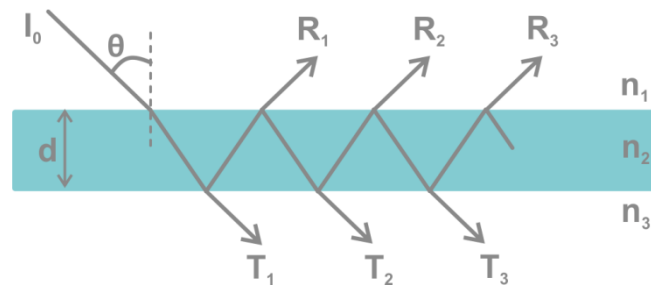

Figure 2.12: Schematic illustration of the light propagation of a multilayered system in one dielectric layer.

For normal incidence with stacked layers along the *z-axis*, and assuming that the field within one layer can be represented as the superposition of left (*l*) and right (*r*) traveling wave with wave number *k*, the electric field can be formulated as:

$$E(z) = E_r e^{ikz} + E_l e^{-ikz} \qquad (2.7)$$

The field gradient *F(z)* can be expressed as the derivative of *E(z)*:

$$F(z) = ik E_r e^{ikz} - ik E_l e^{-ikz} \qquad (2.8)$$

According to Maxwell`s equations, **E** and **F** must be continuous across a boundary, whereby one can express the field as a vector of *(E(z), F(z))*.

A propagation of light in the multilayered structure over a distance *d* into a positive *z* direction can be described by the matrix in (2.9):

$$\mathbf{M} = \begin{pmatrix} \cos kd & \frac{1}{k}\sin kd \\ -k\sin kd & \cos kd \end{pmatrix} \qquad (2.9)$$

Using this, we can express the field at point *z+d* as:

$$\begin{pmatrix} E(z+d) \\ F(z+d) \end{pmatrix} = \mathbf{M} \cdot \begin{pmatrix} E(d) \\ F(d) \end{pmatrix} \qquad (2.10)$$

whereby *k* is the wave number in the medium and *d* the layer thickness. For a system with *N* layers, the system transfer matrix M_s is a product of all matrices. With this, at all points of the structure, by applying the according matrix, the field can be calculated.

The main goal of these calculations is to extract the reflectance and transmittance after the interaction with light. Assuming the multilayer starts at *z* = 0, the reflectance can be calculated for negative *z* values and the transmission for *z > d´* values, where *d´* corresponds to the total thickness:

$$E_L(z) = E_0 e^{ik_l z} + r E_0 e^{-ik_l z} \qquad (2.11)$$

$$E_R(z) = t E_0 e^{ik_r z} \qquad (2.12)$$

whereby *r* and *t* are the amplitude of the reflectance and transmittance coefficients, k_l and k_r the wave numbers in the medium of the left (*l*) and right (*r*) propagating light waves. Finally, the transmittance and the reflectance values are given by equations (2.13 and 2.14):

$$T = \frac{k_r}{k_l}|t^2| \qquad (2.13)$$

and

$$R = |r^2| \qquad\qquad (2.14)$$

respectively.

One example for the application of this method is illustrated in Figure 2.13. The reflectance and transmittance spectra of a multilayered system consisting of 12 layers of alternating layers of silica (n = 1.40, d = 100 nm) and titania nanoparticles (n = 1.90, d = 100 nm) is calculated, and the corresponding spatial (y-axis) and spectral (x-axis) field intensity distribution along the sample (y-axis) is shown as an intensity map.
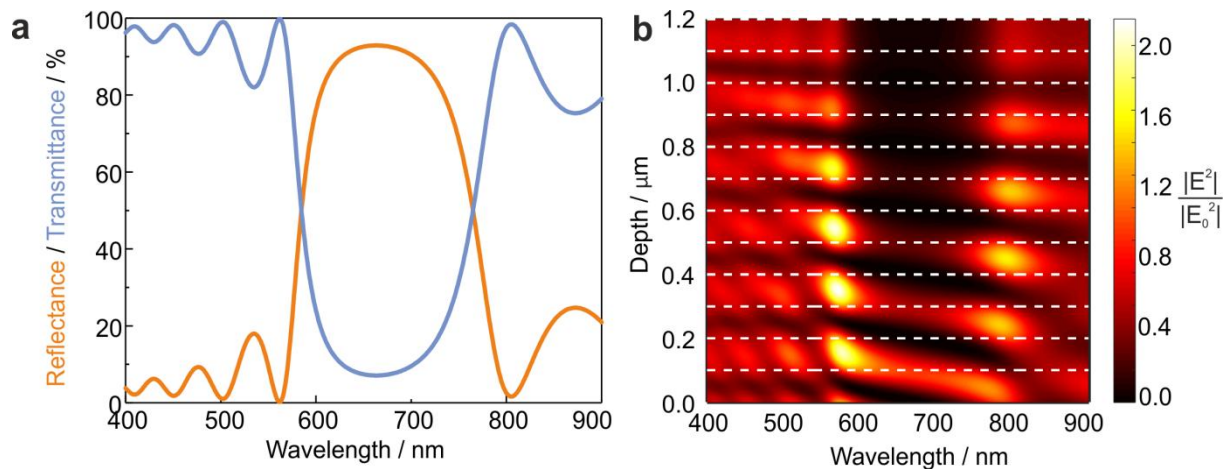
Figure 2.13: Calculated optical properties of the multilayered system described in the text. (a) Calculated reflectance and transmittance spectra. (b) Calculated spectral (x-axis) and spatial (y-axis) field intensity distribution within the multilayered system. The white dashed lines show the layer interfaces within the multilayered system. Light is traveling in the positive y-axis direction.

The original MATLAB code based on the TMM for the calculations for this thesis was written by Dr. Gabriel Lozano and Dr. Alberto Jiménez-Solano, Multifunctional Optical Materials Group, Institute of Materials Science of Seville, Spanish National Research Council (ICMSE-CSIC). The code was modified and adopted for the systems shown in chapters 3, 4, 5 and 6 by Katalin Szendrei-Temesi.

2.3.2 GENETIC ALGORITHMS

Genetic Algorithms (GAs) is a commonly used numerical method for optimization problems.[77] This technique is inspired by biology, and utilizes actions, which are known from biological evolution in order to generate solutions for the optimum, the objective function (Figure 2.14).[78] The evolution usually starts with a population of randomly generated individuals, and the GA creates the next generation by different methods: by selecting directly the best individuals from the current population (elitism), by selecting random individuals (selection), using the original individuals as

parents to create the next generation (crossing) or by mutating certain individuals (mutation). After creating several generations, the population evolves towards an optimal solution. The stop criteria can be diverse depending on the goals, e.g. reaching the maximum number of generations, reaching a certain precision of the objective function or by creating a certain amount of generations, where the objective function remains constant.
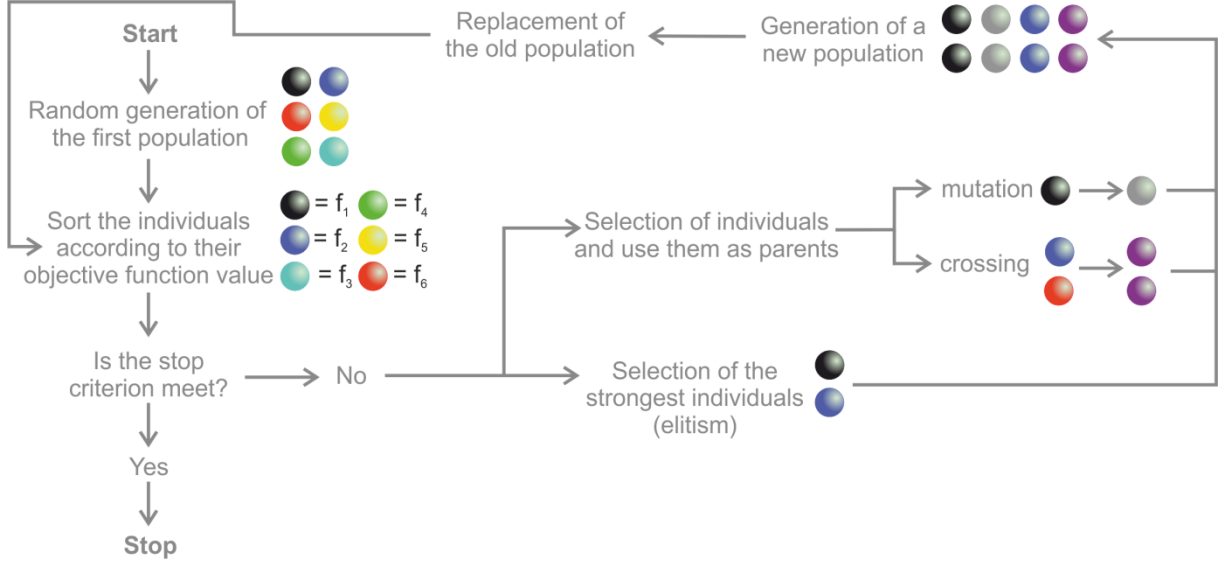
Figure 2.14: Schematic illustration of the utilized genetic algorithm.

In this thesis, GAs were combined with the TMM in order to reproduce the optical response of a multilayered system theoretically as well as to obtain the structure, which presents the optical properties on demand. For instance, for the former example, the populations consist of layer thicknesses and the deviation of them, relative to the theoretical values in a perfect system. The goal of the GA for these systems is to minimize the objective function (equation 2.15), namely to optimize the layer thicknesses of the multilayered structure in order to reproduce the measured reflectance spectra. The objective function for this problem can be expressed as:

$$f = \sum_{i=\lambda} (R_i^{exp} - R_i^{theo})^2 \qquad (2.15)$$

whereby R_i^{exp} and R_i^{theo} correspond to the experimental and theoretical reflectance spectra.

TMM combined with GAs was further applied to study diffusion processes into the multilayers, hereby a time-dependent analysis was performed and for each time point the objective function was optimized. These calculations were performed by Dr. Alberto Jiménez-Solano, MPI for Solid State research.

2.4   REFERENCES

[1]   A. G. Emslie, F. T. Bonner, L. G. Peck, *J. Appl. Phys.* **1958**, *29*, 858-862.

[2]   M. D. Tyona, *Adv. Mater. Res.* **2013**, *2*, 195-208.

[3]   N. C. Thomas, *J. Chem. Educ.* **1991**, *68*, 631.

[4]   I. Newton, *Phil. Trans. Roy. Soc.* **1672**, *5*, 3075.

[5]   J. v. Fraunhofer, *J. Ann. Phys.* **1817**, *26*, 264.

[6]   G. Kirchhoff, *Ann. Phys.* **1860**, *185*, 275-301.

[7]   G. Kirchhoff, *Ann. Phys.* **1860**, *185*, 148-150.

[8]   N. Bohr, *The theory of spectra and atomic constitution*, The University Press, Cambridge Eng., **1922**.

[9]   N. Bohr, *On the quantum theory of line-spectra*, A. F. Høst, København, **1918**.

[10] I. R. Altemose, *J. Chem. Educ.* **1986**, *63*, A216.

[11] L. R. Koller, *Ultraviolet radiation*, 2d ed., Wiley, New York, **1965**.

[12] A. Cary, *History of High Performance UV-Vis-NIR Spectroscopy*, Varian.

[13] H. H. Perkampus, *UV-VIS spectroscopy and its applications*, Springer-Verlag, **1992**.

[14] M. Bass, O. S. o. America, *Handbook of optics*, McGraw-Hill, **2001**.

[15] Bronkhorst-High-Tech, https://www.bronkhorst.com/products/liquid-flow/, accessed on 13.03.2018.

[16] H. J. Boer, *Liquid-Injection System Based on Mass Flow Controllers, Solid State Technol*. **1996**.

[17] *Fundamentals of Mass Flow Control: Critical Terminology and Operation Principles for Gas and Liquid MFCs; Advance Energy Ltd.,* Fort Collins, Colorado, **2005**.

[18] Bronkhorst-High-Tech*, Vol. 2015*, www.fluidat.com, accessed on 13.03.2018.

[19] P. Drude, *Ann. Phys.* **1887**, *268*, 584-625.

[20] P. Drude, *Ann. Phys.* **1891**, *279*, 126-157.

[21] D. E. Aspnes, A. A. Studna, *Appl. Opt.* **1975**, *14*, 220-228.

[22] R. H. Muller, J. C. Farmer, *Rev. Sci. Instrum.* **1984**, *55*, 371-374.

[23] H. Fujiwara, *Spectroscopic Ellipsometry*, John Wiley & Sons, Ltd, **2007**, pp. 1-11.

[24] H. Fujiwara, *Spectroscopic Ellipsometry*, John Wiley & Sons, Ltd, **2007**, pp. 81-146.

[25] S. P. Pavunny, R. Thomas, R. S. Katiyar, *ECS Trans.* **2012**, *45*, 219-223.

[26] Y. T. Kim, R. W. Collins, K. Vedam, *Surf. Sci.* **1990**, *233*, 341-350.

[27] M. R. Baklanov, K. P. Mogilnikov, V. G. Polovinkin, F. N. Dultsev, *J. Vac. Sci. Technol., B: Microelectron. Nanometer Struct.-Process., Meas., Phenom.* **2000**, *18*, 1385-1391.

[28] https://goldbook.iupac.org, accessed on 06.02.2018.

[29] S. Deniard-Courant, Y. Piffard, P. Barboux, J. Livage, *Solid State Ionics* **1988**, *27*, 189-194.

– Methods –

[30] K. Szendrei, P. Ganter, O. Sánchez-Sobrado, R. Eger, A. Kuhn, B. V. Lotsch, *Adv. Mater.* **2015**, *27*, 6341-6348.

[31] E.-P. Ng, S. Mintova, *Microporous Mesoporous Mater.* **2008**, *114*, 1-26.

[32] B. Valeur, M. N. Berberan-Santos, *J. Chem. Edu.* **2011**, *88*, 731-738.

[33] G. G. Stokes, *Philos. Trans. R. Soc. London* **1852**, *142*, 463-562.

[34] G. G. Stokes, *Philos. Trans. R. Soc. London* **1853**, *143*, 385-396.

[35] E. Becquerel, *La lumière, ses causes et ses effets: Effets de la lumière*, Firmin Didot frères, fils et cie, **1868**.

[36] A. Einstein, *Ann. Phys.* **2005**, *14*, 280-291.

[37] C. R. Ronda, *Luminescence: From Theory to Applications*, Wiley, **2008**.

[38] https://www.nobelprize.org/educational/physics/microscopes/fluorescence/, accessed on 02.02.2018.

[39] K. Przibram, *Irradiation Colours and Luminescence: A Contribution to Mineral Physics*, Pergamon Press, **1956**.

[40] A. Jiménez-Solano, *PhD thesis*, ICMSE-CSIS, Sevilla, Spain, **2017**.

[41] A. Jiménez-Solano, J. F. Galisteo-López, H. Míguez, *Small* **2015**, *11*, 2727-2732.

[42] M. Knoll, *Zeitschrift für technische Physik* **1935**, *16*, 467-475.

[43] M. von Ardenne, *Improvements in electron microscopes*, **1939**, GB19380005181 19380218.

[44] M. von Ardenne, *Z. Phys.* **1938**, *109*, 553-572.

[45] V. A. Zworykin, Hillier, J., Snyder R. L., *ASTM Bull.* **1942**, *117*, 15-23.

[46] C. W. Oatley, *The Early History of the Scanning Electron Microscope*, University of Cambridge Department of Engineering, **1979**.

[47] C. W. Oatley, T. E. Evekhart, *J. Electron. Control* **1957**, *2*, 568-570.

[48] E. Abbe, *Archiv für mikroskopische Anatomie* **1873**, *9*, 413-418.

[49] D. B. Williams, C. B. Carter, *Transmission Electron Microscopy: A Textbook for Materials Science*, Springer, **2009**.

[50] https://www.nobelprize.org/educational/physics/microscopes/tem/, accessed on 1.3.2018.

[51] L. Reimer, H. Kohl, *Transmission Electron Microscopy: Physics of Image Formation*, Springer New York, **2008**.

[52] P. K. Dash, P. B. S. Murty, R. B. K. Aamanchi, *Am. J. Nanomater.* **2015**, *3*, 28-39.

[53] K. Szendrei-Temesi, O. Sanchez-Sobrado, S. B. Betzler, K. M. Durner, T. Holzmann, B. V. Lotsch, *Adv. Func. Mater.*, **2018**, *28*, 1705740.

[54] R. F. Egerton, *Electron Energy-Loss Spectroscopy in the Electron Microscope*, Springer US, New York, US, **2011**.

[55] F. Hofer, F. P. Schmidt, W. Grogger, G. Kothleitner, *IOP Conf. Ser.: Mater. Sci. Eng.* **2016**, *109*, 012007.

[56] https://www.nobelprize.org/nobel_prizes/physics/laureates/1901/, accessed on 18.02.2018.

[57] https://www.nobelprize.org/nobel_prizes/physics/laureates/1914/, accessed on 18.02.2018.

[58] https://www.nobelprize.org/nobel_prizes/physics/laureates/1915/, accessed on 18.02.2018.

[59] R. A. Gordon, D. Yang, E. D. Crozier, D. T. Jiang, R. F. Frindt, *Phys. Rev. B: Condens. Matter Mater. Phys.* **2002**, *65*, 125407/125401-125407/125409.

[60] D. Yang, R. F. Frindt, *J. Mater. Res.* **1996**, *11*, 1733-1738.

[61] W. SEARCH, Vers. 2.08, 2005.

[62] WINXPOW, Vers. 2.12, 2005.

[63] S. Kabekkodu, *International Centre for Diffraction Data*, Newtown Square, PA, USA **2010**.

[64] D. K. Carpenter, *J. Chem. Educ.* **1977**, *54*, A430.

[65] L. Rayleigh, *The London, Edinburgh, and Dublin Philosophical Magazine and Journal of Science* **1881**, *12*, 81-101.

[66] G. Mie, *Ann.Phys.* **1908**, *330*, 377-445.

[67] A. Einstein, *Ann. Phys.* **2005**, *14*, 368-391.

[68] R. Pecora, *J. Chem. Phys.* **1964**, *40*, 1604-1614.

[69] G. Haugstad, *Atomic Force Microscopy: Understanding Basic Modes and Advanced Applications*, Wiley, **2012**.

[70] https://www.nobelprize.org/nobel_prizes/physics/laureates/1986/, accessed on19.02.2018.

[71] G. Binnig, C. F. Quate, C. Gerber, *Phys. Rev. Lett.* **1986**, *56*, 930-933.

[72] G. K. Bennig, *Atomic force microscope and method for imaging surfaces with atomic resolution*, US4724318A, **1988**.

[73] P. Eaton, P. West, *Atomic Force Microscopy*, OUP Oxford, **2010**.

[74] F. J. Giessibl, *Reviews of Modern Physics* **2003**, *75*, 949-983.

[75] E. Hecht, *Optics*, Addison-Wesley, Reading, Mass., **2002**.

[76] P. Yeh, *Optical waves in layered media*, Wiley-Interscience, Hoboken, **2005**.

[77] J. H. Holland, *Adaptation in Natural and Artificial Systems: An Introductory Analysis with Applications to Biology, Control and Artificial Intelligence*, MIT Press, **1992**.

[78] D. E. Goldberg, *Genetic Algorithms in Search, Optimization and Machine Learning*, Addison-Wesley Longman Publishing Co., Inc., **1989**.

3. NOVEL SENSING APPLICATIONS ENABLED THROUGH ULTRAHIGH HUMIDITY SENSITIVITY: AN OPTICAL TOUCHLESS POSITIONING INTERFACE

3.1 SUMMARY
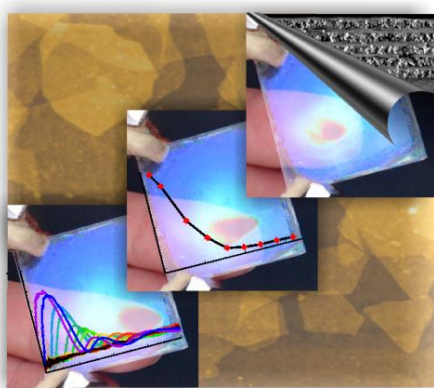
This project introduces a novel, functional material based optical sensing platform with an ultrahigh humidity sensitivity, which allowed for the realization of a *touchless positioning interface*. The "heart" of the sensor – robust 2D phosphatoantimonate ($H_3Sb_3P_2O_{14}$) nanosheets cast into a photonic thin film device – shows giant moisture responsiveness and swelling capability when exposed to relative humidity changes. The high sensitivity could be realized by the intercalation of the analyte – water molecules – into the interlayer space of the nanosheets, resulting in two effects: decreased resistance and swelling of the film upon relative humidity increase.

First, we have realized a robust, resistive humidity sensor showing a decrease in resistance by five orders of magnitude between 0 and 100% relative humidity. Secondly, the changes in layer thickness were utilized for the development of optical sensors. By integrating the nanosheets as stimuli-responsive layers into 1-dimensional Photonic Crystals (1DPCs), fast, reversible and full-spectrum stopband changes can be produced. We present two different 1DPC systems, namely the combination of $H_3Sb_3P_2O_{14}$ nanosheets with either TiO_2 or with SiO_2 nanoparticles acting as porous optical contrast materials. On the one hand, the TiO_2 nanoparticle based system shows unprecedented sensitivity towards in the entire ambient humidity range, associated with a fast and fully reversible shift of the photonic bandgap by as much as 500 nm at the highest relative humidity, which translates into a full-spectrum stopband shift. On the other hand, the key feature of the SiO_2 nanoparticle based system is its unique capability to reversibly switch from colored to transparent

(and *vice versa*) due to humidity-induced refractive index matching of the constituent layers, rendering it a promising candidate for applications in ambient monitoring, such as smart windows. The combination of beneficial sensing properties, such as fast response times in the subsecond range, high reversibility, and large signal changes allow these devices to detect the humidity sheath of a human finger and also track finger motions across the sensor surface in real-time and real-color in a touchless fashion. To the best of our knowledge, this is the first example of a photonic approach to next-generation touchless positioning interfaces and tracking devices.Besides, for the resistive device, we could create an axial touchless positioning interface with a 170-fold resistive signal change between *finger-on* and *finger-off* states, which is significant and appropriate for these applications.

Contributions: Katalin Szendrei optimized the nanosheet based thin film fabrication, designed and fabricated the 1DPCs, performed the theoretical calculations in order to understand the sensing mechanism, characterized the 1DPCs in optical sensing applications and in touchless devices, wrote the manuscript and edited the figures. Pirmin Ganter synthesized, exfoliated and characterized the $H_3Sb_3P_2O_{14}$ nanosheets, fabricated the resistive thin film devices, performed the resistivity measurements, characterized the fabricated systems as resistive humidity sensors and resistive touchless positioning interfaces, wrote the manuscript and edited the figures. Olalla Sánchez-Sobrado assisted with the optical measurements and with the theoretical calculations and helped with writing the manuscript. Roland Eger synthesized and characterized the bulk $K_3Sb_3P_2O_{14}$ and the protonated $H_3Sb_3P_2O_{14}$. Alexander Kuhn proposed the idea of using the $H_3Sb_3P_2O_{14}$ nanosheets in humidity sensing applications and in touchless devices and helped writing the manuscript.

This project and the work described in Chapter 5 and an oral presentation at the Spring Meeting of the Material Research Society (MRS) in Phoenix, USA, in 2017 was awarded with the Graduate Student Silver award.

3.2 TOUCHLESS OPTICAL FINGER MOTION TRACKING BASED ON 2D NANOSHEETS WITH GIANT MOISTURE RESPONSIVENESS

Katalin Szendrei,* Pirmin Ganter,* Olalla Sánchez-Sobrado, Roland Eger, Alexander Kuhn, Bettina V. Lotsch

* These authors contributed equally to this work.

3.3 INTRODUCTION

One of the key challenges in the development of next-generation electronic devices such as laptops, smartphones, or tablets is the design of powerful hardware control systems. In this context, humidity sensors exhibiting high spatial sensitivity to the degree of environmental moisture are promising candidates for smart touchless positioning interfaces (TPI), which operate based on local variations in the humid atmosphere around a pointing object, such as the human finger.[1]

Although porous BSs have been extensively used to detect organic vapors and humidity through RI changes induced by infiltration with analytes,[6-12] the observed shifts in the Bragg peak (BP) are rarely larger than a few tens of nanometers, and typically well below 100 nm,[9-11, 13] which limits the resolution in terms of humidity sensing.[14] An alternative mechanism to trigger changes in the structural color of a BS is to modify the layer thicknesses,[3, 4, 6, 15-18] which is particularly powerful when integrating dimensionally flexible polymer layers into a BS.[3,16,17] The demonstrated panchromatic BP shift in such systems induced by liquid water however comes at the expense of low thermal and chemical stability, as well as slow response times of the active organic layers to organic solvent vapors or humidity. The largest shift for photonic humidity sensors was reported by Tian *et al.* using a photonic hydrogel with a stop band shift of around 300 nm and a response time in the range of 100 s.[19] Xuan *et al.* reported a Fe_2O_3 nanoparticle–polymer hybrid sensor with a stop band shift of around 150–230 nm, depending on the polymer cross-linking degree. Here again, due to the characteristic polymer swelling, the response time was in the range of hours.[20] A similar sensor performance was reported by Kim *et al.*, who observed a stop band shift of 137 nm in a polymer-based 3D opal structure with high cycling stability of thousands of cycles.[21] In addition, several humidity sensors were reported with smaller stopband shifts in the range of tens of nanometers and response times on the order of a few seconds.[22, 23] Recently, Steele *et al.*[24] and Hawkeye and

Brett[25] presented mesoporous TiO_2 gratings used for humidity applications, which show an ultrafast response time in the subsecond range, but rather small stop band shifts (and therefore resolution) on the order of 30 nm.

Here, we replace the dimensionally flexible organic component in BS by phosphatoantimonic acid $H_3Sb_3P_2O_{14}$ nanosheets[26, 27] with giant moisture responsiveness. The protonic bulk material, which has long been known for its remarkable swelling characteristics driven by moisture and the resulting humidity-dependent proton conductivity,[28, 29] can be readily delaminated into 2D nanosheets, giving rise to stable liquid crystalline suspensions with anisotropic optical properties.[26, 27]

The integration of other 2D nanosheets into resistive sensing devices has already led to a superior sensing performance as compared to the corresponding bulk materials, exemplified by a VS_2 nanosheet-based TPI featuring moisture-sensitive electric, rather than ionic conductance.[1] While flexible in their design, these resistive VS_2 nanosheet sensors have certain drawbacks such as low chemical stability under ambient conditions and rather poor sensitivity. Further examples of nanosheet-based humidity sensors include NbS_2,[30] graphene oxide,[31, 32] MoS_2,[33] and ZnO.[34] Nearly all of these nanosheet sensors have either slow response times (e.g., 600 s for ZnO),[34] or low sensitivity[30,32,33] (e.g., factor 5 increase in resistance for a change from 6% RH to 74% RH for NbS_2).[30] Therefore, it still remains a major challenge to design nanosheet-based humidity sensors for real-time interaction devices with sufficient sensitivity.

In this work, we fashion thin films of phosphatoantimonic acid nanosheets into chemically stable, transparent, and low-cost humidity sensing devices operating either with resistive or optical read out, both of which can be applied as TPI based on spatially resolved humidity tracking. Drawing on the smoother (i.e., less stepwise) relative humidity (RH)-dependent swelling behavior of the nanosheets compared to the bulk material[28] and the fabrication of mechanically stable, yet flexible thin films, we detect a significantly enhanced response to a humid pointer as compared to existing devices. The novel optical TPI introduced in this work is capable of contactless finger movement tracking through a combination of unique features such as ultra large stop band shift (>500 nm), along with reversible transparency switching and a fast response time.

3.4 RESULTS AND DISCUSSION

The layered phosphatoantimonate $K_3Sb_3P_2O_{14}$ and the proton exchanged phosphatoantimonic acid $H_3Sb_3P_2O_{14}$ (Figure S 3.1, Supporting Information) were synthesized by a conventional solid-state reaction followed by ion-exchange with 8 M HNO_3 (Figures S 3.2, S 3.3, Table S 3.1, Supporting Information).[28, 35] The protonation and exfoliation process in pure water is schematically shown in

Figure 3.1a. The schlieren texture and the Tyndall effect of the resulting aqueous suspension indicate successful delamination and the anisotropic nature of the nanosheets (Figure S 3.4, Supporting Information), while drop-casting the suspension gives rise to randomly overlapping, *c*-oriented nanosheets (Figure 3.1b,c; Figures S 3.5, S 3.6, Supporting Information). The thickness of the $Sb_3P_2O_{14}^{3-}$ nanosheets as determined by AFM amounts to 1.3 ± 0.1 nm on average (Figure 3.1b), which agrees well with the crystallographic thickness of 1.10 nm for a single $Sb_3P_2O_{14}^{3-}$ layer.[26, 35] Transmission electron microscopy–energy dispersive X-ray (TEM–EDX) analysis and scanning electron microscopy-energy dispersive X-ray (SEM–EDX) analysis confirm the expected elemental composition (Tables S 3.2 and S 3.3, Supporting Information) and the *d* values of the selected area diffraction (SAD) pattern agree well with those of the nanosheet pellet by powder X-ray diffraction (XRD) (Table S 3.4, Supporting Information). The XRD pattern of a turbostratically disorderd nanosheet pellet obtained by centrifugation at 18000 rpm can be indexed on the basis of a trigonal layer group (Figure S 3.7, Supporting Information) and exhibits Warren like peak profiles of the (*hk*) reflections typical of 2D materials.[36, 37]

Nanosheet thin films with thicknesses around 100 nm can directly be used as resistive humidity sensors. The transparent thin film device is displayed in Figure S 3.8 (Supporting Information) along with two SEM cross-section images from different areas, which illustrate the ultrathin nature of the device. Drawing on the well-known moisture-dependent proton conductivity of phosphatoantimonic acid,[28] we first measured the RH-dependent ionic conductance between 0% and 100% RH using two methods, a gas flow setup and saturated salt solutions (for details see Figure 3.1d; Figures S 3.8, S 3.9, S 3.10, Supporting Information). Remarkably, we observed an increase in conductance of the sample with increasing RH by five orders of magnitude over the complete humidity range, with only a small hysteresis loop (Figure 3.1d), which is at least three orders of magnitude larger than that observed for VS_2 nanosheet devices. To the best of our knowledge, this level of sensitivity is the highest observed for any nanosheet-based conductance or resistance humidity sensor reported to date.[1,30-34] The cycling behavior of the thin film device between 0% and 47% RH shows good reversibility (Figure 3.1e).[38] Notably, the RH dependence of the proton conductance of our thin film device is quite different from that of phosphatoantimonic acid bulk material reported in the literature.[28] While the bulk material shows distinct step like behavior, this is not the case for the nanosheet film device. We attribute the smoother increase in conductance to the smaller particle size, leading to an increased amount of grain boundary adsorption, and to the non uniform interlayer space resulting in less well-defined water adsorption sites between the randomly oriented nanosheets. Such textural effects likely change the water uptake mechanism from that of a lattice hydrate (bulk material) to that of a particle hydrate (nanosheets), which accommodates a large amount of water molecules on the internal and external surfaces of the nanosheets.

To further explore the sensing capabilities of the phosphatoantimonate nanosheets, thin films with tunable thicknesses in the range of 50–150 nm were prepared by spin-coating the colloidal suspension of exfoliated nanosheets at different spinning speeds. Upon increasing the RH from 0-100%, the nanosheet film swells to the double of its thickness (e.g., Figure S 3.11, Supporting Information: from 72 to 128 nm). Hereby, a particularly pronounced change is observed in the high humidity range above 90% RH (112–128 nm) as determined by spectroscopic ellipsometry. This effect is accompanied by a RI decrease (from 1.62 to 1.52), again with a pronounced drop in the RH range above 90%, corresponding to the water uptake and the resulting thickness change. The continuous RI decrease in the higher RH range then is the result of mixing the refractive indices of water (1.33) and the nanosheets. The RI increase and the nearly unchanged layer thickness in the low humidity range up to 10% RH are rationalized by the structural pore filling of the randomly restacked nanosheets (Figure S 3.1, Supporting Information). While the bulk material shows distinct step like swelling behavior,[28] this is not the case for the nanosheet film device. We attribute the smoother increase to the same morphology reasons as discussed for the conductance changes.
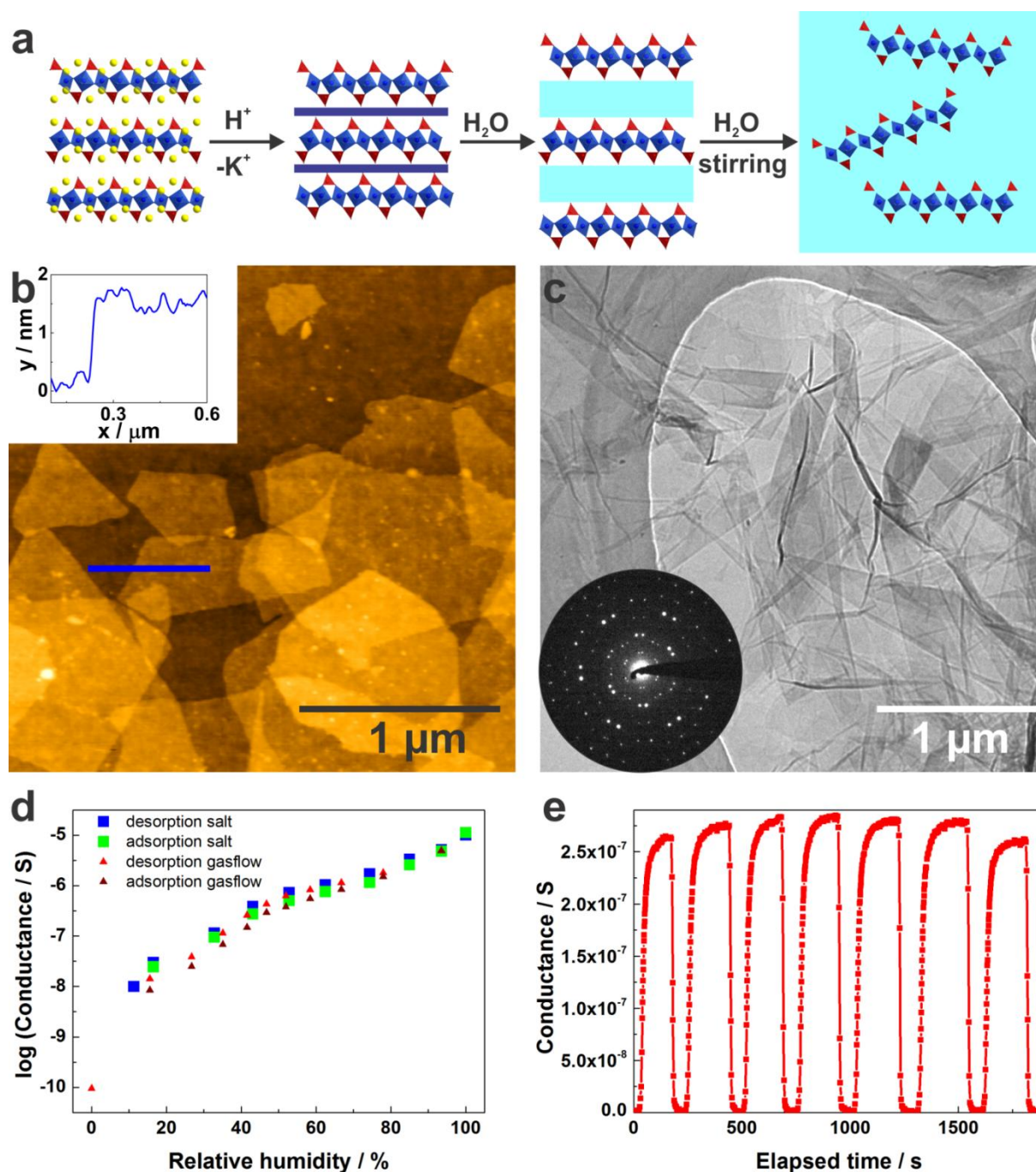
Figure 3.1 Exfoliation scheme, nanosheet characterization and conductance based humidity sensing. a) Schematic process of ion exchange and exfoliation for $K_3Sb_3P_2O_{14}$, assuming that swelling takes place first, followed by exfoliation. b) AFM image of randomly oriented $Sb_3P_2O_{14}^{3-}$ nanosheets with a corresponding height profile of a single nanosheet labeled by the blue line. c) TEM image of overlapping exfoliated $Sb_3P_2O_{14}^{3-}$ nanosheets with a representative SAD pattern of the sample, which here is the pattern resulting from two nanosheets rotated against each other. d) Ionic conductance as a function of RH obtained from measurements above saturated salt solutions (salt adsorption &desorption) and with an argon flow setup (gas flow desorption & adsorption) for a film device with a thickness of 112 nm. e) Cycling behavior of the same film device between 0 and 47% RH, measured in a chamber with an approximate volume of 100 mL.[38]

Inspired by the unprecedentedly large swelling properties of the nanosheet films, BSs were assembled from $H_3Sb_3P_2O_{14}$ nanosheets as the humidity-sensitive component and either TiO_2 or SiO_2 nanoparticle layers providing the required RI contrast. At ambient air (30% RH), the nanosheet film shows a refractive index of 1.56 as determined by spectroscopic ellipsometry (Figure S 3.11b, Supporting Information). While TiO_2 nanoparticles exhibit a higher RI (1.85), SiO_2 nanoparticle layers show a lower RI (1.35) Figure S 3.12 (Supporting Information). The particle nature of the TiO_2 and SiO_2 layers acts as a gate, ensuring the access of the water molecules to the moisture-sensitive nanosheet layers through textural porosity.[10] Figure 3.2a,b show cross sectional SEM images of two BSs containing 12 and 11 alternating layers of $H_3Sb_3P_2O_{14}$ nanosheets and SiO_2 and TiO_2 nanoparticles, respectively, evidencing long range stacking order and lateral layer uniformity across at least several microns. The spectral position of the first-order BP maximum and, hence, the structural color at normal incidence is given by Equation (1):[39]

$$\lambda_B = 2 \cdot (n_1 d_1 + n_2 d_2) \qquad (1)$$

where n_1 and n_2 are the RIs of the different layers and d_1 and d_2 their respective thicknesses.

The BSs depicted in Figure 3.2c ($H_3Sb_3P_2O_{14}/SiO_2$) and 2d ($H_3Sb_3P_2O_{14}/TiO_2$) show pronounced structural colors, which can be judiciously adjusted and gradually fine-tuned during the fabrication procedure across the visible spectrum.
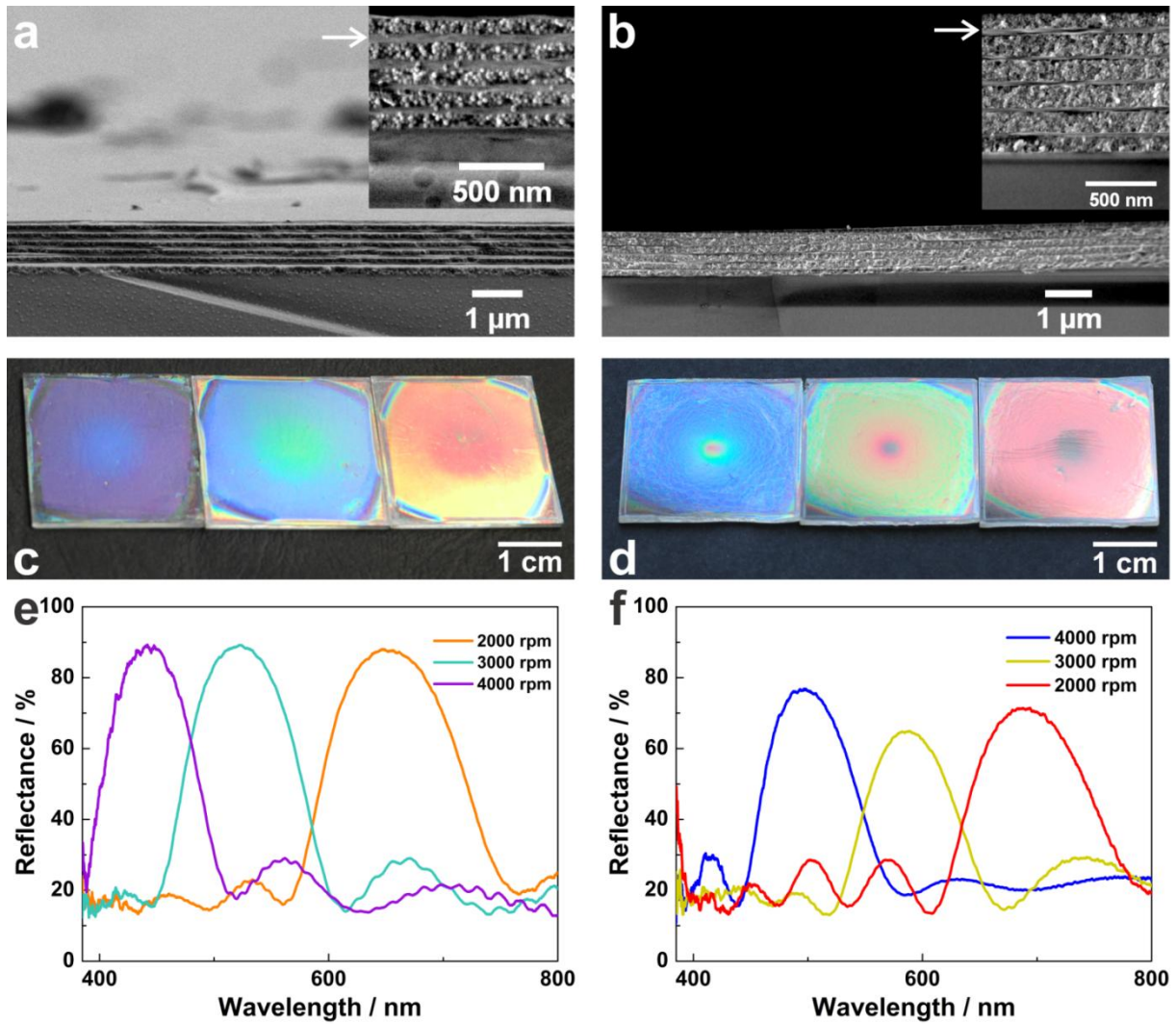
Figure 3.2: Optical and structural characterization of the SiO_2/$H_3Sb_3P_2O_{14}$ and TiO_2/$H_3Sb_3P_2O_{14}$ nanosheet-based BSs. a) SEM cross section images of the SiO_2/$H_3Sb_3P_2O_{14}$ BS fabricated by 4000 rpm spin-coating speed. The lower magnification image was taken with the SE detector and the higher-magnification inset with the in-lens detector. The white arrows indicate the nanosheet layers. b) SEM cross section images of the TiO_2/$H_3Sb_3P_2O_{14}$ BS fabricated at 4000 rpm spin-coating speed. Both images were taken with the in-lens detector. c) Photographs of the SiO_2/$H_3Sb_3P_2O_{14}$ BSs fabricated at different spin-coating speeds, from left to right: 2000 rpm, 3000 rpm, 4000 rpm, respectively. d) Photographs of the TiO_2/$H_3Sb_3P_2O_{14}$ BSs fabricated at different spin-coating speeds, from left to right: 2000 rpm, 3000 rpm, 4000 rpm, respectively. e) Optical spectra of the corresponding SiO_2/$H_3Sb_3P_2O_{14}$ BSs shown in the photographs (c) in the corresponding order. f) Optical spectra of the corresponding TiO_2/$H_3Sb_3P_2O_{14}$ BSs shown in the photographs (d) in the corresponding order.

In order to study the key features of our optical humidity sensors, the two BSs were introduced into a closed chamber with a transparent upper window, and the position of the BP was measured for different RH values controlled by saturated salt solutions at 25 °C.[40,41] The supposed sensing mechanism of the BSs is schematically depicted in Figure 3.3a. Here, the thickness of the particle layers is assumed invariable, so three main processes affect the humidity-dependent optical

response of the BS: i) The RI changes of the TiO_2 and SiO_2 nanoparticle layers with the adsorption/desorption of water into their textural pores (i.e., interparticle voids, Figure S 3.12, Supporting Information), ii) the change of the RI of the nanosheet layers through uptake/loss of water (Figure S 3.11b, Supporting Information), iii) the humidity-dependent thickness of the nanosheet layers (Figure S 3.11a, Supporting Information). While for SiO_2 and TiO_2 the effective RI of the layers increases with increasing water content due to the pore filling process, it decreases for the nanosheet layers as the effective RI approaches that of pure water with increasing degree of hydration. The latter phenomenon is driven by the massive swelling of the nanosheet layers in contrast to the more compact nanoparticle layers. These features can be extracted from the humidity-dependent reflectance spectrum and the overall optical changes can also be monitored as color changes with the naked eye. The two BSs qualitatively behave differently: In the $H_3Sb_3P_2O_{14}/SiO_2$ BS, the photonic stop band red-shifts by 100 nm in the lower RH range (up to 90%) as plotted in Figure 3.3b (solid lines). The set of microscope images shown below corresponds to the color displayed by the BS for three different RH values (32%, 93%, 100%). For increasing values of the RH, the BP redshifts, while its reflectance intensity gradually decreases and finally vanishes (Figure 3.3b, black spectrum). The color displayed by the sensor (Figure 3.3c) follows this behavior and for the highest value of humidity, the 1DPC switches off, i.e., becomes completely transparent (Figure S 3.13, Supporting Information). This effect finds its explanation in the elimination of the optical contrast between the layers forming the BS with increasing RH. While the RI of the particle layer increases and its thickness roughly remains constant, the RI of the nanosheet layer decreases while the layer thickness increases, leading to an overall redshift of the BP. Since the RIs of the nanosheet and nanoparticle layers follow opposite trends, both values ultimately become nearly equal at above 95% RH, leading to the disappearance of the optical contrast. As the BP is canceled out, the optical sensor turns completely transparent and light is transmitted by the structure throughout the visible range (Figure S 3.13, Supporting Information). Complete transparency switching through reversible refractive index matching has previously been realized by rational porosity and refractive index tuning of the constituent layers.[42, 43] These hygrochromic multilayers however are only capable of detecting liquid water, rather than humidity sensors.

The specular reflectance spectra taken for the $TiO_2/H_3Sb_3P_2O_{14}$ BS are plotted in Figure 3.3d (solid lines), along with the corresponding surfaces of the BS for different RH values (Figure 3.3e). The BP redshifts by 100 nm in the RH range of 0–90%. Contrary to the SiO_2 containing BS, the reflectance rises with increasing RH and the stop band broadens, which can be rationalized by the increase in optical contrast of the layers with increasing RH. We observe a total redshift of more than 517 nm, shifting the BP out of the visible range into the IR, while the second-order BP is observed at 495 nm (red curve of Figure 3.3d). The observed red shift at high RH is the largest ever observed for a BS for

moisture sensing applications. Note that besides these unique color changes, the fast response time, high reproducibility, and cyclability of the BS device (Figures S 3.14, S 3.15, Supporting Information) are unprecedented. Although there have been a few systems reported in the literature, which show stop band shifts larger than 100 nm, these systems invariably exhibit slow response times due to diffusion limitations in the swelling of the integrated polymers.[19-21] The porous nature of the nanoparticle layers in our BS sensor and the fast equilibration time of the nanosheet layers ensure easy access of the water molecules into the device and a fast response time throughout the entire device. Simulations of the optical spectra were carried out with a Matlab code[9] to confirm the optical properties observed for our BSs (Figure 3.3b,d, dashed lines; for the input parameters used, see Figures S 3.11, S 3.12, Tables S 3.5, S 3.6, Supporting Information). The excellent agreement between the values obtained in both cases proves the validity of the proposed sensing mechanism (Figure 3.3a).
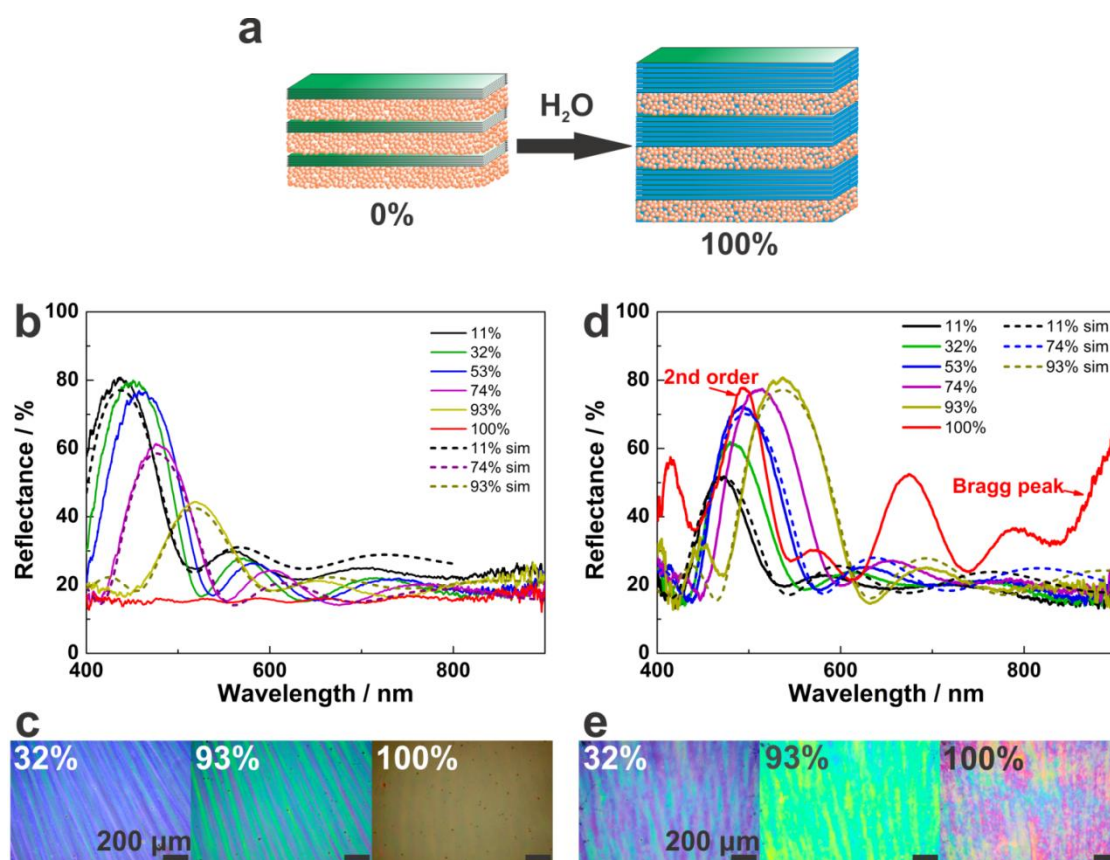
Figure 3.3: Optical humidity sensing features of the $SiO_2/H_3Sb_3P_2O_{14}$ and $TiO_2/H_3Sb_3P_2O_{14}$ BSs. a) Scheme of the suggested humidity sensing mechanism. b) Experimental (solid spectra) and simulated (dashed spectra) reflectance spectra of the $SiO_2/H_3Sb_3P_2O_{14}$ BS at different RH values. c) Microscope images of the $SiO_2/H_3Sb_3P_2O_{14}$ BS surface at RH values of 32%, 93% and 100%, respectively. d) Experimental (solid spectra) and simulated (dashed spectra) reflectance spectra of the $TiO_2/H_3Sb_3P_2O_{14}$ BS at different RH values. e) Microscope images of the $TiO_2/H_3Sb_3P_2O_{14}$ BS surface at RH values of 32%, 93% and 100%, respectively.

Both, the conductance of the nanosheet thin film and the optical properties of the BSs show a reproducible, fast, and selective response to changes in RH, which are important performance parameters for position-sensitive user control interfaces. Since the fingertip is surrounded by a distance dependent humidity atmosphere, the read-out schemes developed above present intriguing candidates for the development of 3D (i.e., lateral and height-sensitive) non-contact interactive interfaces. To probe the touchless sensing capability of our nanosheet thin films and the Bragg stack, first, the nanosheet film on a quartz substrate was studied. Hereby, an increase of the conductance by more than a factor of 170 was observed when the distance of the finger from the sensor surface was reduced from 1.6 to 0.1 cm at 30% ambient RH (Figure 3.4a). This is notably higher than the values recently reported for VS_2 or graphene oxide thin film devices with a reported 3- or 0.35-fold signal increase.[1,32] Note also that the fast full response (<2 s) and recovery times (3 s) towards "tapping" finger motion even allow to resolve subsecond events as shown in Figure S 3.16 (Supporting Information). The observed response times are rather fast compared to other nanostructured humidity sensing devices with typical response times on the order of tens to hundreds of seconds,[34,44-47] and even faster than those of state-of-the-art resistive sensors based on GO or VS_2,[1,32] or commercially available sensors.[48-50]

The finger-tip induced conductance changes monitored in a dynamic measurement (Video S1, Supporting Information) also demonstrate that the thin film device indeed has a very fast and reversible response to finger distance changes.

With the highly sensitive photonic read-out scheme presented above, the tools are at hand to go one step further and develop a novel optical TPI based on the lateral tracking of a humid pointer with an optical read-out visible by the naked eye. For such optical devices, no integration with an electronic assembly is necessary to visualize the lateral finger position above a photonic surface. Our experiments, which demonstrate the feasibility of this touchless optical sensing principle, are summarized in Figure 3.4 and visualized by Videos S2, S3, S4, and S5 (Supporting Information). Positioning the finger in a vertical distance of 1 mm from both presented BS surfaces leads to a color gradient along a distance between 1.0 and 1.8 mm from the finger tip, as shown in the microscope pictures corresponding to the two configurations proposed for $TiO_2/H_3Sb_3P_2O_{14}$ and $SiO_2/H_3Sb_3P_2O_{14}$ BSs, respectively (Figure 3.4d,e). This is in perfect agreement with the conductance behavior, as in the small distance range the sensing signal drops similarly fast (Figure 3.4a) due to the spatially dependent humidity gradient around the finger. Looking at the structural colors of the gradient, the color at 1.0 mm real distance corresponds to the 100% RH sensing signal (where the optical contrast and reflectance are lost) in the case of the $SiO_2/H_3Sb_3P_2O_{14}$ BS. In both cases, the structural color for a distance of 1.5 mm corresponds to a RH of around 90% (see Figure 3.3). In Figure S 3.17 (Supporting

Information), we show that the Bragg stack can be operated as a TPI also at longer distances up to ≈12 mm. The stop band shift is observed immediately (Figure 3.4f,g), and the captured reflectance spectra for the $SiO_2/H_3Sb_3P_2O_{14}$ BS show a response time of 3 s (defined as the time it takes for 90% of the stopband shift before the structural color vanishes). Further cycling experiments (Figures S 3.18, S 3.19, and S 3.20, Supporting Information) demonstrate that a $SiO_2/H_3Sb_3P_2O_{14}$ BS responds instantaneously to fast "tapping" finger motion, resulting in a subsecond time resolution (note that the "tapping" motion was also carried out under touchless conditions). The fast response is also obvious from lateral movement of the finger across the BS (Figure 3.4h–l, Video S5, Supporting Information). An instantaneous color response precisely following the finger movement was observed, which is equivalent to a high-accuracy tracking of the finger movement (see Figure 3.4h–l, Video S5, Supporting Information). The BS response occurs exclusively due to the local water vapor atmosphere surrounding the finger, rather than a temperature effect, as: i) the response in the finger-on state (Video S2, Supporting Information) is completely analogous to the measurement at very high RH carried out at RT, and ii) no color change is observed if the finger is protected by a nitrile glove (Figure 3.4c), while a fast and pronounced color change is directly seen by approaching the naked finger (Figure 3.4b, Figure 3.4h–l). Notably, the humidity response is fully reversible during cycling (Figure 3.4g inset, Figures S 3.18, S 3.20, Supporting Information) and the Bragg stack can be cycled for more than 1000 times without observing any signs of degradation (Figures S 3.19, S 3.20, Supporting Information) or changes in its response behavior. Finally, the Bragg stacks show long term stability without any loss of functionality after repeated usage and storing them in air for more than 8 months (see Figure S 3.21, Supporting Information).
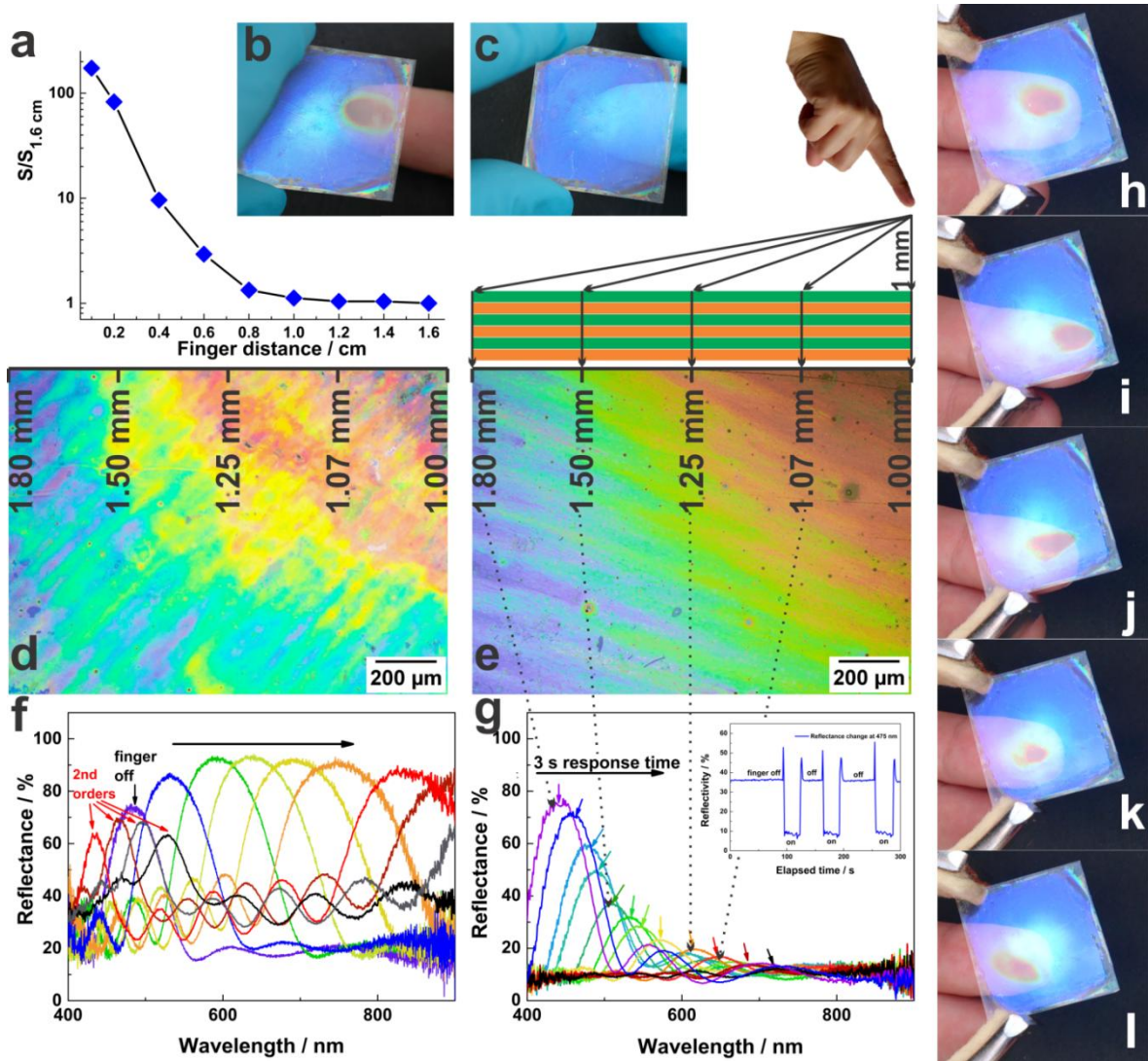
Figure 3.4: H$_3$Sb$_3$P$_2$O$_{14}$ nanosheet-based devices acting as a TPI. a) Sensing response characteristics as a function of the finger distance of a thin film device obtained by spin-coating at 3000 rpm. The measurement was performed at around 30 % RH. b) Photograph of the SiO$_2$/H$_3$Sb$_3$P$_2$O$_{14}$ BS with an approaching finger. Note that the finger is not in direct contact with the stack. c) Photograph of the SiO$_2$/H$_3$Sb$_3$P$_2$O$_{14}$ BS with an approaching finger covered with a nitrile glove. No response is observed in this case. d) Real color microscope image of the TiO$_2$/H$_3$Sb$_3$P$_2$O$_{14}$ BS, showing the lateral color gradient around the finger position. The finger was positioned at the top right corner, in a vertical distance of 1 mm from the BS surface. Real distances from the finger to the corresponding image positions are indicated. e) Real color microscope image of the SiO$_2$/H$_3$Sb$_3$P$_2$O$_{14}$ BS showing the lateral color gradient around the finger position. The scheme shows the position of the finger in the top right image corner in a vertical distance of 1 mm. The real distances from the finger at the corresponding image positions (calculated by the Pythagorean theorem) are indicated. f) Evolution of the reflectance spectra of the TiO$_2$/H$_3$Sb$_3$P$_2$O$_{14}$ BS upon keeping the finger at 1 mm vertical distance to the BS surface. The different colors correspond to the different magnitudes of the response. g) Evolution of the reflectance spectra of the SiO$_2$/H$_3$Sb$_3$P$_2$O$_{14}$ BS taken after 3 s optical response time upon keeping the finger at 1 mm vertical distance to the BS surface. Inset: Intensity changes of the SiO$_2$/H$_3$Sb$_3$P$_2$O$_{14}$ BS while cycling

between the finger-on and finger-off states. h-l) Photographs showing the finger movement tracking capability of the photonic TPI. The pictures are video frames from a similar video as Video S5 taken at 1, 2, 3, 4 and 5 seconds, while the finger was continuously moved laterally along the $SiO_2/H_3Sb_3P_2O_{14}$ Bragg stack without direct contact with the photonic TPI surface.

In summary, we have demonstrated the potential of phosphatoantimonic acid nanosheet-based resistive and photonic humidity sensors as TPI, which represents a novel concept complementary to the contact-based technology. Transparent nanosheet thin films can be applied as a resistive RH sensor, since the ionic conductance of the film strongly depends on the surrounding RH, featuring high sensitivity with a response of five orders of magnitude, good cyclability, and ultrafast response characteristics in the subsecond range. We have demonstrated that due to these properties, the nanosheet thin film device can be applied as a touchless axial positioning interface with a change of ionic conductance between the finger on and finger off state by a factor of 170. Further, "smart" 1DPCs were developed as versatile humidity sensors with a simple optical read out. The ultrahigh stop band shift of 517 nm of the TiO_2 based BSs and the switchable transparency through optical contrast loss of the SiO_2 based BSs are unique features of the proposed sensing platform. This second property, the gradual loss of reflectance accompanied by a color change, makes these multilayers potential candidates for privacy windows or smart window applications. Due to the straightforward optical tunability, the extremely high sensitivity, reproducibility, ultrafast response and recovery times, a new concept of a position-sensitive optical TPI was demonstrated for the first time. As the humidity-responsive photonic device gives the user direct optical feedback about successful interaction, no additional soft- and hardware, which is implemented for contact visualization in current state of the art capacitive touch screens, is needed. Using the contactless optical read out proposed in this work, the disadvantages of conventional touch screens such as scratches or fingerprints could be eliminated, while touchless tracking of finger motion is achieved in a simple fashion without complex electronic circuitry.

3.5 ACKNOWLEDGEMENTS

3.6 REFERENCES

[1]   J. Feng, L. Peng, C. Wu, X. Sun, S. Hu, C. Lin, J. Dai, J. Yang, Y. Xie, *Adv. Mater.* **2012**, *24*, 1969-1974.

[2]   J. D. Joannopoulos, P. R. Villeneuve, S. Fan, *Nature* **1997**, *386*, 143-149.

[3]   A. C. Arsenault, T. J. Clark, G. von Freymann, L. Cademartiri, R. Sapienza, J. Bertolotti, E. Vekris, S. Wong, V. Kitaev, I. Manners, R. Z. Wang, S. John, D. Wiersma, G. A. Ozin, *Nat. Mater.* **2006**, *5*, 179-184.

[4]   Z. Wang, J. Zhang, J. Xie, C. Li, Y. Li, S. Liang, Z. Tian, T. Wang, H. Zhang, H. Li, W. Xu, B. Yang, *Adv. Funct. Mater.* **2010**, *20*, 3784-3790.

[5]   J. H. Holtz, S. A. Asher, *Nature* **1997**, *389*, 829-832.

[6]   B. V. Lotsch, G. A. Ozin, *Adv. Mater.* **2008**, *20*, 4079-4084.

[7]   L. D. Bonifacio, D. P. Puzzo, S. Breslav, B. M. Willey, A. McGeer, G. A. Ozin, *Adv. Mater.* **2010**, *22*, 1351-1354.

[8]   D. Lee, D. Omolade, R. E. Cohen, M. F. Rubner, *Chem. Mater.* **2007**, *19*, 1427-1433.

[9]   M. C. Fuertes, S. Colodrero, G. Lozano, A. R. González-Elipe, D. Grosso, C. Boissière, C. Sánchez, G. J. d. A. A. Soler-Illia, H. Míguez, *J. Phys. Chem. C* **2008**, *112*, 3157-3163.

[10]   S. Colodrero, M. Ocaña, H. Míguez, *Langmuir* **2008**, *24*, 4430-4434.

[11]   N. Hidalgo, M. E. Calvo, H. Míguez, *Small* **2009**, *5*, 2309-2315.

[12]   J. Kobler, B. V. Lotsch, G. A. Ozin, T. Bein, *ACS Nano* **2009**, *3*, 1669-1676.

[13]   F. M. Hinterholzinger, A. Ranft, J. M. Feckl, B. Ruhle, T. Bein, B. V. Lotsch, *J. Mater. Chem.* **2012**, *22*, 10356-10362.

[14]   C. Fenzl, T. Hirsch, O. S. Wolfbeis, *Angew. Chem. Int. Ed.* **2014**, *53*, 3318-3335.; *Angew. Chem.*, **2014**, *126*, 3384-3402.

[15]   B. V. Lotsch, G. A. Ozin, *ACS Nano* **2008**, *2*, 2065-2074.

[16]   Y. Kang, J. J. Walish, T. Gorishnyy, E. L. Thomas, *Nat. Mater.* **2007**, *6*, 957-960.

[17]   A. C. Arsenault, D. P. Puzzo, I. Manners, G. A. Ozin, *Nat. Photonics* **2007**, *1*, 468-472.

[18]   F. Castles, S. M. Morris, J. M. C. Hung, M. M. Qasim, A. D. Wright, S. Nosheen, S. S. Choi, B. I. Outram, S. J. Elston, C. Burgess, L. Hill, T. D. Wilkinson, H. J. Coles, *Nat. Mater.* **2014**, *13*, 817-821.

[19]   E. Tian, J. Wang, Y. Zheng, Y. Song, L. Jiang, D. Zhu, *J. Mater. Chem.* **2008**, *18*, 1116–1122.

[20]   R. Xuan, Q. Wu, Y. Yin, J. Ge, *J. Mater. Chem.* **2011**, *21*, 3672–3676.

[21]   S. Kim, J. Lee, H. Jeon, H. J. Kim, *Appl. Phys. Lett.* **2009**, *94*, 133503.

[22]   J. Shi, V. K. S. Hsiao, T. R. Walker, T. J. Huang, *Sens. Actuators, B* **2008**, *129*, 391-396.

[23]   R. A. Barry, P. Wiltzius, *Langmuir* **2006**, *22*, 1369-174.

[24]   J. J. Steele, A. C. van Popta, M. M. Hawkeye, J. C. Sit, M. J. Brett, *Sens. Actuators, B* **2006**, *120*, 213-219.

[25]   M. M. Hawkeye, M. J. Brett, *Adv. Funct. Mater.* **2011**, *21*, 3652-3658.

[26]   J.-C. P. Gabriel, F. Camerel, B. J. Lemalre, H. Desvaux, P. Davidson, P. Batall, *Nature* **2001**, *413*, 504-508.

[27]   F. Camerel, J. C. P. Gabriel, P. Batail, P. Panine, P. Davidson, *Langmuir* **2003**, *19*, 10028-10035.

[28]   S. Deniard-Courant, Y. Piffard, P. Barboux, J. Livage, *Solid State Ionics* **1988**, *27*, 189-194.

[29]   Y. Piffard, A. Verbaere, A. Lachgar, S. Deniard-Courant, M. Tournoux, *Rev. Chim. Miner.* **1986**, *23*, 766-775.

[30]   W. M. R. Divigalpitiya, R. F. Frindt, S. R. Morrison *J. Phys. D: Appl. Phys.* **1990**, *23*, 966-970.

[31]   S. Borini, R. White, D. Wei, M. Astley, S. Haque, E. Spigone, N. Harris,J. Kivioja, T. Ryhänen, *ACS Nano* **2013**, *7*, 11166-11173.

[32]   X. Wang, Z. Xiong, Z. Liu, T. Zhang, *Adv. Mater.* **2015**, 27, 1370-1375.

[33]   S.-L. Zhang, H.-H. Choi, H.-Y. Yue, W.-C.Yang, *Current Applied Physics* **2014**, 14, 264-268.

[34]   F.-S. Tsai, S.-J. Wang, *Sens. Actuators, B* **2014**, *193*, 280-287.

[35]   Y. Piffard, A. Lachgar, M. Tournoux, *J. Solid State Chem.* **1985**, *58*, 253-256.

[36]   D. Yang, R. F. Frindt, *J. Appl. Phys.* **1996**, *79*, 2376-2385.

[37]   A. Kuhn, T. Holzmann, J. Nuss, B. V. Lotsch, *J. Mater. Chem. A* **2014**, *2*, 6100-6106.

[38]   For further details on the determination of the response time and measurement of the response characteristics, see Supporting Information, Figure S 3.16a-c.

[39]   J. D. Joannopoulos, S. G. Johnson, J. N. Winn, R. D. Meade, *Photonic crystals: molding the flow of light*, Princeton university press, **2011**.

[40]   P. W. Winston, D. H. Bates, *Ecology* **1960**, *41*, 232-237.

[41]   L. Greenspan, *J. Res. Nat. Bur. Stand.* **1977**, *81A*, 89-96.

[42]   M. N. Ghazzal, O. Deparis, J. De Coninck, E. M. Gaigneaux, *J. Mater. Chem. C* **2013**, *1*, 6202-6209.

[43]   K. E. Shopsowitz, H. Qi, W. Y. Hamad, M. J. MacLachlan, *Nature* **2010**, *468*, 422-425.

[44]   H. Jamil, S. S. Batool, Z. Imran, M. Usman, M. A. Rafiq, M. Willander, M. M. Hassan, *Ceram. Int.* **2012**, *38*, 2437-2441.

[45]   J. Wang, M.-Y. Su, J.-Q. Qi, L.-Q. Chang, *Sens. Actuators, B* **2009**, *139*, 418-424.

[46]   Q. Kuang, C. Lao, Z. L. Wang, Z. Xie, L. Zheng, *J. Am. Chem. Soc.* **2007**, *129*, 6070-6071.

[47]   Y. Zhang, W. Fu, H. Yang, Q. Qi, Y. Zeng, T. Zhang, R. Ge, G. Zou, *Appl. Surf. Sci.* **2008**, *254*, 5545-5547.

[48]   Sensirion AG, http://www.sensirion.com/en/products/humidity-temperature/, accessed: 05, 2015.

[49]   E+E ELEKTRONIK Gesellschaft m.b.H., http://www.epluse.com/en/products/humidity-instruments/humidity-sensor/, accessed: 05, 2015.

[50]   Vaisala, http://www.vaisala.com/en/products/humidity/Pages/default.aspx, accessed: 05, 2015.

4. PRACTICAL ASPECTS OF THE OPTICAL TOUCHLESS POSITIONING INTERFACE: SELECTIVITY, REPRODUCIBILITY, TEMPERATURE DEPENDENCY

4.1 SUMMARY

In this chapter, important aspects regarding the optical touchless positioning interfaces (Chapter 3) were studied: the selectivity towards water vapor, the temperature dependency of the optical response to the presence of a human finger, and the reversibility of the signal change.

In order to test the selectivity towards water vapor, the optical response to another relevant analyte, i.e. ethanol vapor, was investigated and compared to the optical response of water vapor. As we know from previous works (Chapter 3), the sensing mechanism of $H_3Sb_3P_2O_{14}$ nanosheet based thin films relies on the intercalation of water vapor into the interlayer space, which is highly hydrophilic due to the charge compensating protons, which are located between the single nanosheet layers. For the selectivity studies, we chose ethanol as it is also polar and protic – similar to water vapor – and it is also capable of creating hydrogen bonds with the protons in the nanosheet interlayer space. However, upon testing the selectivity, a very different optical behavior is observed, namely a slight stopband shift accompanied by slow response times, which is substantially different from the fast response times and large stopband shifts caused by water vapor. The differences most likely lay in the dielectric and other molecule size-related properties, such as the polarity or acidity and cause the inhibited diffusion of the ethanol molecules throughout the 1DPC.

Further, the temperature dependency of the optical behavior of these humidity sensors was analyzed. The multilayered structures were tested between 40°C and 0°C, whereby the temperature increase did not have important impacts on the sensing capability, but the cooling of the sample did. Upon reaching the dew point, the ambient humidity condenses on the sensor, thus limiting the

sensor's response below the dew point. Once the temperature rises above the dew point, the condensed water can be desorbed again and the humidity responsiveness is restored.

Finally, the reversibility and reproducibility of the touchless positioning interface was tested. Hereby, the humidity response was tested by approaching a human finger, which is surrounded by a distance-dependent humid atmosphere, responsible for the sensing response. The cycling stability and reversibility was proven to be stable for at least 100 cycles.

Contributions: Katalin Szendrei fabricated the 1DPCs, performed the spectroscopic and the ellipsometry measurements and the theoretical calculations, edited the figures and wrote the manuscript. Pirmin Ganter synthesized and characterized the 2D nanosheets and assisted with the manuscript writing.

This project was presented at the SPIE Photonics Europe Conference, in Brussels, 2016 and published as a conference proceeding. It was awarded, together with the work presented in Chapter 3, with the Best Student Paper award.

4.2 TESTING THE SELECTIVITY, CYCLING STABILTY AND THE TEMPERATURE DEPENDENCY OF TOUCHLESS FINGER MOTION TRACKING DEVICES BASED ON 1D PHOTONIC CRYSTALS

Katalin Szendrei, Pirmin Ganter, Bettina V. Lotsch

4.3 ABSTRACT

Thin film devices composed of 2D phosphatoantimonate nanosheets are optically characterized and by investigating the humidity-induced swelling behavior, the water uptake mechanism was suggested. By integrating this intrinsically active material into 1D Photonic Crystal devices, the layer thickness changes caused by humidity changes are translated into an optical signal, a full-spectral color change, which can be read out by the naked eye. Additionally, a unique property, a reversible transparency switching at high humidity values is ensured by the optical contrast canceling upon water adsorption. Besides the large signal changes, the study of the optical response to ethanol vapor shows a noticeably higher sensitivity to humidity compared to ethanol vapor, justified by the different intercalation degree into the nanostructure. Based on the ultrahigh sensitivity to humidity, phosphatoantimonate nanosheet based Bragg stacks were able to detect finger positions and track finger motions without touching the sensor surface, only by responding to the humidity sheath of the human finger. The cycling stability and the reversibility of these optical touchless positioning interfaces are given for more than 100 cycles, as well as the sensing performance at increased temperatures about 40 °C is unaffected. Although, we found the limits of these devices at the dew point, as the water-based sensing mechanisms are not applicable below 0 °C anymore, the optical tracking of the spontaneous and reversible water condensation into the structure can pave the way towards other sensing applications.

4.4 INTRODUCTION

Bioinspired periodic nanostructures, 1-dimensional Photonic Crystals (PCs) or also referred to as Bragg stacks (BS) have gained research interest since the 80s, as the theoretical backgrounds were established and a comprehensive description of the photonic phenomena within these periodic multilayers was published by Yablonovitch and John.[1,2] Since this basic work, a plethora of different photonic structures with potential applications was presented in the literature, such as radiation shielding,[1] wavelength-selective optical filters,[2, 3] and sensing.[4-12] Especially in the field of sensing, PCs present an important sensor configuration due to the ease of wet chemical bottom-up fabrication utilizing the spin- or dip-coating technique, low production and time cost, and well-defined and simply tunable optical properties.[13] PCs exhibit a periodic medium presented by the alternating refractive index (RI) defines the optical properties by forming a forbidden energy region for electromagnetic wave in which no waves are allowed propagating the structure. This "photonic band gap", the spectral range with the maximum reflection and the minimum transmission, is defined by the Bragg-Snell law (1):[14, 15]

$$m\,\lambda = 2(n_1\,d_1 +\ n_2 d_2) \qquad (1)$$

whereby m is the order of diffraction, λ the wavelength, n_1 and n_2 the RIs of the composing materials and d_1 and d_2 the layer thicknesses of the structure. According to (1), the photonic band gap or stop band also determines the "structural color". Due to the dynamic manipulation of the photonic stop band by varying the optical thickness ($\tau = n \cdot d$) of the constituent layers, these platforms are capable of translating chemical or physical environmental recognition events, into an optical read-out, a color change.[16]

Although PC based sensors are competitive candidates to sensors based on other readout mechanisms, there are some remaining challenges in this research field. According to a review by C. Fenzl *et al.,*[17] some crucial points and challenges are currently limiting the performance of PC based sensors: (1) the selectivity, (2) signal- and sensor stability, (3) larger signal changes gaining a higher signal resolution and (4) the utilization of simpler readout techniques besides of microscopy and reflectometry. Previously presented BS based humidity and organic vapor sensors were extensively discussed in the literature, but due to singly the RI changes upon infiltration, the stop band shifts are typically small, which massively limits the resolution in terms of vapor sensing.[18,19] An alternative sensing mechanism to detect environmental changes with a higher resolution was suggested predominantly for humidity sensors by applying flexible organic polymers.[20-22] These show a pronounced swelling upon liquid water or water vapor infiltration. In general, the layer thickness change, *e.g.* the swelling of the integrated polymers ends up in a massive structural color change of

hundreds of nanometers.[20] Unfortunately, the powerful potential of swelling comes at the expense of slow response times, low chemical and thermal stability, which restricts these systems for real-life applications.

Herein, we present humidity responsive Bragg stacks with integrated intrinsically active materials: robust inorganic 2D phosphatoantimonate nanosheets. The protonated bulk material is known since the 80s for its remarkable swelling capability driven by humidity changes.[23] This layer distance changes are attributed due to intercalation of the water molecules between the crystal lattice planes, whereby the polar character of the containing the protons favors the intercalation. The protonated bulk material can be readily delaminated into 2D nanosheets, giving rise to stable liquid crystalline suspensions with anisotropic properties.[24,25] In our previous work, we proved that these phosphato antimonate nanosheets can be exfoliated in pure water into single nanosheets with a thickness of 1.3 ± 0.1 nm and lateral dimensions of several microns.[26] In this work, we optimized the liquid crystalline suspension in order to create homogenous thin films, and investigate its optical properties and sensing performance in terms of humidity sensing. For this, we adjusted the colloidal concentration to 42 mmol L^{-1}, which allows us to tune the layer thickness in a wide range by singly varying the spin-coating speed. Also the solvent composition of the suspension was adjusted to a water/ethanol mixture of 40/60 wt%, which on the one hand ensures due to the ethanol content the easy applicability in spin-coating and on the other hand allows the complete exfoliation due to the water content. Additionally, to obtain a homogenous thin film, 2 h of sonication was applied to get rid of the agglomerates and to completely exfoliate the nanosheets.

4.5 RESULTS AND DISCUSSION

Being spin-coated, the delaminated nanosheets randomly restack in a c-oriented fashion and form a 50-200 nm thick film on the substrate. In form of a thin film, the nanosheets are applicable for investigating its optical properties and the sensing capability in terms of humidity sensing. First, we determined the optical properties, such as the complex RI ($\underline{n} = n + ik$), via spectroscopic ellipsometry at ambient conditions, at room temperature and ca. 30% relative humidity (RH). For this, we measured Ψ and Δ and fitted the data using a layer model in order to extract the optical constants. According to Fig 1a, we show the real part of the RI (n) and the extinction coefficient (k) values depending on the wavelength in the visible spectral range. The low k value in the entire visible range ($k = 6 \cdot 10^{-4}$ - $22 \cdot 10^{-4}$) indicates a negligibly low absorbtance of the material, which was expected due to the thin film character. The real part of the RI varies in the visible range only slightly, between 1.55-1.70. For further analysis and for simplicity reasons, we assume a constant value and analyze the RI and its changes at 633 nm. In order to determine the humidity sensing capability, these thin

films were placed into a closed chamber and the RH was adjusted to different values, while the layer thickness changes and the RI were measured at each value. Upon increasing the RH from 0-100%, the nanosheet film swells almost to double its thickness (from 72 nm to 128 nm). Hereby, a particularly pronounced change is observed in the high humidity range above 90% RH (112-128 nm) as determined by spectroscopic ellipsometry. Notably, the RH dependence of the layer thicknesses of our thin film device is quite different from that of phosphatoantimonic acid bulk material reported in the literature.[23] While the bulk material shows distinct step-like behavior, we observe a less-stepwise and smoother behavior for the thin films. We attribute these changes to the morphology changes upon exfoliation and the thin film fabrication. The large particle size and the well-defined adsorption sites in the crystalline bulk phase change upon exfoliation to smaller particle size, leading to an increased amount of grain boundary adsorption, and to the non-uniform interlayer space. This results in less well-defined water adsorption sites between the randomly oriented nanosheets and a larger adsorption capacity. Such textural effects likely change the water uptake mechanism from that of a lattice hydrate (bulk material) to that of a particle hydrate (nanosheets), which accommodates a large amount of water molecules on the internal and external surfaces of the nanosheets and increase the total amount of adsorbed water. As the dispersion of the RI in the visible range is quite small (Fig 1a), we evaluated the RI changes at 633 nm for the whole humidity range. The RI behavior with changing humidity supports our suggested sensing mechanism. The RI is decreasing with the increasing RH value (from 1.62 to 1.52), again with a pronounced drop in the RH range above 90%, corresponding to the water uptake and the resulting thickness change. The continuous RI decrease in the higher RH range then is the result of mixing the RIs of water (1.33) and the nanosheets, in other words, the nanosheets become more "water-like" upon intercalation. According to Fig b, these massive changes are completely reversible and the adsorbed water amount is desorbed completely upon RH decrease. The RI increase and the nearly unchanged layer thickness in the low humidity range up to 10% RH are rationalized by the structural pore filling of the randomly restacked nanosheets.

To translate this humidity induced swelling behavior into an optical signal, we combined the nanosheet thin films with colloidal SiO_2 in form of thin films, and fabricated Bragg stacks with these two robust inorganic materials. The optical contrast material was selected carefully according to the system`s requirements. First, the contrast material has to be porous to ensure the infiltration and the diffusion of the analyte molecules into the entire structure. Secondly, a sufficient RI contrast has to be ensured that a Bragg peak appears. Colloidal SiO_2 fulfills both requirements, as the porosity is present through the interparticle voids and the RI varies according to Fig 1c, gray curve. Upon water uptake, the RI changes from 1.35 to 1.42, which ensures at low RH values a sufficient contrast.
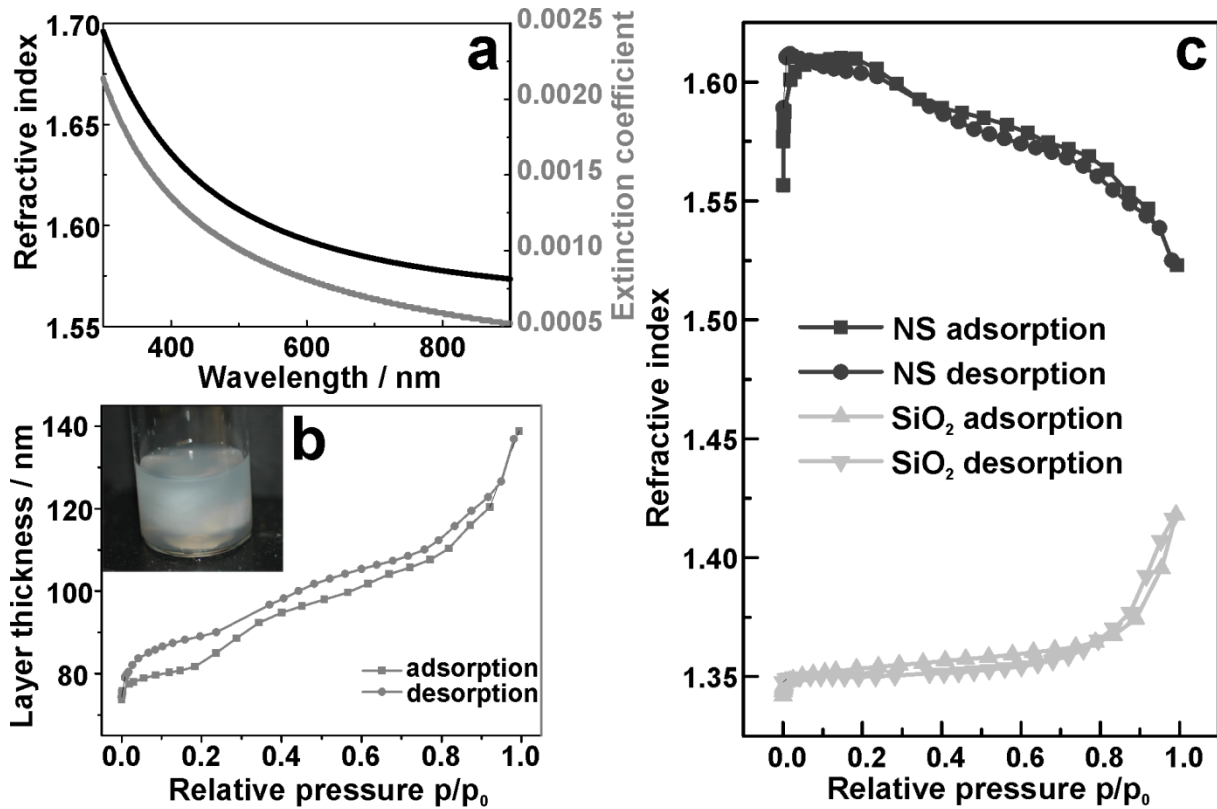
Figure 4.1: Optical properties of the applied materials. a) Wavelength-dependent RI and extinction coefficient of the $H_3Sb_3P_2O_{14}$ nanosheet thin film, determined by spectroscopic ellipsometry. b) Layer thickness changes of the $H_3Sb_3P_2O_{14}$ nanosheet thin film upon changing relative humidity. Inset: Photograph of the colloidal $H_3Sb_3P_2O_{14}$ nanosheet suspension. c) RI changes (at 633 nm) of the $H_3Sb_3P_2O_{14}$ nanosheet thin films and the SiO_2 nanoparticles upon relative humidity changes.

The schematic sample fabrication using the colloidal SiO_2 and the phosphatoantimonate nanosheets is shown in Fig 2a. The materials were deposited alternating on the glass substrate starting with the nanoparticles to guarantee a better adhesion to the substrate and finishing with the nanosheets to ensure a higher RI contrast with the surrounding air. After each deposited layer, a heating step was applied, which improved the adhesion of the thin films within the stack. According to Fig 2d, the cross-sectional SEM images of the BS containing 12 layers show a long-range stacking order and lateral layer uniformity across several microns. The spectral position of the Bragg peak (BP) and, hence, the structural color at normal incidence is given by the expression (1),[27] which can be adjusted and gradually fine-tuned across the visible spectral range. Singly by varying the spin-coating speed, we can access structural colors all over the visible range, as exemplary shown in Fig 2c and d. With theoretical calculations using the RI values from the ellipsometry measurements and the layer thicknesses from the SEM, we could simulate the Bragg peaks of all samples, determine the layer thicknesses at ambient pressure and prove the color tunability.
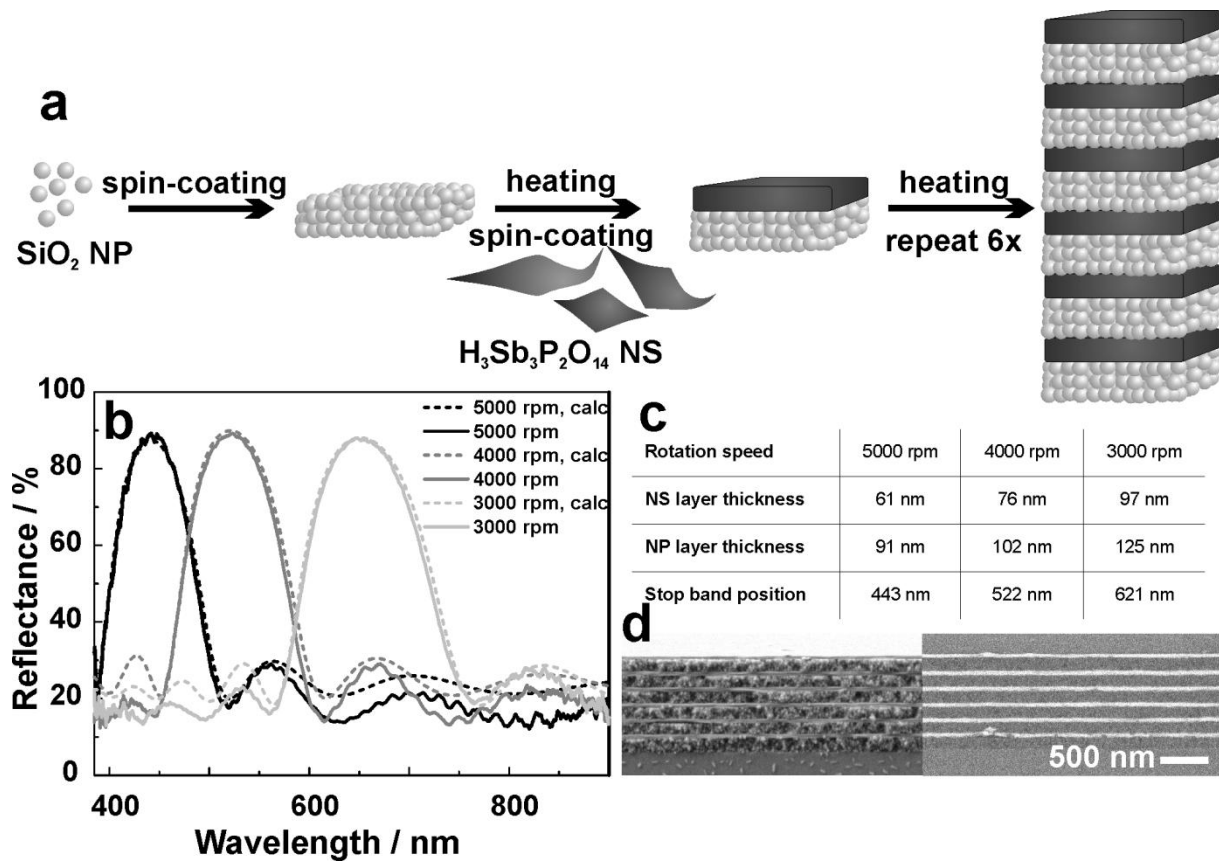
Figure 4.2: Fabrication and characterization of the silica SiO_2 nanoparticle/$H_3Sb_3P_2O_{14}$ nanosheet Bragg stack. a) Fabrication scheme of the SiO_2 nanoparticle/$H_3Sb_3P_2O_{14}$ nanosheet Bragg stack. b) Reflectance spectra and theoretical calculations of the SiO_2/$H_3Sb_3P_2O_{14}$ Bragg stacks prepared at different spin-coating speeds. c) Layer thicknesses, RIs of the SiO_2/$H_3Sb_3P_2O_{14}$ Bragg stacks fabricated at different spin-coating speeds. The data are determined by theoretical calculations. d) SEM cross section images (left: secondary electron image, right: back-scattered image) of the SiO_2/$H_3Sb_3P_2O_{14}$ Bragg stack containing 12 layers.

In order to study the key features of our optical humidity sensors, the two BSs were introduced into a closed chamber with a transparent upper window, and the position of the BP was measured for different RH values.[28,29] The supposed sensing mechanism of the BSs is schematically depicted Figure 4.3a. Here, the thickness of the particle layers is assumed to be invariable. Three main processes affect the humidity-dependent optical response of the BS: (1) the RI changes of the SiO_2 layer with the adsorption/desorption of water into their textural pores (Fig 1c), (2) the change of the RI of the nanosheet layers through uptake/loss of water (Fig 1c), (3) the humidity-dependent thickness of the nanosheet layers (Fig 1b). While for SiO_2 the effective RI of the layers increases with increasing water content due to the pore filling process, it decreases for the nanosheet layers as the effective RI approaches that of pure water with increasing degree of hydration (Fig 1c). The latter phenomenon is driven by the swelling mechanism of the nanosheet layer as described above. For the BS, we observe a qualitatively similar behavior than for the thin films, as the response can be divided

into two RH ranges, the low range 0-90% and the high range 90-100%.The photonic stop band redshifts by 100 nm in the lower RH range (up to 90%) as plotted in Fig 3b. This shift is accompanied by a gradual reflectance intensity decrease, which finally vanishes (Fig 3b, light gray spectrum), the color of the BS switches off, *i.e.* becomes completely transparent. This effect finds its explanation in the elimination of the RI contrast between the layers forming the BS with increasing RH (Fig 1c). While the RI of the particle layer increases, the RI of the nanosheet layer decreases while the layer thickness increases, leading to an overall redshift of the BP. Since the RIs of the nanosheet and nanoparticle layers follow opposite trends, the difference becomes sufficiently low at above 95% RH, leading to the disappearance of the optical contrast. As the BP is canceled out, the optical sensor turns completely transparent and light is transmitted by the structure throughout the visible range. Transparency switching through reversible RI matching has previously been realized by rational porosity tuning and RI tailoring of the constituent layers.[30,31] These hygrochromic multilayers however are only capable of detecting liquid water, rather than humidity changes.

To obtain another important key feature of these ultrasensitive humidity sensors, the selectivity was tested. For this, we placed the sensors into a closed atmosphere and the ethanol relative pressure was raised, while the optical response of the system was detected. According to Fig 3c, we observe a total shift of around 50 nm, which is escorted by a gradual reflectance intensity decrease of 10%. The trends are similar to the trend observed upon humidity adsorption, but the magnitude of the changes is smaller. As the nanoparticle layer presents only the optical contrast material and a gate to ensure the infiltration over the whole structure, the selectivity is presumably given by the nanosheet layers. Taking this into account, the different optical response to the two analytes is determined by the intercalation degree. We assume that due to size effects, only a lower intercalation degree of ethanol molecules in the interlayer space is favorable. This lower intercalation rate means a smaller layer thickness increase and also a smaller RI decrease. The RI contrast is not cancelled out completely and the structural color and a photonic stop band are present over the whole ethanol relative pressure range. With these two qualitatively similar but quantitatively different behavior we could demonstrate the selectivity to humidity against ethanol vapor.
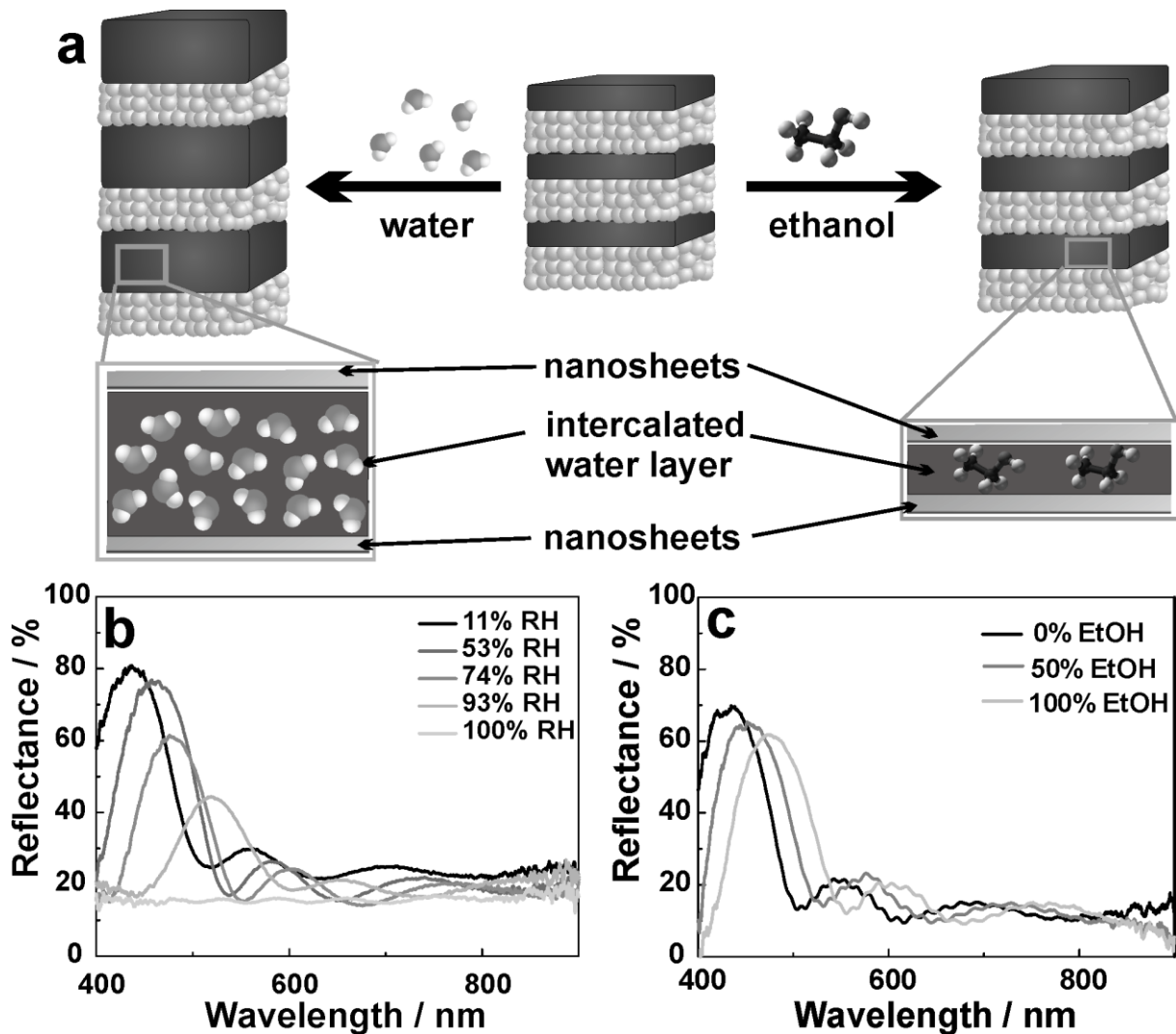
Figure 4.3: Humidity sensing properties of the SiO_2 nanoparticle/$H_3Sb_3P_2O_{14}$ nanosheet Bragg stack. a) schematic illustration of the suggested humidity and ethanol sensing mechanism of the SiO_2 nanoparticle/$H_3Sb_3P_2O_{14}$ nanosheet Bragg stacks. b) Reflectance spectra of the SiO_2/$H_3Sb_3P_2O_{14}$ Bragg stack at different relative humidity values. c) Reflectance spectra of the SiO_2/$H_3Sb_3P_2O_{14}$ Bragg stack at different ethanol relative pressure.

According to this high sensitivity and fast response times, we demonstrated in our previous work the potential of applying these platforms as optical touchless positioning interfaces.[26] As the human finger is surrounded by a humid atmosphere, it was possible to detect finger positions and to track finger motions by color changes along the Bragg stack in a touchless fashion. In this work, we demonstrate the real-life applicability of the touchless positioning interfaces by showing the reproducibility in form of a high cycling stability and the temperature dependency of these platforms. In Fig 4a, we show the optical response of the Bragg stack to an approaching finger. The black curve shows the Bragg peak at ambient condition. The dark grey curve shows the optical response to a tapping finger, which means a short stimuli by an approaching finger but without touching the BS

surface, while the bright gray curve shows the full response of the Bragg stack, the canceling of the BP and the structural color by the complete infiltration of the structure caused by the humidity sheath of the finger. In the following experiments, we operate with the finger tapping stimuli, in all cases without touching the Bragg stack directly, as this already causes a stopband shift of at least 20 nm and exhibits a faster response time compared to the full response. For real-life applications, the reproducibility, the signal stability and the high cycling stability is a crucial requirement. According to Fig 4b, we tested our sensor in a 100x cycling experiment. Hereby, we approached a human finger 10-times to the BS surface in shorter time, and repeated this experiment 10-times, which results a cycling experiment with in total 100 cycles. According to Fig 4b, one signal package corresponds to 10 cycles in a shorter time (Fig 4c). In all cases, we detect the reflectance intensity changes at 550 nm, which is the easiest way to detect small stop band shifts by intensity increases at the red stop band edge due to the high slope. According to Fig 4c, we observe an instantaneous response of the sensor, for all cases, a signal change of at least 20% is observed in a time range of subseconds. Notably, the humidity response is fully reversible during cycling and the Bragg stack can be cycled for more than 100 times without observing any signs of degradation or changes in its response behavior.

Additionally, we investigated the influence of the temperature on the humidity sensing performance. We compared the optical responses at room temperature with the responses at 40 °C and 0 °C. To heat/cool the sample, we placed the sample on a copper plate, which was heated/cooled to the given temperature. Note, the increasing baselines of the reflectance spectra at higher wavelengths in Fig 4d und e originate from the reflectance properties of the copper plate and are not caused by the sample itself. At 40 °C, the sample shows a similar optical response as at room temperature: a slight reflectance intensity decrease caused by the RI contrast decrease and a slight stopband shift caused mainly by the nanosheet swelling. Note, in this experimental only an artificial finger could be used, – a humid nitrogen flow – which can be the reason for the slightly smaller stopband shift compared to the room temperature measurements. Although the sensing performance is unchanged at slightly increased temperatures, we found the limits of these local ultrasensitive humidity sensors at the dew point. Upon cooling the sample to 0 °C, we observe a spontaneous condensation of water into the system. This comes to expression by the vanishing Bragg peak and the loss of the structural color (Fig 4e, gray spectrum). The time resolved optical response is shown in Fig 4f, whereby the spontaneous condensation can be followed by the rapid decrease of the reflectance intensity decrease. Once the cooling source is removed and the sample warms up to room temperature, we observe a complete self-recovery without any external influence, which is detected by the blueshift of the Bragg peak and the reappearance of the structural color. Note, after removing the heat source, a peak in the time-resolved plot occurs, which is due to refocusing of the sample. The water condensation and loss is

completely reversible and could be repeated several times (not shown). Therefore, we propose that the spontaneous condensation at 0°C and the local sensitivity to humidity changes can be utilized for other applications, such as a photonic dew point sensor. We would like to note, however, that in real life, devices such as smartphones or touchscreens in general are heated by internal electrics and/or Joule heating to well above 0°C, even if the surrounding temperatures are lower. For this reason, the condensation of humidity from the atmosphere can be avoided and the water uptake and loss is fully reversible. Therefore, we do not expect major problems if the external temperature decreases to and below 0°C, but the operation temperature of the possible device should be above the dew point.
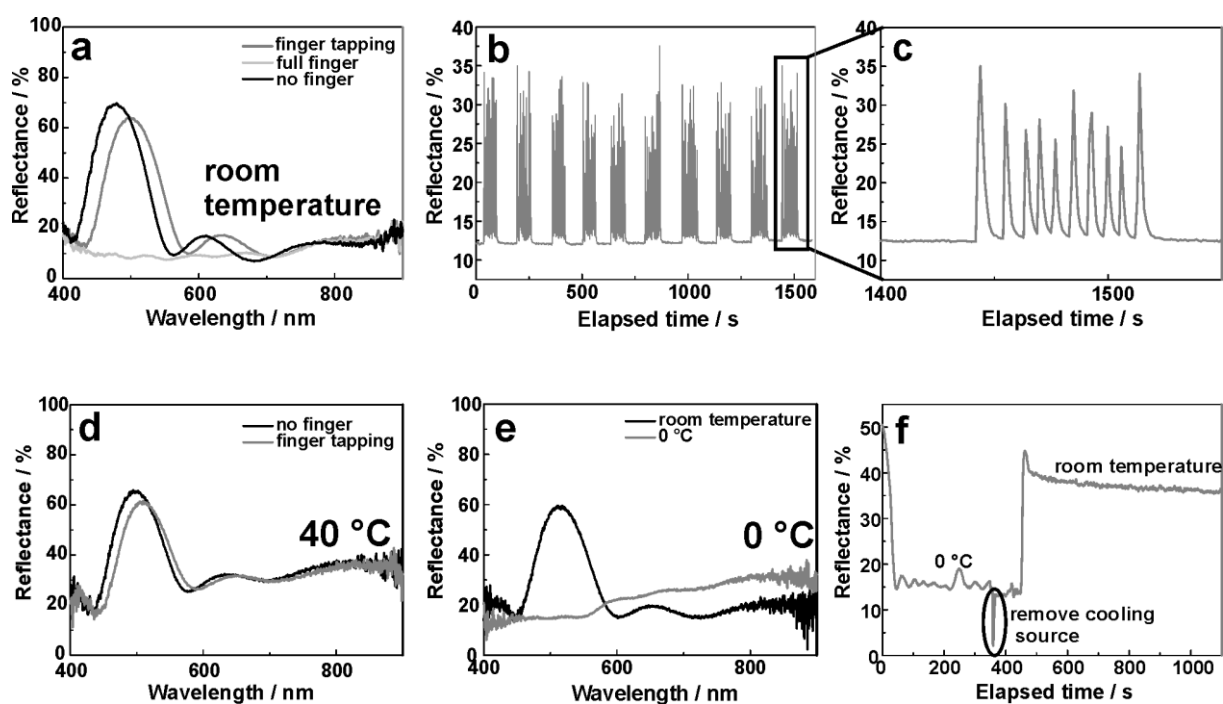

Figure 4.4: Optical touchless positioning interface tested at different temperatures. a) Reflectance spectra of the silica SiO_2 nanoparticle/$H_3Sb_3P_2O_{14}$ nanosheet Bragg stack showing witout a finger, with a full-finger stimuli and with a tapping finger stimuli. b) Time resolved response of the SiO_2/$H_3Sb_3P_2O_{14}$ Bragg stack in a 100x cycling experiment. c) Magnification of one "signal package" of 10 cyclings. For one cycle, a finger "tapping" experiment was used in which a human finger was only shortly approached to the SiO_2/$H_3Sb_3P_2O_{14}$ Bragg stack surface. In such a "tapping experiment" a reflectance intensity change of at least 20% is observed. d) Reflectance spectra of the SiO_2/$H_3Sb_3P_2O_{14}$ Bragg stack at 40 °C without a finger and at tapping stimuli. e) Reflectance spectra of the SiO_2/$H_3Sb_3P_2O_{14}$ Bragg stack at 0 °C without a finger and at tapping stimuli. f) Time resolved response of the SiO_2/$H_3Sb_3P_2O_{14}$ Bragg stack upon cooling the sample from room temperature to 0 °C.

In conclusion, we studied the optical properties and the sensing performance of 2D phosophatoantimonate nanosheets. Hereby, we determined the complex RI depending on the wavelength via spectroscopic ellipsometry and showed the evolution of the RI and the layer thickness of thin films depending of the relative humidity. Observing massive changes in these two

properties, we integrated these 2D nanosheets into Bragg stacks, which show besides the high sensitivity to humidity changes, a high selectivity to water against ethanol vapor. Finally, we investigated further properties of our previously published optical touchless positioning interface. Hereby we proved the high reversibility, signal stability and reproducibility, the influence of the temperatures, whereby the natural limits of these humidity sensing devices were detected to be at the dew point.

4.6 EXPERIMENTAL

Solid state synthesis, protonation and exfoliation of nanosheets

For the synthesis of $K_3Sb_3P_2O_{14}$ the precursors (KNO_3 (99 %, Merck), Sb_2O_3 (99.6 %, Alfa Aesar), $NH_4H_2PO_4$ (98 %+, Acros Organics)) were thoroughly ground in a stoichiometric ratio and heated up in a two-step solid state synthesis as described elsewhere.[32] For the proton exchange reaction, 2 g of $K_3Sb_3P_2O_{14}$ were treated with 250 mL of 8 M nitric acid (diluted 65 wt%, Merck) overnight, filtrated, washed with ethanol and dried at room temperature. For a complete exchange reaction, this was repeated once. Exfoliation was carried out by stirring the $H_3Sb_3P_2O_{14}$ vigorously overnight in pure water with a concentration of bulk protons of 7.3 mmol L^{-1}.[26] The obtained colloidal suspensions were centrifuged at 3000 rpm for 30 min to remove agglomerates and non-exfoliated bulk material. To obtain the nanosheet pellet, an additional centrifugation step was applied at 18000 rpm for 30 min. The supernatant was discarded and the gel-like colourless wet aggregate was dried at 100 °C.

Preparation of colloidal suspensions

The dried colorless precipitate of the water exfoliated $H_3Sb_3P_2O_{14}$ nanosheets was redispersed with a concentration of 42 mmol L^{-1} in a water/ethanol mixture (60 vol% ethanol) and sonicated for 2 h. The The commercial colloids of SiO_2 (LUDOX TMA, Sigma) were redispersed at 3 wt% in methanol and sonicated for 15 min.

Fabrication of thin films and Bragg stacks

All films were fabricated by spin-coating (WS-650S-NPP-Lite, Laurell Technologies Corporation) using concentrations given above. Different film thicknesses were accessed by varying the spin-coating speed, which allows the fine-tuning of the optical properties.[13] On plasma cleaned glass slides (2.5 cm x 2.5 cm), 400 µl of the colloidal suspensions were spin-coated alternatingly for 1 min with a defined speed (2000 rpm, 3000 rpm and 4000 rpm were applied, a constant speed within one BS), and heated to 80 °C for 15 min after each layer deposition. Other parameters such as colloidal concentration, spin-coating time and acceleration rate were kept constant.

Characterization

SEM cross-sectional images of the Bragg stacks were taken with a Zeiss Merlin FE-SEM.

All reflectance spectra were measured with a fiber optic spectrometer (USB2000+, Ocean Optics) attached to a microscope (DM2500, Leica) with normal incidence and the reflectance spectra were always taken at the same spot (1×1 mm^2 in area). To obtain the optical changes with relative humidity change, the Bragg stacks were kept in a stainless steel chamber with a total volume of 5 mL, placed above 0.7 mL of the saturated salt solutions[5,6] at around 25 °C in a closed stainless steel chamber with a transparent glass window. At each step, 20 min atmosphere equilibration time was needed. In the ethanol vapor sorption measurements, the BSs were placed into a closed chamber with the dimensions of $2.5\times2.5\times0.5$ cm^3, where well-defined relative analyte relative pressure values were realized by connecting the inserted pipette tip with a liquid-gas flow controller (Bronkhorst) and a vaporizer (CEM) with a massflow-controlled carrier gas flow. To observe a specific relative pressure, the carrier gas nitrogen (200 mL min^{-1}) and the liquid analyte were dosed into the CEM (controlled evaporation and mixing, W101A-130-K, Bronkhorst High-Tech),[8] where the thermal evaporation of the analyte took place. The CEM was heated to temperatures above the boiling point. The relative vapor pressures were calculated via the software FLUIDAT (CEM calculation), which considers the actual atmospheric pressure, the temperature and the properties of the analyte, such as vapor pressure and heat capacity.[33] The obtained data were analyzed with the SPECTRA SUITE software.

Porosimetry measurements were carried out by the porosimetry tool of Sopra PS-1000 SAM, whereby the sample was equilibrated at all vapor relative pressures values for 15 min. The measurement results were fitted with the software Sopra SAE using the model combination Cauchy and Lorentz. The thickness of the SiO$_2$ layers was considered as unchanged and only the RI was fitted over the relative pressure range. For the nanosheet thin films both values, the layer thickness and also the RI were fitted. Before all measurements, the nanoparticle samples were heated for 30 min to 200 °C and the nanosheets thin films for 30 min to 60 °C in vacuum to remove the atmospheric water from pores and between the nanosheets. To obtain the optical isotherms, all fitted measurement results were plotted against the analyte relative pressure.

Touchless positioning interface measurements

To test the reproducibility of the touchless positioning interfaces, cycling experiments was carried out by finger tapping experiments by approaching (but not touching) and distancing the finger in regular intervals of ca. 30 s. This measurement was used to determine the response time of the Bragg stack, which was defined as the time it takes for 90% of the stopband shift before the

structural color vanishes. To detect the stopband changes, the intensity changes at the wavelength 550 nm were followed. To test the temperature dependency, the optical response was tested at 40°C and 0°C and was compared to room temperature. Hereby, the BS was heated/cooled via a copper plate and an approaching finger was used as stimuli.

4.7 REFERENCES

[1]   S. John, *Phys. Rev. Lett.* **1987**, *58*, 2486-2489.

[2]   E. Yablonovitch, *Phys. Rev. Lett.* **1987**, *58*, 2059-2062.

[3]   J. R. C. Smirnov, M. Ito, M. E. Calvo, C. López-López, A. Jiménez-Solano, J. F. Galisteo-López, P. Zavala-Rivera, K. Tanaka, E. Sivaniah, H. Míguez, *Adv. Opt. Mater.* **2015**, *3*, 1633-1639.

[4]   N. Hidalgo, M. E. Calvo, H. Míguez, *Small* **2009**, *5*, 2309-2315.

[5]   O. Sanchez-Sobrado, M. E. Calvo, H. Miguez, *J. Mater. Chem.* **2010**, *20*, 8240-8246.

[6]   L. D. Bonifacio, D. P. Puzzo, S. Breslav, B. M. Willey, A. McGeer, G. A. Ozin, *Adv. Mater*. **2010**, *22*, 1351-1354.

[7]   L. D. Bonifacio, G. A. Ozin, A. C. Arsenault, *Small* **2011**, *7*, 3153-3157.

[8]   T. L. Kelly, A. Garcia Sega, M. J. Sailor, *Nano Lett*. **2011**, *11*, 3169-3173.

[9]   K. P. Raymond, I. B. Burgess, M. H. Kinney, M. Loncar, J. Aizenberg, *Lab Chip* **2012**, *12*, 3666-3669.

[10] A. T. Exner, I. Pavlichenko, D. Baierl, M. Schmidt, G. Derondeau, B. V. Lotsch, P. Lugli, G. Scarpa, *Laser Phot. Rev.* **2014**, *5*, 726-733.

[11] I. Pavlichenko, E. Broda, Y. Fukuda, K. Szendrei, A. K. Hatz, G. Scarpa, P. Lugli, C. Brauchle, B. V. Lotsch, *Mater. Horiz*. **2015**, *2*, 299-308.

[12] B. V. Lotsch, G. A. Ozin, *J. Am.Chem. Soc.* **2008**, *130*, 15252-15253.

[13] B. V. Lotsch, G. A. Ozin, *ACS Nano* **2008**, *2*, 2065-2074.

[14] B. V. Lotsch, F. Scotognella, K. Moeller, T. Bein, G. A. Ozin, *SPIE*, *7713, Vol. 7713*, **2010**, p. 7713V.

[15] M. E. Calvo, O. Sánchez-Sobrado, S. Colodrero, H. Míguez, *Langmuir* **2009**, *25*, 2443-2448.

[16] L. D. Bonifacio, B. V. Lotsch, D. P. Puzzo, F. Scotognella, G. A. Ozin, *Adv. Mater*. **2009**, *21*, 1641-1646.

[17] J. D. Joannopoulos, S. G. Johnson, J. N. Winn, R. D. Meade, *Photonic crystals: molding the flow of light*, Princeton university press, **2011**.

[18] I. Pavlichenko, A. T. Exner, M. Guehl, P. Lugli, G. Scarpa, B. V. Lotsch, *J. Phys. Chem. C* **2011**, *116*, 298-305.

[19] C. Fenzl, T. Hirsch, O. S. Wolfbeis, *Angew. Chem. Int. Ed*. **2014**, *53*, 3318-3335.

[20] F. M. Hinterholzinger, A. Ranft, J. M. Feckl, B. Ruhle, T. Bein, B. V. Lotsch, *J. Mater. Chem.* **2012**, *22*, 10356-10362.

[21] A. Ranft, F. Niekiel, I. Pavlichenko, N. Stock, B. V. Lotsch, *Chem. Mater*. **2015**, *27*, 1961–1970.

[22] Z. Wang, J. Zhang, J. Xie, C. Li, Y. Li, S. Liang, Z. Tian, T. Wang, H. Zhang, H. Li, W. Xu, B. Yang, *Adv. Funct. Mater*. **2010**, *20*, 3784-3790.

[23] Y. Kang, J. J. Walish, T. Gorishnyy, E. L. Thomas, *Nat. Mater*. **2007**, *6*, 957-960.

[24] A. C. Arsenault, D. P. Puzzo, I. Manners, G. A. Ozin, *Nat. Photonics* **2007**, *1*, 468-472.

[25] S. Deniard-Courant, Y. Piffard, P. Barboux, J. Livage, *Solid State Ionics* **1988**, *27*, 189-194.

[26] J.-C. P. Gabriel, F. Camerel, B. J. Lemalre, H. Desvaux, P. Davidson, P. Batail, *Nature* **2001**, *413*, 504-508.

[27] F. Camerel, J. C. P. Gabriel, P. Batail, P. Panine, P. Davidson, *Langmuir* **2003**, *19*, 10028-10035.

[28] K. Szendrei, P. Ganter, O. Sánchez-Sobrado, R. Eger, A. Kuhn, B. V. Lotsch, *Adv. Mater*. **2015**, *27*, 6341-6348.

[29] S. Joannopoulos, J. N. Winn, R. D. Meade, *Photonic crystals: molding the flow of light,* Princeton University press, **2008**, 2nd edition, 4.

[30] P. W. Winston, D. H. Bates, *Ecology* **1960**, *41*, 232-237.

[31] L. Greenspan, J. Res. *Nat. Bur. Stand*. **1977**, *81A*, 89-96.

[32] M. N. Ghazzal, O. Deparis, J. De Coninck, E. M. Gaigneaux, *J. Mater. Chem. C* **2013**, *1*, 6202-6209.

[33] K. E. Shopsowitz, H. Qi, W. Y. Hamad, M. J. MacLachlan, *Nature* **2010**, *468*, 422-425.

[34] Y. Piffard, A. Lachgar, M. Tournoux, *J. Solid State Chem*. **1985**, *58*, 253-256.

[35] Bronkhorst High-Tech, www.fluidat.com, accessed: 06-12/2014.

5.

TAILORING THE SENSOR`S SELECTIVITY: OPTICAL DISCRIMINATION OF DIFFERENT SOLVENTS BY 2D NANOSHEET BASED 1D PHOTONIC CRYSTALS

5.1 SUMMARY

The development of single-component sensors with high sensitivity and selectivity is one of the key challenges in sensor design. In addition, the ability of a sensor to distinguish between chemically similar analytes usually requires either multicomponent sensor arrays or sophisticated device fabrication, combined with complex statistical data processing such as principal component analysis, to enhance the selectivity. In this project, we address these aspects by introducing another member of the antimony phosphate nanosheet family, $HSbP_2O_8$ as highly chemo-selective components in thin-film based sensors, which operate based on either resistive or optical read-out. The main difference between the previously presented nanosheets ($H_3Sb_3P_2O_{14}$) and the here presented $HSbP_2O_8$ lies in the crystal structure: while $H_3Sb_3P_2O_{14}$ shows inherent pores in the nanosheet layer itself, $HSbP_2O_8$ nanosheets are dense and the analyte diffusion is limited to pathways along the grain boundaries, which turned out to be relevant for the sensor's selectivity.

Similar to $H_3Sb_3P_2O_{14}$ nanosheets, the high sensitivity of $HSbP_2O_8$ nanosheets towards water vapor is given by the intercalation of the water molecules into the interlayer space, causing significant swelling, which translates into structural color changes when the nanosheets are integrated into 1DPC architectures. Not only full-spectrum stopband shifts with a fast response time were shown in this project, but also the response to other volatile organic compounds (VOCs) is of interest. By comparing the saturation times and the photonic stopband shifts for different VOCs, we could optically distinguish between non-protic (polar and non-polar) and protic solvent vapors. Due to different interactions and intercalation rates of the analytes, protic analytes showed slow response

times combined with large stopband shifts, while non-protic analytes exhibited fast response times accompanied by smaller shifts. With this, the protic and the non-protic analytes could be clearly differentiated by their optical response. Further, the different alcohols (ethanol and methanol) and even constitutional isomers (i.e. 2-butanol and 1-butanol) could be optically distinguished by the response times and the stopband shifts. The obtained trends could be lead back to the different interactions of the analytes with the nanosheets, and these could be correlated with the dielectric properties, the molecular size and other size-related properties, such as acidity or polarity.

Besides creating a platform for high humidity sensitivity and the optical differentiation of VOCs, the optical readout was complemented by designing a thin film device with a resistive readout. Hereby, the sensing event was represented by changes in the proton conductivity with changing humidity levels. Besides a large increase in conductivity by five orders of magnitude, we demonstrated an ultrahigh sensitivity to water vapor by detecting trace amounts of water (down to 0.2%) in alcohols based on conductance changes. These results show the versatility of the 2D nanosheet material based sensing platform, which can simultaneously act as an optical and a resistive sensor for detecting humidity as well as VOCs.

Contributions: Pirmin Ganter synthesized, exfoliated and characterized the $HSbP_2O_8$ nanosheets, fabricated the thin films, performed the resistivity measurements and characterized the fabricated systems as resistive humidity sensors and the trace water detection devices, wrote the manuscript and edited the figures. Katalin Szendrei optimized the nanosheet based thin film fabrication procedure, designed and fabricated the 1DPCs, performed the theoretical calculations, measured and analyzed the optical response of the multilayered structures to the different analytes, wrote the manuscript and edited the figures.
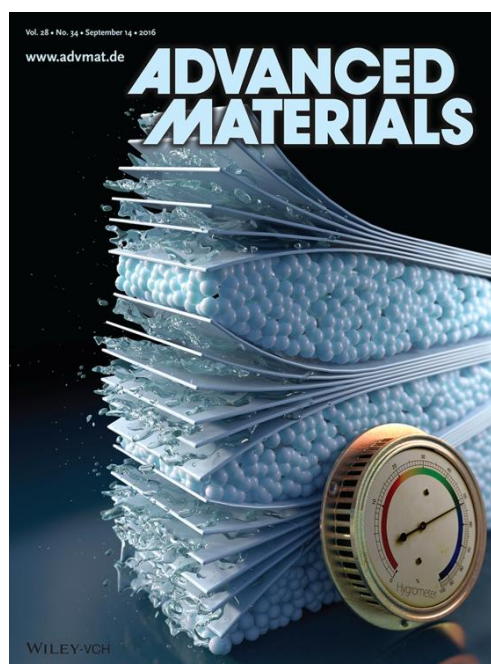
This project was highlighted as an inside cover image of the journal *Advanced Materials*, the cover image was designed by Christoph Hohmann, NIM München.

5.2 TOWARDS THE NANOSHEET-BASED PHOTONIC NOSE: VAPOR RECOGNITION AND TRACE WATER SENSING WITH ANTIMONY PHOSPHATE THIN FILM DEVICES

Pirmin Ganter,* Katalin Szendrei,* Bettina V. Lotsch

* These authors contributed equally to this work.

5.3 INTRODUCTION

Artificial noses, mimicking the animal olfactory system, are of increasing interest in various technologically relevant fields such as medical diagnostics, pharmaceutics, food and beverage control, ambient monitoring, and homeland security.[1–3] Currently, the optical discrimination and classification of organic vapors by photonic noses still requires complicated experimental procedures or sophisticated data processing methods.[1–4]

State of the art photonic noses can be divided into three main groups: single-element sensors,[5–10] sensing arrays,[1–3,11] and complex sensing structures, e.g., topologically complex architectures or biological systems which are challenging to emulate in the lab.[4,12] While each system can be adapted to specific environments, the following drawbacks remain: Current single sensor photonic noses, which are easy to fabricate, suffer from low resolution in terms of analyte recognition and classification into solvent vapors with different polarity.[5,7–10] Sensing arrays rely on multiple sensors for good analyte resolution, requiring a complex mixture of materials or functionalization strategies. In addition, they necessitate complicated data processing algorithms for pattern recognition and discrimination.[1,3,11] Complex sensor nanostructures, such as multiple stacked, porous Si photonic crystals (PC),[4] or the Morpho butterfly wing—a naturally occurring photonic nose—can show good analyte identification, but invariably need sophisticated sample preparation or are not applicable on the large scale.[12] Due to these reasons, there is a strong need for a smart but easy to fabricate single sensor photonic nose, which is able to distinguish and classify different types of analytes.

Recently, we have demonstrated the successful integration of 2D phosphatoantimonate ($H_3Sb_3P_2O_{14}$) nanosheets into 1D PC.[13] Their ultrahigh sensitivity to local humidity changes enables color-coded touchless finger motion tracking, thus illustrating the high potential of swellable 2D materials as

active sensing components in photonic nanostructures. To demonstrate the generality of this approach and to highlight the potential of an intercalative sensing mechanism for analyte discrimination, we here introduce a new type of stimuli responsive 2D material, namely $HSbP_2O_8$ antimony phosphate nanosheets.

Similar to $H_3Sb_3P_2O_{14}$, $HSbP_2O_8$ as a bulk material has extraordinary swelling properties, [14] which have been used to produce nematic liquid crystalline phases in water. [15] In contrast to $H_3Sb_3P_2O_{14}$, $HSbP_2O_8$ loses water completely at zero humidity, hence making it a superior sensor candidate owing to its higher sensitivity in this humidity regime.[14,16] The reason for the incomplete water loss of $H_3Sb_3P_2O_{14}$ can be rationalized by the presence of structural pores which can host water molecules, while the layers in $HSbP_2O_8$ are dense. The highly polar and acidic interlayer environment of $HSbP_2O_8$, its high sensitivity at low relative humidity[14,16] and the generally higher sensitivity of nanosheets compared to their bulk materials[13,17,18] renders $HSbP_2O_8$ nanosheet-based thin film devices promising candidates for tracking trace amounts of water as well as for the discrimination of organic vapors.

Here, we report the first comprehensive characterization of $HSbP_2O_8$ 2D nanosheets and demonstrate their outstanding sensitivity to humidity—especially in the low humidity range. Based on these features, we develop resistive thin film sensors that are able to detect even trace amounts of water in alcohols. We then exploit the unique film forming capability of the 2D nanosheets to develop highly sensitive photonic crystal sensors which can identify various organic vapors with high accuracy, which is superior to all other single-component photonic vapor sensing structures reported to date.[5-10]

5.4 RESULTS AND DISCUSSION

$KSbP_2O_8$ was synthesized by a solid-state reaction starting from KNO_3, Sb_2O_3, and $NH_4H_2PO_4$ and protonated with 8 M HNO_3 (Figures S5.1 and S 5.2, and Table S 5.1, Supporting Information).[14,15,19,20] The antimony phosphate and its corresponding solid acid consist of anionic 2D $SbP_2O_8^-$ sheets separated by charge compensating cations which occupy the interlayer space (Figure S 5.3, Supporting Information).[19,20] The hexagonal crystal habit of $HSbP_2O_8$ is shown in Figure 5.1a. Upon exfoliation with pure water (Figure S 5.4, Supporting Information), the morphology becomes "silk-like" (Figure 5.1b, Figure S 5.5, Supporting Information), indicating successful delamination. Exfoliation into single layer nanosheets was further confirmed by various analytical techniques (see Figures 5.1, Figures S 5.6, S 5.7, and S 5.8, and Tables S 5.2 and S 5.3, Supporting Information). The thickness of a single nanosheet was determined to be 0.9 ± 0.1 nm by atomic force microscopy (AFM) (Figure 5.1 d), which agrees well with the crystallographic single layer thickness of 0.66 nm.[21]

The high aspect ratio and film texture can be clearly seen by transmission electron microscopy (TEM) (Figure 5.1 e). The selected area electron diffraction (SAD) pattern of an individual nanosheet (Figure 5.1 e inset) exhibits *d* -values that are in excellent agreement with those obtained from powder X-ray diffraction measurements (see Table S 5.2, Supporting Information, and Figure 5.1 c) illustrating the structural in-plane integrity. Rietveld refinement of the diffraction pattern of a precipitated nanosheet pellet, showing a characteristic Warren-type peak profile (Figure 5.1 c) evidences the turbostratically disordered nanosheet arrangement.

Large area thin films were prepared by spin-coating nanosheets from the colloidal suspension and investigated by thin film X-ray diffraction (Figure S 5.9, Supporting Information) and by ellipsometric porosimetry (Figure S 5.10, Supporting Information). Only the *00l* reflections were observed in the out ofplane XRD pattern pointing toward a parallel orientation of the nanosheets to the surface of the substrate. Upon exposure to moisture, the thin film swells to almost double its thickness. The swelling of the film is caused by intercalation of water molecules between the turbostratically disordered nanosheets and into the resulting grain boundaries. The refractive index (RI) *n* decreases from 1.57 to 1.50 with increasing humidity as the film becomes more "water-like" with increasing water uptake. Water uptake was also monitored by the Raman spectra of the bulk material as well as the nanosheet pellet (Figure S 5.11, Supporting Information). Slight changes are observed by the emergence of a band at 482 cm^{-1} (Sb O···P stretching vibration) and by narrowing of the terminal P-O stretching vibration at 1270 cm^{-1}. The latter band is sensitive to water uptake as the P-O bond points toward the interlayer space in which water is intercalated.
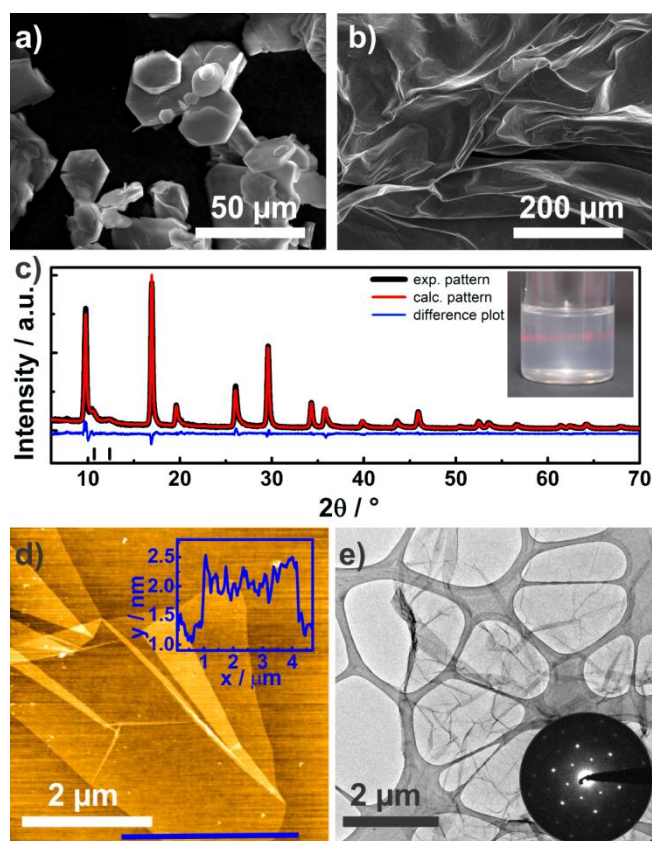
Figure 5.1: Characterization of $HSbP_2O_8$ nanosheets. a) SEM image of the $HSbP_2O_8$ crystallites featuring hexagonal shapes. b) SEM image of the exfoliated and randomly restacked nanosheet pellet, exhibiting a 'silk-like' morphology. c) Rietveld refinement of the XRD pattern of a $HSbP_2O_8$ nanosheet pellet showing a Warren-type peak profile (experimental pattern in black, calculated pattern in red and difference plot in blue).[32] The inset in (c) shows the Tydnall effect of the nanosheet colloidal suspension. d) AFM image of overlapping $HSbP_2O_8$ monolayer nanosheets with the corresponding height profile of a single layer nanosheet. e) TEM image of randomly overlapping $HSbP_2O_8$ nanosheets with a representative SAD of a single nanosheet (inset).

Inspired by the swelling capability as well as the humidity dependent proton conductivity reported for the bulk material,[14] we developed two ultrathin sensing devices based on $HSbP_2O_8$ nanosheets (Figure 5.2): first, we constructed a resistive thin film device by spin coating the nanosheet suspension on quartz substrates; the contacts were obtained by sputtering gold on top of the thin film (Figure 5.2 a). Second, we combined the $HSbP_2O_8$ nanosheet films with TiO_2 nanoparticles (NPs) as high RI optical contrast material to fabricate a photonic multilayer structure known as 1D PC or Bragg stack (BS) (Figure 5.2). By combining these two robust inorganic materials in an alternating fashion, we observe the emergence of a pronounced photonic stop band (Figure 5.2b). The band gap and, hence, structural color can be adjusted and gradually fine-tuned across the visible spectrum (Figure 5.2b and c) by simply changing the layer thicknesses through varying the spin-coating speed in the fabrication steps. The position of the Bragg peak (BP) for normal incidence is given by the optical equivalent of the Bragg equation[22]

$$\lambda_B = 2(n_1 d_1 + n_2 d_2) \qquad\qquad (1)$$

where n_1 and n_2 are the RIs of the different layers and d_1 and d_2 their respective thicknesses.

Although BSs with up to eleven layers and good optical quality could be reproducibly made (Figure S 5.12, Supporting Information), an average number of seven layers deposited on a reflective silicon substrate turned out to be an optimal compromise in terms of optical quality (reflectance of 60%) and sensing performance, the latter resulting from fast analyte uptake and short diffusion pathways. The scanning electron microscope (SEM) cross-section images (Figure 5.2d) indicate stacking periodicity and excellent lateral layer uniformity across several micrometers, which is crucial for high optical quality multilayer films.
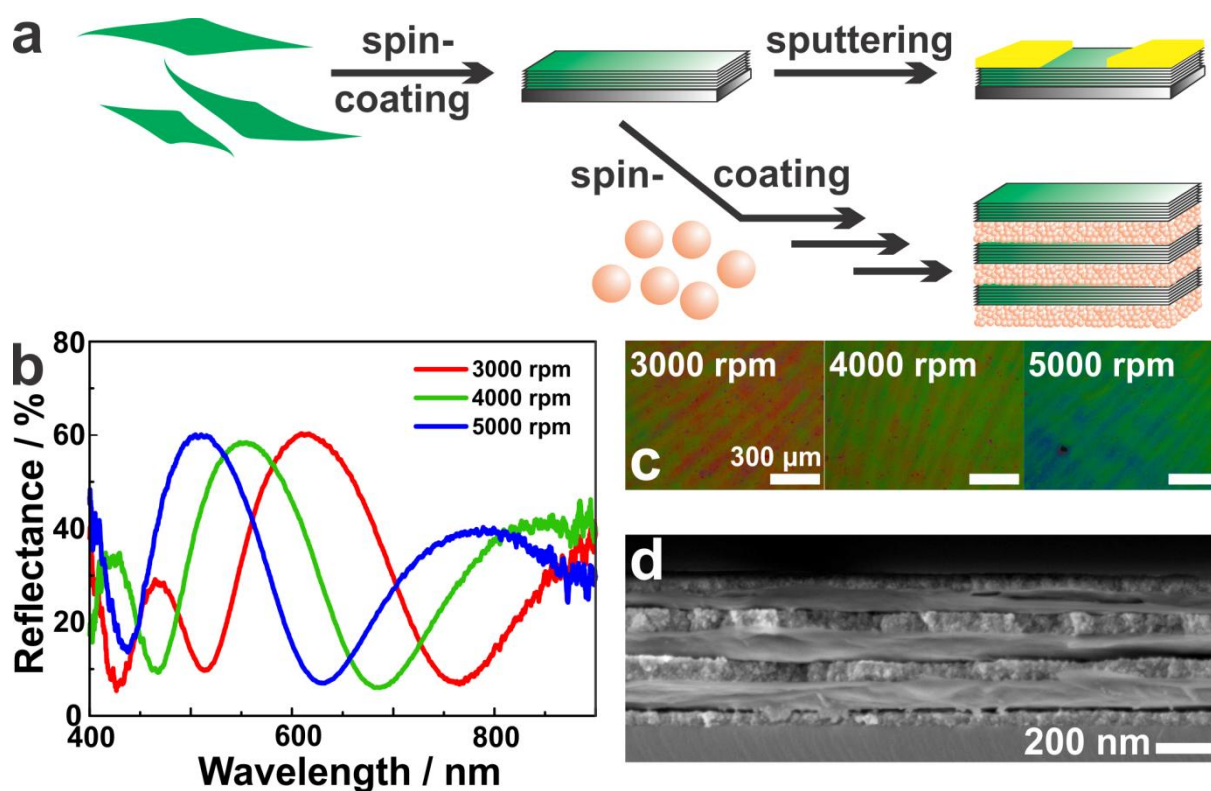
Figure 5.2: Fabrication and characterization of the nanosheets thin film devices: a) Schematic processing of $HSbP_2O_8$ nanosheets into thin film resistive devices (top) and 1D PC (bottom). b) Reflectance spectra of the $HSbP_2O_8$ nanosheet/TiO_2 NP BS with 7 layers, fabricated at 3000 rpm, 4000 rpm and 5000 rpm rotational speeds and c) the corresponding microscope images, showing the different structural colors. d) In-lens SEM cross-section image of a $HSbP_2O_8$ nanosheet/TiO_2 NP BS comprising 7 layers.

Next, we studied the humidity sensing capabilities of the resistive nanosheet thin film and the BS (Figure 5.3a). We observe an increase in proton conductance of the thin film of five orders of magnitude upon humidity exposure from 0% to 100% relative humidity (RH) (Figure 5.3b), which is larger than the change observed for the non-exfoliated bulk material [14] and comparable to the best nanosheet thin film humidity sensing devices reported to date.[13,17] Interestingly, in comparison to

$H_3Sb_3P_2O_{14}$ nanosheet thin film sensors [13] and the $HSbP_2O_8$ bulk material, [14] the $HSbP_2O_8$ thin films show higher sensitivity in the low humidity regime. Comparing to the bulk material, this can be explained by the fact that the thin film is able to desorb water molecules more easily due to its higher surface to volume ratio as well as the smaller domain size, most likely one nanosheet, compared to the bulk material, hence resulting in a greater water loss at low humidity values. The increased sensitivity of $HSbP_2O_8$ as compared to $H_3Sb_3P_2O_{14}$ can be understood by the complete water loss by $HSbP_2O_8$ due to the lack of structural adsorption sites for water. Moreover, the response of the thin film toward humidity is completely reversible as demonstrated by cycling experiments between 0% and 93.5% RH (Figure 5.3b inset). Inspired by this exceptional sensitivity to humidity, we tested the sensing performance of the photonic nanostructures. To this end, the BS was introduced into a closed chamber with a transparent glass window, whereby the humidity within the chamber was controlled by saturated binary salt solutions at around 25 °C.[23,24] Simultaneously, reflectance spectra and microscope images were taken as shown in Figure 5.3c and Figure S 5.13 (Supporting Information). The proposed sensing mechanism is depicted in Figure 5.3a. The sensor response is dominated by three effects: (i) the thickness of the nanosheet layers changes upon water adsorption/desorption, (ii) the effective RI of the nanosheet layers changes, and (iii) the effective RI of the NP layers changes upon water uptake/loss into/from the textural pores, while at the same time the thickness of the NP layers is constant over the entire humidity range as confirmed by spectroscopic ellipsometry. The combination of these effects gives rise to a pronounced optical response of the multilayer structure: with increasing humidity, a significant redshift of the stop band is observed, while the intensity of the BP increases. The main contribution to the stop band shift is caused by the massive swelling of the nanosheet layers during humidity uptake. As depicted in Figure S 5.10 (Supporting Information), the nanosheet film swells from 85 to 132 nm between 0% and 100% RH. In the lower humidity range up to 93% RH, a nearly linear stop band shift of 150 nm is observed, while in the high humidity range (>93% RH) the stop band shifts dramatically by 400 nm, shifting the BP out of the visible spectral range (the second order of the BP is observed at 500 nm, see Figure S 5.13 (Supporting Information), red curve). As shown in Figure S 5.13 (Supporting Information), we simulated the reflectance spectra for different RH values using the layer thicknesses from the SEM cross-section image combined with the swelling behavior at higher RH values and the RIs from the porosimetry measurements (see Table S 5.4, Supporting Information).[25] The excellent agreement with the measured spectra confirms the correctness of the proposed sensing mechanism and the water vapor distribution in the system. The observed shift is similar to that reported previously[13] and thus larger than those observed for all vapor sensing devices.[26–29] The microscope images displayed in Figure 5.3c convey the concomitant color changes which are easily detected by the naked eye. The second effect—the increase in reflectance intensity—is explained by the RI

118

changes upon water uptake: while the RI of the NP layers increases (from 1.84 to 1.96) by filling the textural pores (Figure S 5.14, Supporting Information), the RI of the nanosheet layer decreases (from 1.56 to 1.50) by water intercalation. These opposite trends induce an increase in the RI contrast and, hence, in the reflectivity of the multilayer system at increasing humidity levels (Figure S 5.13, Supporting Information).

Besides sensitivity, another important performance parameter for sensors is the response time, defined as the time which is needed to reach 90% of the stop band shift between 0% and 100% RH. The fast response time of 23 s (Figure S 5.15, Supporting Information), which is superior to most existing humidity sensing devices with a large signal resolution based on a swelling mechanism,[26–29] again underlines the applicability of these platforms for practical humidity sensing. It is important to note in this context that the time response of the reflectance intensity change represented by its time derivative (Figure S 5.15, Supporting Information) is instantaneous and so is the associated optical response: humidity changes cause an immediate stop band shift, which translates into an ultrafast increase or decrease in reflectance intensity at the observed wavelength within seconds (see inset of Figure S 5.15, Supporting Information). Other important sensor properties such as long-term stability and cycling stability were tested by applying a 2-month-old sample in a multiple cycling experiment (shown in Figure S 5.15, Supporting Information). As a result, the sensing performance (stop band shift and response time) was found unchanged as compared to the freshly prepared samples.
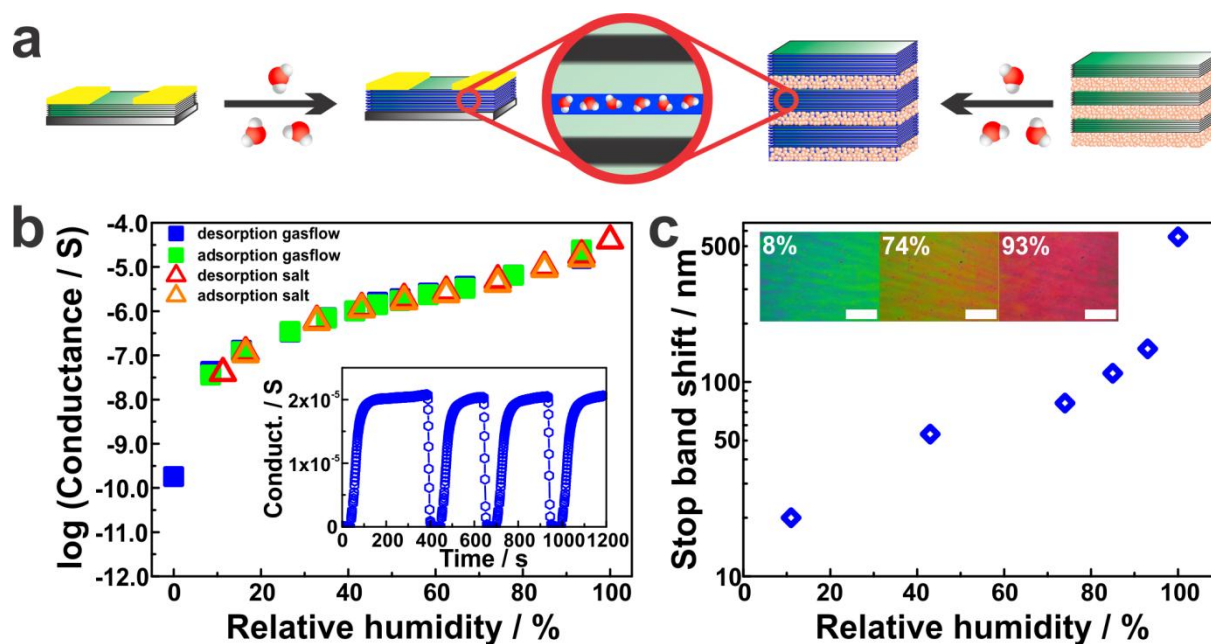
Figure 5.3: Humidity sensing of the $HSbP_2O_8$ nanosheet thin film and the HSb_2PO_8/TiO_2 BS sensor. a) Schematic of the analyte (water) – sensor interaction, shown for the resistive thin film sensor (left) and for the $HSbP_2O_8/TiO_2$ BS (right). The middle depicts a close-up of the swollen nanosheet layer. b) Humidity-dependent conductance behavior of the resistive thin film sensor with a film thickness of ca. 120 nm, shown for two different methods (saturated salt solutions and Ar gas flow), and reversible cycling behavior between 0 and 93.5% RH (inset). c) Influence of humidity on the Bragg peak positions for the $HSbP_2O_8/TiO_2$ BS, and microscope images of the $HSbP_2O_8/TiO_2$ BS taken at different RH values (inset).

The high sensitivity in the low humidity regime renders the resistive thin film device an intriguing candidate for trace water sensing. Thus, we tested its selectivity toward water by analyzing alcohol-water mixtures. The large changes in conductance in response to water enabled us to detect amounts of water as low as 2000 ppm (Figure 5.4a), which are typical concentrations of trace water in polar solvents. Moreover, an exponential relationship between the measured conductance (Figure 5.4a,b inset) and the water content in the range between 2000 and 20 000 ppm is overserved, which is highly desirable for sensing applications. Moreover, the results for trace water detection are reproducible as shown by the insets which report data averaged over three different samples. The antimony phosphate nanosheet sensor hence provides an attractive alternative to the more time consuming traditional methods for water determination such as the Karl–Fischer titration in the high ppm regime, thus pointing toward a new field of application of nanosheet thin film sensors in low-cost and high-throughput trace water analysis.

Besides achieving high sensitivity and selectivity toward one particular analyte (such as water), it is of major interest to optically distinguish between several different analytes. Here, we use a single 1D PC platform as a solution to both requirements—

sensitivity and vapor discrimination capability—as demonstrated in Figure 5.4c,d. To this end, we plot the sensitivity— i.e., the magnitude of the stop band shifts—and saturation times of the sensor for different solvent vapors. To render the data for the different analytes comparable, the saturation times were calculated as the full time which is needed for the stop band to shift from 0% to 100% relative solvent vapor pressure. Similar to the water response described above, the onset of the optical shift is significantly faster than the saturation times implies but still differs for different solvents. As demonstrated in Figure 5.4c, the responses of the investigated solvents differ significantly and, besides water, can be grouped into two types of analytes: nonprotic vapors (nonpolar and polar) and protic vapors.

For water vapor, the sensor shows the largest stop band shift as well as the fastest saturation time, as expected. Nonpolar analytes (n-heptane and toluene) and the polar, nonprotic analyte acetonitrile show similar behavior; their saturation times are rather fast and the stop band shifts small. A qualitatively different response is seen if the BS is exposed to polar and protic analytes, namely alcohols: long response times are accompanied by larger stop band shifts (Table S 5.5, Supporting Information). According to the distinct optical responses (Figures S 5.16 and S 5.17, Supporting Information) as probed by spectroscopy, we derive an interaction mechanism between analyte and sensor (Figure 5.4d), which is corroborated by optical simulations (Figures S 5.16 and S 5.17, dashed lines, Supporting Information). The selectivity is defined by the interplay of several effects such as interlayer hydration and protonation, which determine the chemical environment as well as the molecular size of the analyte and its chemical and dielectric properties.

The nonpolar analytes and aprotic acetonitrile show small stop band shifts (9, 9, and 10 nm for heptanes, toluene, and acetonitrile, respectively) combined with relatively fast saturation times (317, 1936, and 201 s for n-heptane, toluene, and acetonitrile, respectively). These vapors do not wet the polar and protic interlayer space of the nanosheets but only fill the textural pores of the NP layers, as corroborated by optical simulations. As a consequence, the stop band is broadened and its reflectance increases, while the blue edge of the stop band remains constant (Figure S 5.16, Supporting Information). This behavior is due to the increase in RI contrast,[30] caused by the NP layer filling, while the RI and the thickness of the nanosheet layer remains nearly constant, as confirmed by the good agreement between the measured and simulated reflectance spectra (Figure S 5.16, dashed line, and Table S 5.6, Supporting Information). As the stop band shifts are nearly the same for all these analytes, we assume that the dielectric properties only play a minor role regarding the extent of the stop band shift. The saturation time is determined by the interplay of several analyte specific parameters, such as the kinetic diameter and the dipole moment. Although these effects are molecule specific and interrelated, we found the saturation time for the nonpolar and polar,

nonprotic analytes to correlate most clearly with the kinetic diameter of the molecules (Figures S 5.18 and S 5.19, Supporting Information): increasing saturation times correlate with the increasing molecular sizes and the resulting delayed diffusion of toluene (1936 s, 6.1 Å) compared to n-heptane (317 s, 4.3 Å) and acetonitrile (201 s, 3.4 Å).

In contrast, the optical response of the BS to protic solvent vapors—alcohols—signifi cantly differs from that seen for aprotic analytes. Here, rather large stop band shifts were detected across the series methanol (33 nm) < ethanol (58 nm) < 2-propanol (120 nm) < 1-propanol (132 nm) < 2-butanol (150 nm) < 1-butanol (170 nm), with slow response times increasing in the following order: methanol (897 s) < ethanol (3130 s) < 1-propanol (4043 s) < 1-butanol (9320 s) < 2-propanol (12 140 s) < 2-butanol (≈70 000 s). In all cases, larger stop band shifts are observed compared to the stop band broadening for nonprotic vapors (nonpolar vapors and acetonitrile). Contrary to the nonprotic analytes, however, the color shift is dominated by changes in the nanosheet layer thickness upon analyte infiltration, as evidenced by ellipsometric porosimetry and as exemplarily shown for ethanol (Figure S 5.20, Supporting Information): the protic character of the analytes allows for stronger interactions with the protic interlayer space and causes layer swelling upon intercalation. Further, we analyzed the time-dependent stop band changes and could distinguish two different phases during vapor sorption (Figure S 5.21, Supporting Information). Within the first ≈6 s, we observe a fast response expressed by a broadening of the stop band, accompanied by an increase in reflectance, similar to the overall response observed for the nonprotic analytes. We attribute this initial behavior to the filling of the more easily accessible porous NP layers. In a second stage, a slower, analyte-specific response is observed, corresponding to a distinct stop band shift and giving rise to the analyte-specific saturation time, which is due to the intercalation of the analyte into the nanosheet layer. According to this time-dependent behavior, we clearly see that the rate-limiting step is associated with the intercalation of the analytes between the nanosheet layers, while the infiltration of the NP layers is rather fast, as shown also for the nonprotic solvents as well as for water vapor. This interpretation is in line with rather weak interactions of the NP layer and the analytes, which is expected since no surface functionalization was carried out and the diffusion through a mesoporous layer is generally rather fast.[31] To understand the sensing mechanism, which for the alcohols is dominated by the nanosheet layer–analyte interaction, we investigate the influence of several parameters on the stop band shift, such as the analyte's kinetic diameter, dipole moment, dielectric constant, and the RI. These parameters give rise to the analyte's dielectric, optical, and physicochemical properties such as its polarity and ability to form hydrogen bonds. The stop band shift and the saturation times most obviously correlate with the analyte's kinetic diameter, whereby we could confirm by optical simulations that the layer thickness swelling is increasing with increasing molecular sizes (Table S 5.6, Supporting Information). However, empirical correlations can be found

as well for the dielectric constant and the RI of the analytes (Figures S 5.18 and S 5.19, Supporting Information). In summary, although the above parameters are interrelated and most likely their complex interplay determines the stop band shift, it is this interplay that is distinct for each individual analyte, hence giving rise to an analyte-specific response.

It is of note that even constitutional isomers, e.g., those of propanol and butanol, can be distinguished by our nanosheet based photonic nose. The saturation time is increased for 2-propanol compared to 1-propanol by a factor of 3 (12 140 s vs 4043 s), and for 2-butanol compared to 1-butanol by a factor > 7 ($\approx$70 000 s vs 9320 s), whereby the stop band shifts are comparable for both isomers (132 nm vs 120 nm and 170 nm vs 150 nm). Although the kinetic diameters for both isomers are similar, subtle differences in the molecular shape and polarity may have a significant effect on the analyte's interaction with the nanosheet layers and, hence, its diffusivity, which is reflected in the signifycantly different saturation times. Overall, while the degree of swelling caused by the two isomers is similar, a differentiation of both constitutional isomers is clearly possible through the saturation times. Note that the reproducibility of the sensor response was verified by measuring each solvent vapor three times. The error bars in Figure 5.4c are testament to the high reproducibility and the ability of our system to reliably discriminate between different solvent vapors.

In addition, we studied the sensor performance for analyzing multiple component mixtures. For water–ethanol mixtures (Figure S 5.22, Supporting Information) we find that with increasing water amount in the mixture the stop band shifts also increase. With this, the relative amount of water in a water–ethanol mixture can be reliably determined by evaluating the stop band shift, which is as large as 80 nm for water contents between 0% and 90% (Figure S 5.22 b–e, Supporting Information).
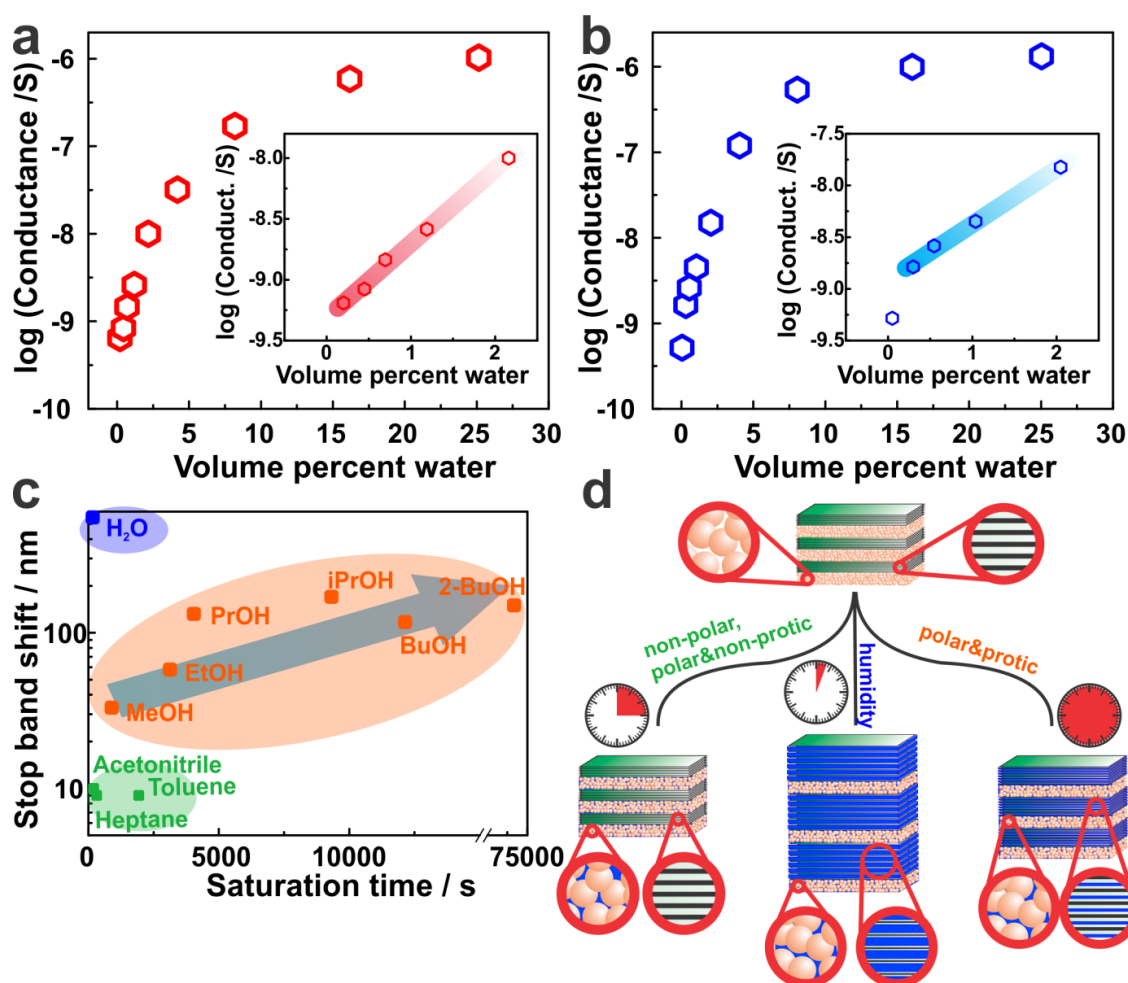
Figure 5.4: Sensitivity and selectivity features of the two devices. Trace water sensing in a) ethanol and b) isopropanol with resistive thin films (100 nm and 120 nm, respectively). In both insets a close-up of the region between 0 and 2.5 volume percent of water is displayed. c) Logarithmic stop band shifts plotted against the response times for the different solvent vapors (BS fabricated at 5000 rpm). d) Schematic showing the interactions of the $HSbP_2O_8$ nanosheet/TiO_2 NP BS with the different types of solvent vapors, which serve as a fingerprint for analyte identification.

In summary, we have introduced a new type of $HSbP_2O_8$ nanosheet-based humidity sensor which can operate in two different modes, i.e., with a resistive and an optical readout. The resistive humidity sensor shows superior sensitivity for water in the low humidity regime, which we utilize for tracking trace amounts of water in alcohol–water mixtures. The photonic humidity sensor, while exhibiting high sensitivity for humidity, shows also an exceptionally high selectivity toward water vapor. Further, this new type of photonic nose, based on swellable nanosheets embedded in a BS, presents a single-component sensor, which can clearly distinguish between water vapor, nonprotic (nonpolar and polar), and protic solvent vapors (alcohols) based on the saturation time and color shift as two independent descriptors. In particular, we find that even chemically similar solvent vapors, such as homologous alcohols, or even isomers, which interact with both the nanosheet and nanoparticle

layers, can be reliably distinguished based on their sorption and diffusion characteristics. This single-component sensor adds to a new generation of nanosheet sensing devices which operate based on an interaction-driven, intercalative sensing mechanism that uniquely exploits both thermodynamic and kinetic properties of the host–guest system, namely dispersive analyte-nanosheet interactions and the diffusion properties of the analyte within the nanosheet layers. The rapidly increasing library of accessible and chemically distinct nanosheet systems bodes well for the development of highly analyte-specifi c colorimetric artificial noses, which opens up new possibilities in environmental monitoring, trace water analysis, and biosensing.

5.5 ACKNOWLEDGEMENTS

5.6 REFERENCES

[1]   L. D. Bonifacio, D. P. Puzzo, S. Breslav, B. M. Willey, A. McGeer, G. A. Ozin, *Adv. Mater.* **2010**, *22*, 1351-1354.

[2]   L. D. Bonifacio, G. A. Ozin, A. C. Arsenault, *Small* **2011**, *7*, 3153-3157.

[3]   Z. Xie, K. Cao, Y. Zhao, L. Bai, H. Gu, H. Xu, Z.-Z. Gu, *Adv. Mater.* **2014**, *26*, 2413-2418.

[4]   T. L. Kelly, A. Garcia Sega, M. J. Sailor, *Nano Lett.* **2011**, *11*, 3169-3173.

[5]   A. Ranft, F. Niekiel, I. Pavlichenko, N. Stock, B. V. Lotsch, *Chem. Mater.* **2015**, *27*, 1961–1970.

[6]   R. A. Potyrailo, H. Ghiradella, A. Vertiatchikh, K. Dovidenko, J. R. Cournoyer, E. Olson, *Nat. Photonics* **2007**, *1*, 123-128.

[7]   Y.-n. Wu, F. Li, W. Zhu, J. Cui, C.-a. Tao, C. Lin, P. M. Hannam, G. Li, *Angew. Chem. Int. Ed.* **2011**, *50*, 12518-12522.

[8]   F. M. Hinterholzinger, A. Ranft, J. M. Feckl, B. Ruhle, T. Bein, B. V. Lotsch, *J. Mater. Chem.* **2012**, *22*, 10356-10362.

[9]   C. Cui, Y. Liu, H. Xu, S. Li, W. Zhang, P. Cui, F. Huo, *Small* **2014**, *10*, 3672-3676.

[10]   L. Li, X. Jiao, D. Chen, B. V. Lotsch, C. Li, *Chem. Mater.* **2015**, *27*, 7601-7609.

[11]   Y.-n. Wu, F. Li, Y. Xu, W. Zhu, C.-a. Tao, J. Cui, G. Li, *Chem. Commun.* **2011**, *47*, 10094-10096.

[12]   Z. Hu, C.-a. Tao, F. Wang, X. Zou, J. Wang, *J. Mater. Chem. C* **2015**, *3*, 211-216.

[13]   K. Szendrei, P. Ganter, O. Sànchez-Sobrado, R. Eger, A. Kuhn, B. V. Lotsch, *Adv. Mater.* **2015**, *27*, 6341-6348.

[14]   S. Deniard-Courant, Y. Piffard, P. Barboux, J. Livage, *Solid State Ionics* **1988**, *27*, 189-194.

[15]   N. Miura, H. Mizuno, N. Yamazoe, *Jpn. J. Appl. Phys., Part 2* **1988**, *27*, L931-L933.

[16]   F. Camerel, J. C. P. Gabriel, P. Batail, P. Panine, P. Davidson, *Langmuir* **2003**, *19*, 10028-10035.

[17]   S. Borini, R. White, D. Wei, M. Astley, S. Haque, E. Spigone, N. Harris, J. Kivioja, T. Ryhänen, *ACS Nano* **2013**, *7*, 11166-11173.

[18]   J. Feng, L. Peng, C. Wu, X. Sun, S. Hu, C. Lin, J. Dai, J. Yang, Y. Xie, *Adv. Mater.* **2012**, *24*, 1969-1974.

[19]   Y. Piffard, S. Oyetola, S. Courant, A. Lachgar, *J. Solid State Chem.* **1985**, *60*, 209-213.

[20]   Y. Piffard, A. Verbaere, S. Oyetola, S. Deniard-Courant, M. Tournoux, *Eur. J. Solid State Inorg. Chem.* **1989**, *26*, 113-127.

[21]   G. K. Prasad, N. Kumada, J. Yamanaka, Y. Yonesaki, T. Takei, N. Kinomura, *J. Colloid Interface Sci.* **2006**, *297*, 654-659.

[22]   J. D. Joannopoulos, S. G. Johnson, J. N. Winn, R. D. Meade, *Photonic crystals: molding the flow of light*, Princeton university press, **2011**.

[23]   P. W. Winston, D. H. Bates, *Ecology* **1960**, *41*, 232-237.

[24]   L. Greenspan, *J. Res. Nat. Bur. Stand.* **1977**, *81A*, 89-96.

[25]   M. C. Fuertes, S. Colodrero, G. Lozano, A. R. González-Elipe, D. Grosso, C. Boissière, C. Sánchez, G. J. d. A. A. Soler-Illia, H. Míguez, *J. Phys. Chem. C* **2008**, *112*, 3157-3163.

[26]   E. Tian, J. Wang, Y. Zheng, Y. Song, L. Jiang, D. Zhu, *J. Mater. Chem.* **2008**, *18*, 1116-1122.

[27]   J. H. Kim, J. H. Moon, S.-Y. Lee, J. Park, *Appl. Phys. Lett.* **2010**, *97*, 103701.

[28]   Z. Wang, J. Zhang, J. Xie, C. Li, Y. Li, S. Liang, Z. Tian, T. Wang, H. Zhang, H. Li, W. Xu, B. Yang, *Adv. Funct. Mater.* **2010**, *20*, 3784-3790.

[29]   R. Xuan, Q. Wu, Y. Yin, J. Ge, *J. Mater. Chem.* **2011**, *21*, 3672-3676.

[30]   L. D. Bonifacio, B. V. Lotsch, D. P. Puzzo, F. Scotognella, G. A. Ozin, *Adv. Mater.* **2009**, *21*, 1641-1646.

[31]   I. Pavlichenko, E. Broda, Y. Fukuda, K. Szendrei, A. K. Hatz, G. Scarpa, P. Lugli, C. Brauchle, B. V. Lotsch, *Mater. Horiz.* **2015**, *2*, 299-308.

[32]   The two weak reflections marked with vertical scatters (Figure 5.1c) are stacking reflections and result from non-complete preferred sample orientation. These peaks were fitted with a single peak phase function

6.

Optimizing the Optical Properties: Lithium Tin Sulfide Nanosheet Based 1D Photonic Crystals

6.1 SUMMARY
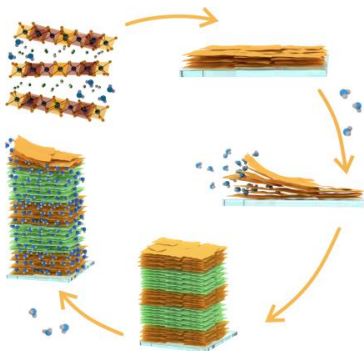
The development of photonic devices relies on the development of novel solution-processable optical functional materials. In order to minimize the number of layers in the 1DPC and, consequently, the production costs, and to optimize the optical properties, such as the reflectance of 1DPC-based sensors – the development of novel high refractive index materials, which are stable, earth-abundant and non-toxic, is in high demand.

This project presents a layered 2D material – lithium tin sulfide (LTS) with an ultrahigh refractive index of $n = 2.50$ – as a new optical material, which at the same time is amenable to solution processing *via* exfoliation. The RI of this material even exceeds that of the commonly used high RI material in 1DPCs, TiO_2 $n = 1.70$-2.12, for porous layers), thus setting the stage for new applications in photonic crystal devices.

First, we demonstrated the exceptional film forming capability and the unique optical properties of this new ultrahigh RI material, LTS nanosheets, and showed that thin films as well as 1DPCs fabricated using different optical contrast materials are highly responsive to humidity changes by intercalating ambient water molecules between the 2D sulfide layers. In order to demonstrate the diversity of the possible applications of this novel optical material, we fabricated three different 1DPC systems: LTS nanosheets combined with TiO_2 NPs, with SiO_2 NPs, and with $H_3Sb_3P_2O_{14}$ nanosheets. To our knowledge, the TiO_2 NPs / LTS nanosheet based system is the first hybrid (consisting of two different materials) 1DPC in which TiO_2 NPs form, the low RI material. These architectures are interesting in terms of novel light managing devices. In addition, the combination of two high RI materials facilitates the creation of 1DPCs with a stopband in the IR range and allows for

the reduction of the device thickness by as much as 60-65%, with obvious benefits for production costs. Secondly, we introduced the highest RI contrast presented so far in the literature, to the best of our knowledge, by combining SiO_2 nanoparticles as a commonly used low RI material with LTS nanosheets as the high RI material. These results are promising not only in terms of resource efficiency and cost reduction, but also they directly entail relevant optical properties such as an extremely broad bandwidth of the photonic stopband. Finally, we demonstrated the development of highly sensitive humidity sensors by combining two nanosheet materials with individual ultrahigh swelling capabilities – LTS nanosheets and $H_3Sb_3P_2O_{14}$ nanosheets – in a single 1DPC, rendering this platform the first all-nanosheet 1DPC containing of two different simuli-responsive 2D materials. This combination gives rise to ultralarge signal changes in response to changes in relative humidity and opens the door to a new generation of high-performance humidity sensors.

Contributions: Katalin Szendrei-Temesi optimized the LTS nanosheet based thin film fabrication procedure, characterized the thin films, designed and fabricated the 1DPCs, performed optical measurements and the theoretical calculations, wrote the manuscript and edited the figures. Olalla Sánchez-Sobrado fabricated the first LTS nanosheet based thin films, proposed the idea of the NP-based (SiO_2 and TiO_2) 1DPCs, fabricated the initial Bragg stacks, helped writing the manuscript and discussed the results. Sophia B. Betzler performed the TEM-EELS measurements, assisted with writing the manuscript and discussed the results. Katharina M. Durner fabricated the multilayered structures and performed some of the optical measurements. Tanja Holzmann designed some 3D images for the figures, synthesized for the first time the LTS nanosheets, optimized the exfoliation and discussed the results.

This project was highlighted as a back cover in the journal *Advanced Functional Materials* and the cover image was designed by Katalin Szendrei-Temesi.

6.2   LITHIUM TIN SULFIDE – A HIGH-REFRACTIVE-INDEX 2D MATERIAL FOR HUMIDITY-RESPONSIVE PHOTONIC CRYSTALS

Katalin Szendrei-Temesi, Olalla Sanchez-Sobrado, Sophia Betzler, Katharina M. Durner, Tanja Holzmann, Bettina V. Lotsch

6.3   ABSTRACT

Extending the portfolio of novel stimuli-responsive, high-refractive-index (RI) materials besides titania is key to improve the optical quality and sensing performance of existing photonic devices. Herein, lithium tin sulfide (LTS) nanosheets are introduced as a novel solution processable ultrahigh RI material (n = 2.50), which can be casted into homogeneous thin films using wet-chemical deposition methods. Owing to its 2D morphology, thin films of LTS nanosheets are able to swell in response to changes of relative humidity. Integration of LTS nanosheets into Bragg stacks (BSs) based on TiO_2, SiO_2, nanoparticles or $H_3Sb_3P_2O_{14}$ nanosheets affords multilayer systems with high optical quality at an extremely low device thickness of below 1 μm. Owing to the ultrahigh RI of LTS nanosheets and the high transparency of the thin films, BSs based on porous titania as the low-RI material are realized for the first time, showing potential application in light-managing devices. Moreover, the highest RI contrast ever realized in BSs based on SiO_2 and LTS nanosheets is reported. Finally, exceptional swelling capability of an all-nanosheet BS based on LTS and $H_3Sb_3P_2O_{14}$ nanosheets is demonstrated, which bodes well for a new generation of humidity sensors with extremely high sensitivity.

6.4   INTRODUCTION

New materials solutions are key for the development of novel sensing platforms with improved optical properties and sensing performance compared to existing device concepts. One of the main challenges in the development of photonic sensors is to identify high-refractive-index (RI) materials which can easily be processed by wet-chemistry techniques and can be integrated into existing device architectures. In addition, for an effective application in sensor technology, these materials need to be stimuli responsive, which is typically achieved via inherent structural or textural porosity or swelling behavior in the presence of analytes. The simplest photonic nanostructures used for optical sensing applications, which are capable of translating external stimuli into an optical signal by

structural color changes, are 1D photonic crystals (1D PCs), also referred to as Bragg stacks (BSs).[1,2] BSs are composed of a high- and a low-RI material, which are stacked in an alternating fashion. The periodic modulation of the RIs creates a photonic stopband: a forbidden energy range for photons that are not allowed to propagate in the PC along certain directions in reciprocal space.[1] The photonic stopband defines the structural color and is dependent on the layer thickness *d* and the RI *n* of the constituent layers, given by the optical thickness $\tau = n \cdot d$.[3,4] By this means, dynamic variations in the layer thickness or in the RI induced by an analyte can be translated into changes in the stopband position and, hence, the structural color of the sensor.[5–12] The reflectance intensity—the intensity of the photonic stopband—is mostly defined by the RI contrast, i.e., the RI difference between the two materials.[2,3] Consequently, a high RI contrast results in devices with high reflectance intensities and better optical qualities featuring a lower overall device thickness of well below 1 µm.[13]

To create BSs with an ultrahigh RI contrast, high-RI materials are needed which preferably can be deposited via straightforward wet-chemical methods such as spin- or dip-coating. The most prominent candidate in the literature used as a high-RI material in BSs is titanium dioxide (TiO_2), which is applied either as a dense sol or as nanoparticles, forming a dense or a highly porous thin film, respectively.[4,14,15] Although sol–gel-based dense TiO_2 films or titania-based composite films have a maximum RI of around n (dense) $= 2.12$,[16–19] and n (composite) $= 2.38$,[20] respectively, volatile analytes cannot efficiently infiltrate the dense sol film, leading to significantly reduced or even inhibited vapor responsiveness.[16,17] On the contrary, nanoparticulate TiO_2 forms a highly porous thin film through textural porosity, and mesopore filling can be monitored by optical isotherms as a function of the relative pressure of the analyte.[7,16,21] Such porous TiO_2 layers exhibit an effective RI of $n = 1.70$–2.00, depending on the degree of porosity.[5,14,15] Combined with SiO_2 nanoparticles as the classical low-RI material, at least 10–12 layers are required to reach reflectance intensities of 90%, resulting in rather thick devices of several micrometers. A strategy to reduce the layer numbers and, hence, the device thickness, is the combination of highly porous SiO_2 with dense TiO_2 films.[17–19] Although a high RI contrast and good optical device quality were achieved, the sensitivity toward vapors is severely reduced due to the limited textural porosity of the titania layer. Another approach to increase the RI contrast is to identify new porous materials with a similar or even higher RI compared to TiO_2, although current alternatives such as WO_3 sol ($n = 2.03$),[22] ZrO_2 nanoparticles ($n = 1.70$),[23,24] Ta_2O_5 [25] nanoparticles ($n = 1.80$), undoped or antimony-doped SnO_2 films (n (undoped) $= 1.83$, n (3% Sbdoped) $= 2.34$)[3,26] all feature lower RIs compared to dense titania or suffer from low transparency in the visible range. Thus, the highest RI contrast BSs reported so far combine highly

porous silica layers stacked with dense titania layers, exhibiting an RI contrast of $\Delta n = 0.83$,[17] $\Delta n = 0.84$,[19] and $\Delta n = 0.89$.[18] To further increase the RI contrast is an important objective when aiming at high-quality optical devices, such as solar mirrors,[27] optical fibers,[28] or other light-managing devices. All titania-based photonic structures employed for sensing feature textural porosity in order to facilitate analyte diffusion. However, to achieve high sensitivity toward analytes, swelling materials are preferred over porous materials as they cause larger stopband shifts via changes in their optical thickness.[6,12,29,30] Thus, the combination of two different swelling materials in one BS[31] is a promising strategy to induce ultralarge stopband shifts. To implement this strategy, the development of novel functional nanomaterials featuring both high swelling capability and high RI is one of the key challenges to be addressed.

Here, we present a new material platform for addressing both challenges: (i) we introduce a new solution processable high-RI material—lithium tin sulfide (LTS) nanosheets[32,33] ($n = 2.50$, 0% relative humidity (RH), 633 nm)—which forms high-quality BSs with TiO_2 as the low-RI material and produces ultrahigh RI contrast in PCs when combined with a low-RI material such as silica; and (ii) we demonstrate full-spectral color changes of an all-nanosheet BS composed of LTS and antimony phosphate ($H_3Sb_3P_2O_{14}$) nanosheets. Taking advantage of the swelling capability of both 2D materials in the presence of water vapor, such stimuli-responsive all-nanosheet BSs are promising candidates for highly sensitive optical humidity sensors with good optical quality. The combination of two robust, swellable nanosheet materials ensures both high stability, especially compared to flexible

organic materials, and presents a generic material platform that can be chemically tailored for diverse applications in chemooptical sensing. In addition, the high RI contrast imparted by the inorganic nanosheets, combined with their high sensitivity to humidity, ensures superior optical quality combined with large signal changes, which makes LTS-based sensors competitive or even superior to other state-of-the-art optical sensors.[34,35]

6.5 RESULTS AND DISCUSSION

Material synthesis

Layered bulk lithium tin sulfide ($Li_2Sn_2S_5$) was synthesized by a classical solid-state reaction as previously described.[32] The successful synthesis was confirmed by powder X-ray diffraction (XRD) analysis, and the elemental composition was validated by energy-dispersive X-ray (EDX) and inductively coupled plasma (ICP) analysis, as shown in Figure S 6.1 and Tables S 6.1 and S 6.2 in the Supporting Information. The crystal structure consists of covalent layers of edge sharing SnS_6 octahedra, whereby the Sn atoms are partially substituted by Li as depicted in Figure 6.1a.[33] The

charge-compensating Li+ ions are located in the interlayer gallery and allow for facile intercalation of water molecules between the covalent Sn(Li)S layers (Figure 6.2b). Spontaneous exfoliation in aqueous solution results in a stable colloidal suspension containing single nanosheets (Figure 6.1c) as demonstrated in the literature.[32] Upon drying, the stable suspensions of LTS nanosheets form thin films by random restacking of the single nanosheets in a turbostratically disordered fashion, as confirmed by the selected area electron diffraction (SAED) patterns (Figure S 6.2, Supporting Information). Motivated by this film forming capability, spin-coating was explored to synthesize homogeneous thin films of exfoliated LTS nanosheets with a widely tunable thickness (see Figure S 6.3 in the Supporting Information). The colloidal concentration was optimized to 60 mg mL^{-1}, which was sufficient to create homogeneous thin films with a thickness of around 20–40 nm (at 3000–5000 rpm spin-coating speeds). The layer thickness can be fine-tuned by varying the number of the deposition steps and the spin-coating speed as further described in the Supporting Information.
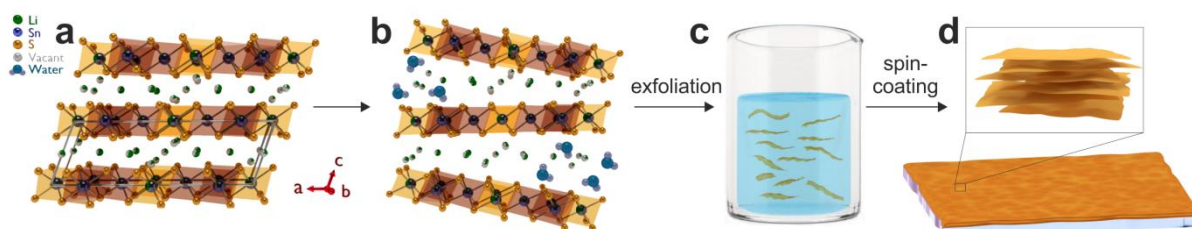
Figure 6.1: Thin film fabrication from colloidal suspensions of exfoliated LTS nanosheets. a) Crystal structure of layered bulk $Li_2Sn_2S_5$; b) intercalation of water molecules into the interlayer space of $Li_2Sn_2S_5$; c) spontaneous exfoliation of $Li_2Sn_2S_5$ into single layered nanosheets in water; d) thin film fabrication starting from the stable colloidal suspension of single layered LTS nanosheets *via* spin-coating.

Optical Properties of LTS Nanosheets

In the first step, optical characterization of the LTS thin films was carried out as a basis for the optical design and rational tuning of the target photonic nanostructure. To this end, we studied homogeneous LTS nanosheet thin films via spectroscopic ellipsometry under ambient conditions (30% RH) and with varying RH. In Figure 6.2a, the optical properties at ambient conditions (at 30% RH), the wavelength-dependent RI (*n*) and the extinction coefficient (*k*) of a 40 nm film are shown.

As demonstrated in Figure 6.2a, the RI shows exceptionally high values, varying from $n = 2.65$ (at 350 nm, 30% RH) down to $n = 2.20$ (at 950 nm, 30% RH) with increasing wavelengths. The extinction coefficient was fitted to 0.30 at 400 nm, but decreases strongly and is below 0.10 in the range >450 nm. This small value indicates that thin films within this thickness range are essentially transparent, which is an important prerequisite for applying LTS as optical material in PCs. To test the response of LTS nanosheet films to humidity changes, the change of the optical properties with

gradually increasing RH was monitored. According to Figure 6.2b, the layer thickness more than doubles (from 30 to 70 nm) throughout the entire humidity range (0–100% RH). As a second effect, the RI (at 633 nm) decreases with increasing humidity from $n = 2.50$ (0% RH) to $n = 1.75$ (100% RH), shown in Figure 6.2c. These two effects and the full reversibility as visible from the isotherms (Figure 6.2b,c) point to the facile intercalation of ambient water molecules between the nanosheets and subsequent swelling of the LTS film as shown in Figure 6.2d. While the effective layer thickness d increases as water intercalates between the nanosheets, the effective RI decreases through the increasing volume fraction of water ($n = 1.33$) contained in the pure nanosheets ($n = 2.50$, at 633 nm), thus leading to a significant response of the optical thickness ($\tau = n \cdot d$) to RH variations.
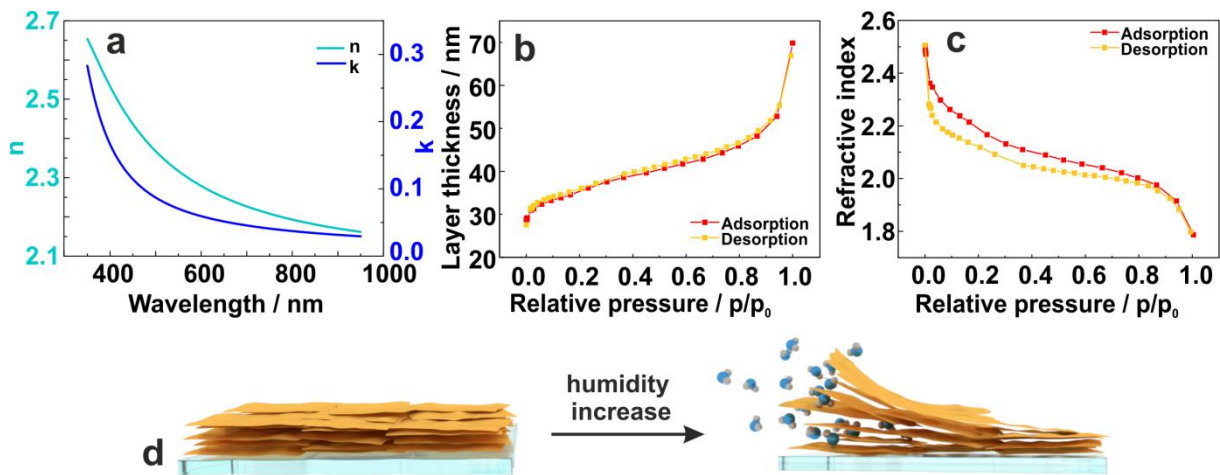
Figure 6.2: Optical properties of the fabricated LTS thin films. a) Wavelength-dependent n and k values for a LTS nanosheet film with a thickness of about 40 nm, measured under ambient conditions (30% RH); b) layer thickness changes of a LTS film with changing partial pressure of water vapor, measured by ellipsometric porosimetry; c) RI changes with changing water vapor pressure in the atmosphere, measured by ellipsometric porosimetry; d) scheme of the RH dependent behavior of the LTS nanosheet thin films, showing the intercalation of ambient water molecules between the single nanosheets.

The remarkably high RI of the LTS nanosheets ($n = 2.50$) at 633 nm and 0% RH is significantly higher than the RI of dense ($n = 2.12$) or porous ($n = 1.70$–2.00, depending on the porosity) TiO_2 thin films. So far, TiO_2 with varying porosity has been most commonly used as the high-RI material in hierarchical photonic devices for vapor sensing.[8,10,21,36,37] However, due to only limited effective RI changes induced by the adsorption of analytes in the textural pores, only slight stopband shifts and, hence, generally low analyte sensitivity are observed.[17,21,38] In contrast, LTS nanosheet films show an even larger RI and significantly more pronounced swelling behavior, which is expected to give rise to greatly improved sensitivity in sensing applications. To test this hypothesis and demonstrate the impact of the ultrahigh RI LTS material on the optical properties of the resulting PCs, we combine LTS nanosheet films with three different materials, namely TiO_2 nanoparticles, SiO_2 nanoparticles

(Figure S 6.4, Supporting Information), and $H_3Sb_3P_2O_{14}$ nanosheets.[11,39] We then characterize the resulting BSs regarding their structural and optical properties and investigate their behavior in terms of humidity sensing.

TiO$_2$ Nanoparticles and LTS Nanosheets

The first photonic architecture we present is a BS built from LTS nanosheets and TiO$_2$ nanoparticles (Figure 6.3a). Owing to the high RI of LTS, this is the first reported multilayer structure where TiO$_2$ the lower RI. The scanning electron microscope (SEM) cross-sectional images displayed in Figure 6.3b,c show that the stacking of LTS nanosheets and TiO$_2$ nanoparticles in a periodic fashion was successful, leading to a highly homogeneous multilayer structure across large lateral dimensions on the micrometer range. The material contrast is clearly visible in the backscattered electron image (Figure 6.3b), where the LTS nanosheet layers appear brighter due to their higher atomic number (Z). The secondary electron images show two different morphologies, i.e., the sheet-like morphology for LTS and the particle nature of the TiO$_2$ nanoparticles (Figure 6.3c). The high stacking quality observed by SEM directly translates into excellent optical properties such as pronounced structural colors across large sample areas (Figure 6.3d) and high reflectance intensities (Figure 6.3e). The widely tunable structural color is demonstrated in Figure 6.3d-e, whereby the different hues were accessed by applying different rotation speeds in the fabrication procedure via spin-coating, resulting in different layer thicknesses. The reflectance spectra in Figure 6.3e correspond to the devices shown in the photograph in Figure 6.3d and are composed of only seven layers on a glass substrate (LTS serving as the bottom and the top layer). This means that the RI contrast of LTS and TiO$_2$ is sufficiently high ($\Delta n = 0.40$ at 30% RH) to reach reflectance intensities over 90%. Simulations based on the transfer-matrix method[21] (Figure 6.3e, dashed spectra) confirm excellent agreement between the measured and the calculated spectra (for details, see Table S 6.4 in the Supporting Information). Figure 6.3f depicts the calculated spectral and spatial field distribution within the BS (for the sample showing the blue structural color fabricated at 4000 rpm in Figure 6.3d), which is inhomogeneous throughout the photonic structure. We observe a field enhancement at the red stopband edge (600 nm), which is located in the LTS layers, and enhanced field intensities in the layers at the blue band edge region (400 nm) located in the TiO$_2$ layers. This again confirms that in this BS, TiO$_2$ serves as the low-RI material ($n = 1.80$ at 633 nm) for the first time, while the LTS nanosheets serve as the high-RI material ($n = 2.20$ at 30% RH, 633 nm). Maximizing the field intensities where TiO$_2$ has its maximum absorbance (around 370 nm) can be potentially useful for "slow photon" applications,[40,41] while the combination of two high-RI materials allows for the creation of significantly thinner photonic structures (65–70% device thickness reduction compared to a SiO$_2$/LTS nanosheet BS containing only one high-RI material) and, hence, lower productions costs. Along similar lines, stopbands located in

the IR range are more easily accessible, which may be useful, e.g., for applications in IR radiation shielding.
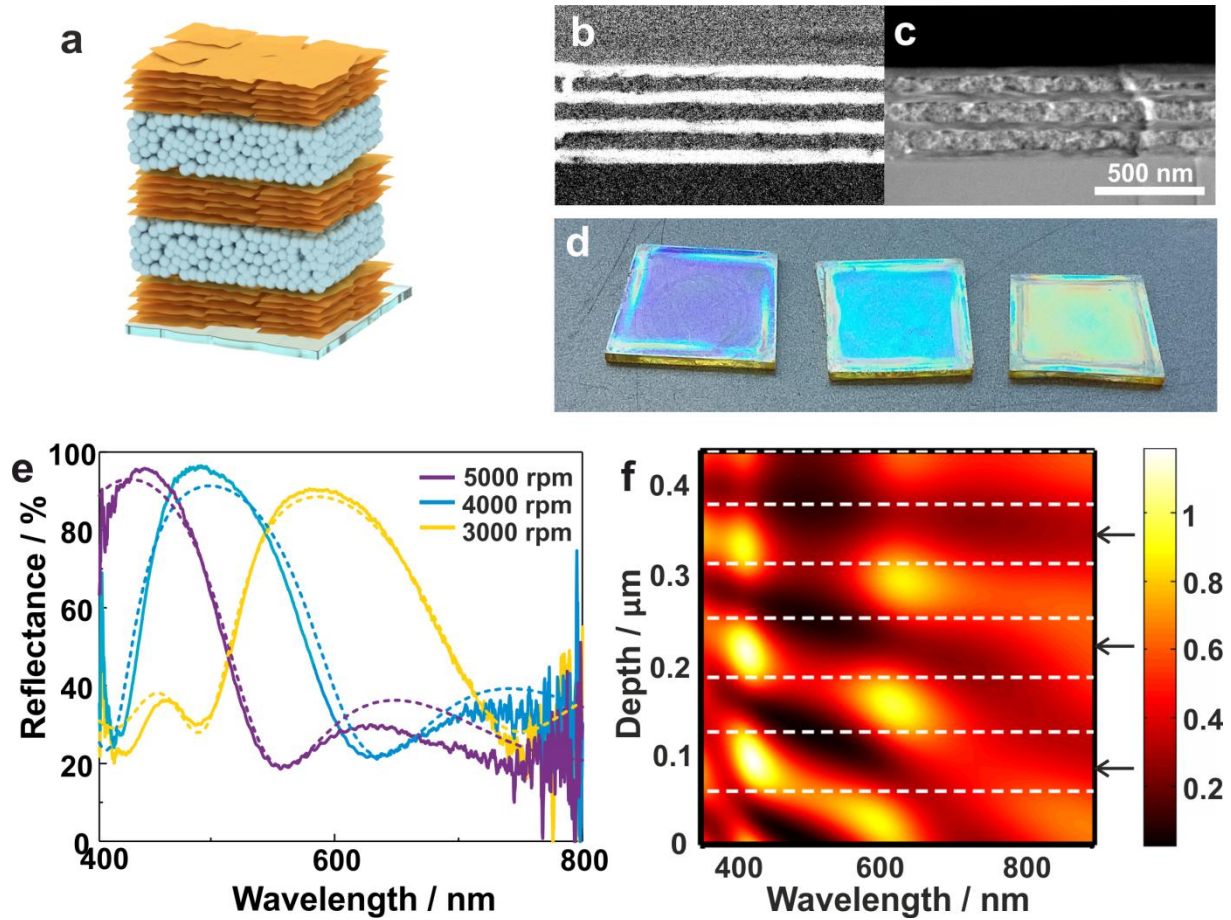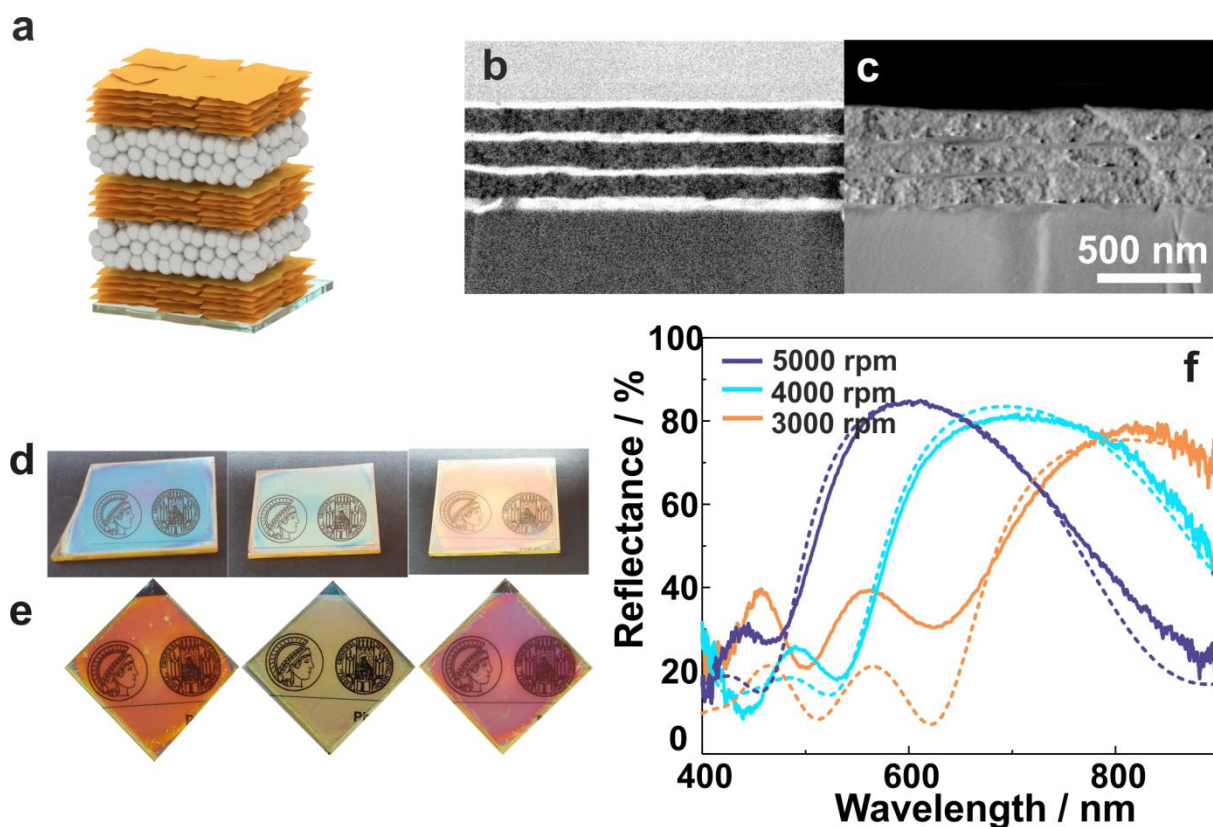

Figure 6.3: Optical properties of the TiO$_2$ nanoparticle / LTS nanosheet Bragg stacks. a) Scheme of the hybrid nanoparticle / LTS nanosheet Bragg stack; b) back-scattered and c) secondary electron SEM cross section images of the fabricated samples, showing the homogenous layered structure; d) photographs of three samples consisting of seven layers on a glass substrate at ambient conditions, showing different structural colors caused by different layer thicknesses (the samples were spin-coated at 3000 rpm, 4000 rpm and 5000 rpm rotation speed from left to right). The sample dimensions are 1.5x1.5 cm². e) Reflectance spectra (solid lines) and simulated spectra (dashed lines, Table S 6.4) of the three samples fabricated at different spin-coating speeds: 3000 rpm, 4000 rpm and 5000 rpm; f) spatial and spectral field distribution within the sample fabricated at 4000 rpm rotation speed, whereby the structure is shown in reverse, i.e. the substrate is located at 0.45 µm depth and the light source at 0 µm depth. The TiO$_2$ layers are indicated with arrows.

SiO$_2$ Nanoparticle and LTS Nanosheet Based Bragg Stacks

Motivated by the fact that LTS nanosheets are able to form high quality BSs with TiO$_2$, we combined this ultrahigh RI material with SiO$_2$ nanoparticles ($n = 1.30$, Figure 6.4a; Figure S 6.4, Supporting Information), which is the most commonly used low-RI material in PC research. The secondary electron and backscattered SEM images (Figure 6.4b,c) indicate homogeneous layering without

intermixing and confirm the textural porosity of the nanoparticle layers, which provides accessibility to analytes. The well-defined photonic stopbands of different five-layer systems on glass substrates, along with their pronounced structural colors over a large area, viewed in reflectance, are shown in Figure 6.4d,f. The photograph row in Figure 6.4e was taken in transmission mode. The good visibility of the emblems below the glass substrate is a testament to the high transparency of the samples, while the structural colors are still pronounced and complementary to the reflection colors shown in Figure 6.4d. According to Figure 6.4f, the reflectance spectra of the fabricated samples (Figure 6.4d,e) show high reflectance values of over 80% (for only five layers) and a bright Bragg peak with a peak width of 350 nm. This hybrid multilayer system has the highest RI contrast ($\Delta n = 0.90$ at 30% RH, 633 nm) that was reported in any BS to date (Figure 6.4a). The RI contrast value is even higher at lower RH values ($\Delta n = 1.20$ at 0% RH, 633 nm), as the RI of the LTS nanosheets strongly depends on the ambient water amount. So far, the highest RI contrasts found in BSs in the literature reach maximum values of $\Delta n = 0.83$,[17] $\Delta n = 0.84$,[19] and $\Delta n = 0.89$,[18] well below the RI contrast of our system. Comparing the experimental reflectance spectra with the simulated spectra (Figure 6.4f dashed lines, Table S 6.5, Supporting Information) shows good agreement and confirms that the broad stopband arises from the superior RI contrast,[1] rather than from defects or other inhomogeneities. Increasing the number of layers above five resulted in more defects and more pronounced scattering, which is indicated by the higher reflectance minima (Figure S 6.5, Supporting Information). Hence, for further studies, we use samples with five layers, as they already have a sufficiently high optical quality.

Figure 6.4: Optical properties of the SiO_2 nanoparticle / LTS nanosheet Bragg stacks. a) Schematic picture of the hybrid nanoparticle-nanosheet BS; b) back-scattered and c) secondary electron SEM cross section image of a SiO_2 nanoparticle / LTS nanosheet BS containing seven layers; d) photographs showing highly reflective samples, each based on five layers, with different structural colors caused by different layer thicknesses; e) photographs taken in transmission mode demonstrate the high transparency of the samples. f) Reflectance spectra (solid lines) and simulated spectra (dashed lines) of the SiO_2 nanoparticles / LTS nanosheet BS containing five layers on a glass substrate. The samples were fabricated at different rotation speeds: 5000 rpm, 4000 rpm and 3000 rpm, respectively.

Next, we tested the humidity sensitivity of the SiO_2/LTS hybrid system, as the swelling behavior of the LTS layers, the high porosity of the SiO_2 layers, and the strong humidity-dependent RI variations indicate that this system is highly responsive to humidity variations. We observe two main effects, generated by RH changes (Figure 6.5a): (i) a stopband shift of 120 nm in the humidity range of 11–93% RH and (ii) continuously decreasing reflectance intensities from 80% to 55% in this humidity range. Finally, at 100% RH, the stopband completely vanishes, i.e., the reflectance intensity is minimized (Figure 6.5a, darkest red spectrum). As shown by our calculations (Figure 6.5a, dashed line; Table S 6.7, Supporting Information), this is due to the fact that the RIs of the two layer materials gradually become equal (11–93% RH) due to the water uptake, and at 100% RH, the RI contrast completely vanishes, turning the device transparent. The large stopband shifts and the transparency switching exhibit fast response (7.0 s) and recovery times (1.1 s) (Figure S 6.11,

Supporting Information), and are completely reversible for at least 15 cycles (Figure S 6.9, Supporting Information). Upon RH decrease, the structural color and the photonic stopband reappear (Figure S 6.12, Supporting Information). With this, we present the largest RI contrast in a BS, which is tunable and switchable due to environmental changes, i.e., changes in the humidity level.
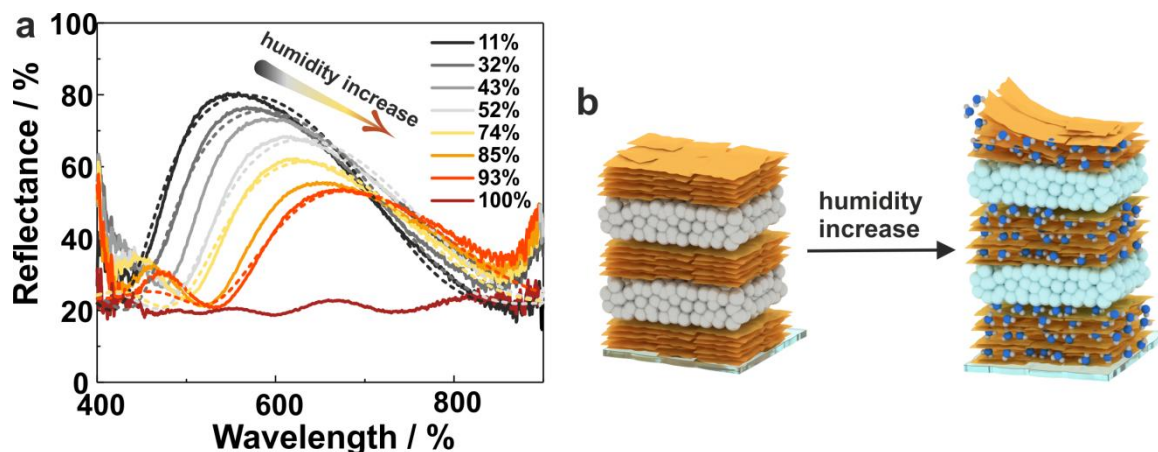

Figure 6.5: Humidity sensing properties of the SiO_2 nanoparticles / LTS nanosheet BSs. a) Measured (solid lines) and calculated (dashed lines) reflectance spectra of the SiO_2 nanoparticle / LTS nanosheet BS with changing RH; b) proposed sensing mechanism based on the intercalation of water into the interlayer space of the LTS nanosheets and sorption of water in the textural pores of the SiO_2 nanoparticles.

$H_3Sb_3P_2O_{14}$ Nanosheet and LTS Nanosheet-Based Bragg Stacks

To probe whether we can further increase the BS's sensitivity to humidity, we combine humidity-responsive LTS nanosheet films with films based on $H_3Sb_3P_2O_{14}$ nanosheets,[11,39,42,43] which have previously been reported to exhibit the largest response to ambient humidity ever recorded in a BS. Combining these two functional dielectrics into an all-swellable photonic architecture is expected to further increase the sensitivity of humidity as compared to existing devices.[11,12,44–46] The structure of the all-nanosheet 1D PCs, as depicted in Figure 6.6a, is validated by the SEM cross-sectional image (Figure 6.6b) and shows the layered morphology with uniform layer stacking, low level of defects, and lateral homogeneity of the BS on the micrometer scale. However, since both materials exhibit a sheet-like morphology and similar atomic numbers (*Z*), their individual layer thicknesses cannot be determined by SEM. Likewise, EDX analysis cannot be used either as the signals of Sn and Sb appear at almost identical energies, prohibiting their distinction. Therefore, we applied electron energy loss spectroscopy (EELS) analysis in the transmission electron microscope (TEM) to differentiate the two materials at high spatial resolution. $H_3Sb_3P_2O_{14}$ nanosheets show a dominant feature at 531.5 eV, which can be attributed to a superposition of the Sb–$M_{4,5}$ and the O–K edge. The EEL spectrum of LTS nanosheets exhibits the Sn–$M_{4,5}$ edge with an onset at 507.5 eV and a maximum at 536 eV (Figure S 6.6, Supporting Information). Additionally, for LTS, we observe the S–$L_{2,3}$ edge with an onset

at 166 eV. For both materials, an additional feature is visible at 686.5 eV in the spectra. This minor feature cannot be identified unequivocally and most likely originates from a contamination introduced by the focused ion beam (FIB) sample preparation. To extract the spatial distribution of the nanosheets across the BS (TEM cross–sectional image shown in Figure 6.6c), the local EELS edge intensities were determined, and the resulting elemental distribution maps are depicted in Figure 6.6d–g. For experimental details, see the experimental section and Figures S 6.6 and S 6.7 in the Supporting Information. The EELS maps (Figure 6.6d,e) clearly confirm the layered morphology composed of alternating $H_3Sb_3P_2O_{14}$ and LTS layers with thicknesses of 50 ± 8 and 41 ± 8 nm, respectively. This alternating arrangement of the two different nanosheet materials is also confirmed by the mapping of the $S–L_{2,3}$ edge (Figure S 6.7, Supporting Information), and is only found in the LTS nanosheet layer, yielding a thickness of 49 nm, which corresponds well to the layer thicknesses determined from the Sn edges. Additionally, the layer thicknesses were also confirmed by spectroscopic ellipsometry measurements at ambient conditions (Figure S 6.8 and Table S 6.3, Supporting Information). Hereby, the experimental data were fitted with a periodic model including three double layers on a silicon substrate. The layer thicknesses and the RIs were fitted to $d = 44$ nm and $n = 2.50$ (at 633 nm) for LTS and $d = 62$ nm and $n = 1.56$ (at 633 nm) for $H_3Sb_3P_2O_{14}$ at ambient RH, which is in excellent agreement with the EELS element mapping data. According to Figure 6.6h, the homogeneously stacked layered structure is also confirmed by the high reflectance intensities of the Bragg peak, created by the alternating arrangement of seven layers of LTS and $H_3Sb_3P_2O_{14}$ nanosheets on a glass substrate, terminated by a top layer of LTS nanosheets. By changing the spin-coating speeds and the layer thicknesses within the stack, different structural colors are accessible all over the visible spectral range (Figure 6.6h,i). Simulations of the reflectance spectra (Figure 6.6h, dashed lines; Table S 6.6, Supporting Information) based on the RIs extracted by ellipsometric porosimetry confirm the layer thicknesses determined by the EELS mapping. As shown in Figure 6.6h, seven alternating layers of the two nanosheet materials with an RI contrast of $\Delta n = 0.65$ are sufficient to obtain reflectance intensities of 90%. This allows for the fabrication of ultrathin photonic structures with good optical quality, as only a few layers are needed to reach high reflectance values.
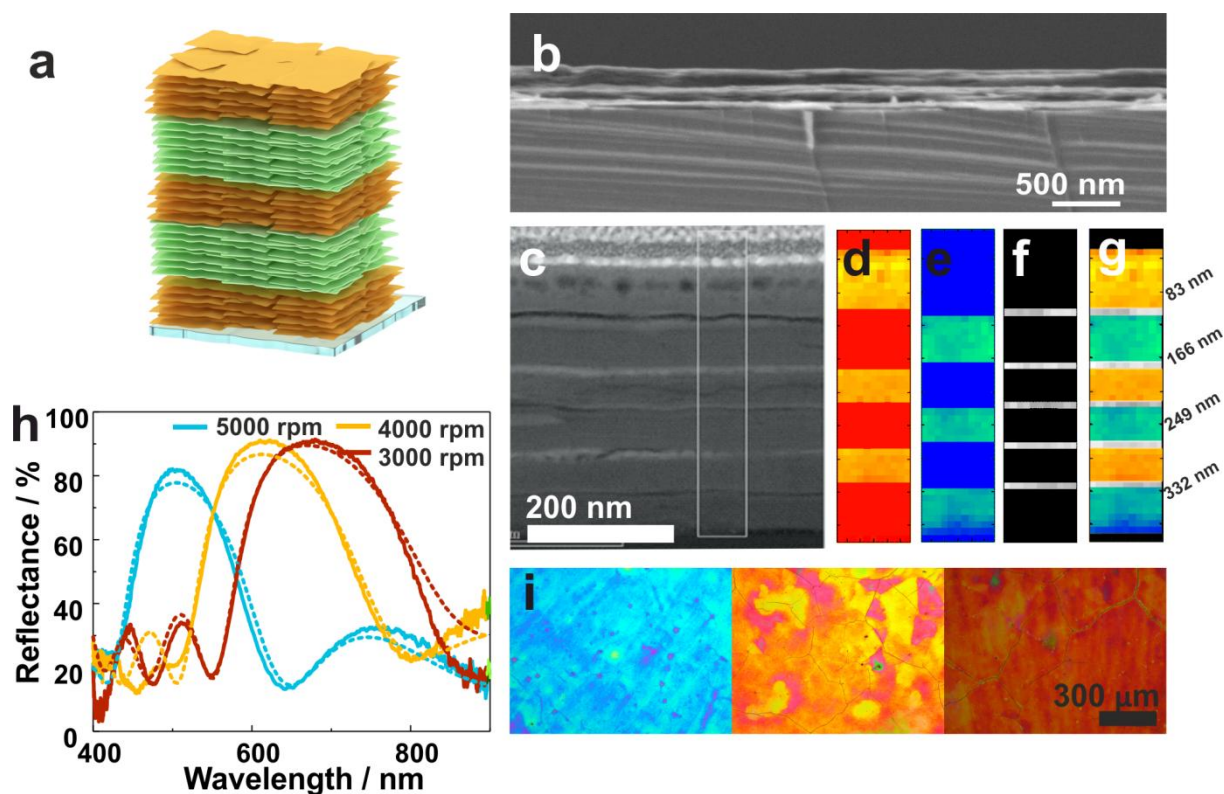
Figure 6.6: Architecture and structural properties of an all-nanosheet BS consisting of $H_3Sb_3P_2O_{14}$ nanosheets and LTS nanosheets. a) Schematic picture of the all-nanosheet BS deposited by spin-coating of the colloidal nanosheet suspensions; b) secondary electron SEM cross section image of the all-nanosheet BS showing the layered morphology across the entire sample and lateral homogeneity on the micron scale; c) TEM cross section image of the all-nanosheet sample. The top layer appears to be thicker due to Ga and Pt integration caused by the FIB sample preparation. d) Electron energy loss (EEL) element mapping images taken from the sample area depicted in c); d) Sn-$M_{4,5}$ edge; e) O-K and Sb-$M_{4,5}$ edges; f) all three edges detected at the same time; g) summarizing element map of the three edges; h) Reflectance spectra (solid lines) and simulated spectra (dashed lines) of three all-nanosheet BSs containing seven layers on a glass substrate at ambient conditions (30% RH). The different Bragg peak positions result from different rotation speeds in the spin-coating process: 5000 rpm, 4000 rpm and 3000 rpm; i) microscope images depicting the different structural colors associated with the spectra shown in a).

Given the observed swelling capability of both individual nanosheet materials in the presence of water,[11] we tested the humidity sensing performance of the all-nanosheet photonic structure. As shown in Figure 6.7a,b, the all-nanosheet stack shows a significant color change (in the range of 11–93% RH), larger than for any other photonic system reported for humidity sensing applications so far.[11,46,47] In the range of 11–93% RH (Figure 6.4c), a stopband shift of 140 nm is observed (Figure 6.4a,b), resulting in a very high sensitivity of 1.54 nm per percent of analyte, which is larger compared to BSs, which contain only one swelling compound (see above and previous works).[11,12] The high sensitivity combined with fast response (9.2 s) and recovery times (2.4 s) (Figure S 6.11,

Supporting Information) makes these optical sensors competitive or even superior to other existing devices. Notably, the stopband redshifts nearly linearly with increasing RH values, which is highly desirable for sensing applications (Figure 6.7b). The excellent agreement between the performed theoretical calculations (Figure 6.7a, dashed lines; Table S 6.8, Supporting Information) and the measured spectra (Figure 6.7a, solid lines) indicates that the large stopband shifts arise from 50% swelling for the LTS nanosheets and 60% swelling for $H_3Sb_3P_2O_{14}$ due to water intercalation (Figure 6.7d). In addition, a gradual decrease in the RI contrast upon water intercalation is noticeable by changes in the reflectance intensity from 95% to 60% in the RH range of 11–93%, induced by the water uptake (Table S 6.8, Supporting Information). Both materials take up water, leading to reduced effective RIs of n (LTS) $= 1.78$ and n ($H_3Sb_3P_2O_{14}$) $= 1.52$ at 93% RH, espectively, ranging between those of the pure materials and water.[11] We further find that the intercalation of water has a higher impact on the RI of the LTS nanosheets, which changes by $\Delta n = 0.72$ as compared to that of the $H_3Sb_3P_2O_{14}$ nanosheets, $\Delta n = 0.08$ (Table S 6.8, Supporting Information). This effect can most likely be traced back to the significantly higher initial RI of the LTS nanosheets, whereby the intercalation of water causes larger changes in the effective RI of the thin films compared to the $H_3Sb_3P_2O_{14}$ nanosheets, which exhibit an initial RI more similar to water ($n = 1.33$). Between 93% and 100% RH, the reflectance intensity further decreases and, finally, the RI contrast is fully compensated and the stopband completely vanishes, such that the BS appears transparent (i.e., dark in the reflection mode, Figure 6.7d, 100% RH). This effect of reversible transparency switching is a rare phenomenon and was observed only for very few systems so far, as a careful material choice and adjustment of structural and dielectric parameters is required.[11,48] Since water intercalation happens at equilibrium, the structural color and the photonic stopband can be restored with decreasing humidity. The observed ultralarge stopband shifts as well as the transparency switching (Figure S 6.12, Supporting Information) are fully reversible, and the sensor is stable for at least ten cycles (10–95% RH) of humidity increase and decrease (Figure S 6.10, Supporting Information).
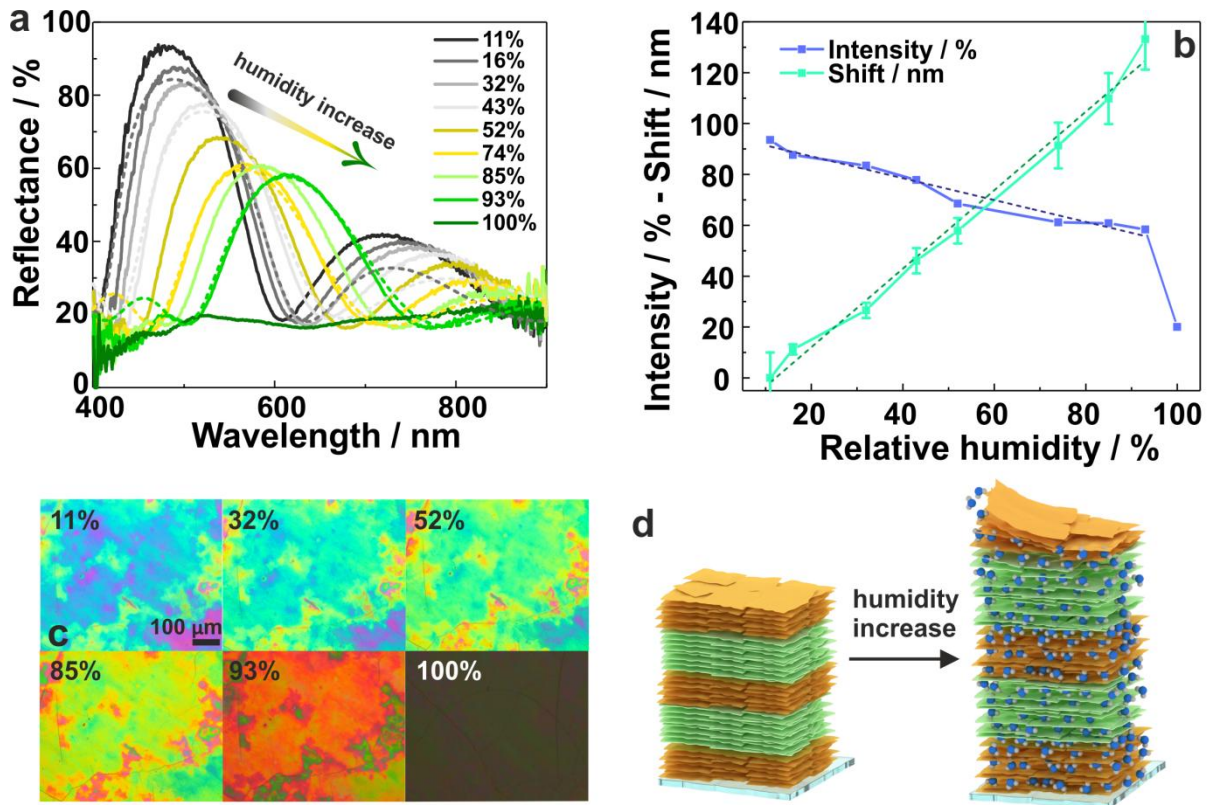
Figure 6.7: Humidity dependent behavior of the all-nanosheet BS. a) Humidity dependent reflectance spectra (solid lines) and simulated spectra (dashed lines) taken at different RH values; b) humidity dependent stopband shifts and reflectance intensity maximum changes of the all-nanosheet sample with increasing RH; c) series of microscope images taken at different RH values showing the different structural colors; d) schematic illustration of the proposed sensing mechanism, i.e. the swelling of both nanosheet materials by water intercalation into the interlayer space.

Conclusion

In summary, we have introduced LTS nanosheets as a solution processable novel high-refractive-index material ($n = 2.50$ at 0% RH at 633 nm), which, owing to its nanosheet morphology and excellent film-forming properties, lends itself well as constituent material for the fabrication of ultrathin, high optical contrast photonic nanostructures. We have demonstrated the first PC featuring TiO$_2$ as low-index material, and achieved the highest refractive index contrast in SiO$_2$ nanoparticle—LTS nanosheet Bragg stacks ($\Delta n = 1.20$ at 0% RH, 633 nm, $\Delta n = 0.90$ at 30% RH) reported to date. The high RI of LTS nanosheets offers enhanced flexibility in the creation of novel light-managing devices, such as antireflection coatings, optical waveguides, solar cells, solar mirrors, displays, or ophthalmic devices. Another field of interest relates to titania-based photonic nanostructures where both maximum electric field concentration and absorption of TiO$_2$ can be tuned into the UV range for "slow photon" applications. In addition, combining two high-RI materials in a BS can lead to a significant reduction in device thickness and with it, material and cost efficiency.

This effect could be exploited, for example, for devices used in radiation shielding, with a photonic stopband placed in the IR spectral range. We have further demonstrated the first allnanosheet Bragg stacks composed of LTS and antimony phosphate, $H_3Sb_3P_2O_{14}$, nanosheets, which are both able to take up significant amounts of water into their interlayer space. Upon exposure to ambient humidity, we observe a full-spectral, linear stopband shift with increasing relative humidity between 11% and 93% RH, which is fully reversible. Notably, due to the high RI contrast, we achieve reflectance intensities above 90% (at 10% RH) for a device consisting of only seven layers ($<1\ \mu$m) in total. This novel BS architecture, therefore, presents an ultrasensitive colorimetric humidity sensor entirely based on functional 2D materials, which, more generally, constitutes a generic material platform for the detection of a variety of analytes.

6.6 EXPERIMENTAL SECTION

Material synthesis

Bulk $Li_2Sn_2S_5$ was synthesized via a one-step solid state synthesis.[32] The precursors, Li_2S, Sn and S were stoichiometrically mixed under inert gas atmosphere, filled into a glassy carbon crucible and vacuum-sealed in a quartz tube. A slight excess of sulfur (3wt%) was applied in order to ensure the complete oxidation of Sn. The tubes were heated to 750 °C with a ramp of 1 °C min^{-1} for 48 h and subsequently quenched to room temperature.

$K_3Sb_3P_2O_{14}$ was also synthesized by a solid state reaction as described elsewhere.[11] For protonation, 4 g of the resulting white powder was stirred in 250 ml of 8 M HNO_3 overnight and washed with pure water. To ensure complete protonation, this step was repeated once again.

Preparation of colloidal suspensions

For exfoliation, the bulk $Li_2Sn_2S_5$ was shaken in water for several hours with a concentration of 1 g L^{-1}. To ensure complete exfoliation, the suspension was sonicated for 60 min. To collect the exfoliated nanosheets, the suspension was centrifuged at 24000 rpm for 30 min. The brownish pellet was resuspended in a water-ethanol mixture (60vol% ethanol) with a concentration of 60 mg mL^{-1}. Afterwards, the suspension was sonicated for 2 h before using it in the BS fabrication.

The bulk $H_3Sb_3P_2O_{14}$ was exfoliated likewise by stirring the protonated compound in pure water overnight. The suspension was centrifuged first at 3000 rpm to get rid of the non-exfoliated residual bulk and then at 18000 rpm to obtain the nanosheets. The gel-like pellet was dried at 100 °C and re-suspended in a water-ethanol mixture (60 vol% ethanol) with a concentration of 27.5 mg mL^{-1}. This suspension was sonicated 2 h before spin-coating.

TiO_2 was synthesized by hydrolysis of $Ti(OEt)_4$ in diluted acid.[9] 12.5 mL TEOT (Tetraethylorthotitanate, Sigma Aldrich) was added dropwise under vigorous stirring to 75 mL of 0.1 M HNO_3 and heated at 80 °C for 8 h. The white suspension was sonicated for 3 h and washed three times by centrifuging the particles at 24000 rpm and redispersing the pellet in methanol. A final concentration of 3wt% was used for spin-coating.

Colloidal SiO_2 (LUDOX, SigmaAldrich) was diluted with methanol to 3.2wt% and after 10 min sonication directly used for spin-coating.

Bragg stack preparation

All BSs were prepared by spin-coating (WS-650S-NPP-Lite, Laurell Technologies Corporation) using the stable colloidal suspensions with the concentrations given above. To access different film thicknesses and, hence, structural colors, different spin-coating speeds and the number of deposition steps were varied. 150 µL of the colloidal suspensions were spin-coated alternatingly on plasma-cleaned glass substrates (1.5 cm x 1.5 cm) for 1 min with defined speeds (3000 rpm, 4000 rpm and 5000 rpm) and with an acceleration of 7000 rpm s^{-1}. The first layer on top of the glass substrate and also the last one were the LTS nanosheets, to achieve the highest achievable RI contrast at the interfaces. To create one layer within the Bragg stack, LTS was deposited for all samples in two steps and the samples were heated after each deposition step to 80 °C for 15 min in order to stabilize the layers and to get rid of the residual solvents.

Characterization

SEM images of the LTS bulk material and the EDX analysis to verify the S:Sn ratio was performed on a FEI Helios G3 UC scanning electron microscope (SEM). In addition, inductively coupled plasma (ICP) measurements were performed on a Varian Vista RL. X-ray diffraction (XRD) patterns were recorded on a powder X-ray diffractometer (Stadi P, STOE) working with Ge(111) monochromated Mo-K$_{\alpha 1}$ radiation (λ = 70.926 pm) and a Mythen 1K Detector (Dektris). The crystalline nanosheet compounds were identified by comparing them the powder diffraction patterns of the bulk materials.[32, 49] Cross-section images of the BSs were taken with a Zeiss Gemini Ultra Field Emission SEM. For the TEM measurement, the sample was cut via focused ion beam (FIB, Zeiss 1540EsB) with a 30 kV Ga ion beam and the surface was polished with a 3 kV beam. The TEM cross section measurement was performed on a FEI Titan Themis microscope 60-300 kV equipped with a Cs corrector for the probe. EELS investigations were performed in scanning transmission mode with a convergence semi-angle of 16.6 mrad and an energy resolution of 0.75 eV. To reduce the effect of the electron irradiation on the material, sub-pixel scanning was applied during the spectrum image acquisition. The EELS maps for the spectral region of 100 to 612.25 eV were generated by integrating the intensity of background

corrected spectra in defined energy windows. The background was subtracted by performing a power law fit for an energy width of 60 eV starting from 429 eV for the Sn-$M_{4,5}$ edge and from 467 eV for the Sb-$M_{4,5}$/O-K edge. Subsequently, the intensity of the edges was integrated in an energy window of 100 eV starting at 507.5 eV for the Sn-$M_{4,5}$ and at 530.5 eV for the Sb-$M_{4,5}$/O-K edge. The same procedure was used to generate the intensity map of the S-$L_{2,3}$ edge, but in that case the background was corrected by a power law fit in the spectral range of 130.25 to 160.25 eV and the intensity was integrated between 161 and 216 eV.

Ellipsometric porosimetry measurements on the thin films were carried out by the porosimetry tool of a Sopra PS-1000 ellipsometer, whereby the samples were equilibrated at selected partial pressure values of water vapor for 15 min. The measured spectra were fitted with the software Sopra SAE using the model combination Cauchy and Lorentz. For the nanosheet thin films, both the layer thickness and the RI were fitted over the relative pressure range simultaneously.

Microscope images were taken from the BS surface with an optical microscope (DM2500, Leica) and simultaneously reflectance spectra were measured at normal incidence with a fiber optic spectrometer (USB2000+, Ocean Optics) attached to the microscope.

To monitor the optical changes with changes in RH, the BSs were kept in a closed stainless steel chamber with a total volume of 5 mL and with a transparent glass window. In the chamber, 0.7 mL of saturated salt solutions were filled without touching the sample surface, and kept at 25 °C to define the humidity in the closed atmosphere.[50-51] At each step, 20 min equilibration time was needed. Dynamic cycling measurements between 10-95% RH were performed using a nitrogen flow setup.

Simulations

Numerical calculations of the reflectance spectra were carried out using a Matlab code based on a full-vector calculation using the transfer matrix method as reported elsewhere.[21] The layer thicknesses at 0% RH were taken from the SEM cross section images. The (wavelength dependent) RIs were taken from the porosimetry measurements.

6.7 ACKNOWLEDGEMENTS

6.8 REFERENCES

[1] J. D. Joannopoulos, S. G. Johnson, J. N. Winn, R. D. Meade, *Photonic crystals: molding the flow of light*, Princeton university press, **2011**.

[2] J. D. Joannopoulos, P. R. Villeneuve, S. Fan, *Nature* 1997, *386*, 143-149.

[3] L. D. Bonifacio, B. V. Lotsch, D. P. Puzzo, F. Scotognella, G. A. Ozin, *Adv. Mater.* **2009**, *21*, 1641-1646.

[4] S. Colodrero, M. Ocaña, H. Míguez, *Langmuir* **2008**, *24*, 4430-4434.

[5] S. Colodrero, M. Ocana, A. R. Gonzalez-Elipe, H. Miguez, *Langmuir* **2008**, *24*, 9135-9139.

[6] B. V. Lotsch, G. A. Ozin, *ACS Nano,* **2008**, *2*, 2065-2074.

[7] S. Y. Choi, M. Mamak, G. von Freymann, N. Chopra, G. A. Ozin, *Nano Lett.* **2006**, *6*, 2456-2461.

[8] A. Ranft, F. Niekiel, I. Pavlichenko, N. Stock, B. V. Lotsch, *Chem. Mater.* **2015**, *27*, 1961–1970.

[9] F. M. Hinterholzinger, A. Ranft, J. M. Feckl, B. Ruhle, T. Bein, B. V. Lotsch, *J. Mater. Chem.* **2012**, *22*, 10356-10362.

[10] I. Pavlichenko, E. Broda, Y. Fukuda, K. Szendrei, A. K. Hatz, G. Scarpa, P. Lugli, C. Brauchle, B. V. Lotsch, *Mater. Horiz.* **2015**, *2*, 299-308.

[11] K. Szendrei, P. Ganter, O. Sànchez-Sobrado, R. Eger, A. Kuhn, B. V. Lotsch, *Adv. Mater.* **2015**, *27*, 6341-6348.

[12] P. Ganter, K. Szendrei, B. V. Lotsch, *Adv. Mater.* **2016**, *28*, 7294-7294.

[13] M. Anaya, J. P. Correa-Baena, G. Lozano, M. Saliba, P. Anguita, B. Roose, A. Abate, U. Steiner, M. Gratzel, M. E. Calvo, A. Hagfeldt, H. Miguez, *J. Mater. Chem. A* **2016**, *4*, 11214-11221.

[14] J. J. Steele, A. C. van Popta, M. M. Hawkeye, J. C. Sit, M. J. Brett, *Sens. Actuators, B* **2006**, *120*, 213-219.

[15] M. M. Hawkeye, M. J. Brett, *Adv. Func. Mater.* **2011**, *21*, 3652-3658.

[16] N. Hidalgo, M. E. Calvo, H. Míguez, *Small* **2009**, *5*, 2309-2315.

[17] M. Anaya, A. Rubino, M. E. Calvo, H. Miguez, *J. Mater. Chem. C* **2016**, *4*, 4532-4537.

[18] W. J. Nimens, L. Whittaker-Brooks, M. H. Bartl, *J. Mater. Chem. C* **2016**, *4*, 668-672.

[19] B. Brudieu, A. L. Bris, J. Teisseire, F. Guillemot, G. Dantelle, S. Misra, P. R. i. Cabarrocas, F. Sorin, T. Gacoin, *Adv. Opt. Mater.* **2014**, *2*, 1105-1112.

[20] J. L. H. Chau, Y.-M. Lin, A.-K. Li, W.-F. Su, K.-S. Chang, S. L.-C. Hsu, T.-L. Li, *Mater. Lett.* **2007**, *61*, 2908-2910.

[21] M. C. Fuertes, S. Colodrero, G. Lozano, A. R. González-Elipe, D. Grosso, C. Boissière, C. Sánchez, G. J. d. A. A. Soler-Illia, H. Míguez, *J. Phys. Chem. C* **2008**, *112*, 3157-3163.

[22] E. Redel, C. Huai, M. Renner, G. von Freymann, G. A. Ozin, *Small* **2011**, *7*, 3465-3471.

[23] M. E. Calvo, J. R. Castro Smirnov, H. Míguez, *J. Polym. Sci., Part B: Polym. Phys.* **2012**, *50*, 945-956.

[24] J. R. C. Smirnov, M. Ito, M. E. Calvo, C. López-López, A. Jiménez-Solano, J. F. Galisteo-López, P. Zavala-Rivera, K. Tanaka, E. Sivaniah, H. Míguez, *Adv. Opt. Mater.* **2015**, *3*, 1633-1639.

[25] B. Gospodinov, J. Dikova, S. Mintova, T. Babeva, *J. Phys.: Conf. Ser.* **2012**, *398*, 012026.

[26] S. Gürakar, T. Serin, N. Serin, *Appl. Surf. Sci.* **2015**, *352*, 16-22.

[27] A. Jiménez-Solano, M. Anaya, M. E. Calvo, M. Alcon-Camas, C. Alcañiz, E. Guillén, N. Martínez, M. Gallas, T. Preussner, R. Escobar-Galindo, H. Míguez, *Adv. Opt. Mater.* **2017**, *5* , 1600833.

[28] C. Bariáin, I. R. Matías, F. J. Arregui, M. López-Amo, *Sens. Actuators, B* **2000**, *69*, 127-131.

[29] B. V. Lotsch, G. A. Ozin, *Adv. Mater.* **2008**, *20*, 4079-4084.

[30] Z. Wang, J. Zhang, J. Xie, C. Li, Y. Li, S. Liang, Z. Tian, T. Wang, H. Zhang, H. Li, W. Xu, B. Yang, *Adv. Funct. Mater.* **2010**, *20*, 3784-3790.

[31] B. V. Lotsch, G. A. Ozin, *J. Am. Chem. Soc.* **2008**, *130*, 15252-15253.

[32] A. Kuhn, T. Holzmann, J. Nuss, B. V. Lotsch, *J. Mater. Chem. A* **2014**, *2*, 6100-6106.

[33] T. Holzmann, L. M. Schoop, M. N. Ali, I. Moudrakovski, G. Gregori, J. Maier, R. J. Cava, B. V. Lotsch, *Energy Environ. Sci.* **2016**, *9*, 2578-2585.

[34] H. S. Jung, P. Verwilst, W. Y. Kim, J. S. Kim, *Chem. Soc. Rev.* **2016**, *45*, 1242-1256.

[35] S. Sikarwar, B. C. Yadav, *Sens. Actuators A* **2015**, *233*, 54-70.

[36] G. von Freymann, V. Kitaev, B. V. Lotsch, G. A. Ozin, *Chem. Soc. Rev.* **2013**, *42*, 2528-2554.

[37] A. T. Exner, I. Pavlichenko, B. V. Lotsch, G. Scarpa, P. Lugli, *ACS Appl. Mater. Interfaces* **2013**, *5*, 1575-1582.

[38] A. Ranft, I. Pavlichenko, K. Szendrei, P. M. Zehetmaier, Y. Hu, A. von Mankowski, B. V. Lotsch, *Microporous Mesoporous Mater.* **2015**, *216*, 216-224.

[39] Y. Piffard, A. Verbaere, A. Lachgar, S. Deniard-Courant, M. Tournoux, *Rev. Chim. Miner.* **1986**, *23*, 766-775.

[40] J. I. L. Chen, G. von Freymann, S. Y. Choi, V. Kitaev, G. A. Ozin, *Adv. Mater.* **2006**, *18*, 1915-1919.

[41] T. Baba, *Nat. Photon* **2008**, *2*, 465-473.

[42] J.-C. P. Gabriel, F. Camerel, B. J. Lemalre, H. Desvaux, P. Davidson, P. Batail, *Nature* **2001**, *413*, 504-508.

[43] S. Deniard-Courant, Y. Piffard, P. Barboux, J. Livage, *Solid State Ionics* **1988**, *27*, 189-194.

[44] C.-Y. Lee, G.-B. Lee, *Sens. Lett.* **2005**, *3*, 1-15.

[45] R. A. Barry, P. Wiltzius, *Langmuir* **2005**, *22*, 1369-1374.

[46] E. Tian, J. Wang, Y. Zheng, Y. Song, L. Jiang, D. Zhu, *J. Mater. Chem.* **2008**, *18*, 1116-1122.

[47] R. Xuan, Q. Wu, Y. Yin, J. Ge, *J. Mater. Chem.* **2011**, *21*, 3672-3676.

[48] M. N. Ghazzal, O. Deparis, J. De Coninck, E. M. Gaigneaux, *J. Mater. Chem. C* **2013**, *1*, 6202-6209.

[49] Y. Piffard, A. Lachgar, M. Tournoux, *J. Solid State Chem.* **1985**, *58*, 253-256.

[50] P. W. Winston, D. H. Bates, *Ecology* **1960**, *41*, 232-237.

[51] L. Greenspan, *J. Res. Nat. Bur. Stand.* **1977**, *81A*, 89-96.

7. ■ TOWARDS ALTERNATIVE READOUT SCHEMES: FLUORESCENT HUMIDITY SENSORS BASED ON OPTICAL RESONATORS

7.1 SUMMARY
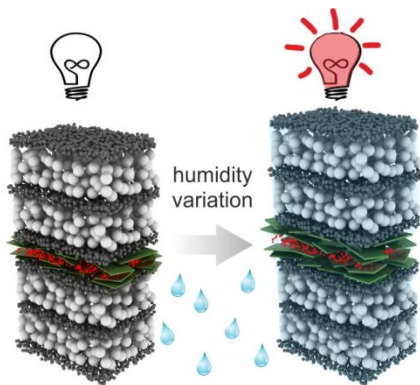
There is an increasing interest in identifying alternative sensing schemes that provide fast and easy read-out of the signal, such as fluorescent sensors. Although different designs of colorimetric sensors, especially in the field of humidity sensing, have been demonstrated in recent years, most of them are based on photonic architectures and were restricted to image based read-outs or spectroscopic detection schemes. This prevents their integration into a compact device, in which the optical signal can be readily converted in an electrical signal. For this reason, alternative output signals, such as photoemission are required.

To find such alternative read-out schemes, in this project we present the first fluorescent humidity sensors based on photonic structures. After a careful theoretical design, we created a highly porous photonic resonator structure with a swellable nanosheet "defect" layer with integrated nanoemitters, which generate the actual sensing signal in the form of luminescence. The rationally designed sensor architecture is based on two highly porous 1DPCs consisting of the usually used TiO_2 and SiO_2 NPs and a functional, humidity sensitive $H_3Sb_3P_2O_{14}$ cavity. Upon humidity changes, the spectral position of the resonance is shifted due to the humidity driven swelling of the nanosheet defect layer. Into this humidity sensitive cavity layer, luminescent nanospheres (d = 30 nm) were integrated at a spatially tailored position and as a well-defined monolayer. These hierarchical systems were first designed by numerical calculations and afterwards realized experimentally by bottom-up spin-coating. Upon exposing these platforms to humidity changes, the photonic environment changes mainly due to the cavity thickness variation, which leads to modulation of the spectral and spatial electromagnetic field intensity distribution. As the emission of the integrated

dyes couples to the photonic modes sustained by the multilayered structure, changes in the distribution of these modes cause variations in the photoluminescence. In extreme cases, this results in the complete suppression of the emission; in other words, we could turn on and off the emission by humidity variations. The interplay between the luminescent properties of an emitter and its photonic environment is a central concept in our approach and implies a fundamental advantage, as the emitters are not chemically altered during the detection process. We also showed evidence of their versatility, in terms of structural design, to provide a tailored response to specific levels of humidity. Guided by theoretical optical design of the resonator architecture and subsequent experimental realization, we presented two embodiments of fluorescent photonic humidity sensors featuring turn-on and turn-off detection schemes.

7.2 FLUORESCENT HUMIDITY SENSORS BASED ON PHOTONIC RESONATORS

Katalin Szendrei,* Alberto Jiménez-Solano,* Gabriel Lozano, Bettina V. Lotsch, Hernán Míguez

* These authors contributed equally to this work.

7.3 ABSTRACT

Among the different approaches to humidity sensing available, those based on fluorescent signals are gathering a great deal of attention due to their fast response and versatility of detection and design. So far, all proposals have focused on the use of luminescent probes whose emission is either triggered or inhibited by the presence of water that reacts or alters their chemical environment, hence inducing the signal change. Here, a novel concept in fluorescent humidity sensing based on combining stimuli-responsive photonic resonators with molecular fluorescent probes is introduced. The resonator is assembled from humidity-swellable antimony phosphate nanosheets embedding a planar light-emitting probe, whose emission is dramatically modified by the changes that ambient humidity causes in its photonic environment. Guided by "in silico" optical design of the resonator architecture and subsequent experimental realization, two embodiments of fluorescent photonic humidity sensors featuring turn-on and turn-off detection schemes are presented. The interplay between the luminescent properties of an emitter and its photonic environment implies a fundamental advantage as the emitters are not chemically altered during the detection process. At the same time, it paves the way toward a new generation of photonic humidity sensors which can conveniently be interfaced with common fluorescence detection schemes.

7.4 INTRODUCTION

Fluorescent sensors for the detection of humidity have experienced an extraordinary development over the past years.[1] They have emerged as an alternative to their capacitive or resistive counterparts, accurate and stable over years, but that suffer from slow response times of the order of tens or hundreds of seconds.[2, 3] Simultaneously, color-encoded humidity sensors based on, for example, stimuli-responsive photonic materials have been extensively studied. Structural color changes may, for example, arise from infiltration of textural pores with water vapor, which gives rise

to variations of the refractive index, Δn, translating into a red shift of the characteristic reflection peak or transmission dip, $\Delta\lambda$.[4-7] In addition, very significant $\Delta\lambda/\Delta n$ values have been achieved by employing swelling materials, such as hydrogels,[8] Fe_2O_3 nanoparticle-polymer hybrids,[9] and polymer-based opal-like structures.[10] Here, dimensional changes act in concert with (sometimes small) changes in Δn. In spite of their larger sensitivity and resolution, the use of swelling materials also typically implies slow response times in the range of tens of minutes. In a previous work,[11,12] some of us proposed stimuli-responsive humidity sensors based on 2D antimony phosphate nanosheets integrated in 1D photonic crystals. These colorimetric sensors show fast (on the subsecond timescale), full-spectrum color changes due to the swelling of the nanosheet layers in the presence of water, as well as high long-term and cycling stability.[11,12] In this regard, although photonic nanostructures provide naked eye observation of color changes, the development of more accurate readout schemes have led to different approaches in which such changes are converted into an electrical signal.[13, 14] In this context, one aspect that, as far as we know, has not been considered, is the potential interplay of photonic resonances and emission to create a fluorescent photonic humidity sensor.

It has been demonstrated that control over the spectral and spatial location of optical resonances in porous 1D photonic crystals (1DPCs), identified by a reinforcement of the electromagnetic field intensity at specific wavelength ranges and at well-defined depths within the stratified structure, can be exploited for tuning the absorption[15,16] or emission[17-20] properties of active nanomaterials embedded in the photonic crystal matrix. Conveniently tailored, these effects might allow developing humidity sensors based on a fluorescence signal readout, whose emission would change as a function of the modification of the local photonic environment caused by the presence of water molecules in the swellable matrix. In terms of performance, when compared to other fluorescent thin film devices that do not make use of photonic effects,[21,22] this would imply added functionalities, such as predesigned *on-off* signal responses, fast and easy optical-to-electrical signal translation, and fine tunability of the detector sensitivity to preselected water contents in the atmosphere. From another perspective, larger stability and hence longer durability is expected as the sensing principle is not based on a chemical reaction that involves the luminescent probes, as it is the case for most fluorescent humidity sensors.[23-25]

In this work, we present the first fluorescent humidity sensor based on a porous and at the same time swellable photonic structure. The correlation between the photon local density of states and the changes induced by the modification of the ambient conditions is used to create a sensing architecture that responds to variations in relative humidity (RH) with a well-defined, predesigned photoluminescence (PL) spectrum. Our resonators are composed of thin films of dyed polystyrene

nanospheres precisely deposited at the desired depth within 2D antimony phosphate ($H_3Sb_3P_2O_{14}$) nanosheets. These are in turn sandwiched between two 1DPCs, thus creating an optical cavity and allowing for a precise control of the luminescence of the nanospheres. Upon humidity changes, the cavity dynamically swells as a result of the intercalation of water molecules, hence modifying the local photonic environment of the emitters. This translates into dramatic changes of the emission properties, which, depending on the design employed, may lead to enormous enhancements or complete suppression of the fluorescence in response to the stimulus. We demonstrate this concept by realizing two designs displaying, respectively, *turn-on* and *turn-off* behaviors of the luminescence with increasing humidity.

7.5 RESULTS AND DISCUSSION

Optical Simulations / Theoretical Design

We start by designing two different fluorescent optical resonators that show opposite behavior (namely, luminescence *turn-on* and *turn-off*) versus moisture changes in the environment. In order to do so, we first carry out simulations of the photonic properties of two prototype architectures, based on the dielectric properties of the constituent materials. Guided by our optical design, we then experimentally realize those architectures that according to our simulations emulate the desired sensing characteristics in an optimal way.

To this end, we take into account the following considerations: first, our model systems are planar multilayered structures in which two porous 1DPC mirrors made of alternated silica (SiO_2) and titania (TiO_2) nanoparticles sandwich a cavity made of $H_3Sb_3P_2O_{14}$ nanosheets. As this middle cavity is the actual moisture responsive material, we must allow the analyte to reach it. This is ensured by using nanoparticle-based 1DPCs presenting open textural porosity.[5, 26] Second, a thin monolayer of light-emitting nanospheres ($d \approx 30$ nm) is embedded at a predesigned depth within this middle slab. As emitter we chose Firefly Fluorescent Red as a dye molecule whose fluorescence lies in the visible spectrum, since it is more convenient for detection purposes. Hence, nanospheres of polystyrene embedding organic dye molecules, with an emission maximum at $\lambda \approx 570$ nm and an excitation maximum at $\lambda \approx 534$ nm, were selected as building blocks of the light-emitting layer. A generic scheme of the type of the multilayered sensing system herein employed is depicted in Figure 7.1a. The experimental photoexcitation and PL spectra of the dyed nanospheres are displayed in Figure 7.1b. As photonic crystals present an angular-dependent photonic response, our simulations must consider the geometry of our optical characterization setup. We thus establish that fluorescent signals would be collected in directions quasi-normal to the hierarchical film surface. We note that strict definition of the geometry of the sensing configuration is a common feature of photonic

sensors.[27] Also, our design assumes that the dynamic fluorescent response of our sensing material is determined by the relative spatial location of the light-emitting layer of nanospheres with respect to the optical cavity modes, as obtained from a calculation of the electric field intensity profile along our ensemble. By doing this, we are applying a reciprocity principle that states that the coupling efficiency of light emitted at a given wavelength from inside the system to free propagating modes along a specific direction may be estimated by analyzing the efficiency of the reverse process, that is, the coupling of an incoming plane wave of similar wavelength impinging on the system along that same direction.[28-31] Thus, from active nanomaterials located in regions within the stratified medium for which intensification of the in-coupling electric field is expected, enhanced PL is also expected as long as the spectral positions of such resonance and the PL band coincide at least partially. Conversely, emitters placed in regions where the electric field intensity is depleted will present lower fluorescence. As the spectral and spatial positions of those resonances shift mainly due to the swelling of the $H_3Sb_3P_2O_{14}$, a concomitant modification of light emission intensity from the embedded active layer is expected. Recent results support the validity of this approximation for systems in which strict control over the position of the emitters is achieved.[17, 32] In Figure 7.1c,d, we show the calculated spatial and spectral distribution of the normalized electric field intensity, $|E|^2/|E_0|^2$, which results from the coupling of an incident electromagnetic plane wave with the two types of multilayers. In both cases, nonpolarized normal incidence light with respect to its surface is assumed. Optical resonances can be readily identified as bright spots in the electric field intensity. The interface between alternate layers as well as the position of the light-emitting layer of nanospheres are indicated with horizontal white lines (solid and dashed, respectively). Figure 7.1c displays the results for the multilayer architecture designed to maximize the electric field intensity, in the absence of moisture, at the depth at which the emitters are located and for wavelengths comprised within the emission band of the dye molecules (*in-resonance* configuration). So, when moisture increases, emission will take place off-resonance at some point and thus diminish (fluorescence *turn-off* sample). On the other hand, Figure 7.1d shows the opposite behavior: the structure is designed with the dye fluorescence off-resonance at zero RH, the in-resonance state being reached when moisture rises (fluorescence *turn-on* sample). All details about the structural parameters such as the thicknesses of the different layers and the relative position of the emitter layer are given in the Supporting Information for both resonant structures.
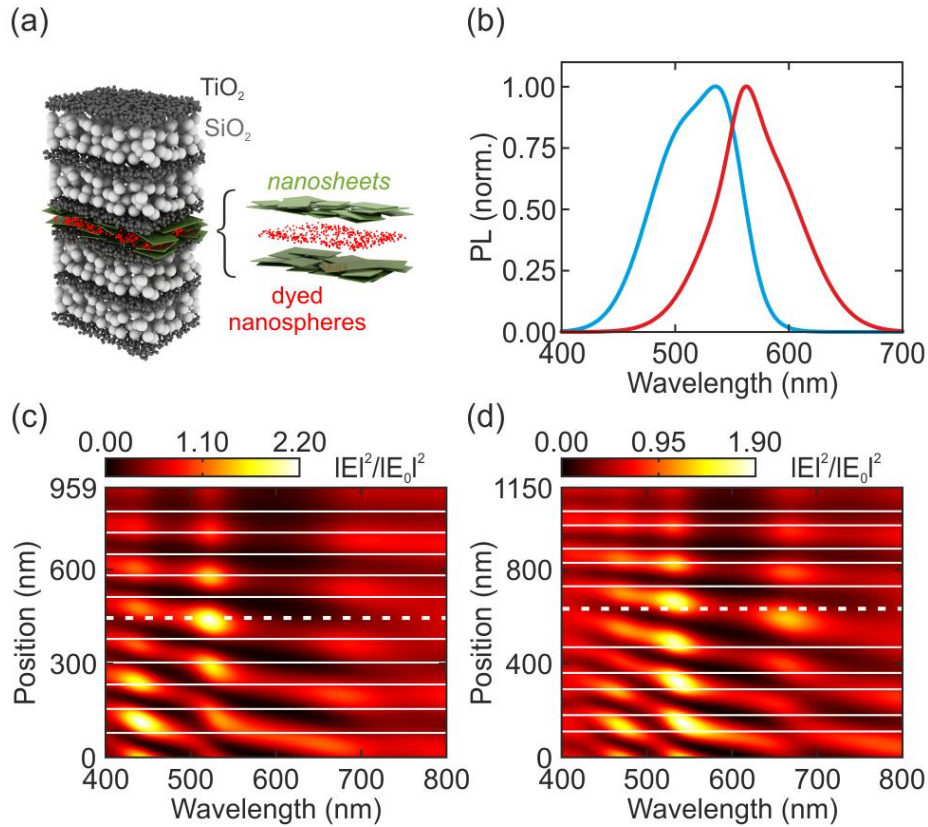
Figure 7.1: a) Schematic model of the fluorescent photonic humidity sensor. It shows a thin emitting layer embedded in an optical cavity made of $H_3Sb_3P_2O_{14}$ nanosheets that are surrounded by two dielectric mirrors fabricated with SiO_2 and TiO_2 nanoparticles. b) Excitation (blue) and emission spectra (red) of the dye molecules employed in the fluorescent sensor. Spatial and spectral distribution of the electric field intensity of the c) turn-off and d) turn-on samples at 0% relative humidity (RH). Plane wave illumination at normal incidence is assumed in the calculations. For the turn-on sample, calculations consider that the thicknesses of the SiO_2 and TiO_2 layers are 80 and 82 nm, respectively, and constant over the entire humidity range, and the optical cavity is 149 nm thick, the emitting layer being positioned in the middle of the cavity. For the turn-off sample, calculations consider that the thicknesses of the SiO_2 and TiO_2 layers are 65 and 105 nm, respectively, and the optical cavity is 260 nm thick, the emitting layer being located at a depth of one quarter of the cavity width. Interfaces between different layers in the multilayer are indicated with thin white lines, whereas the position of the light-emitting layer is signaled with a white dashed line in each case.

Finally, in order to estimate the expected optical response of these resonators versus changes in the environmental humidity, we make use of the experimental data available for the swelling response of $H_3Sb_3P_2O_{14}$ nanosheets (see our previous work).[11] As ambient moisture rises, water is gradually intercalated between the $H_3Sb_3P_2O_{14}$ nanosheets and the thickness of the optical cavity increases, and so does the spectral and spatial position of the resonant modes. Simultaneously, water is adsorbed onto the walls of the porous 1DPC sandwiching the cavity,[4,5] which also modifies the optical properties of the ensemble and thus the response of the resonator. This is also taken into

account in our simulations. Our theoretical analysis reveals that the optical response of the ensemble versus increasing moisture is expected to be mainly determined by the swelling of the $H_3Sb_3P_2O_{14}$ cavity, while the adsorption of water in the textural pores of the 1DPCs will have a lesser effect. In Figure 7.2, we show the simulated evolution of the reflectance (R) (Figure 7.2a,b), electric field intensity at the position of the emitter (Figure 7.2c,d), and the expected PL extracted from a model architecture (Figure 7.2e,f) for the turn-off and turn-on sensors, respectively.
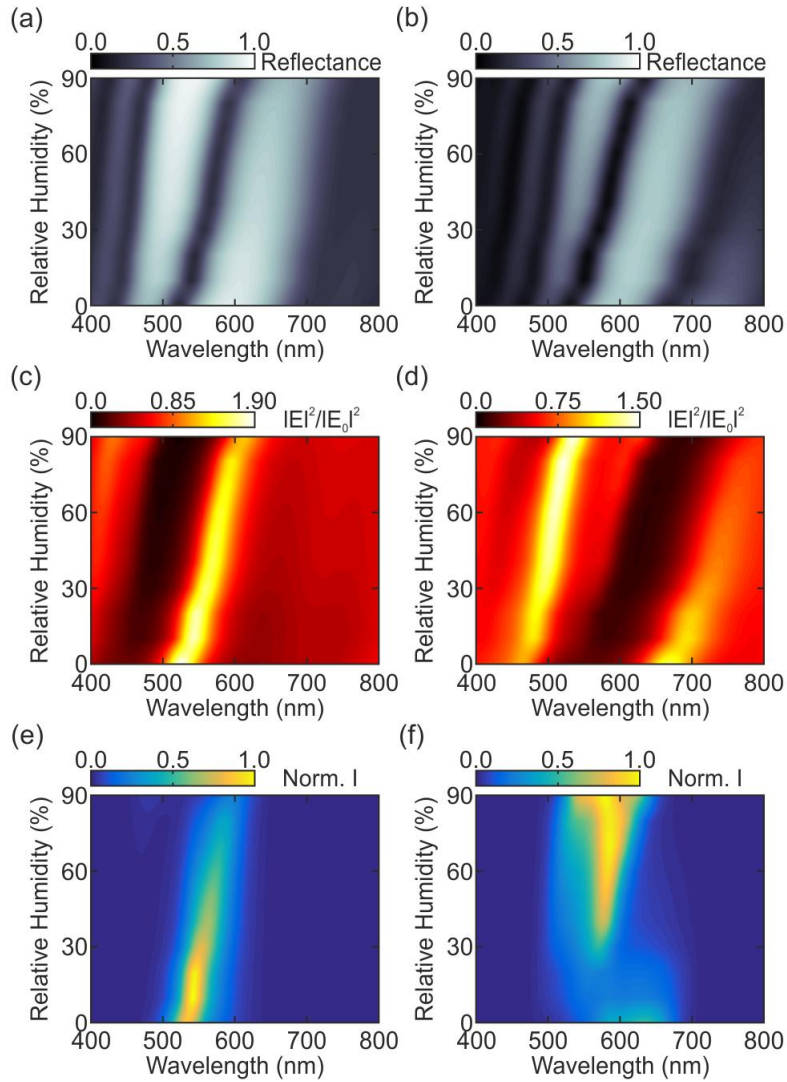
Figure 7.2: Calculated specular reflectance spectra as a function of the relative humidity for the a) turn-off and b) turn-on samples. Electric field intensity at the emitting layer position of the c) turn-off and d) turn-on sample. Estimated emitted intensity of the e) turn-off and f) turn-on sensor.

Sample Fabrication

In the next step, we experimentally realize the two photonic model architectures by sequentially spin-coating the different layers they are composed of. First, alternate layers of SiO_2 and TiO_2

nanoparticles were deposited from stable colloidal precursor suspensions to create the first multilayer. Then, the humidity-responsive optical cavity was formed by spin-casting a suspension of $H_3Sb_3P_2O_{14}$ exfoliated nanosheets directly onto it. Once a homogenous thin film of the predesigned thickness was formed, a monolayer of light-emitting polystyrene nanospheres was deposited and then covered by a new layer of $H_3Sb_3P_2O_{14}$. In this way, an embedded layer of emitters of ≈30 nm thick is attained. Guided by our simulations, the light-emitting layer was positioned in the middle of the optical cavity in the case of the fluorescence turn-off system, while for the turn-on sensor it was located at a depth of one-quarter of that width. Finally, the second 1DPC was deposited onto the humidity responsive layer. In order to enable the diffusion of water molecules through the dielectric mirrors so that they can reach the middle layer, both mirrors were designed to be highly porous (porosity of ≈ 50% in both silica and titania layers), and at the same time highly reflecting, which results from the contrast between the average refractive indices of the SiO_2 nanoparticle (n_{av} = 1.3) and TiO_2 nanocrystal (n_{av} = 1.8). The n_{av} of the intermediate nanosheet layer changes from 1.61 to 1.52 when humidity increases from 2 to 99%, while its thickness is enlarged by a factor of 1.75.[11] With these parameters, our calculations indicate that 1DPCs of five layers (starting and terminating with the high refractive index TiO_2 nanoparticle layer) are sufficient to attain well-defined cavity modes. The experimental thicknesses achieved for the middle nanosheet layers, that is, the optical cavities, were 140 ± 15 and 250 ± 15 nm (both measured at 0% RH in the scanning electron microscope (SEM)) for the fluorescence turn-on and turn-off systems, respectively. These values are in good agreement with the theoretical designs shown in Figure 7.1. Figure 7.3a shows a schematic illustration of the sample fabrication. Secondary (left panels) and back-scattered (right panels) electron microscopy images of the cross-sections of the two types of ensembles are displayed in Figure 3b,c. The stratified structure can be readily seen in both cases. Since the layer of dyed nanospheres has the lower atomic number (Z), its position can be easily identified in all images as a darker thin line. Schemes of the two stratified media are superimposed to the back-scattered electron images to ease the recognition of each type of slab.
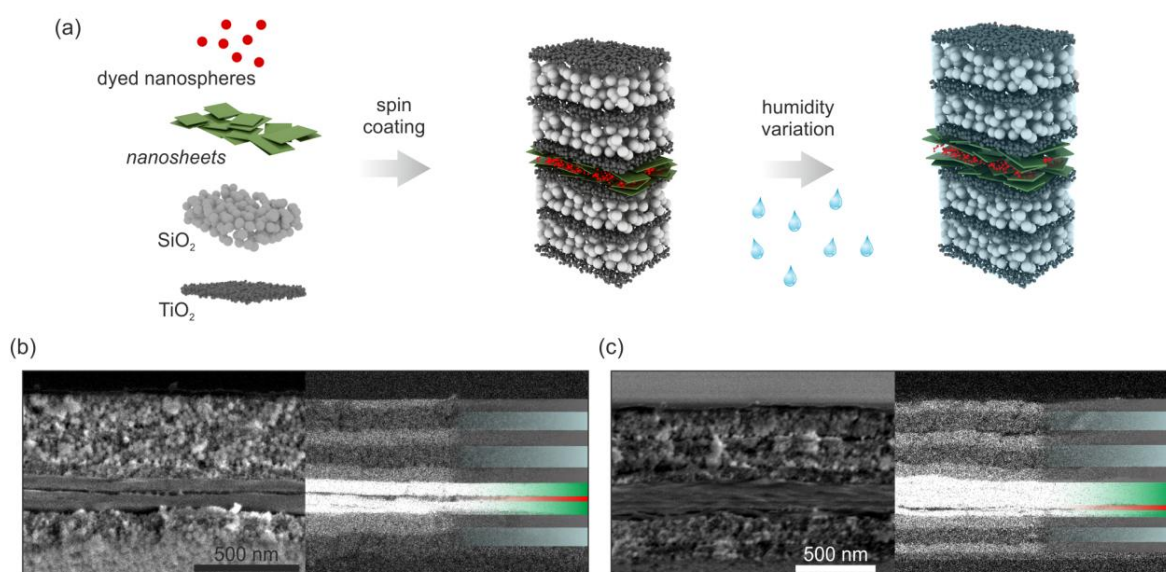
Figure 7.3: a) Schematic illustration of the sample fabrication via spin-coating using TiO_2 and SiO_2 nanoparticles, $H_3Sb_3P_2O_{14}$ nanosheets, and dyed nanospheres. b) SEM cross-section image of the turn-off sample with a cavity thickness of 140 nm (at 0% RH) with the emitting layer located in the middle of the cavity. c) SEM cross-section image of the turn-on sample with a cavity thickness of 250 nm (at 0% RH) with the emitting layer located at a depth of one quarter of the cavity width. Note that the multilayer that is closer to the substrate in both samples shows only three layers due to the peeling off behavior of the sample in high vacuum in the FESEM. The entire structure was fabricated to be symmetric and both dielectric mirrors were composed of five layers.

Optical Response to Environmental Humidity Changes

The evolution of R and PL of both fluorescent resonators as humidity is gradually increased in a chamber (see Figure S 7.2, Supporting Information) is displayed in Figure 7.4. RH is set by means of saturated salt solutions.[33, 34] The responses of both systems follow the behavior expected from our simulations in each case. For the turn-off system, when the spectral position of the cavity mode, identified as a dip in *R* (Figure 7.4a), red-shifts as a result of the swelling of the middle layer, the extracted PL (Figure 7.4c) experiences an initial increase and then a distinct drop when RH ≈ 75%. Conversely, for the fluorescent turn-on system a qualitatively similar shift of the resonance (Figure 7.4b) gives rise to the opposite response in PL (Figure 7.4d), as planned, with a prompt increase of the emitted signal at RH ≈ 75%. In both cases, the variation of PL is a consequence of the different initial relative spectral positions of the cavity mode and the emission band of the dyed nanospheres, as can be inferred from the field distribution patterns depicted in Figure 7.2 and Figures S 7.3 and S 7.4 (Supporting Information). These results confirm that these stratified ensembles provide humidity sensing by both fluorescent and reflectance readouts, arising as a result of their environmentally responsive photonic properties. Please notice that the Bragg mirror resonators were designed to prevent the blocking of the excitation wavelength, λ = 475 nm, by the

photonic stop band. As a reference, we measured the emission spectrum of the dyed nanospheres located at the same depth within two nanosheet layers like the ones employed to build the photonic fluorescent turn-on and turn-off systems, respectively, but without the two surrounding dielectric mirrors. Figure 7.4e,f displays the evolution of the maximum PL intensity, normalized for the two fluorescent humidity sensing ensembles (Figure 7.4e) and for the corresponding references (Figure 7.4f). The PL of the references remains barely affected by the changes in humidity in the environment, with both the photoexcitation and PL spectra essentially preserving the same shape and intensity for the whole range of RH values tested. This comparison confirms that the modification of the chemical environment of the dyed nanospheres as a result of water intercalation—albeit responsive to humidity—is not enough by itself to produce the changes observed in PL. We thus show that the fluorescence switching is in fact based on the tailored interplay between photonic and emissive modes, that is, the stimuli-responsive photonic environment acts on the fluorescent properties of the emitters, which in turn sensitively depends on the level of moisture in the surrounding atmosphere. Notably, the fluorescence switching points can be designed by the photonic architecture and placement of the emitters so as to address specific sensing applications. For example, the turning-on/off point of the architectures presented herein corresponds to a relative humidity of 75%, which renders such systems interesting for environmental monitoring applications in the high humidity regime. This regime is particularly relevant for ambient room monitoring, since mold formation in damp rooms starts around 75% RH, depending on the wall material.[35,36] Finally, the reproducibility and stability of the response versus several cycles of exposure to increasing and decreasing humidity were confirmed by performing these sequential experiments several times. These results represent the first proof of concept of a fluorescent photonic humidity sensor structure. Further studies with encapsulated dyes with a wider Stokes shift would allow a higher accuracy on the detection of humidity changes.
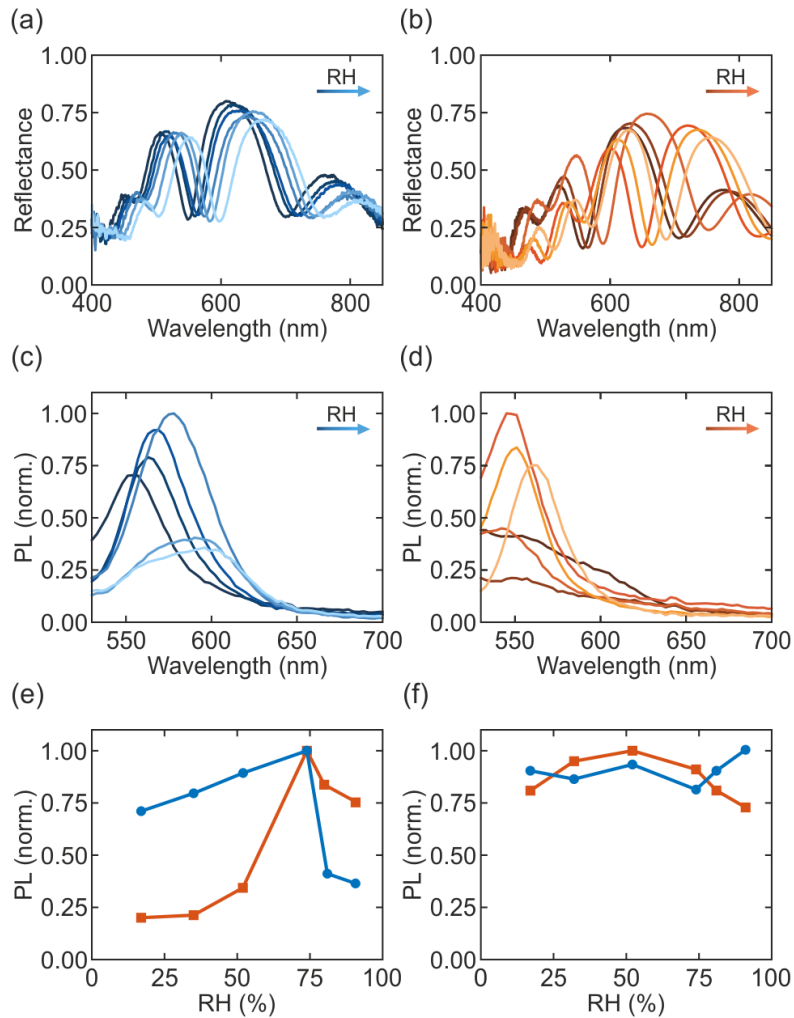
Figure 7.4: Reflectance spectra of the a) turn-off and b) turn-on sample measured at different values of the relative humidity (RH). Normalized emission spectra of the c) turn-off and d) turn-on sample for different RH values. e) Maximum photoluminescence intensity as a function of RH for the turn-off (blue) and turn-on sample (red). f) Maximum photoluminescence intensity as a function of RH for the corresponding reference samples.

Conclusion

In summary, we have proposed and demonstrated a fluorescent photonic humidity sensor based on an optical resonator, which was designed to present a tailored photoluminescence response to changes in ambient humidity. This was achieved by including antimony phosphate nanosheets, which swell upon water uptake, as a stimuli-responsive cavity layer embedding a light-emitting layer at a well-defined depth, sandwiched between 1D photonic crystal mirrors. The gradual swelling of the nanosheet layer, caused by water intercalation as the humidity is controllably raised, changes the spatial and spectral positions of the optical cavity resonances with respect to those of the emission band of the embedded dyes. Two different scenarios were realized which either show a fluorescent turn-off or a turn-on response versus increasing relative humidity. In summary, our work paves the

way toward the development of a new generation of smart photonic devices that do not only display a gradual reflected or transmitted color variation, but also additionally feature a tailorable fluorescent signal read-out. As such, specific analytes can sensitively be traced by means of a distinct luminescent signal change in response to variations in analyte concentration, which bodes well for the development of versatile photonic sensing platforms compatible with luminescence detection schemes.

7.6   EXPERIMENTAL SECTION

Numerical Calculations

The optical response of the photonic structures was calculated using a full wave vector model based on the transfer matrix formalism. The PL was estimated by multiplying the field intensity at the position of the organic dye molecules with the emission spectrum of the dye molecules deposited on glass.

Synthesis of the $H_3Sb_3P_2O_{14}$ Nanosheets

$K_3Sb_3P_2O_{14}$ was prepared in a two-step solid-state reaction.[37] The precursors KNO_3 (99%, Merck), Sb_2O_3 (99.6 %, Alfa Aesar), and $NH_4H_2PO_4$ (98%+, Acros Organics) were ground in a stoichiometric ratio and heated up first to 350 °C for 12 h with a heating rate of 5 °C min^{-1}. In a second step, the mixture was heated to 950 °C for 12 h with a heating rate of 5 °C min^{-1}. To obtain $H_3Sb_3P_2O_{14}$, $K_3Sb_3P_2O_{14}$ was treated with 8 m HNO_3 (250 mL, diluted 65 wt%, Merck) overnight, filtrated, washed with ethanol, and dried at room temperature. This treatment was repeated once more to complete the ion exchange reaction.[11] For exfoliation, $H_3Sb_3P_2O_{14}$ was vigorously stirred overnight in pure water (7.3 mmol L^{-1}). The resulting colloidal suspension was then centrifuged at 3000 rpm for 30 min to remove non-exfoliated bulk material. The supernatant, which consists mainly of exfoliated single-layer nanosheets, was collected and centrifuged at 18 000 rpm for 30 min to yield the nanosheet pellet. The gel-like, colorless wet aggregate was dried at 100 °C.

Preparation of the Colloidal Suspensions

The dried nanosheets were redispersed in a water-ethanol mixture (60 wt% ethanol) with a concentration of 21 mmol L^{-1}. To ensure homogeneity and the complete exfoliation into single-layered nanosheets, the suspension was sonicated for 2 h. TiO_2 nanoparticles were synthesized using a procedure described elsewhere.[5] Colloidal SiO_2 nanoparticles with a particle diameter of 30 nm were purchased from Sigma Aldrich (LUDOX-TMA). Both suspensions were diluted with methanol to 3.4 and 2.3 wt%, respectively, and directly taken for layer preparation after 10 min sonication.

Fabrication of the Photonic Structures

All layers comprising the photonic resonators were fabricated via spin-coating. Zero-fluorescent microscope slides (Proscitech, cut to 2 × 2 cm^2 pieces) employed as substrates were cleaned with oxygen plasma. Porous dielectric mirrors made of five layers were deposited via spin-coating. SiO$_2$ and TiO$_2$ colloids were deposited using 6000 rpm rotation speed, with an acceleration of 5000 rpm s^{-1} for 1 min, the first and the last layers of the stack correspond to the high refractive index material, that is, TiO$_2$. Afterward, the samples were heated for 15 min at 80 °C before the cavity deposition. The cavity was composed of H$_3$Sb$_3$P$_2$O$_{14}$, which was deposited in 6/8 steps (turn-off/on sample). Spinning conditions for each deposition step were 3000 rpm and 5000 rpm s^{-1}. The samples were heated for 15 min at 80 °C after each deposition step. The position of the emitters was determined during the cavity fabrication. After three (turn-off sample) or two (turn-on sample) nanosheet deposition steps, the commercially available Firefli Fluorescent Red dyed nanospheres (R25, Thermo Fisher Scientific) were deposited without dilution or further purification directly on top of the nanosheets using 3000 rpm and 5000 rpm min^{-1} for 1 min. To remove the excess of emitters, samples were washed with pure methanol at 3000 rpm and 5000 rpm min^{-1}. After heating again at 80 °C for 15 min, the rest of the cavity was deposited on top of the emitter layer and another 3/6 deposition steps (turn-off/on sample) were applied, respectively. Finally, a porous 1DPC composed of five layers was deposited on top of the cavity in the same fashion as described above. Finally, the samples were heated at 80 °C for 30 min.

Optical Characterization

Specular reflectance spectra were measured from areas of 1 × 1 mm^2 using a fiber coupled spectrometer (USB2000+, Ocean Optics) attached to a microscope (DM2500, Leica). To obtain the reflectance changes with relative humidity change, dielectric mirrors stacks were kept over saturated salt solutions at around 25 °C in a stainless steel chamber with a transparent glass window.[31,32] Fluorescence measurements were carried out using a commercial spectrofluorometer (Fluorolog-3 Horiba Jobin Yvon). The photoemission spectra were measured from 450 to 700 nm with a step of 3 nm using an excitation wavelength of 440 ± 3 nm. All this photoluminescence characterization was performed collecting emitted light at an angle of 11.25°. Spectroscopic ellipsometry and porosimetry measurements were carried out with a Sopra PS-1000 SAM, whereby the sample was equilibrated at all water vapor relative pressure values for 15 min. The resulting spectra were fitted with the software Sopra SAE applying the Cauchy–Lorentz model. The nanoparticle layer thickness was estimated to be constant and only the refractive indices were fitted for the whole relative pressure range. For the nanosheet thin films, both the layer thickness and the refractive index were fitted.

Before all measurements, the nanoparticle samples were heated for at least 30 min at 200 °C and the nanosheet thin films for 30 min at 80 °C in vacuum to make sure that the pores are empty.

Structural Characterization

Field-emission SEM cross-section images were collected by a Zeiss Merlin working at 1.5 kV using both back scattered as well as secondary electrons.

7.7 ACKNOWLEDGEMENTS

7.8 REFERENCES

[1] H. S. Jung, P. Verwilst, W. Y. Kim, J. S. Kim, *Chem. Soc. Rev.* **2016**, *45*, 1242.

[2] E+E ELEKTRONIK Gesellschaft m.b.H., commercially available humidity sensors, http://www.epluse.com/en/products/humidity-instruments/humidity-sensor (accessed: April 2017).

[3] Vaisala, commercially available humidity sensors, http://www.vaisala.com/en/products/humidity/Pages/default.aspx (accessed: April 2017).

[4] M. C. Fuertes, S. Colodrero, G. Lozano, A. R. González-Elipe, D. Grosso, C. Boissière, C. Sánchez, G. J. d. A. A. Soler-Illia, H. Míguez, *J. Phys. Chem. C* **2008**, *112*, 3157.

[5] S. Colodrero, M. Ocaña, A. R. Gonzalez-Elipe, H. Miguez, *Langmuir* **2008**, *24*, 9135.

[6] N. Hidalgo, M. E. Calvo, H. Miguez, *Small* **2009**, *5*, 2309.

[7] F. M. Hinterholzinger, A. Ranft, J. M. Feckl, B. Ruhle, T. Bein, B. V. Lotsch, *J. Mater. Chem.* **2012**, *22*, 10356.

[8] E. Tian, J. Wang, Y. Zheng, Y. Song, L. Jiang, D. Zhu, *J. Mater. Chem.* **2008**, *18*, 1116.

[9] R. Xuan, Q. Wu, Y. Yin, J. Ge, *J. Mater. Chem.* **2011**, *21*, 3672.

[10] H. Kim, J. Ge, J. Kim, S. E. Choi, H. Lee, H. Lee, W. Park, Y. Yin, S. Kwon, *Nat. Photon.* **2009**, *3*, 534.

[11] K. Szendrei, P. Ganter, O. Sanchez-Sobrado, R. Eger, A. Kuhn, B. V. Lotsch, *Adv. Mater.* **2015**, *27*, 6341.

[12] P. Ganter, K. Szendrei, B. V. Lotsch, *Adv. Mater.* **2016**, *28*, 7436.

[13] I. Pavlichenko, E. Broda, Y. Fukuda, K. Szendrei, A. K. Hatz, G. Scarpa, P. Lugli, C. Brauchle, B. V. Lotsch, *Mater. Horiz.* **2015**, *2*, 299.

[14] A. T. Exner, I. Pavlichenko, D. Baierl, M. Schmidt, G. Derondeau, B. V. Lotsch, P. Lugli, G. Scarpa, *Laser Photon. Rev.* **2014**, *5*, 726.

[15] O. Sanchez-Sobrado, G. Lozano, M. E. Calvo, A. Sánchez-Iglesias, L. M. Liz-Marzán, H. Míguez, *Adv. Mater.* **2011**, *23*, 2108.

[16] A. Jimenez-Solano, C. Lopez-Lopez, O. Sanchez-Sobrado, J. M. Luque, M. E. Calvo, C. Fernandez-Lopez, A. Sanchez-Iglesias, L. M. Liz-Marzán, H. Miguez, *Langmuir* **2012**, *28*, 9161.

[17] A. Jimenez-Solano, J. F. Galisteo-Lopez, H. Miguez, *Small* **2015**, *11*, 2727.

[18] O. Sanchez-Sobrado, M. E. Calvo, N. Nuñez, M. Ocaña, G. Lozano, H. Miguez, *Nanoscale* **2010**, *2*, 936.

[19] D. P. Puzzo, F. Scotognella, M. Zavelani-Rossi, M. Sebastian, A. J. Lough, I. Manners, G. Lanzani, R. Tubino, G. A. Ozin, *Nano Lett.* **2009**, *9*, 4273.

[20] F. Scotognella, D. P. Puzzo, A. Monguzzi, D. S. Wiersma, D. Maschke, R. Tubino, G. A. Ozin, *Small* **2009**, *5*, 2048.

[21] M. G. Choi, M. H. Kim, H. J. Kim, J. E. Park, S. K. Chang, *Bull. Korean Chem. Soc.* **2007**, *28*, 1818.

[22] G. Men, G. Zhang, C. Liang, H. Liu, B. Yang, Y. Pan, Z. Wang, S. Jiang, *Analyst* **2013**, *138*, 2847.

[23] S. Pal, M. Mukherjee, B. Sen, S. Lohara, P. Chattopadhyay, *RSC Adv.* **2014**, *4*, 21608.

[24] S. Colodrero, M. Ocaña, H. Míguez, *Langmuir* **2008**, *24*, 4430.

[25] J. Homola, S. S. Yeea, G. Gauglitz, *Sens. and Actuators B: Chem.* **1999**, *54*, 3.

[26] R. J. Photton, *Rep. Prog. Phys.* **2004**, *67*, 717.

[27] O. T. A. Janssen, A J. H. Wachters, H. P. Urbach, *Opt. Express* **2010**, *18*, 24522.

[28] S. Zhang, E. R. Martins, A. G. Diyaf, J. I. B. Wilson, G. A. Turnbull, I. D. W. Samuel, *Synth. Met.* **2015**, *205*, 127.

[29] G. Lozano, D. J. Louwers, S. R. K. Rodríguez, S. Murai, O. T. A. Jansen, M. A. Verschuuren, J. Gómez Rivas, *Light Sci. Appl.* **2013**, *2*, e66

[30] M. Ramezani, G. Lozano, M. A. Verschuuren, J. Gómez Rivas, *Phys. Rev. B* **2016**, *94*, 125406.

[31] P. W. Winston, D. H. Bates, *Ecology* **1960**, *41*, 232.

[32] L. Greenspan, *J. Res. Nat. Bur. Stand.* **1977**, *81A*, 89.

[33] J. Vučković, D. Fattal, C. Santori, G. S. Solomon, Y. Yamamoto, *Appl. Phys. Lett.* **2003**, *82*, 3596.

[34] O. O. Hänninen, *Fundamentals of mold growth in indoor environments and strategies for healthy living* (Eds.: O. C. G. Adan, R. A. Samson), Wageningen Academic Publishers, Wageningen, **2011**, pp. 277.

[35] Y. Piffard, A. Lachgar, M. Tournoux, *J. Solid State Chem.* **1985**, *58*, 253.

8. TRACKING THE SENSING MECHANISM: DIFFUSION TRACKING OF VAPOR ANALYTES IN MULTILAYERED STRUCTURES

8.1 SUMMARY
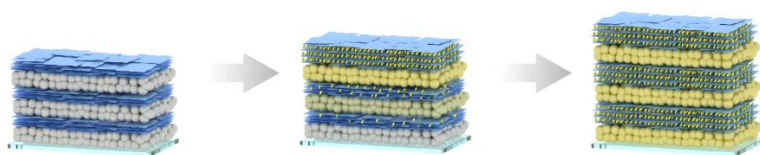
How does the analyte diffuse through the multilayer structure and what is the infiltration mechanism? When does the analyte saturate the sensor and is the infiltration of the multilayer structure with analyte complete? When is the sensing process finished? These are key questions regarding sensor-analyte interactions in general, but answers are largely lacking. In order to understand analyte diffusion in multilayer photonic sensors in depth, we created a rationally designed and well-defined model system composed of 2D nanosheet ($H_3Sb_3P_2O_{14}$) based 1DPCs in order to model and demonstrate molecular diffusion into and throughout the multilayered systems. As an analyte, primary amine vapors were used, which intercalate into the nanosheet layers, leading to large stopband shifts. Based exclusively on optical methods, such as the evaluation of the reflectance spectra, the time-dependent behavior and the penetration depth of the analytes were theoretically modeled to understand analyte uptake by the multilayer system. Hereby we can optically track a vertical layer-by-layer diffusion of the analyte molecules into the multilayered structure with time. To demonstrate the versatility of the system and to carve out trends, we used amines with different chain lengths and derive size-dependent correlations of the infiltration and diffusion behavior. We observed for larger amines (octylamine and hexylamine) compared to smaller amines (butylamine) significantly larger stopband shifts and larger response times. However, for all analytes we could extract information on the individual layers and the time-dependent filling state of the layers. Hereby, we observed for all analytes a gradual filling of the stack, a layer-by-layer filling of the multilayer: the layers near the substrate are infiltrated by the analyte later than the top layers. Although this behavior was observed

for all analytes, significant differences in the delay of the filling of the layers are observed, which were accompanied by large differences of the swelling of the individual layers.

Katalin Szendrei-Temesi planned the project, designed and fabricated the 1DPCs, performed the optical measurements, edited the figures and wrote the manuscript. Alberto Jiménez-Solano performed the theoretical calculations in order to reproduce the analyte diffusion to understand the diffusion mechanism, assisted with the optical measurements, wrote the manuscript and edited the figures.

8.2 TRACKING VERTICAL MOLECULAR DIFFUSION INTO 1-DIMENSIONAL PHOTONIC CRYSTALS

Katalin Szendrei-Temesi,* Alberto Jiménez-Solano,* Bettina V. Lotsch

* These authors contributed equally to this work.

8.3 ABSTRACT

By virtue of their structural color, Photonic crystals have emerged as attractive colorimetric sensors. Their ease of use as well as their inexpensive fabrication have made these devices a successful commercial case. Despite their advanced development stage, insights into the sensing mechanism, in particular the diffusion of analytes through photonic multilayer systems, are largely lacking, but are key for their design. Herein, we use bio-inspired 1D Photonic Crystals based on swellable 2D nanosheets and dielectric nanoparticles as a model system and track the time-dependent intercalation of amine molecules into the structure by optical spectroscopy and theoretical modelling. We follow the consecutive swelling of the layers in real-time and show that with increasing analyte size, both colour shifts and diffusion times increase significantly, while infiltration of the multilayer system is complete in a few seconds. The methodology developed here introduces a new method to study diffusion processes in complex photonic nanostructures and thin films based on a simple optical readout.

8.4 INTRODUCTION

The trend towards digitalization and automation, prominently represented by the Internet of Things (IoT),[1] comes along with an increasing demand for novel sensing schemes, miniaturization of sensors, and sensor fusion.[2-4] This renaissance of sensing technology requires a deep understanding of complex sensing processes, such as the interaction of gaseous analytes with the responsive sensor architecture in environmental sensors.[5, 6] It is thus key to understand the time-resolved sensor response to analyte exposure, diffusion, as well as local analyte concentration and saturation. Photonic vapor sensors are unique sensing platforms in that they offer a colorimetric read-out whilst operating in a label free fashion[7] without requiring complex electric wiring.[8-10] In recent years, 1D Photonic Crystals (1DPCs),[10, 11] which are periodic arrays of materials with different dielectric constants, emerged as versatile sensing platforms[12-15] showing well-defined optical properties, a simple structure and ease of integration. Besides, 1DPCs are compatible with a vast amount of stimuli-responsive materials that can be integrated as functional building blocks, including dielectric

nanoparticles,[13, 16] functional nanoparticles[17-[19] mesoporous structures,[14] 2D materials,[8, 20-23] or polymeric multilayers.[24, 25] In addition, 1DPCs have been used to detect and host guest molecules, thereby showing structural flexibility,[26, 27] emissive properties,[28-30] and superior sensing characteristics in terms of analyte selectivity,[9, 19, 31] sensitivity,[8, 9, 20, 24, 32, 33] response times,[8] compact readout[10, 34, 35] and miniaturization in a lab-on-a-chip fashion.[36] The knowledge of time-resolved analyte infiltration into such multilayer structures is key to understand the kinetics of analyte propagation and, hence, response times, the homogeneity of analyte impregnation, and the impact of interfaces. Insights into such microscopic processes would help to design and optimize the sensing architecture, especially with regards to chemical functionalization and modification.[37-40] Several approaches were presented in the literature to analyze the diffusion of vaporous analytes into porous periodic multilayers[37] and optical cavity structures.[41] However, all approaches used spatially averaging techniques and none of them was able to track analyte diffusion in a spatially and temporally resolved fashion. In addition, correlation of analyte diffusion with material specific host-guest interactions remains a formidable task.

In this work, we tackle this challenge by employing a stimuli-responsive 1DPC based on swellable 2D antimony phosphate $H_3Sb_3P_2O_{14}$ nanosheets (NSs)[8, 42, 43] and TiO_2 nanoparticles (NPs)[8] to track time-resolved molecular diffusion into the multilayer system (for the fabrication details see Experimental Section, Supporting Information). While being structurally simple and solution-processable, 1DPCs feature well-defined optical properties which are easy to characterize.[44, 45] To develop 1DPCs into a powerful detection platform, the selection of stimuli-responsive materials showing pronounced environmentally induced dimensional changes and changes in their dielectric properties is decisive. Thus, the material choice is crucial and the integrated NS layers show significant swelling behavior upon intercalation of analytes, such as water or volatile organic compounds;[9, 30] in addition, the RI contrast between NS and NP layers increases upon analyte uptake, as does the reflectance intensity,[8] which is favorable for precise optical analysis.

To be able to track the time-dependent diffusion, we use primary straight-chain amines as the analytes, which have been shown to intercalate into 2D NSs and to induce a pronounced swelling of these layers.[46] The study of adsorption and vertical diffusion of analytes into the periodic multilayer crucially depends on the size, polarity and chemical affinity of the analyte to the host layer. Amines interact strongly with the interlayer protons of the solid acid $H_3Sb_3P_2O_{14}$ and at the same time show high molecular and chemical variety. They are able to form ammonium ions with the protons and are thus trapped between the NSs, causing the NS layers to swell to a different extent depending on their molecular size.[46-48] This layer swelling translates into changes in the structural color,[44] which can be detected with conventional optical methods. By applying these different amines with trending

molecular sizes and chemical properties, we were able to optically track molecular diffusion within the 1DPC. By theoretical analysis of the time-dependent reflectance measurements using the Transfer Matrix Method (TMM)[49, 50] combined with Genetic Algorithms (GAs),[51] we were able to extract information about the temporal evolution of the thickness changes of each NS single layer within the structure upon analyte exposure. Evaluation of the latter allows us to extract accurate information about the layer thicknesses and refractive index (RI) of the individual layers,[52] which is crucial for diffusion studies.

Translating information at the macroscopic level (i.e. color changes) into microscopic information, this study delivers basic insights into the photonic sensing mechanism at the molecular level. In addition, amine intercalation may be used to chemically modify the sensor and tailor its response as shown previously.[46] This study delivers the framework for understanding such time-dependent intercalation processes aiming at sensor functionalization to tailor host-guest interactions and to rationally tune the sensor response.

8.5   RESULTS AND DISCUSSION

In Figure 8.1, the scanning electron microscopy (SEM) cross section image shows a 1DPC comprising 11 layers of alternatingly deposited TiO_2 NPs and $H_3Sb_3P_2O_{14}$ NSs. The homogenous stacking and clean interfaces between the two materials is evidenced by the periodic distribution of the sheet-like and porous morphology in the secondary electron image (Figure 8.1a) and by the material contrast in the back-scattered electron image (Figure 8.1b).

In this work, we study the time-dependent adsorption of primary straight-chain amines with an even number of carbon atoms: butyl- (C4), hexyl- (C6) and octylamine (C8) and investigate the trends arising among the amines with different chain lengths (Figure 8.1c). For consistency, we use an ethanol-amine solution with an amine concentration of 1 M in order to facilitate the evaporation of the larger amines and keep the evaporation rates as comparable as possible. As depicted in Figure 8.1d, the 1DPC was first exposed to the diluted amine through a hole in the glass plate so as to ensure that we exclusively detect the vertical diffusion of the analytes into the stack vertical to the substrate. Subsequently, the reflectance of the ensemble was monitored *in situ* as the amines travel along the structure, whereby the reflectance measurements were performed above the hole, ensuring a homogenous exposure of the monitored area. In addition, to keep all measurements comparable, we used different spots of the same sample for all three sets of measurements. Afterwards, the structure and the reflectance spectra were modeled theoretically.

The initial reflectance maximum at $\lambda \approx 460$ nm was measured (Figure S 8.1), which corresponds to the initial optical response of the sample at ambient conditions ($t = 0_{ambient}$). After exposure to the ethanol-amine mixture, a fast reflectance peak shift, $\Delta\lambda \approx 40$ nm, is observable for all three systems, which is accompanied by an increase in reflectance intensity of $\Delta R \approx 10\%$. By fitting the initial and final spectra after this shift (Figure S 8.1), we correlate the reflectance peak shift to the filling of the structure with ethanol vapor, which is available in excess in the analyte mixture. The magnitude of this initial shift is similar for all three cases, which further confirms that this displacement corresponds to the ethanol uptake of the entire sample. For this reason, we define the time starting point as $t = 0_{EtOH}$, where ethanol already infiltrated the structure. In the fitting procedure, we optimized all layer thicknesses separately, as during the fabrication *via* spin-coating layer thickness variations are common.[15] Further, for the starting point ($t = 0_{EtOH}$), we optimized the effective RI for each material, but restricted it to be equal for the same material in different layers.

In the next step, we analyzed the reflectance spectra monitoring the amine intercalation at $t > 0_{EtOH}$. The time dependent shifts of the reflectance peak were plotted and fitted for ≈ 30 spectra from the $t = 0_{EtOH}$ spectrum till the saturation level. Similar to the previous fitting, the layer thicknesses were optimized separately for each individual layers. The RI of the TiO_2 layers was assumed to be constant, considering that after the filling with ethanol in the initial step, no large changes are expected. The effective RI of the NS layers was estimated by taking into account that the intercalation of the analytes and swelling leads to a decrease in RI of the NS layer. Hence, the RI can be extracted from the optical spectra by applying the volumetric effective medium approximation theory,[53, 54] using the filling fraction of the NS layers as the ratio between the layer thickness at $t = 0_{EtOH}$ and at time t for each NS layer, m:

$$ff^t_{NS_m} = d_m^{t=0_{EtOH}}/d_m^t \tag{1}$$
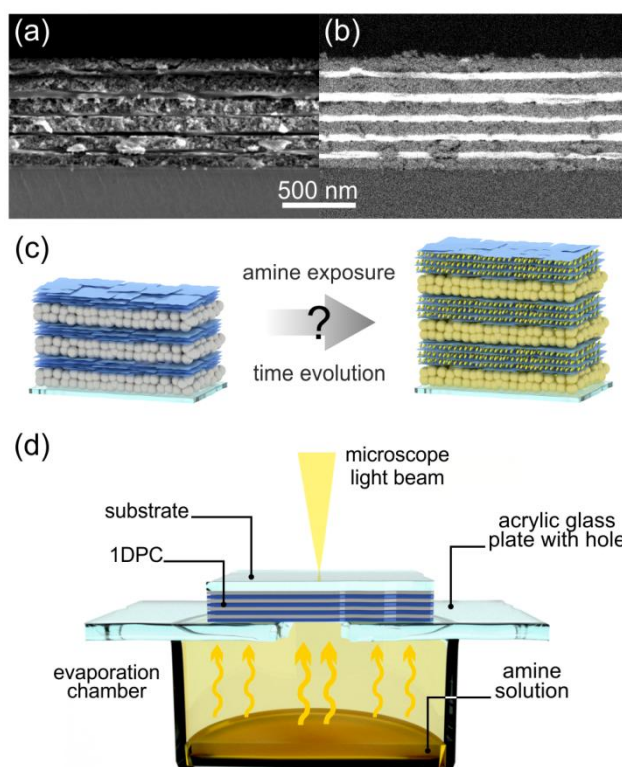
Figure 8.1: (a-b) SEM cross section images of the 1DPC comprised of $H_3Sb_3P_2O_{14}$ NS and TiO_2 NP: (a) secondary electron and (b) back-scattered electron image. (c) Schematic illustration of the objective of this work. The mechanism of analyte uptake and diffusion in the multilayered system is studied in a time and spatially resolved fashion. (d) The schematic experimental setup of the diffusion measurements, showing the exposure and the measurement scheme.

In Figure 8.2, the experimental and corresponding theoretical reflectance spectra are shown in the form of intensity maps. The excellent agreement of the experimental and the theoretical spectra demonstrates that the assumptions made during the fitting process are valid and can be used to extract information on the time evolution and spatial propagation of analyte impregnation of the multilayer system (typical one-dimensional reflectance plots are shown in Figure S 8.2-S 8.4 for different time points).
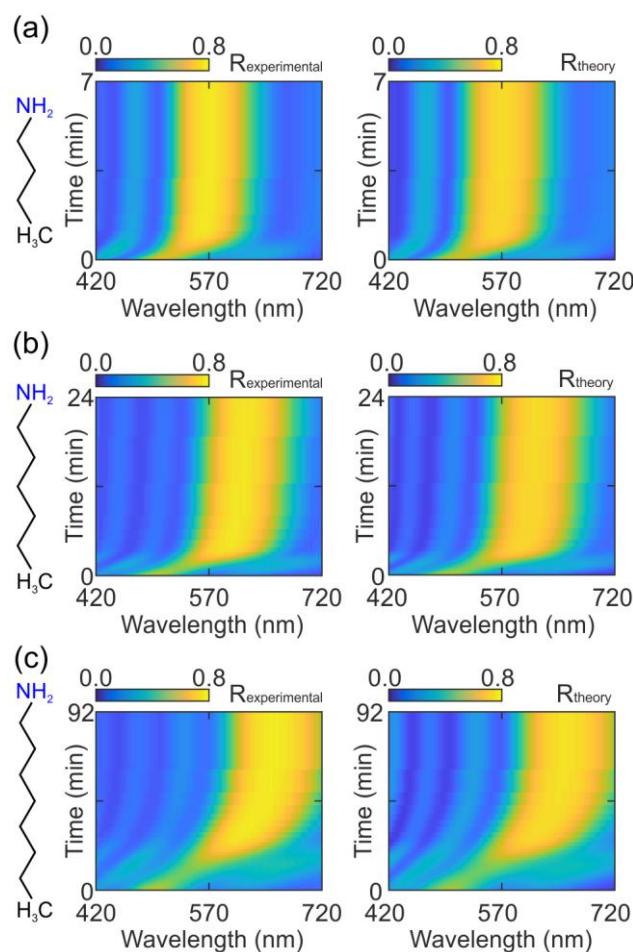
Figure 8.2: Experimental (left hand panels) and theoretical (right hand panels) time-dependent reflectance intensity plots for butylamine (a), hexylamine (b) and octylamine (c) intercalation. Additionally, the analyte molecule structures are shown.

In Figure 8.3, we extract the main features of the course of the optical shifts shown in Figure 8.2. Comparing the changes in the reflectance spectra for the three analytes under study, a clear trend becomes apparent: with increasing size of the analyte molecule, the shifts of the reflectance maximum increase significantly (Figure 8.3a). This effect can be related to the size dependent swelling of the nanosheets,[46] where increasing molecular size of the intercalating species translates into a larger *d*-spacing and, as a consequence, into an increased red-shift of the reflectance band.

A similar trend is observed with respect to the diffusion time defined as the time that is needed to achieve full saturation (i.e. when the reflection peak remains constant): with increasing molecular size from C4 (Figure 8.2a) to C8 (Figure 8.2c), an overall 13-fold increase in the diffusion time can be observed. If we assume that the differences in evaporation rate between the systems are minimized by employing an alcoholic amine solution, these significant differences in the diffusion time can be traced back to differences in the diffusion behavior of the amines in the multilayered structure. For C6 and C8 (Figure 8.3b, red and green curve) a decrease in the reflectance intensity is observed

during the first 50 s and 470 s, respectively, while the drop in intensity is almost negligible for C4 (Figure 8.3b). At longer times, the reflectance peak intensity increases and its spectral position shifts continuously until the saturation point is reached. At this point (Figure 8.3b, dashed lines), high reflectance intensities of about 75% are reached in all cases and the reflectance spectra are broadened compared to the spectra at $t = 0_{ambient}$. These large differences in the diffusion time can be rationalized mostly by the increasing molecule size and kinetic diameter from C4 to C8, and the increasingly hydrophilic molecular interactions, which results in a more inhibited diffusion for the larger amines. However, the unusual behavior of the reflectance intensity needs to be analyzed in order to understand the analyte uptake mechanism. Further explanation along with the time-dependent layer thickness changes will be given in Figure 8.4.

Further, to demonstrate the magnitude of the associated sensing signal and, as a consequence, the applicability of this sensing platform in a current-free environment, the color CIE chromaticity coordinates changes were extracted. As shown in Figure 8.3c-e, the reflectance peak shifts are sufficiently large to allow for detecting the color changes by the naked eye. For the C4 diffusion, a reflectance peak shift of ≈ 75 nm is observed, which corresponds to a color change from green to yellow. For C6, the ≈ 125 nm shift corresponds to a color change of green to orange, while for C8, a reflectance peak shift of ≈ 170 nm with a color change from green to red is observed.
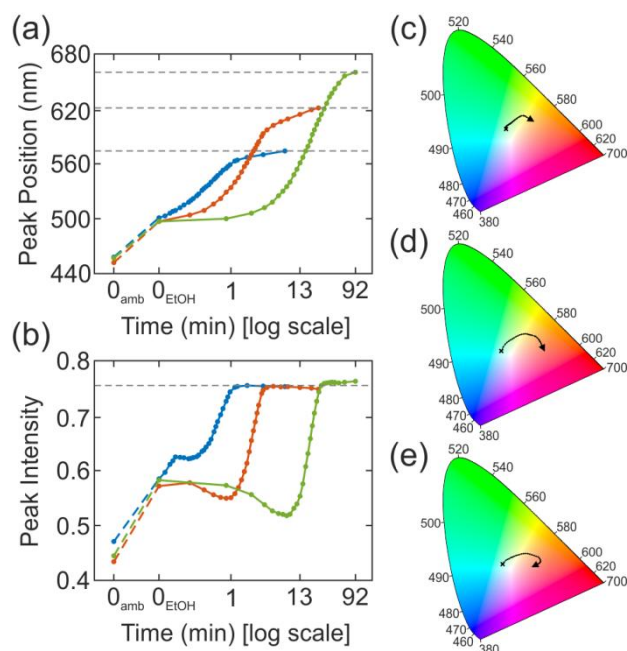
Figure 8.3: (a-b) Time evolution of the reflectance peak position (a) and intensity (b) for C4 (blue), C6 (red) and C8 (green), dashed gray lines show the saturation points. (e-g) CIE chromaticity coordinates evolution extracted from the experimental reflectance spectra during intercalation of the amines C4 (c), C6 (d) and C8 (e).

While the above analysis reveals details of the kinetics of analyte diffusion into the multilayer ensemble, we can go one step further and deconvolute the reflectance changes into the local analyte distribution and, hence, gain spatio-temporal information of the sensing process. To this end, we extracted the single layer thickness changes of each NS layer during the intercalation process and analyzed them with respect to the elapsed time. Using this procedure, the overall spectral evolution is translated into the filling state of the individual layers, yielding further insights into the molecular diffusion and adsorption mechanism. Figure 8.4 show the results of the fittings, where for all plots layer #1 refers to the first NS layer closest to the air/sample interface through which the analyte is introduced into the multilayer system, and layer #5 is the NS layer close to the substrate. The TiO$_2$ NP layer thickness and RI are both assumed to be constant after the saturation with ethanol at t = 0$_{EtOH}$. For C4 (Figure 8.4a and Table S 8.1), layers #1 and #2 behave almost similar, and for both an immediate swelling by ≈ 27 nm is observed after the amines reach the multilayered structure. Layers #3 and #4 are delayed by ≈ 4 s and show the same extent of layer swelling, and finally the growth of layer #5 starts after ≈ 20 s, but the extent of the swelling is similar to the other layers. After a short time, ≈ 77 s, the layer thicknesses reach a collective value and swell together until the saturation after 7 min and a swelling of 31 nm is reached. For C6 (Figure 8.4b and Table S1), the time delay by which the layers consecutively swell is more extreme. The layer thickness increase of #1 and #2 starts immediately, and the other layers follow this behavior at longer times: #3 at 30 s, #4 at 50 s and #5 at 100 s. After 6 min, all layers have nearly reached a collective swollen state (30 to 52 nm) and only a further layer thickness increase of ≈ 7 nm each is observed. While for C4 the layers swell by approximately 31 nm each, the maximum swelling of the individual layers reaches a value between 49 and 57 nm each for C6 in a total diffusion time of 24 min, which can be lead back to the increased molecular size of C6 compared to C4. Similarly, the larger molecular size is also responsible for the slower diffusion times. This trend continues for C8 (Figure 8.4c and Table S1), where the swelling of the individual layer diverges even more with time: #1 and #2 start to grow immediately, while #3 starts at 280 s, #4 at 470 s and #5 at 840 s. The abrupt growth values correspond to an individual layer swelling of all layers of 40 nm. Contrary to the previous systems, the swelling procedure is not finished after the growth of layer #5, but the layers collectively grow more, and a total layer swelling of all individual layers of ≈ 60-72 nm in a total diffusion time of 92 min is reached. These values fit well with the trends of the previously reported systems.[46, 48]

To put these findings into perspective, we rationalize the observed time evolution of the multilayer system based on the host-guest interactions between ethanol, amine and the NS host layers (Figure 8.4d). In all cases, an initial homogenous reflectance peak shift is observed (between

$t = 0_{ambient}$ and $t = 0_{EtOH}$), which corresponds to the ethanol infiltration of the system. While the TiO_2 nanoparticle layers take up only ethanol, the individual nanosheet layers swell with increasing time delays and different magnitudes (Table S1, Supporting Information) with increasing molecular size. For all cases, layers #1 and #2 behave similarly and start to swell immediately after analyte exposure, suggesting that the amine molecules are able to infiltrate the first two NS layers simultaneously. From layer #3, a time delay is observed, which differs in magnitude for all amines and indicates delayed intercalation of the analyte molecules with increasing depth of the layer within the multilayer ensemble. For larger amine chain lengths, the delays are more significant, as the diffusion of the analytes within the stack is slower. For C6 and C8, the different time response of the layers breaks the periodicity of the 1DPC, giving rise to a decrease in the reflectance peak intensity as observed in Figure 8.3b. Once the layers reach similar thicknesses upon swelling, the periodicity is restored and the reflectance intensity further increases due to the enhanced RI contrast between the NS and TiO_2 NP layers.
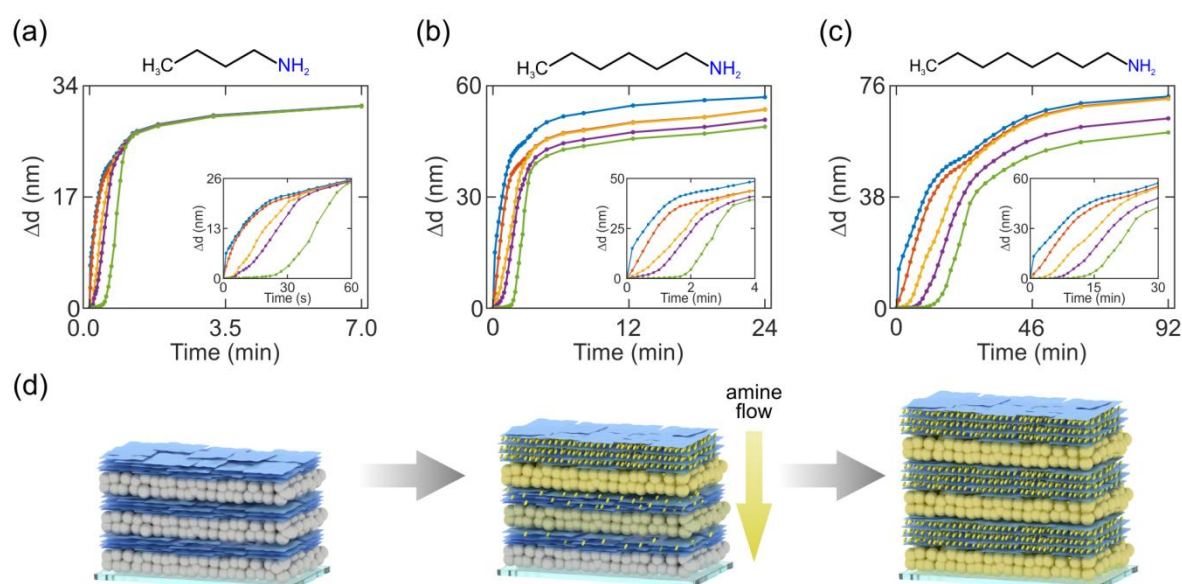
Figure 8.4: (a-c) Calculated layer thickness evolution of the same $H_3Sb_3P_2O_{14}$ NS / TiO_2 NP based 1DPC upon the intercalation of C4 (a), C6 (b) and C8 (c), different layers are coded with different colors: #1 (blue), #2 (red), #3 (yellow), #4 (purple) and #5 (green). (d) Scheme of the proposed intercalation mechanism into the 1DPC based on the measured and theoretical analysis. The amine flow within the system is indicated by a yellow arrow.

In conclusion, we have established a photonic model system composed of $H_3Sb_3P_2O_{14}$ nanosheets and TiO_2 nanoparticles, based on which we could optically track time-dependent molecular diffusion within a periodic multilayer structure for the first time. By combining optical reflectance measurements with theoretical modeling, we have analyzed the vertical diffusion of amines along the multilayer stack and related the observed trends in layer swelling and diffusion times to different

host-guest interactions for the different primary amines under study. With increasing molecular size, the diffusion kinetics is significantly slowed down and the analyte reaches the layers buried beneath the surface with a longer time delay compared to the smaller amines. Importantly, we verified that multilayer filling is complete in all cases, but only after allowing for sufficiently long analyte diffusion times of up to 92 min for the largest analyte octylamine, an issue that is highly relevant for correct sensor handling. Thus, these studies do not only contribute to a better understanding of analyte diffusion through multilayer systems, but they also reveal and rationalize key characteristics of vapor sensors such as response and saturation times, and give insights into the sensing mechanism which is governed by molecular properties and the strength of host-guest interactions. Ultimately, the strategy laid out here sets the stage to study molecular diffusion processes in arbitrary photonic structures and thin film architectures in real time, based on a simple optical read-out.

8.6 ACKNOWLEDGEMENTS

8.7 REFERENCES

[1]   L. Atzori, A. Iera, G. Morabito, *Comput. Networks* **2010**, *54*, 2787-2805.

[2]   R. A. Potyrailo, *Chem. Soc. Rev.* **2017**, *46*, 5311-5346.

[3]   V. Haasz, K. Madani, *Advanced Data Acquisition and Intelligent Data Processing*, River Publishers, **2014**.

[4]   M. M. Cruz-Cunha, *Handbook of Research on Mobility and Computing: Evolving Technologies and Ubiquitous Impacts: Evolving Technologies and Ubiquitous Impacts*, Information Science Reference, **2011**.

[5]   S. Yang, C. Jiang, S.-h. Wei, *Appl. Phys. Rev.* **2017**, *4*, 021304.

[6]   A. M. Azad, S. A. Akbar, S. G. Mhaisalkar, L. D. Birkefeld, K. S. Goto, *J. Electrochem. Soc.* **1992**, *139*, 3690-3704.

[7]   R. Sriram, J. E. Baker, P. M. Fauchet, B. L. Miller, *Proc. SPIE Vol. 8570*, **2013**, pp. 857007.

[8]   K. Szendrei, P. Ganter, O. Sánchez-Sobrado, R. Eger, A. Kuhn, B. V. Lotsch, *Adv. Mater.* **2015**, *27*, 6341-6348.

[9]   P. Ganter, K. Szendrei, B. V. Lotsch, *Adv. Mater.* **2016**, *28*, 7294-7294.

[10]   C. Fenzl, T. Hirsch, O. S. Wolfbeis, *Angew. Chem. Int. Ed.* **2014**, *53*, 3318-3335.

[11]   R. V. Nair, R. Vijaya, *Prog. Quantum Electron.* **2010**, *34*, 89-134.

[12]   S. Y. Choi, M. Mamak, G. von Freymann, N. Chopra, G. A. Ozin, *Nano Lett.* **2006**, *6*, 2456.

[13]   S. Colodrero, M. Ocaña, H. Míguez, *Langmuir* **2008**, *24*, 4430-4434.

[14]   M. C. Fuertes, S. Colodrero, G. Lozano, A. R. González-Elipe, D. Grosso, C. Boissière, C. Sánchez, G. J. d. A. A. Soler-Illia, H. Míguez, *J. Phys. Chem. C* **2008**, *112*, 3157-3163.

[15]   M. E. Calvo, O. Sánchez-Sobrado, S. Colodrero, H. Míguez, *Langmuir* **2009**, *25*, 2443-2448.

[16]   S. Colodrero, M. Ocana, A. R. Gonzalez-Elipe, H. Miguez, *Langmuir* **2008**, *24*, 9135-9139.

[17]   F. M. Hinterholzinger, A. Ranft, J. M. Feckl, B. Ruhle, T. Bein, B. V. Lotsch, *J. Mater. Chem.* **2012**, *22*, 10356-10362.

[18]   A. Ranft, I. Pavlichenko, K. Szendrei, P. M. Zehetmaier, Y. Hu, A. von Mankowski, B. V. Lotsch, *Microporous Mesoporous Mater.* **2015**, *216*, 216-224.

[19]   A. von Mankowski, K. Szendrei-Temesi, C. Koschnick, B. V. Lotsch, *Nanoscale Hori.* **2018**.

[20]   K. Szendrei-Temesi, O. Sanchez-Sobrado, S. B. Betzler, K. M. Durner, T. Holzmann, B. V. Lotsch, *Adv. Func. Mater.* **2018**, *28*, 1705740.

[21]   B. V. Lotsch, G. A. Ozin, *J. Am. Chem. Soc.* **2008**, *130*, 15252-15253.

[22]   B. V. Lotsch, G. A. Ozin, *Adv. Mater.* **2008**, *20*, 4079-4084.

[23]   J. Han, Y. Dou, M. Wei, D. G. Evans, X. Duan, *RSC Adv.* **2012**, *2*, 10488-10491.

[24]   Z. Wang, J. Zhang, J. Xie, C. Li, Y. Li, S. Liang, Z. Tian, T. Wang, H. Zhang, H. Li, W. Xu, B. Yang, *Adv. Funct. Mater.* **2010**, *20*, 3784-3790.

[25]   P. Lova, G. Manfredi, L. Boarino, A. Comite, M. Laus, M. Patrini, F. Marabelli, C. Soci, D. Comoretto, *ACS Photonics* **2015**, *2*, 537-543.

[26]   M. E. Calvo, H. Míguez, *Chem. Mater.* **2010**, *22*, 3909-3915.

[27]   M. E. Calvo, J. R. Castro Smirnov, H. Míguez, *J. Polym. Sci. Part B: Polym. Phys.* **2012**, *50*, 945-956.

[28]   F. Scotognella, D. P. Puzzo, A. Monguzzi, D. S. Wiersma, D. Maschke, R. Tubino, G. A. Ozin, *Small* **2009**, *5*, 2048-2052.

[29]   A. Jiménez-Solano, J. F. Galisteo-López, H. Míguez, *Adv. Opt. Mater.* **2018**, *6*, 1700560.

[30]   K. Szendrei, A. Jiménez-Solano, G. Lozano, B. V. Lotsch, H. Míguez, *Adv. Opt. Mater.* **2017**, *5*, 1700663.

[31]   A. Ranft, F. Niekiel, I. Pavlichenko, N. Stock, B. V. Lotsch, *Chem. Mater.* **2015**, *27*, 1961–1970.

[32]   Y. Kang, J. J. Walish, T. Gorishnyy, E. L. Thomas, *Nat. Mater.* **2007**, *6*, 957-960.

[33]   K. Szendrei-Temesi, O. Sanchez-Sobrado, S. B. Betzler, K. M. Durner, T. Holzmann, B. V. Lotsch, *Adv. Funct. Mater.*, 1705740.

[34]   A. T. Exner, I. Pavlichenko, B. V. Lotsch, G. Scarpa, P. Lugli, *ACS Appl. Mater. Interfaces* **2013**, *5*, 1575-1582.

[35]   I. Pavlichenko, E. Broda, Y. Fukuda, K. Szendrei, A. K. Hatz, G. Scarpa, P. Lugli, C. Brauchle, B. V. Lotsch, *Mater. Horiz.* **2015**, *2*, 299-308.

[36]   K. P. Raymond, I. B. Burgess, M. H. Kinney, M. Loncar, J. Aizenberg, *Lab Chip* **2012**, *12*, 3666.

[37]   P. Allcock, P. A. Snow, *J. Appl. Phys.* **2001**, *90*, 5052-5057.

[38]   P. A. Snow, E. K. Squire, P. S. J. Russell, L. T. Canham, *J. Appl. Phys.* **1999**, *86*, 1781-1784.

[39]   T. L. Kelly, A. Garcia Sega, M. J. Sailor, *Nano Lett.* **2011**, *11*, 3169-3173.

[40]   C. M. Thompson, A. M. Ruminski, A. Garcia Sega, M. J. Sailor, G. M. Miskelly, *Langmuir* **2011**, *27*, 8967-8973.

[41]   L. De Stefano, L. Moretti, I. Rendina, A. M. Rossi, *Sens. Actuators, B* **2004**, *100*, 168-172.

[42]   J.-C. P. Gabriel, F. Camerel, B. J. Lemalre, H. Desvaux, P. Davidson, P. Batail, *Nature* **2001**, *413*, 504.

[43]   Y. Piffard, A. Verbaere, A. Lachgar, S. Deniard-Courant, M. Tournoux, *Rev. Chim. Miner.* **1986**, *23*, 766-775.

[44]   J. D. Joannopoulos, S. G. Johnson, J. N. Winn, R. D. Meade, *Photonic crystals: molding the flow of light*, Princeton university press, **2011**.

[45]   L. D. Bonifacio, B. V. Lotsch, D. P. Puzzo, F. Scotognella, G. A. Ozin, *Adv. Mater.* **2009**, *21*, 1641.

[46]   P. Ganter, L. M. Schoop, M. Däntl, B. V. Lotsch, *Chem. Mater.* **2018**, DOI:10.1021/acs.chemmater.7b04828.

[47]   F. Geng, R. Ma, A. Nakamura, K. Akatsuka, Y. Ebina, Y. Yamauchi, N. Miyamoto, Y. Tateyama, T. Sasaki, *Nat. Commun.* **2013**, *4*, 2641.

[48]   F. Menendez, A. Espina, C. Trobajo, J. Rodriguez, *Mater. Res. Bull.* **1990**, *25*, 1531-1539.

[49]   P. Yeh, *Optical Waves in Layered Media*, John Wiley & Sons, New York, **1988**.

[50]   E. Hecht, *Optics*, Addison-Wesley, Reading, Mass., **2002**.

[51]   D. E. Goldberg, *Genetic Algorithms in Search, Optimization and Machine Learning*, Addison-Wesley Longman Publishing Co., Inc., **1989**.

[52]   M. E. Calvo, L. González-García, J. Parra-Barranco, A. Barranco, A. Jiménez-Solano, A. R. González-Elipe, H. Míguez, *Adv. Opt. Mater.* **2015**, *3*, 171-175.

[53]   A. Garahan, L. Pilon, J. Yin, I. Saxena, *J. Appl. Phys.* **2007**, *101*, 014320.

[54]   N. Nagy, Deak, A., Horvölgyi, Z., Fried, M., Agod, A., Barsony, I., *Langmuir* **2006**, *26*, 8416-8423.

9. CONCLUSION AND OUTLOOK

This thesis addresses current challenges in the evermore developing research field of sensing, which are particularly valid for optical sensing schemes. Here, we suggested new material-based solutions to key sensing characteristics, namely improved selectivity, sensitivity, sensor stability, alternative readout schemes, fast response times and high reversibility. An important motivation of this thesis is to create material-based sensors with inherently robust inorganic materials, which are nanosized, chemically tailorable and solution-processable. Due to the large chemical variety and the possibility for chemical modifications, 2D nanosheet materials carry an inherent potential for resolving the above issues and offer new perspectives in terms of miniaturization and versatility. 2D nanosheet materials were thus chosen as nanosized functional building blocks and were integrated into a simple optical sensing architecture with well-defined optical properties – 1-dimensional Photonic Crystals.

The first approach aiming at an increase of the sensitivity utilizes swellable antimony phosphate nanosheets, $H_3Sb_3P_2O_{14}$, as stimuli-responsive materials in 1DPC architectures. These show a pronounced layer thickness increase in response to changes of environmental humidity (**Chapter 3**). Due to the highly porous character of the multilayer system and the inherently fast response time of the nanosheets, the water uptake process is rapid, which lead to the realization of novel humidity sensing based applications. By realizing optical touchless finger motion tracking, we showed that these ultrasensitive humidity sensors are capable of tracking the humid atmosphere of a human finger under touchless conditions in real-time and true color. Further, several real-world sensor applications were studied, such as the temperature dependency, the cyclability, the reproducibility of the sensing event and the cross sensitivity to other volatile analytes (**Chapter 4**).

In a second approach aiming to increase the selectivity of these platforms, we integrated $HSbP_2O_8$ as another member of the antimony phosphate family into 1DPCs. These nanosheets proved themselves as a smart functional building block with an inherent capability to differentiate various volatile organic analytes (**Chapter 5**). By using a single-component sensor and without any statistical analysis, the response time and the stopband shifts were combined and utilized as useful sensing

descriptors. Based on these two descriptors, we were able to show the potential of this platform to optically differentiate between volatile organic compounds, besides the ultrahigh sensitivity for water vapor. Moreover, different alcohols (i.e. methanol and ethanol) and even constitutional isomers (i.e. 2-butanol and 1-butanol) could be distinguished by our sensor, which are usually difficult to differentiate by optical readout techniques.

Further, to optimize the optical properties of 1DPC based sensing devices, the optical contrast between the two constituent materials of the multilayer system were enhanced by applying the ultrahigh refractive index nanosheet material lithium tin sulfide (**Chapter 6**). With this approach, we could reduce the number of layers that form the structure, leading to a thickness reduction of about 60%, which could result in a significant decrease of production time and cost whilst maintaining the excellent optical properties, such as the high reflectance and the high humidity sensitivity. We could even further increase the humidity sensitivity by combining two swelling nanosheet materials - high RI lithium tin sulfide nanosheets and the previously introduced antimony phosphate nanosheets.

Not only the stimuli-responsive materials in 1DPCs were developed, but also the sensor architectures: we integrated the swelling nanosheets into carefully designed optical resonator structures (**Chapter 7**). Hereby, we utilized the coupling of photoluminescence of nanoemitters with the photonic modes sustained by the structure. To this end, we embedded into rationally designed photonic resonator structures a thin layer of dye-functionalized nanospheres into the humidity-responsive defect layer at a well-defined position. By dynamic humidity induced changes of the optical cavity composed of swellable antimony phosphate nanosheets, changes in the photoluminescence could be induced, which lead to the creation of the first luminescent photonic humidity sensor. Furthermore, complete suppression of the photoluminescence at a certain humidity level was demonstrated, which allowed to construct humidity driven luminescent switches.

Finally, we investigated important features regarding time-dependent sensing mechanisms and the analyte infiltration into the multilayered structure (**Chapter 8**). For this, a model system was constructed, a $H_3Sb_3P_2O_{14}$ nanosheet / TiO_2 nanoparticle based 1DPC, which is capable of intercalating (primary) amines due to the formation of ammonium ions in the interlayer space. By varying the amine chain length, the response time and the stopband shift can be dynamically tuned and different sensor-analyte interactions can be obtained. Additionally, extensive theoretical investigations were performed, whereby the exact layer thicknesses of the 1DPCs depending on the progress of the chemical diffusion were extracted by fitting the time-dependent reflectance measurements. As a result, we can temporally resolve the vertical analyte infiltration into the multilayer, relying on optical methods.

In conclusion, novel material-based solutions were proposed which address key challenges in the design of optical vapor sensors, such as the selectivity, sensitivity, optical properties and readout schemes. However, for the applicability and the integration of such 1DPC-based functional material based sensors into devices, some remaining challenges are to be solved.

9.1 OUTLOOK

Although these material-based solutions offer enhancement in the sensing performance, for an integration of these optical sensors into sensing devices some general issues and case- and application-specific problems are to be overcome. In the following, some of these issues are discussed.

Tuning the Sensitivity Towards Other Analytes

In this thesis, mostly optical sensors were presented where the sensitivity towards water vapor is decisive. Even for the volatile organic compound (VOC) sensors (Chapter 5), the humidity sensitivity was the primary effect. For environmental or industrial applications, diverse target vapors and gases are relevant, e.g. toxic gases, such as CO_2, CO, NO_x or SO_2,[1, 2] or acetone and ethanol for medical diagnostic approaches or breathalyzers. For these approaches it is also crucial that the sensing response is independent of the ambient conditions, such as the temperature or the relative humidity, e.g. there is no cross-sensitivity of the sensor towards water vapor. These goals may be solved with covalent or intercalative modification[3] of the here presented 2D material based sensing devices. This chemical modification of the nanosheets with tailor-made functional groups can lead to specific molecular interactions and a selective adsorption of the gases or vapors.

Flexible Structures

To address diverse sensing needs and application requirements, it would be advantageous to make such optical sensors flexible. One approach aiming a transferable and free standing 1DPCs was presented in the literature.[4, 5] However, through the filling of the porous structure with a flexible polymer, the porosity and with it, the sensing capability, is suppressed. For this reason, other approaches have to be tested in order to make these sensors mechanically flexible, but keep the vapor responsiveness, such as the usage of a flexible substrate or the transfer of the multilayer to a flexible substrate. First preliminary results show that the nanosheets imbue the entire multilayer structure with mechanical stability, which in extreme cases, such as under ultrahigh vacuum in the scanning electron microscopy measurements, can lead to peeling off of the entire structure without destroying the nanostructure (Figure 9.1).
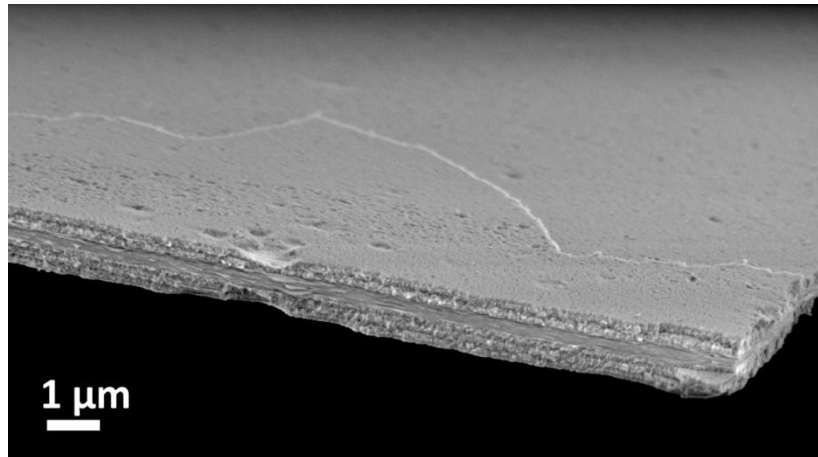
Figure 9.1: SEM cross section image of the optical resonator structure presented in Chapter 7, showing a free standing behavior.

Digital Readout

Although the optical detection with the possibility of a qualitative naked-eye-readout offers possibilities for sensing applications in an electrical current-free environment, for the integration of devices for customer use or sensor arrays, the optical signals most likely have to be converted into electric signals. The luminescence based readout (Chapter 7) presents one step into this direction, as the photoluminescence signal can be easily converted with a photodiode into electric signal changes. Further, for the pure photonic systems, using the "electrophotonic nose" could be a possible solution.[6, 7] Hereby an organic light emitting diode, OLED, i.e. a narrow-band light source, is used for the illumination, and due to the stopband shifts, the intensity of the transmitted light changes, which can be converted with a photodiode into an electric signal.

Mechanical Protection

Especially for the presented optical touchless positioning interfaces (Chapter 3 and 4), but also for all sensing applications in general, a mechanical and chemical protection of these sensing devices is inevitable for commercial use. Hereby, the choice of the protective layer is crucial and has to fit several requirements. One is naturally the mechanical stability; the protective layer has to shield the sensor from environmental impact, such as mechanical forces, chemicals or other damaging effects. Secondly, the protective layer has to be structurally and optically compatible with the 1DPC-based structures, which means that a sufficient adhesion on top of the structure is required, without damaging the sensor and without an impact on the optical properties of the multilayered structures. And finally, a defined vapor permeability has to be ensured, i.e. through a defined porosity of this protective layer. With this defined porosity, the selectivity could also be enhanced through the size-dependent permeability of the membrane. First experiments using carbon nanomembranes

(CNM)[8, 9] confirmed the optical and structural compatibility with the 1DPCs, but further investigations are needed in order to quantify the impact of the CNM layer on analyte diffusion.

9.2 REFERENCES

[1] A. M. Azad, S. A. Akbar, S. G. Mhaisalkar, L. D. Birkefeld, K. S. Goto, *J. Electrochem. Soc.* **1992**, *139*, 3690-3704.

[2] W. Hong, Y. Chen, X. Feng, Y. Yan, X. Hu, B. Zhao, F. Zhang, D. Zhang, Z. Xu, Y. Lai, *Chem. Commun.* **2013**, *49*, 8229-8231.

[3] P. Ganter, L. M. Schoop, B. V. Lotsch, *Adv. Mater.* **2017**, *29*, 1604884.

[4] M. E. Calvo, H. Míguez, *Chem. Mater.* **2010**, *22*, 3909-3915.

[5] M. E. Calvo, J. R. Castro Smirnov, H. Míguez, *J. Polym. Sci. Part B: Polym. Phys.* **2012**, *50*, 945-956.

[6] A. T. Exner, I. Pavlichenko, D. Baierl, M. Schmidt, G. Derondeau, B. V. Lotsch, P. Lugli, G. Scarpa, *Laser Photonics Rev.* **2014**, *5*, 726-733.

[7] I. Pavlichenko, E. Broda, Y. Fukuda, K. Szendrei, A. K. Hatz, G. Scarpa, P. Lugli, C. Brauchle, B. V. Lotsch, *Mater. Horiz.* **2015**, *2*, 299-308.

[8] A. Turchanin, A. Gölzhäuser, *Adv. Mater.* **2016**, *28*, 6075-6103.

[9] P. Angelova, H. Vieker, N.-E. Weber, D. Matei, O. Reimer, I. Meier, S. Kurasch, J. Biskupek, D. Lorbach, K. Wunderlich, L. Chen, A. Terfort, M. Klapper, K. Müllen, U. Kaiser, A. Gölzhäuser, A. Turchanin, *ACS Nano* **2013**, *7*, 6489-6497.

10. APPENDIX

In this section, a list of important abbreviations, the Supporting Informations for Chapter 3, Chapter 5, Chapter 6, Chapter 7 and Chapter 8 are provided, which are followed by a List of Publications and Scientific Contributions and a short *Curriculum Vitae*.

– Appendix –

LIST OF ABBREVIATIONS

1D	**1-dimensional**
2D	2-dimensional
3D	3-dimensional
A	Absorptance
AFM	Atomic Force Microscopy
BF	Bright Field
BP	Bragg Peak
BS	Bragg Stack
CEM	Controlled Evaporation Mixer
DBR	Distributed Bragg reflector
DF	Dark Field
DLS	Dynamic Light Scattering
EDX	Energy-Dispersive X-ray
EELS	Electron Energy Loss Spectroscopy
EM	Eletromagnetic
FIB	Focused Ion Beam
GA	Genetic Algorithm
I	Intensity
ICP	Inductively Coupled Plasma
IoT	Internet of Things
LDH	Layered Double Hydroxide
LFC	Liquid Flow Controller
LTS	Lithium Tin Sulfide
MFC	Mass Flow Controller
MOF	Metal-Organic Framework
NP	Nanoparticle
NS	Nanosheet
PC	Photonic Crystal
PCA	Principal Component Analysis
PL	Photoluminescence
R	Reflectance
RH	Relative Humidity
RI	Refractive Index

SAED	Selected Area Electron Diffraction
SEM	Scanning Electron Microscopy
STEM	Scanning Transmission Electron Microscopy
T	Transmittance
TEM	Transmission Electron Microscopy
TMM	Transfer Matrix Method
UV	Ultraviolet
Vis	Visible
VOC	Volatile Organic Compound
XRD	X-ray Diffraction

10.1 Supporting Information for Chapter 3

Touchless Optical Finger Motion Tracking based on 2D Nanosheets with Giant Moisture Responsiveness

Katalin Szendrei [¶], Pirmin Ganter [¶], Olalla Sànchez-Sobrado, Roland Eger, Alexander Kuhn, Bettina V. Lotsch*

[¶] These authors contributed equally to this work.

Methods

Solid state synthesis, protonation and exfoliation of nanosheets

For the synthesis of $K_3Sb_3P_2O_{14}$ the precursors (KNO_3 (99 %, Merck), Sb_2O_3 (99.6 %, Alfa Aesar), $NH_4H_2PO_4$ (98 %+, Acros Organics)) were thoroughly ground in a stoichiometric ratio and heated up as described elsewhere.[1] For the proton exchange reaction, 2 g of $K_3Sb_3P_2O_{14}$ were treated with 250 mL of 8 M nitric acid (diluted 65 wt%, Merck) overnight, filtrated, washed with ethanol and dried at room temperature. This treatment was repeated one more time to complete the exchange reaction.[2] The success was monitored by XRD. Exfoliation was carried out by stirring the $H_3Sb_3P_2O_{14}$ vigorously overnight in pure water with a concentration of bulk protons of 7.3 mmol L^{-1}. The obtained colloidal suspensions were centrifuged at 3000 rpm for 30 min to remove non-exfoliated bulk material. The supernatant is a suspension of mainly single-layer nanosheets. To obtain the nanosheet pellet, an additional centrifugation step was applied at 18000 rpm for 30 min. The supernatant was discarded and the gel-like colorless wet aggregate was dried at 100 °C.

Synthesis of nanoparticles

TiO_2 nanoparticulate sols were synthesized using a procedure described elsewhere.[3] The colloidal suspension of titania nanoparticles used for spin-coating was obtained by collection of the particles by repeated centrifugation at 24000 rpm and redispersion in methanol.

SiO_2 nanocolloids were purchased from Dupont (LUDOX TMA, Aldrich, 30 nm particle size, 34 wt%).

Preparation of colloidal suspensions

The dried colorless precipitate of the water exfoliated $H_3Sb_3P_2O_{14}$ nanosheets was redispersed with a concentration of 42 mmol L^{-1} in a water/ethanol mixture (60 vol% ethanol) and sonicated for 2 h. The TiO_2 suspensions had a concentration of 2.5 wt% in methanol. The commercial colloids of SiO_2 were redispersed at 3 wt% in methanol.

Fabrication of thin films and Bragg stacks

All films were made by means of spin-coating using a spin-coater (WS-650S-NPP-Lite, Laurell Technologies Corporation) and concentrations given above. Different film thicknesses were accessed by varying the spin-coating speed, which allowed the fine-tuning of the optical properties.[4] On plasma cleaned microscope glass slides with the dimensions of 2.5 cm x 2.5 cm, 400 µl of the colloidal suspensions were spin-coated alternatingly for 1 min with a defined speed, and heated to 80 °C for 15 min after each layer deposition. 2000 rpm, 3000 rpm and 4000 rpm spin-coating speeds were applied (the same speed for each layer within a Bragg stack) to tune the optical properties, while other parameters such as colloidal concentration, spin-coating time and acceleration rate (10000 rpm/s) were kept constant. For conductance measurements, this redispersed $Sb_3P_2O_{14}^{3-}$ nanosheet colloid was spin-coated at 3000 rpm or 2000 rpm for 1 min with a 10000 rpm s^{-1} acceleration ramp on a 1.5 cm x 1.5 cm plasma-cleaned quartz substrate. Gold contacts were sputter-coated (108auto, Cressington) with 180 s sputtering time.

CHARACTERIZATION

Structural characterization

TEM images and selected area electron diffraction (SAD) patterns were obtained with a Phillips CM30 ST TEM (300 kV, LaB_6 cathode) equipped with a Gatan CCD camera. TEM-EDX analysis was performed with a Si/Li detector (Thermo Fisher, Noran System Seven). SEM images of the nanosheet pellet were collected with a Vega TS 5130 MM (Tescan) equipped with Si/Li detector (Oxford). SEM cross-sectional images of the Bragg stacks were taken with a Zeiss Merlin FE-SEM. AFM measurements were done on a Veeco CP II system in non-contact mode. XRD patterns were collected on a powder X-ray diffractometer (Stadi P, STOE) working with Ge(111) monochromated Mo-$K_{\alpha1}$ radiation (λ = 70.926 pm) or Cu-$K_{\alpha1}$ radiation (λ = 154.051 pm) in Debye-Scherrer or transmission geometry with an image-plate detector or a point detector. Well-ground samples were either put between two Mylar® foils or filled in a glass capillary. Indexing was performed with the software DiffracPlus TOPAS v4.2 (Bruker AXS). The images of the Bragg stack surfaces were obtained with an optical microscope (Olympus BX51), operating in reflection mode with a 4x objective.

Conductance measurements

To obtain the conductance measurements, two different methodologies were used. In the first one, the films were kept over saturated salt solutions,[5, 6] at around 25 °C in a closed atmosphere at least 15 min before the conductance measurements. In the second one, we used an argon flow set up (Figure S 3.10). A dry Ar flow and a water vapor saturated Ar stream were mixed in different ratios to

define the humidity between 0-93.5%. The setup was calibrated using the conductance values previously measured at the RH defined by the salt solutions. The cycling experiments were performed with either the Ar flow setup, Figure S 3.10, or by a tapping motion of a human finger. The change in conductance was monitored by impedance spectroscopy (in plane geometry, two point measurement) with an impedance bridge (Princeton Apllied Research, VersaSTAT MC) applying an AC voltage of 500 mV and a frequency range of 1 Hz to 1 MHz. Cycling measurements were performed with a fixed frequency of 300 Hz.

Optical measurements

Porosimetry measurements were carried out by the porosimetry tool of Sopra PS-1000 SAM, whereby the sample was equilibrated at all water vapor relative pressure values for 15 min. The measurement results were fitted with the software Sopra SAE using the model combination Cauchy and Lorentz. The thickness of the nanoparticle layers was considered as constant and only the refractive index was fitted over the relative pressure range. For the nanosheet thin films both values, the layer thickness and also the refractive index were fitted. Before all measurements, the nanoparticle samples were heated for at least 30 min at 200 °C and the nanosheet thin films for 30 min at 60 °C in vacuum to make sure that the pores are empty. To obtain the optical isotherms, all fitted measurement results were plotted against the analyte relative pressure.

All optical spectra were measured with a fiber optic spectrometer (USB2000+, Ocean Optics) attached to a microscope (DM2500, Leica) with normal incidence and the optical spectra were always taken at the same spot ($1 \times 1\ mm^2$ in area). To obtain the optical changes with relative humidity change, the Bragg stacks were kept in a stainless steel chamber with a transparent glass window and a total volume of 5 mL, placed above 0.7 mL of the saturated salt solutions at around 25 °C[5,6] as described above (see conductance measurements). At each step, 20 min atmosphere equilibration time was needed. To illustrate the reversibility, a dynamic method using a nitrogen flow setup (see below) was applied. Hereby, the reflectance intensity changes of the Bragg peak were observed at a certain wavelength placed at the red stop band edge. While the Bragg peak shifts in response to the analyte exposure, the reflectance intensity changes at the observed wavelength. In these dynamic measurements, the BSs were placed into a closed chamber with the dimensions of $2.5 \times 2.5 \times 0.5\ cm^3$, where well-defined relative humidity values were realized by connecting the inserted pipette tip with a liquid-gas flow controller (Bronkhorst) and a vaporizer (CEM) with a massflow-controlled carrier gas flow. To observe a specific relative humidity, the carrier gas nitrogen ($200\ mL\ min^{-1}$) and the liquid water were dosed into the CEM (controlled evaporation and mixing, W101A-130-K, Bronkhorst High-Tech),[7] where the thermal evaporation of water took place. The CEM was heated to temperatures above the boiling point (120 °C for water). The relative vapor

pressures were calculated via the software FLUIDAT (CEM calculation), which considers the actual atmospheric pressure, the temperature and the properties of the analyte (vapor pressure, heat capacity).[8] The spectra were measured in the visible range with an OCEAN OPTICS QP400-2-UV-BX optical fiber interfaced with a LEICA DM 2500 M microscope. The obtained data were analyzed with the SPECTRA SUITE (2008) software.

Touchless positioning interface measurements

Conductance measurements were carried out by impedance spectroscopy (see above) by placing a finger in different distances to the film surface (between 0.1 and 1.6 cm) without touching the thin film device. For determination of the response and recovery time, a human finger was approached (ca. 1 mm distance) to the surface and removed subsequently. The response and recovery times were determined as the time to observe 90% of the conductance change (see Figure S 3.16). The real time conductance manipulation video was recorded using a smartphone camera.

Optical measurements were carried out similarly; a finger was approached to the Bragg stack in 1 mm distance. Hereby, lateral optical changes were detected by the optical microscope (Olympus BX51) coupled to a CMOS camera and an Ocean Optics USB4000-XR1-ES spectrometer. A finger cycling was carried out by approaching and distancing the finger in regular intervals of ca. 30 s. This measurement was used to determine the response time of the Bragg stack, which was defined as the time it takes for 90% of the stopband shift before the structural color vanishes. To detect the stopband changes, the intensity changes at the wavelength 475 nm were followed. The optical tracking of the finger movements close to the Bragg stack surface were recorded by a conventional smartphone camera.

$K_3Sb_3P_2O_{14}$ and $H_3Sb_3P_2O_{14}$ bulk materials synthesis and characterization
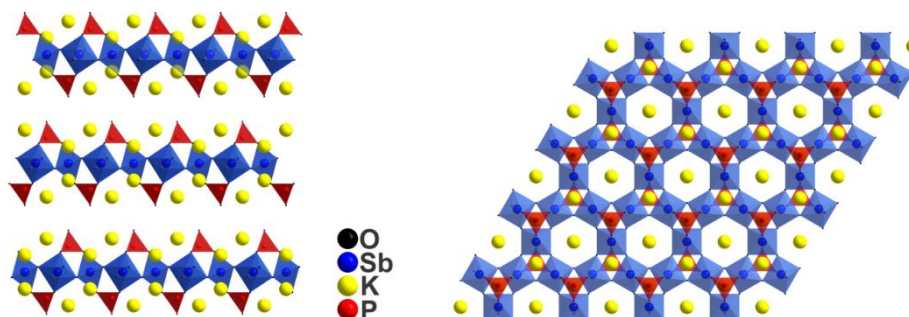
Figure S 3.1: From left to right: Structure of $K_3Sb_3P_2O_{14} \cdot 1.3\ H_2O$ viewed along [010] (left) and [001] (right). For a better overview, only one layer is shown along [001] and for $K_3Sb_3P_2O_{14} \cdot 1.3\ H_2O$ the O positions between the layers were left out.
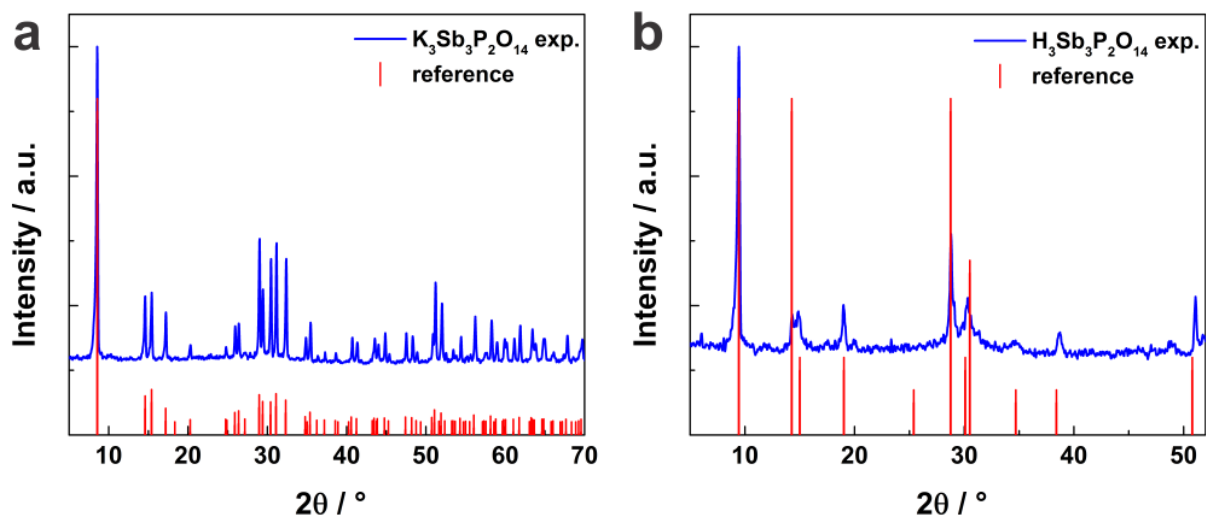
Figure S 3.2: Experimental XRD patterns of a) $K_3Sb_3P_2O_{14}$ and b) $H_3Sb_3P_2O_{14}$ (in blue) and reference XRDs from the literature (red) for (a) $K_3Sb_3P_2O_{14} \cdot 5\ H_2O$ and (b) for $H_3Sb_3P_2O_{14} \cdot 5\ H_2O$, respectively. Experimental XRD patterns were recorded with Cu-K$_{\alpha 1}$ radiation.

Table S 3.1: EDX data for $K_3Sb_3P_2O_{14}$ (measured over five points) and for $H_3Sb_3P_2O_{14}$ (measured over four points). Standard deviations are given in the brackets.

Sample	K Atom%	Sb Atom%	P Atom%	O Atom%	Calc. Formula
Theoretical values	11.1	11.1	7.4	70.4	$K_3Sb_3P_2O_{14} \cdot 5\ H_2O$
Exper.	11 (2)	11 (2)	7.2 (6)	71 (5)	$K_{3.05}Sb_{3.08}P_2O_{19.86}$
Theoretical values	-	15.8	10.5	73.6	$H_3Sb_3P_2O_{14}$
Exper.	-	15 (2)	9.1(7)	76 (3)	$H_3Sb_{3.28}P_2O_{16.72}$
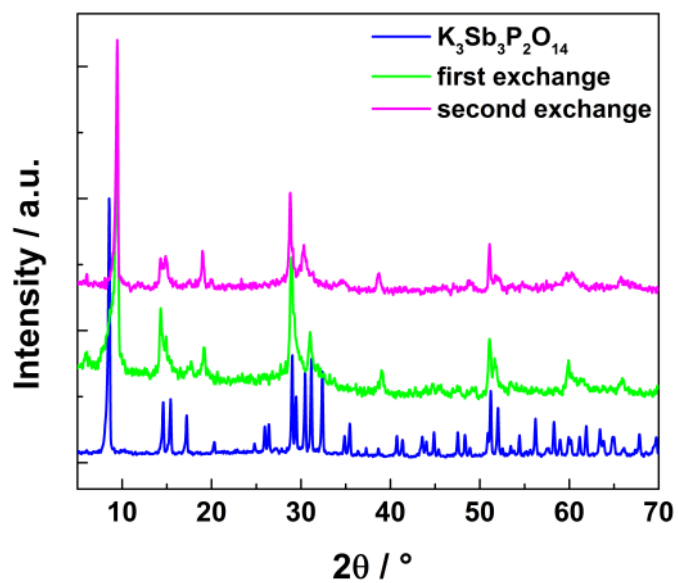
Figure S 3.3: Details of the evolution of the cation‑proton exchange for $K_3Sb_3P_2O_{14}$ (two exchange steps required). Experimental XRD patterns recorded with Cu-$K_{\alpha 1}$ radiation.

Characterization of the nanosheets
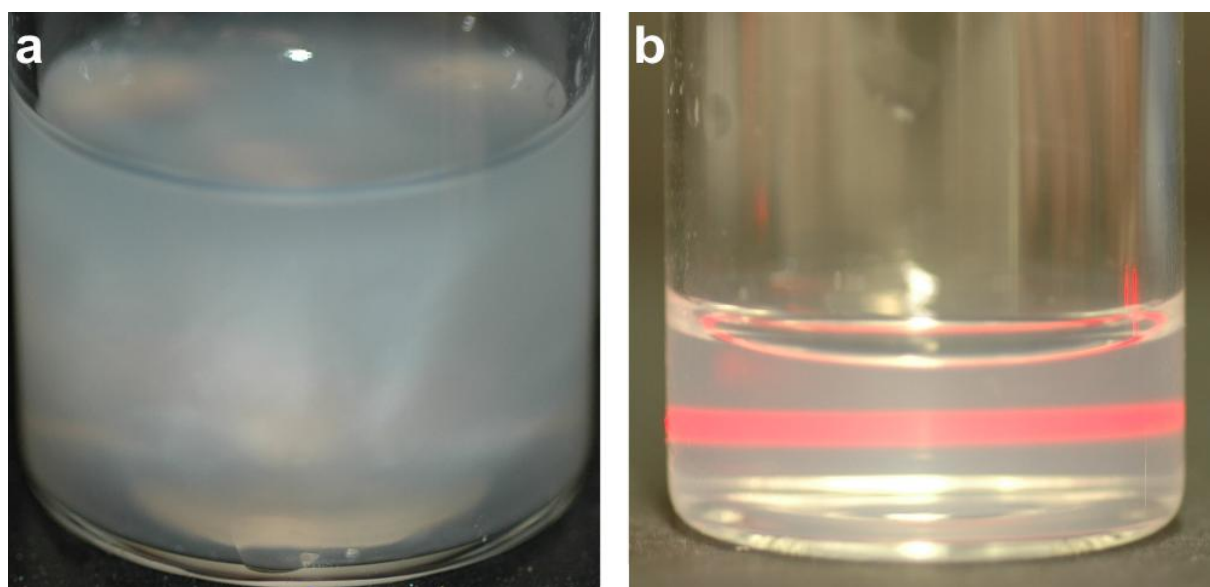
Figure S 3.4: Schlieren texture a) and Tyndall effect b) of $Sb_3P_2O_{14}^{3-}$ nanosheet suspensions in water.

Table S 3.2: TEM-EDX data for the different samples of exfoliated $Sb_3P_2O_{14}^{3-}$ nanosheets.

Sample	Sb Atom%	P Atom%	O Atom%	Calc. Formula
Theoretical values	15.8	10.5	73.6	$Sb_3P_2O_{14}^{3-}$
Exper. (I)	15.23	9.38	75.40	$Sb_{3.25}P_2O_{16.08}$
Exper. (II)	15.23	10.25	74.52	$Sb_{2.97}P_2O_{14.54}$
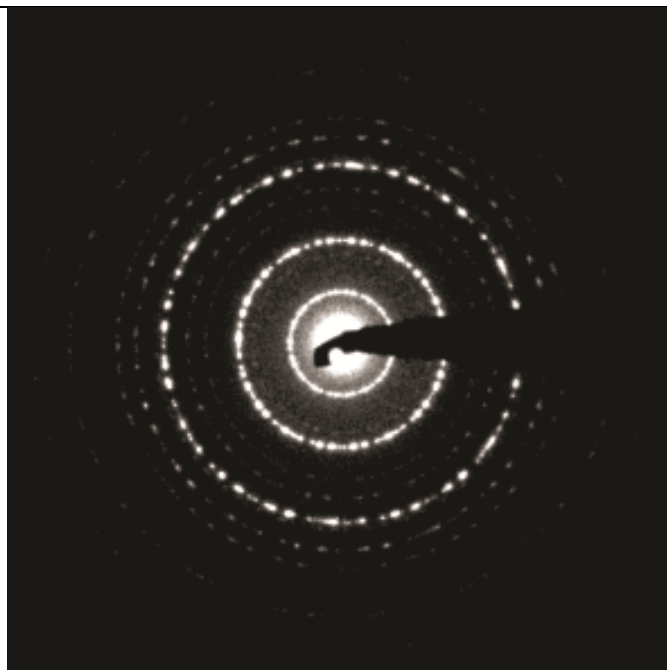
Figure S 3.5: SAD pattern of $Sb_3P_2O_{14}^{3-}$ nanosheets. The concentric circular shaped pattern indicates the turbostratic disorder along the *c*-axis, which indicates exfoliation and random restacking.
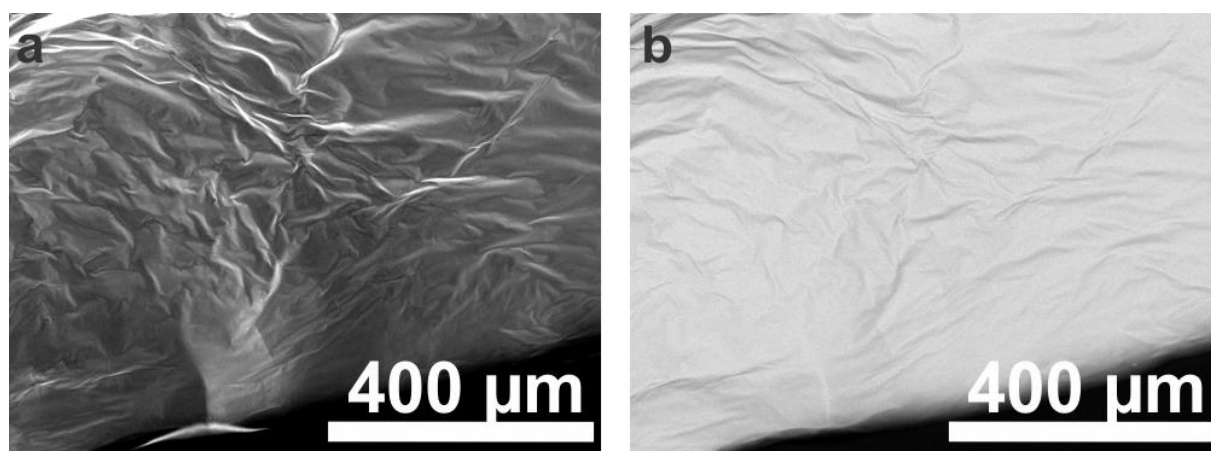
Figure S 3.6: a) SE image and b) BSE image of a $Sb_3P_2O_{14}^{3-}$ nanosheet pellet obtained from centrifugation at 18000 rpm of the sample exfoliated in water.

Table S 3.3: SEM-EDX analysis of a $Sb_3P_2O_{14}^{3-}$ nanosheet pellet obtained from three sample points.

Sample	Sb Atom%	P Atom%	O Atom%	Calc. Formula
Theoretical values	15.8	10.5	73.6	$Sb_3P_2O_{14}^{3-}$
Exper.	13.0 (5)	8.4 (2)	78.6 (7)	$Sb_{3.10}P_2O_{18.71}$

Table S 3.4: Comparison and indexing of *d*-values of SAD and XRD pattern (Figure S 3.7). The value marked with an asterisk cannot clearly be determined because of a broad maximum only slightly above the noise level in the XRD pattern.

	$Sb_3P_2O_{14}^{3-}$	
Miller indices	*d*-value SAD [Å]	*d* value XRD [Å]
(10)	6.02	6.12
(11)	3.55	3.41*
(20)	3.04	3.06
(21)	2.34	2.32
(30)	2.04	2.04
(22)	1.77	1.77
(40)	1.53	1.53
(23)	1.41	1.41
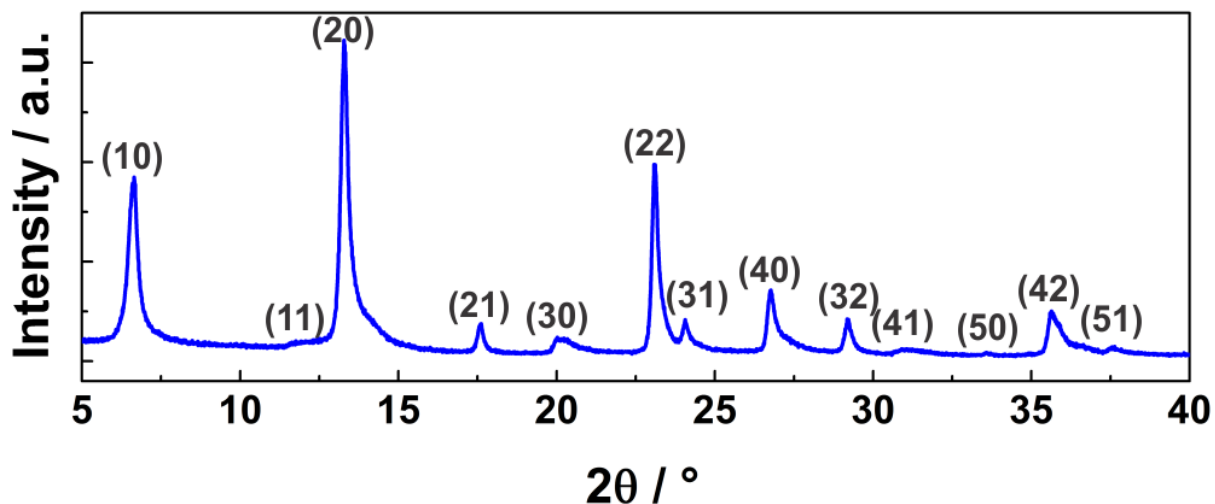
Figure S 3.7: Experimental XRD pattern of $Sb_3P_2O_{14}^{3-}$ nanosheet pellet recorded with Mo-$K_{\alpha 1}$ radiation and indexing based on a trigonal layer group ($p\bar{3}m1$ No. 72) with $a = 7.0914(3)$ Å. Note the Warren-type peak profile of the (*hk*) reflections.

Resistive RH sensing
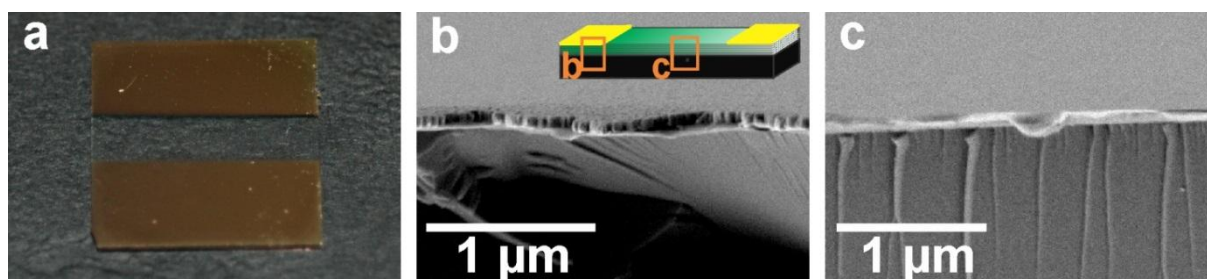
Figure S 3.8: a) Thin transparent nanosheet film device with quartz substrate, spin-coated thin film and sputtered gold contacts on the top. b) SEM cross-section of the region with gold contacts on the top (bottom to top: quartz substrate, thin layer of the nanosheets, Au contacts and vacuum). Inset: scheme of the resistive thin film substrate indicating the glass substrate (black), $H_3Sb_3P_2O_{14}$ nanosheet thin film (green) and the gold contacts (yellow). The orange rectangles indicate the cross section areas corresponding to the SEM images b and c. c) Cross-section of the thin film region without the gold contacts. The nanosheet film (light grey) appears thicker due to charging effects in c.
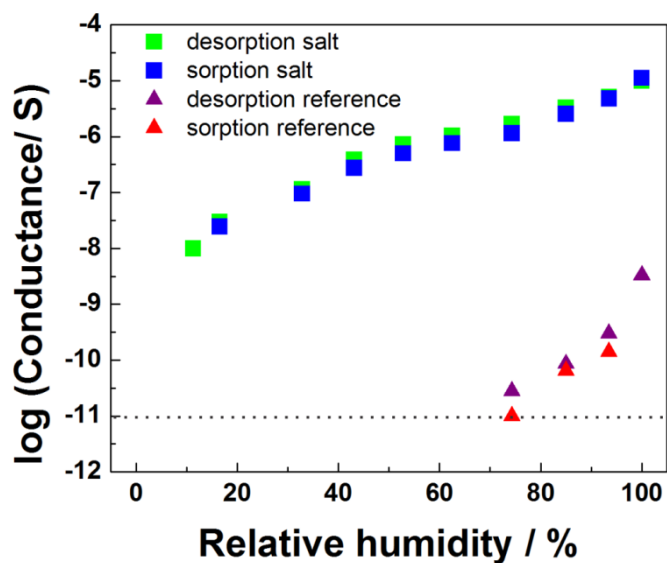
Figure S 3.9: Conductance plotted against RH for the nanosheet sample (salt) and empty quartz substrate with only gold electrodes (reference). The dashed line indicates the detection threshold of our impedance device.

It should be noted that the change in the measured conductance for the nanosheet thin film is substrate-dependent. However, by measuring the conductance increase of an empty quartz substrate as a reference substrate with increasing RH, it can be shown that the increase in conductance is due to the film and film-substrate interactions, rather than due the empty substrate itself (Figure S 3.9).
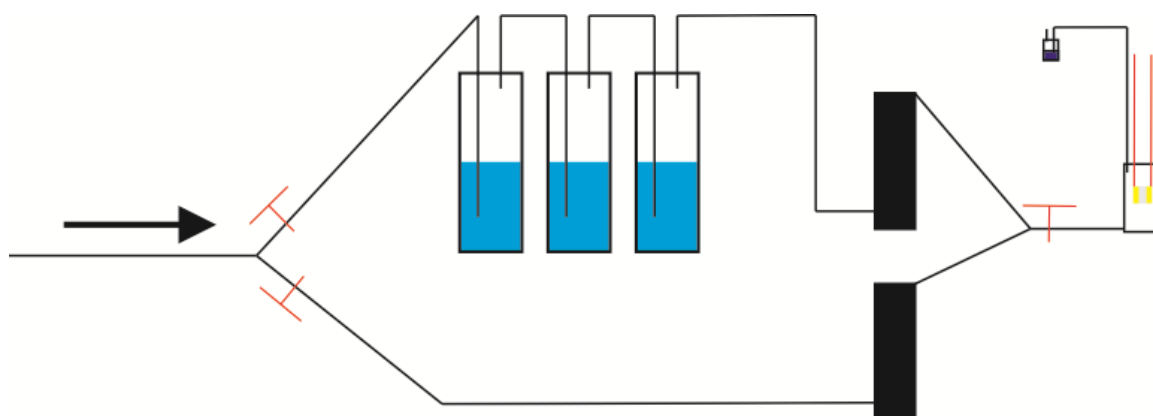
Figure S 3.10: Ar-stream setup for cycling and RH-dependent conductance measurements. The Ar stream splits up into 2 streams, where one is saturated with H_2O by bubbling through three washing bottles. The rotameters for the stream adjustment are shown in black, and the chamber with the film and the gas outlet is shown on the right hand side. In red, the three valves for additional control are depicted.

Thin film characterization
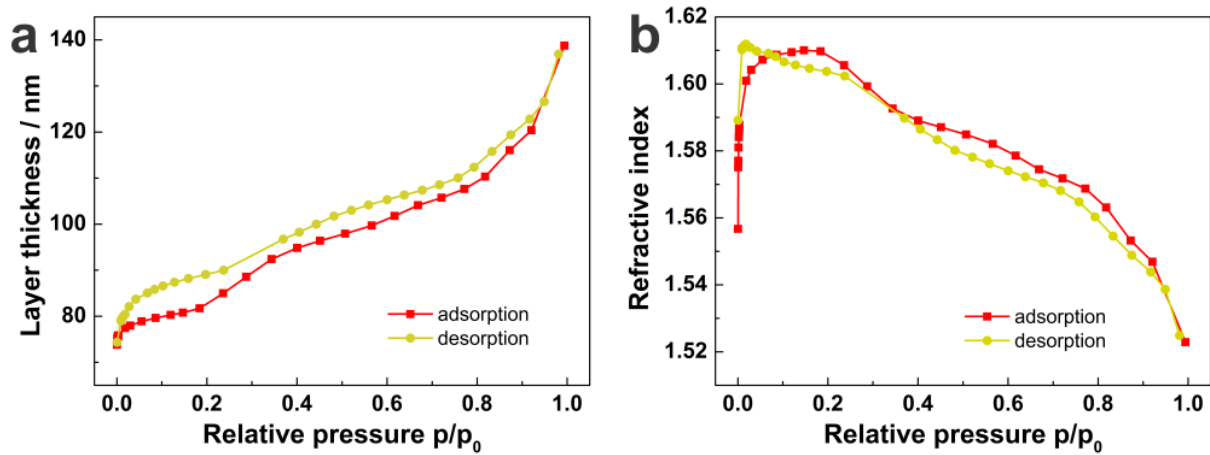
Figure S 3.11: Optical isotherms of a thin film containing $H_3Sb_3P_2O_{14}$ nanosheets. a) Layer thickness and b) refractive index change of a $H_3Sb_3P_2O_{14}$ nanosheet thin film measured at different relative pressures of water vapor.
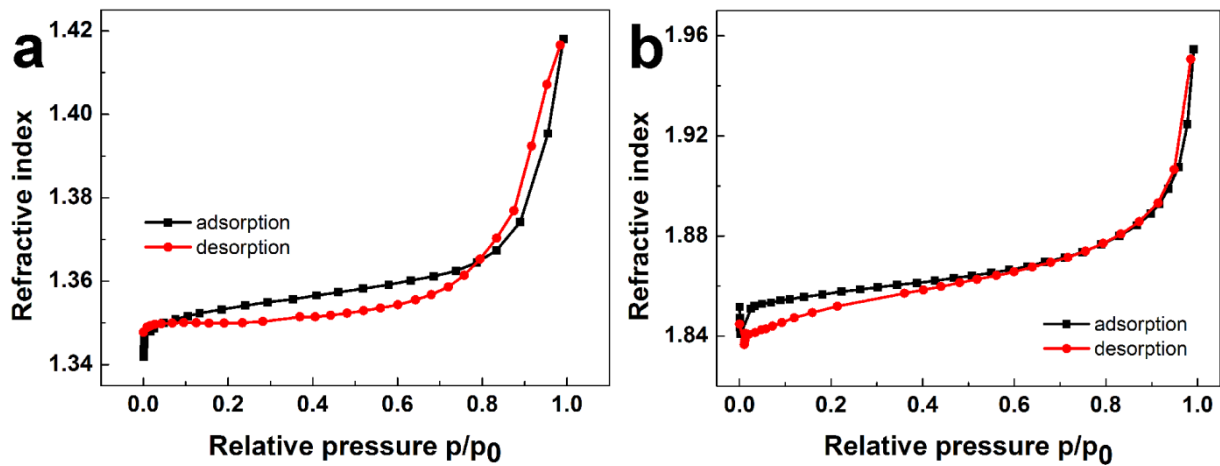
Figure S 3.12: Optical isotherm of the a**)** SiO_2 nanoparticle monolayer and b) TiO_2 nanoparticle monolayer monitoring the refractive index changes upon increasing the relative pressure of water vapor.

Optical humidity sensing and TPI

Table S 3.5: Refractive indices and monolayer thicknesses for the SiO_2/$H_3Sb_3P_2O_{14}$ Bragg stack used for the Matlab simulations at different relative humidity values. The layer thickness changes for the Bragg stack at different RH values were calculated from the ellipsometry measurements (Figure S 3.11a) for the actual thicknesses of the Bragg stack.

Monolayer property	11% RH	74% RH	93% RH
$n(H_3Sb_3P_2O_{14})$	1.6090	1.5708	1.5449
$n(SiO_2$ NP$)$	1.3500	1.3624	1.3980
$d(H_3Sb_3P_2O_{14})$	52.5 nm	70.0 nm	85.0 nm
$d(SiO_2$ NP$)$	90.0 nm	90.0 nm	90.0 nm

Table S 3.6: Refractive indices and monolayer thicknesses for the TiO_2/$H_3Sb_3P_2O_{14}$ Bragg stack used for the Matlab simulations at different relative humidity values. The layer thickness changes for the Bragg stack at different RH values were calculated from the ellipsometry measurements (Figure S 3.11a) for the actual thicknesses of the Bragg stack.

Monolayer property	11% RH	74% RH	93% RH
$n(H_3Sb_3P_2O_{14})$	1.6090	1.5729	1.5449
$n(TiO_2$ NP$)$	1.8400	1.8733	1.8900
$d(H_3Sb_3P_2O_{14})$	53.0 nm	69.0 nm	85.0 nm
$d(TiO_2$ NP$)$	78.0 nm	78.0 nm	78.0 nm
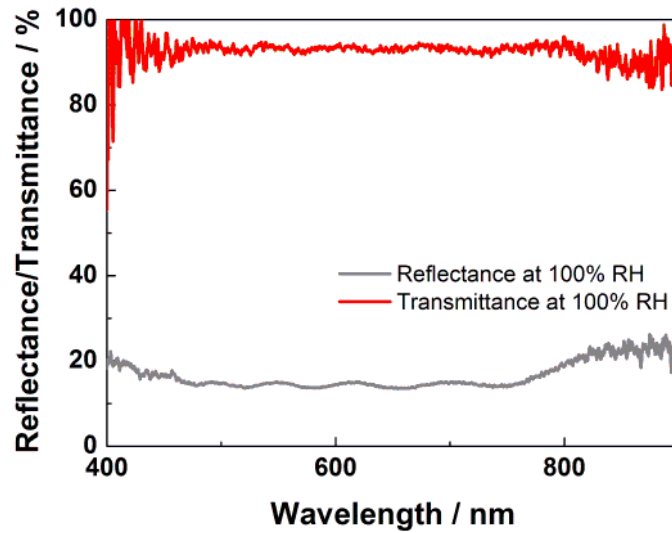
Figure S 3.13: Transmittance (red curve) and reflectance (grey curve) spectrum of the $SiO_2/H_3Sb_3P_2O_{14}$ BS at 100% RH. The spectra show the total transmittance and the loss of reflectance, resulting in complete transparency of the refractive index matching multilayer across the whole visible range.
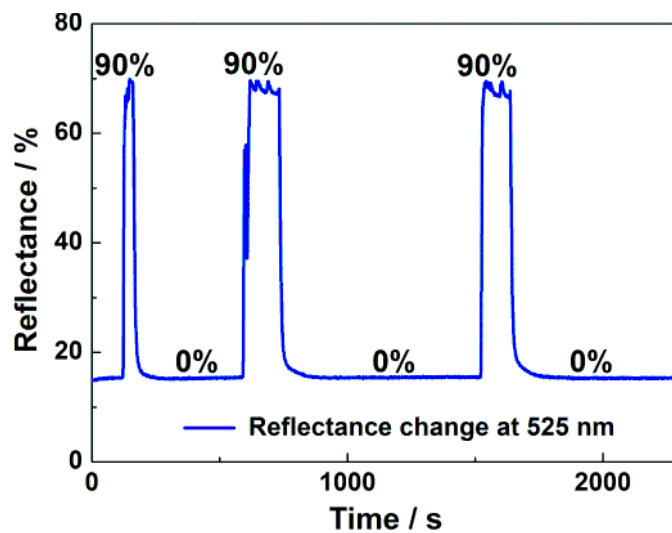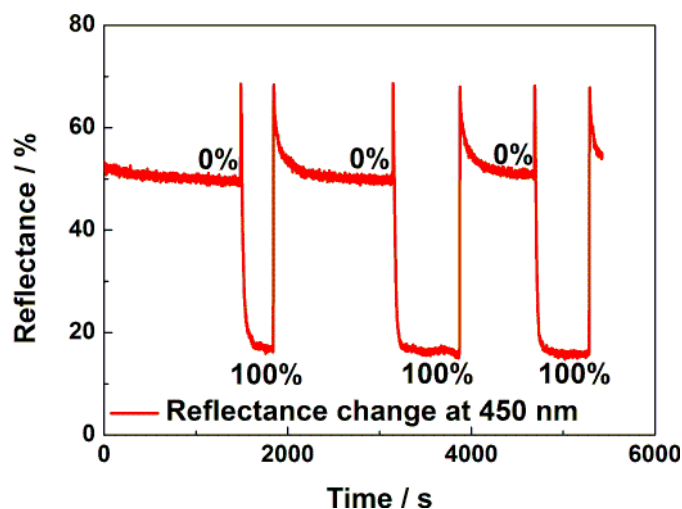

Figure S 3.14: Cycling behavior of the $TiO_2/H_3Sb_3P_2O_{14}$ Bragg stack with time. The cycling was performed using the nitrogen setup and applying 0% and 93% relative pressures of water vapor. The spectral changes were detected by recording the reflectance intensity at 525 nm in the original spectrum. This wavelength was carefully chosen to be at the red edge of the stop band at 0% humidity. The slight reflectance intensity changes were caused by the oscillation character of the vapor dosing system.

Figure S 3.15: Cycling behavior of the $SiO_2/H_3Sb_3P_2O_{14}$ Bragg stack with time. The cycling was performed using the nitrogen setup and applying 0% and 100% relative pressures of water vapor. The spectral changes were detected by recording the reflectance intensity at 450 nm in the original spectrum. This wavelength was carefully chosen to be at the red edge of the stop band at 0% humidity. This chosen wavelength of 450 nm is redshifted compared to the original Bragg peak position (around 430 nm). The sudden intensity drops during the adsorption and also the desorption are observed because the Bragg peak shifts pass the observed wavelength of 450 nm, causing a reflectance maximum at the observed point. The reflectance intensity at 100% RH is lower than at 0% because of the refractive index contrast cancelling upon water vapor adsorption.

Note that the response time cannot be extracted from the cycling behavior shown in Fig. 1e since the chamber used for this measurement reaches saturation slower than the sensor itself. The response time can be measured by excluding the dead volume, which has been done by applying a humidity stimulus given by a finger, as demonstrated in Figure S 3.16 below. The same method was used for the optical sensor, and the response time was determined with a finger stimulus (Figure 3.4g inset, Figure S 3.18).
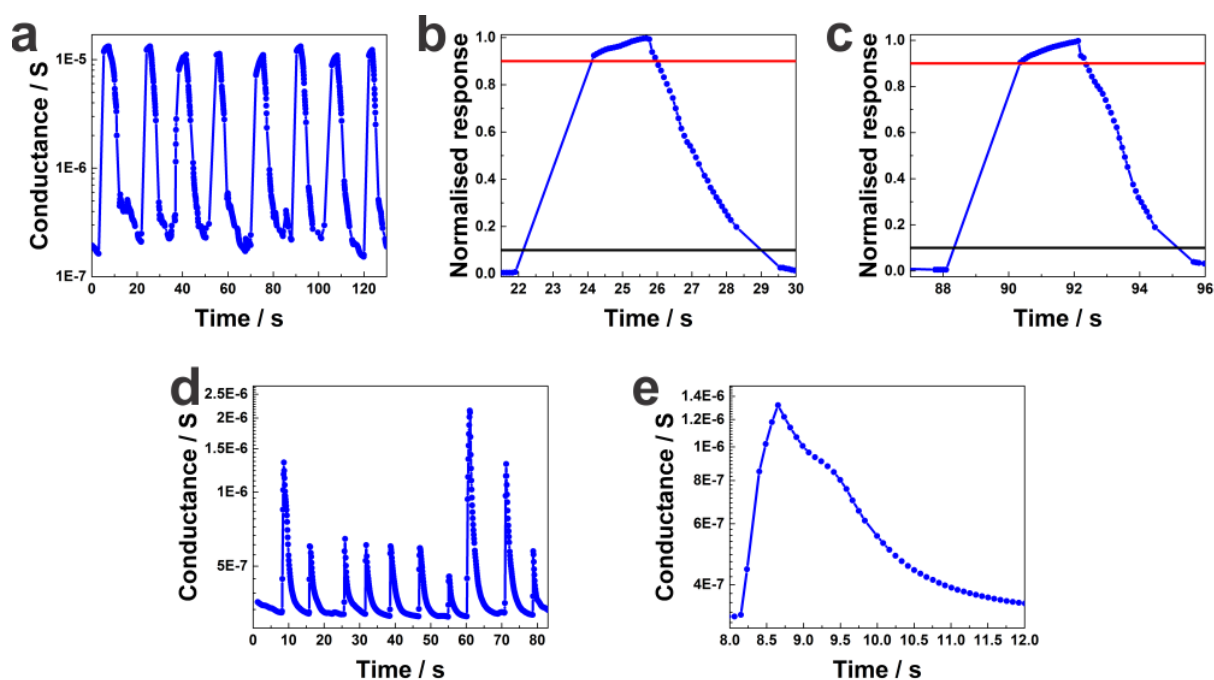
Figure S 3.16: Conductance response of a nanosheet thin film to a finger stimulus under touchless conditions. a) Response towards a "finger-on" state under touchless conditions, with a response time of about 2 s (note that signal saturation is reached within this time). b) and c) normalized magnifications of a) used for determination of the response and recovery time of the sensor (defined as reaching 90% of the total signal change; response time, red line, and recovery time, black line). The response time is around 2 s and the recovery time around 3 s for cycling between ambient conditions and close to 100% RH (finger proximity). d) Conductance response of a nanosheet thin film towards a fast tapping motion (occurring on a timescale of << 0.5 s) and e) magnification of the region of d) between 8 and 12 s. The data show that subsecond events can be resolved as demonstrated by the finger motion trapping detection (the signal triples in less than 0.5 s). Therefore, due to the fast response, the thin film can be used for real-time interactions (note that measurement a) was carried out under slightly different ambient relative humidity values as compared to d), as indicated by the conductance values).

To prove the long-term stability of the optical sensor, the measurements shown in Figure S 3.17-21 were carried out with an 8-months-old Bragg stack.
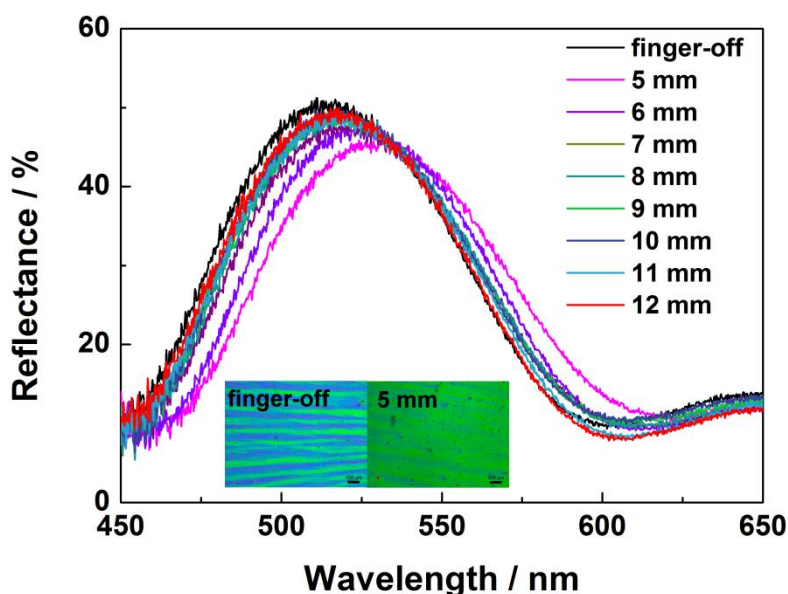
Figure S 3.17: Distance-dependent optical response of the $SiO_2/H_3Sb_3P_2O_{14}$ Bragg stack to a finger stimulus. Inset: Microscope images of the Bragg stack surface at 5 mm finger distance and a finger-off state.
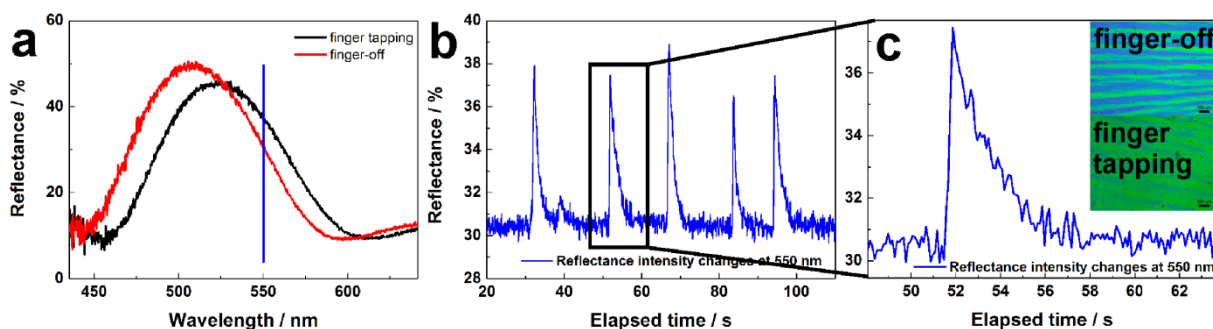
Figure S 3.18: a) Optical response of a $SiO_2/H_3Sb_3P_2O_{14}$ Bragg stack to a fast tapping finger motion as a function of time. Measurements were carried out in a similar way as described in Figure S 3.15, however for detection of the reflection a wavelength of 550 nm was chosen and a finger was used as the humid pointer. a) For the tapping experiments we have chosen a threshold value of 20 nm stop band shift, which is detectable by the naked eye (inset of c)). b) Time-resolved response of a Bragg stack towards a fast finger tapping motion. Even subsecond events can clearly be resolved, e.g. a reflectance change from 30% to 37%, which corresponds to 20 nm shift and is detectable with the naked eye, is observed within less than 0.5 s. c) Close-up of the region between 50-62 s, shown in b), inset: microscope images of the finger-off and tapping structural color, indicating that the 20 nm stop band shift is detectable by the naked eye.
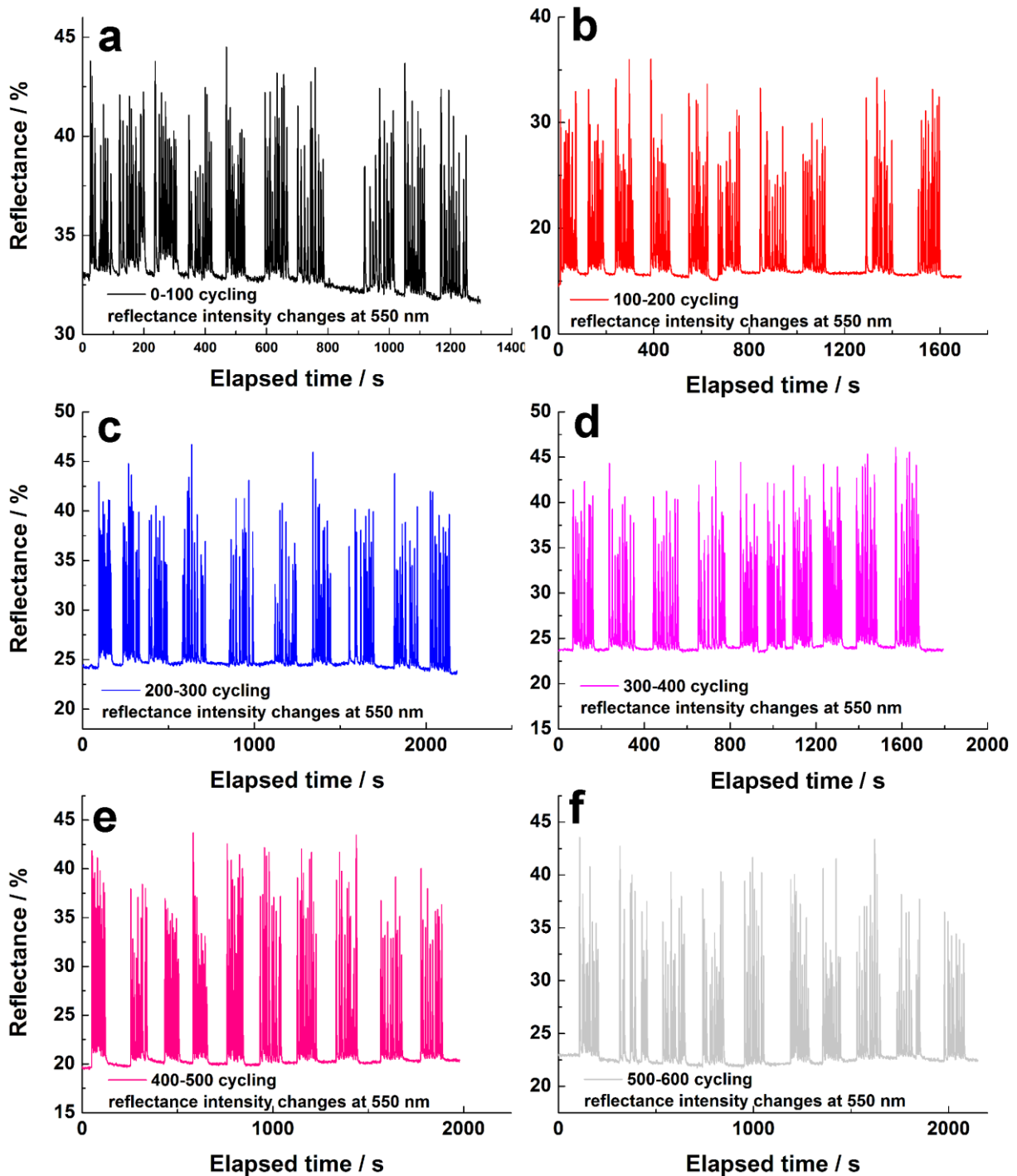
Figure S 3.19: The first part of the 1000 times cycling procedure. a-f) In each diagram 10 x 10 cycles are plotted. For time and simplicity reasons, one cycle corresponds to a finger "tapping" experiment. The human finger was approached for a short time to the Bragg stack surface, thereby only a smaller stop band shift was induced and not the whole stop band shift was reached. This experiment was repeated 10 times in a short time range – this is one "signal package". This 10-cycle-experiment was repeated 10 times to reach 100 cycles in one plot. This was repeated 10 times to reach 1000 cycles. 1-600 cycles are shown in this figure.
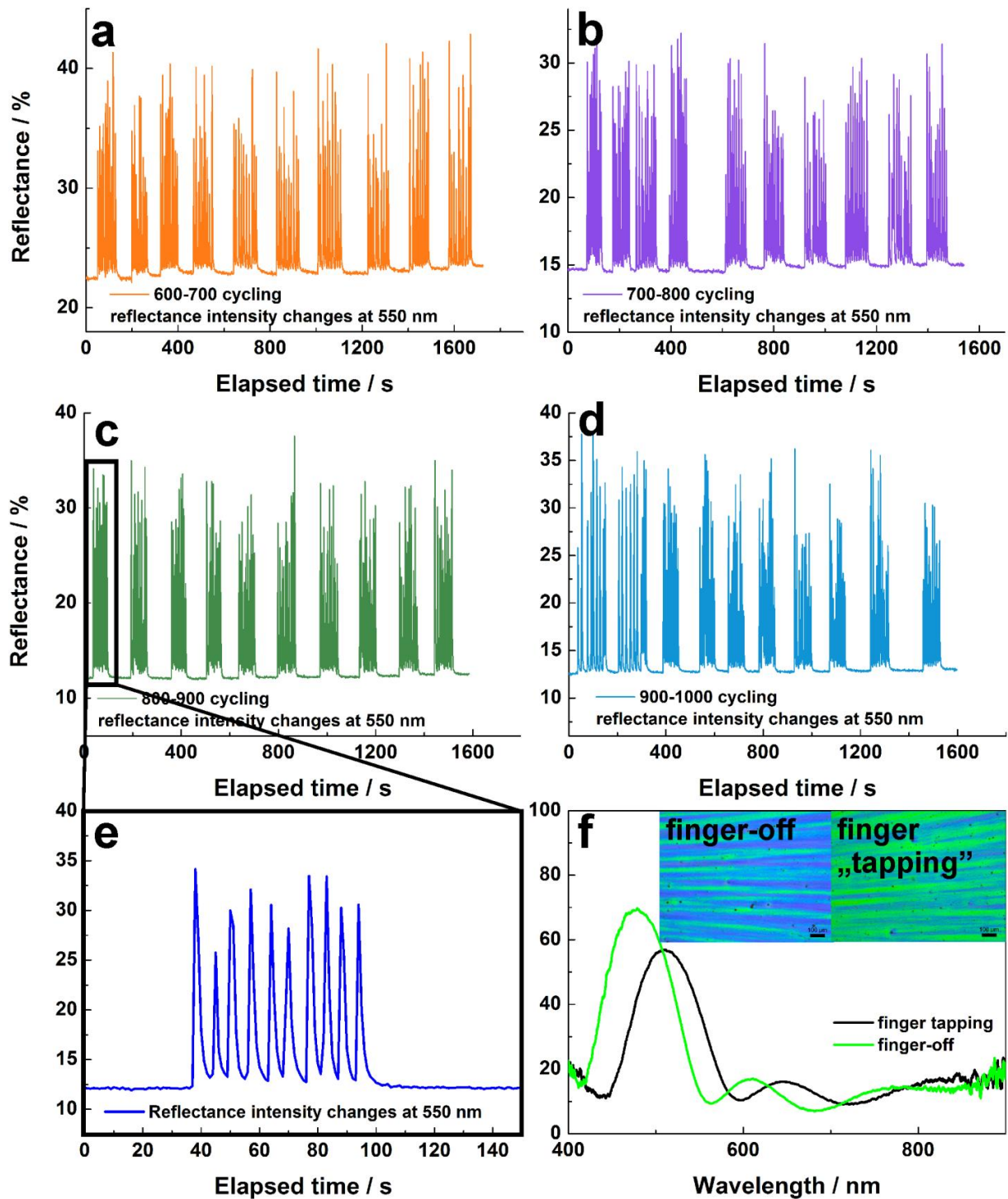
Figure S 3.20: The second part of the 1000 times cycling procedure. a-d) 601-1000 cycles are shown in the diagrams. Similar to Figure 3.3, 10 x 10 cycles are shown in one diagram. e) Magnification of one "signal package" of 10 cyclings. For one cycle, a finger "tapping" experiment was used in which a human finger was only shortly approached to the Bragg stack surface without touching it. In such a "tapping experiment", a reflectance intensity change of 10-20% is observed. f) Reflectance spectra of the finger-off and finger "tapping" scenarios. A finger "tapping" corresponds to a signal change of around 20-30 nm. Inset: the corresponding microscope images indicating the structural color change upon a finger approaching.
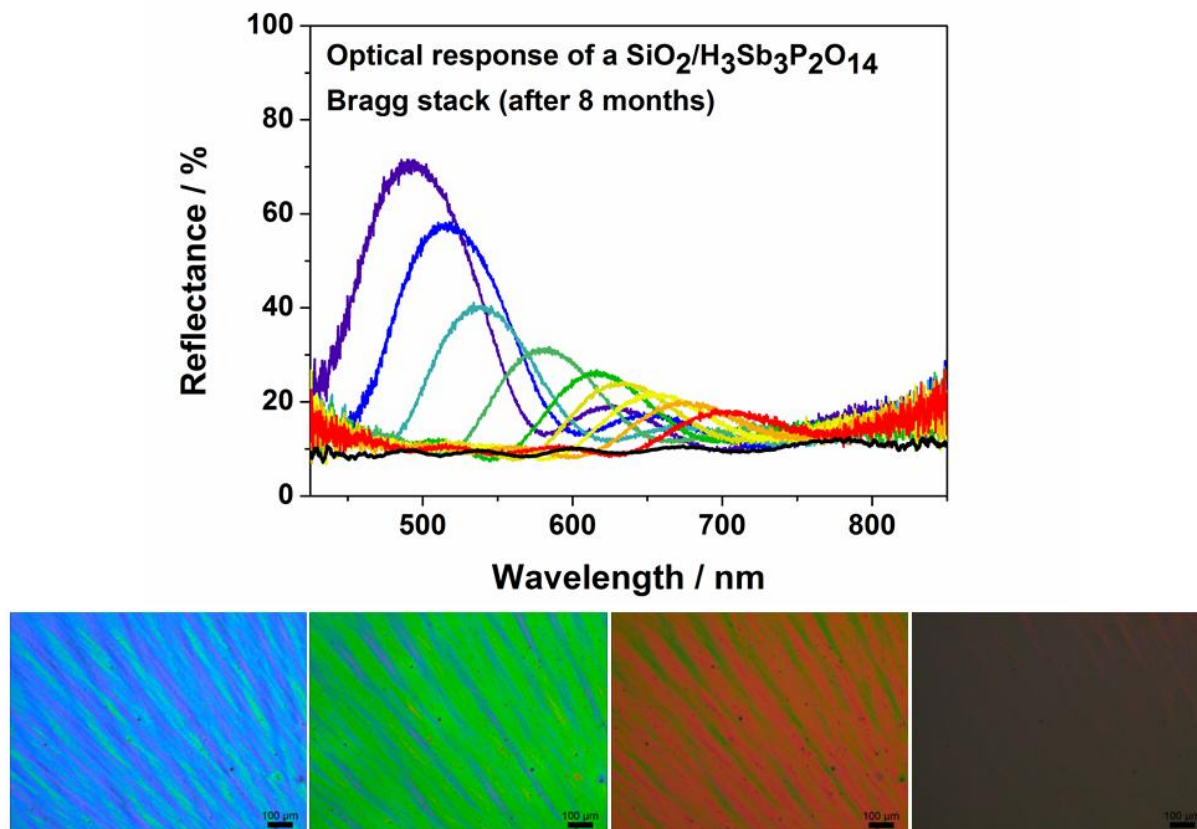
Figure S 3.21: Optical response of a 8-months-old SiO$_2$/H$_3$Sb$_3$P$_2$O$_{14}$ Bragg stack to an approaching finger. The reflectance spectra show an unchanged optical response after 8 months. Also the microscope images indicate the structural color change with changing relative humidity. Finally, at high relative humidities the Bragg peak completely vanishes and optical transparency is observed (indicated by the black color of the right microscope image).

REFERENCES

[1]   Y. Piffard, A. Lachgar, M. Tournoux, *J. Solid State Chem.* **1985**, *58*, 253-256.

[2]   J.-C. P. Gabriel, F. Camerel, B. J. Lemalre, H. Desvaux, P. Davidson, P. Batall, *Nature* **2001**, *413*, 504-508.

[3]   B. V. Lotsch, F. Scotognella, K. Moeller, T. Bein, G. A. Ozin, *SPIE Poc. Vol. 7713*, **2010**, 7713V.

[4]   M. E. Calvo, O. Sánchez-Sobrado, S. Colodrero, H. Míguez, *Langmuir* **2009**, *25*, 2443-2448.

[5]   P. W. Winston, D. H. Bates, *Ecology* **1960**, *41*, 232-237.

[6]   L. Greenspan, *J. Res. Nat. Bur. Stand.* **1977**, *81A*, 89-96.

[7]   A. T. Exner, I. Pavlichenko, D. Baierl, M. Schmidt, G. Derondeau, B. V. Lotsch, P. Lugli, G. Scarpa, *Laser Photon. Rev.* **2014**, *5*, 726-733.

[8]   Bronkhorst High-Tech, www.fluidat.com, accessed: 06-12/2014.

10.2 SUPPORTING INFORMATION FOR CHAPTER 5

Towards the 2D Photonic Nose: Trace Water Sensing and Vapor Identification with Antimony Phosphate Nanosheet-Based Thin Film Devices

Pirmin Ganter[¶], Katalin Szendrei[¶,], Prof. Dr. Bettina V. Lotsch*

[¶] These authors contributed equally to this work.

EXPERIMENTAL SECTION

Synthesis of the bulk, protonation and exfoliation

KNO_3 (99 %, Merck), Sb_2O_3 (99.6 %, Alfa Aesar) and $NH_4H_2PO_4$ (98 %+, Acros Organics) were ground in a stoichiometric ratio and heated up in a corundum crucible as previously described to yield $KSbP_2O_8$.[1] To obtain $HSbP_2O_8$, $KSbP_2O_8$ was treated with 8 M HNO_3 (250 mL, diluted 65 wt%, Merck) overnight, filtrated, washed with ethanol and dried at room temperature. This treatment was repeated at least two more times to complete the ion exchange reaction. The exchange reaction was followed by XRD (Figure S 4.2). For exfoliation $HSbP_2O_8$ was vigorously stirred overnight in water (7.3 mmol L^{-1}). The resulting colloidal suspension was then centrifuged at 3000 rpm for 30 min to remove non-exfoliated bulk material. The supernatant, consisting mainly of single-layer nanosheets, was collected and centrifuged at 18000 rpm for 30 min to yield a nanosheet pellet. The gel-like colorless wet aggregate was dried at 100 °C.

Preparation of colloidal suspensions

The dried $HSbP_2O_8$ nanosheets were suspended in a mixture of water : ethanol (60 : 40 wt%) with a concentration of 41 mmol L^{-1}. To avoid agglomerates, the suspension was sonicated for 2 h. This suspension was directly used for thin film formation without any further treatment.

TiO_2 nanoparticulate sols were synthesized using a procedure described elsewhere.[2] Briefly, 12.4 mL $Ti(OEt)_4$ (Sigma Aldrich) was added dropwise under vigorous stirring to 75 mL 0.1 M HNO_3. This mixture was heated to 80°C for 8 h. After collection of the particles by repeated centrifugation at 20000 rpm and redispersion in methanol, the suspension with 3wt% was directly used in the Bragg stack fabrication.

– Appendix –

Fabrication of thin films and Bragg stacks

All thin films and Bragg stacks were fabricated by means of spin-coating using a spin coater (WS-650S-NPP-Lite, Laurell Technologies Corporation) and colloidal suspensions of the nanosheets and nanoparticles, respectively, with the colloidal concentrations given above, in the previous section.

For conductance measurements, the redispersed nanosheet colloid was spin-coated at 3000 rpm or 2000 rpm for 1 min with a 10000 rpm s^{-1} acceleration ramp on a 1.5 cm x 1.5 cm plasma-cleaned quartz glass substrate. To achieve a sufficient film thickness (around 100 nm) for the conductance measurements, this deposition step was repeated once. Gold contacts were sputter-coated (108auto, Cressington) with 180 s sputtering time.

For the Bragg stack fabrication, different film thicknesses were accessed by varying the spin-coating speed, which allowed for fine-tuning of the optical properties.[3] On plasma cleaned silicon substrates (1.5 cm x 1.5 cm) 150 µl of the colloidal suspensions were spin-coated alternatingly for 1 min with a defined speed and heated to 80 °C for 15 min after each layer deposition. 3000 rpm, 4000 rpm and 5000 rpm spin-coating speeds were applied (the same speed for each layer within a Bragg stack) to tune the optical properties. To create a single nanosheet layer within the Bragg stack, two deposition steps were applied, both with the same speed, as given above, and further an acceleration rate of 500 rpm s^{-1} was used. After both deposition steps, the sample was heated to 80°C for 20 min before the deposition of the next layer. For the TiO$_2$ nanoparticles, an acceleration rate of 5000 rpm s^{-1} was applied. The starting and also the last layers are composed of the high RI NPs (TiO$_2$), in order to ensure the adhesion to the substrate and to increase the refractive index contrast with the surrounding air.

CHARACTERIZATION

Structural characterization

SEM images of the HSbP$_2$O$_8$ crystals and the nanosheet pellet were acquired with a Vega TS 5130 MM (Tescan) equipped with Si/Li detector (Oxford). Cross-section images of the Bragg stacks were taken with a Zeiss Merlin FE-SEM. TEM images and selected area electron diffraction (SAD) patterns were obtained with a Phillips CM30 ST TEM (300 kV, LaB$_6$ cathode) equipped with a Gatan CCD camera. TEM-EDX analysis was performed with a Si/Li detector (Thermo Fisher, Noran System Seven). XRD patterns were recorded on a powder X-ray diffractometer (Stadi P, STOE) working with Ge(111) monochromated Mo-K$_{\alpha1}$ radiation (λ = 70.926 pm) or Cu-K$_{\alpha1}$ radiation (λ = 154.051 pm).

Rietveld refinement of the nanosheet pellet measured in transmission geometry was performed with the software DiffracPlus TOPAS v4.2 (Bruker AXS). A quasi single layer approach similar to the one described in the literature was used to approximate the turbostratic disorder.[4,5] The sample showed preferred orientation effects such that almost exclusively the *hk0* reflections were observed, which allows us to use a simplified model compared to the models as described in the literature, which in addition include modeling of the *00l* reflections. AFM images were acquired on a Veeco CP II system in non-contact mode. The images of the surfaces of the Bragg stack were obtained with an optical microscope (Olympus BX51), operating in reflection mode with a 4x objective.

Conductance measurements

To obtain the conductance measurements for relative humidity, two different methodologies were used. In the first one, the films were kept over saturated salt solutions at around 25 °C[6,7] in a closed atmosphere at least 20 min before the conductance measurements. In the second one we used an argon flow set up. A dry Ar flow and a water vapor saturated Ar stream were mixed in different ratios to define the humidity between 0-93.5%. The setup was calibrated using the conductance values previously measured at the RH defined by the salt solutions. The cycling experiments were performed with the Ar flow setup. For sensing trace amounts of water in alcohol (ethanol 99.8%, water ≤ 0.2%, Roth; 2-propanol 99.8%,water ≤ 0.05%, Merck) water mixtures, an Ar stream at a constant rate of 8.4 L min^{-1} was passed through 100 mL of solution. By passing an Ar stream through the solution the stream takes up certain amounts of moisture and ethanol, which leads to a change in the conductance of the thin film sensor.

The change in conductance was monitored by impedance spectroscopy (in-plane geometry, two point measurement) with an impedance bridge (Princeton Applied Research, VersaSTAT MC) applying an AC voltage of 500 mV and a frequency range of 1 Hz to 1 MHz. Cycling measurements were performed with a fixed frequency of 300 Hz.

Optical characterization

Porosimetry measurements were carried out by the porosimetry tool of Sopra PS-1000 SAM, whereby the sample was equilibrated at all water vapor relative pressure values for 15 min. The measurement results were fitted with the software Sopra SAE using the model combination Cauchy and Lorentz. The thickness of the nanoparticle layers was confirmed by ellipsometry to be constant with changing vapor relative pressure and only the refractive index was fitted. For the nanosheet thin films, both the layer thickness and the refractive index were fitted over the relative pressure range simultaneously. Prior to all measurements, the nanoparticle samples were heated for at least 30 min at 200 °C and the nanosheets thin films for 30 min at 60 °C in vacuum to make sure that the pores

are empty. To obtain the optical isotherms, all fitted measurement results were plotted against the analyte relative pressure.

All optical spectra were measured with a fiber optic spectrometer (USB2000+, Ocean Optics) attached to a microscope (DM2500, Leica) with normal incidence and the optical spectra were always taken at the same spot (1×1 mm^2 in area).

To obtain the optical changes with changes in relative humidity, the Bragg stacks were kept in a stainless steel chamber with a total volume of 5 mL and with a transparent glass window. In the chamber, 0.7 mL of saturated salt solutions[6,7] were filled without touching the sample surface, and kept at around 25 °C to define the humidity in the closed atmosphere. At each step, 20 min equilibration time was needed.

To measure the response to solvent vapors and the saturation times for all analytes (including the cycling experiments), a mass flow controller with a controlled evaporation mixer (CEM) (see below) was applied. To measure the saturation time, the reflectance intensity changes of the Bragg peak were observed at a certain wavelength placed at the red stop band edge. While the Bragg peak shifts as a response to the analyte exposure, the reflectance intensity changes at the observed wavelength. The full response from 0% to 100% vapor relative pressure was taken defined as the saturation time. In these dynamic measurements, the BSs were placed into a closed chamber with the dimensions of 2.5x2.5x0.5 cm^3, where well-defined vapor relative pressure values were realized by connecting the inserted pipette tip with a liquid-gas flow controller (Bronkhorst) and a vaporizer (CEM) with a massflow-controlled carrier gas flow. To observe a specific solvent vapor relative pressure, the carrier gas nitrogen (200 mL min^{-1}) and the liquid solvent were dosed into the CEM (controlled evaporation and mixing, W101A-130-K, Bronkhorst High-Tech), where the thermal evaporation of the solvent took place. The CEM was heated to temperatures slightly above the boiling point. The relative vapor pressures were calculated via the software FLUIDAT (CEM calculation), which considers the actual atmospheric pressure, the temperature and the properties of the analyte (vapor pressure, heat capacity).[8] The obtained data were analyzed with the SPECTRA SUITE (2008) software.

Simulations

Simulations of the reflectance spectra were carried out using a Matlab code based on a full-vector calculation using the transfer matrix method.[9] The layer thicknesses at 0% RH and 0% analyte relative pressure were taken from the SEM cross section images. The refractive indices were taken from the porosimetry measurements. For the simulations of the selectivity measurements, the layer thicknesses at 100% were fitted according to the measured reflectance spectra. The refractive indices in the optical isotherms are given at 623 nm.
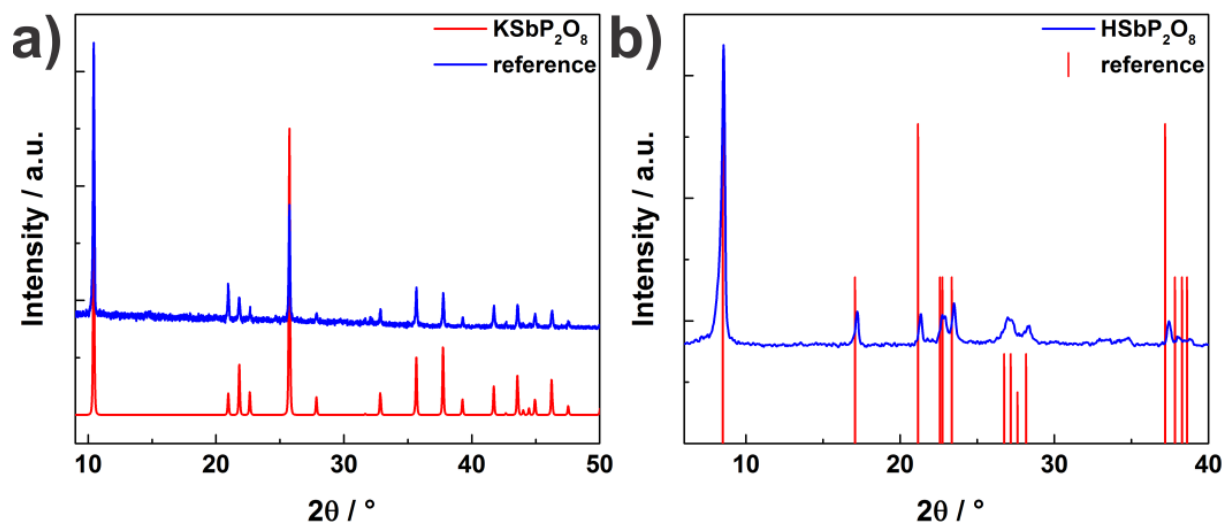
Figure S 5.1: Experimental XRD patterns of a) $KSbP_2O_8$ b) $HSbP_2O_8$ (in blue) and reference XRD patterns (red) from the literature for (a) $KSbP_2O_8$ obtained from single crystal data and (b) for $HSbP_2O_8 \cdot 2\ H_2O$. Both XRD patterns were recorded with Cu-K$_{\alpha 1}$ radiation.
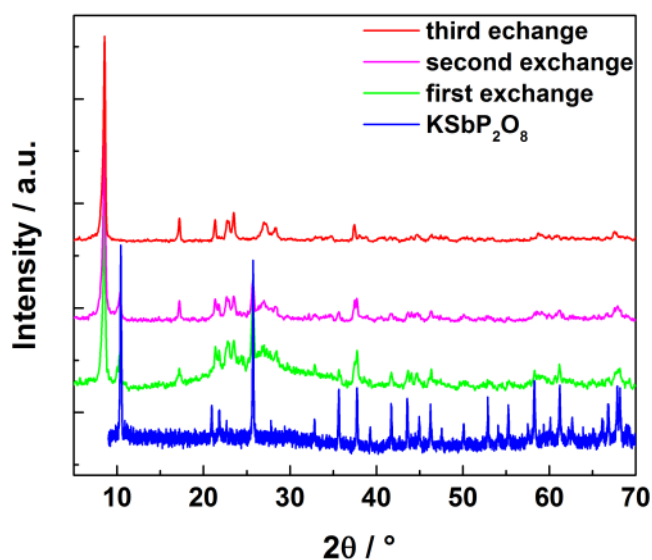

Figure S 5.2: Cation-proton exchange for $KSbP_2O_8$ monitored by XRD. Three exchange steps are necessary for complete cation-proton exchange as illustrated. All XRD patterns were recorded with Cu-K$_{\alpha 1}$ radiation.
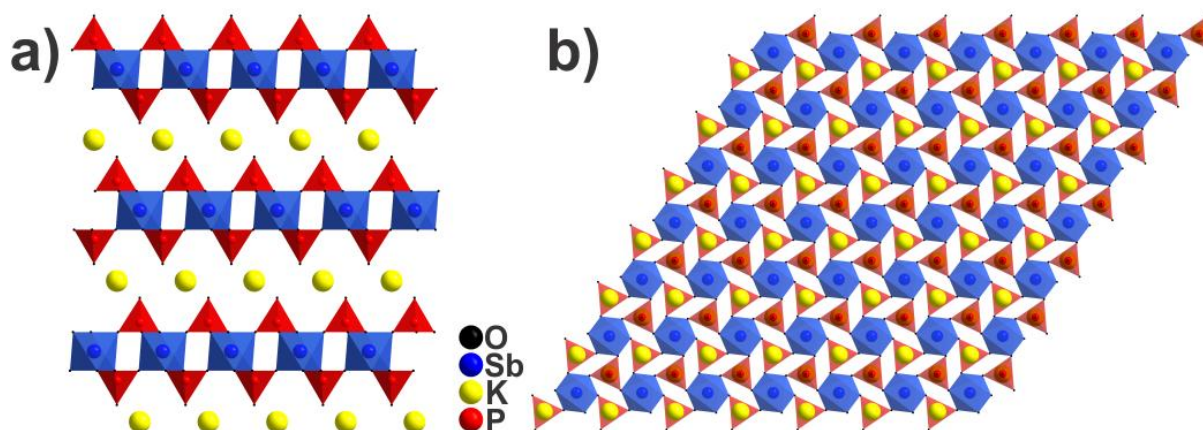
Figure S 5.3: Structure of KSbP$_2$O$_8$ viewed along a) [010] and b) [001]. K atoms in yellow, Sb atoms in blue, P atoms in red and O atoms in black. For a better overview only one layer is shown along [001].

Table S 5.1: EDX data of KSbP$_2$O$_8$ and HSbP$_2$O$_8 \cdot$ H$_2$O. The given data are averaged over four points; standard deviation in brackets. The small amount of Al found is due to the synthesis in corundum crucibles.

	K Atom%	Sb Atom%	P Atom%	O Atom%	Al Atom%	Calc. Formula
Theo. values	8.3	8.3	16.6	66.6		KSbP$_2$O$_8$
Exp. values	8.4 (1.8)	8.4 (1.8)	15.5 (1.9)	66 (5)	0.6 (4)	KSb$_{1.01}$P$_{1.85}$O$_{7.95}$
Theo. values		8.3	16.7	75		HSbP$_2$O$_8 \cdot$ H$_2$O
Exp. values		8.4 (1.4)	15.5 (1.1)	76 (2)		HSbP$_{1.83}$O$_{9.03}$
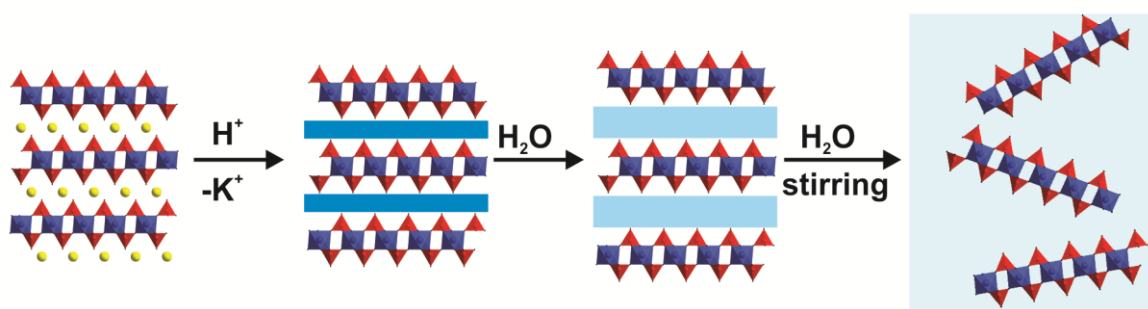
Figure S 5.4: Schematic exfoliation of HSbP$_2$O$_8$ assuming that first swelling takes place, followed by exfoliation.
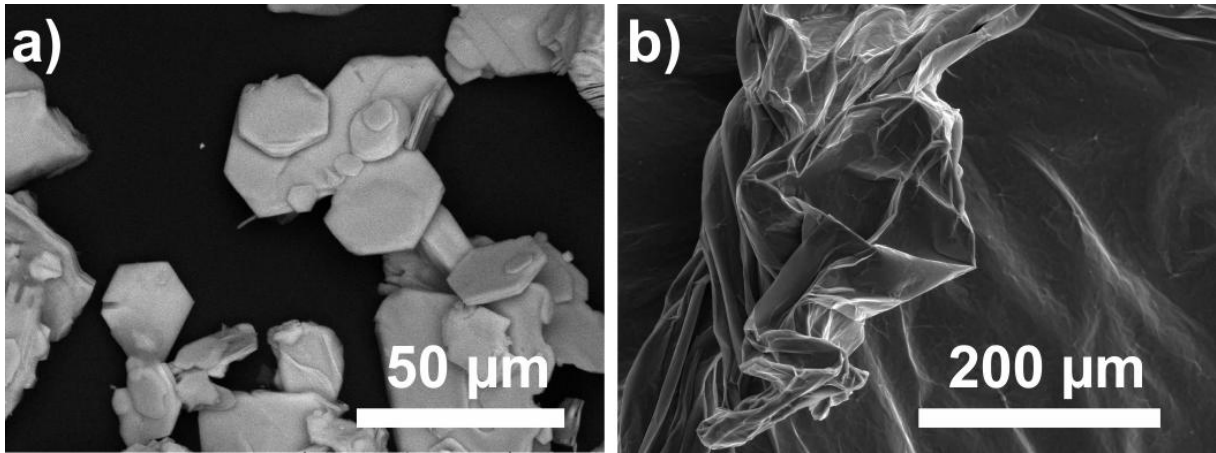
Figure S 5.5: Additional SEM pictures. a) BSE image of $HSbP_2O_8$ bulk phase and b) SE image of a $HSbP_2O_8$ nanosheet pellet.
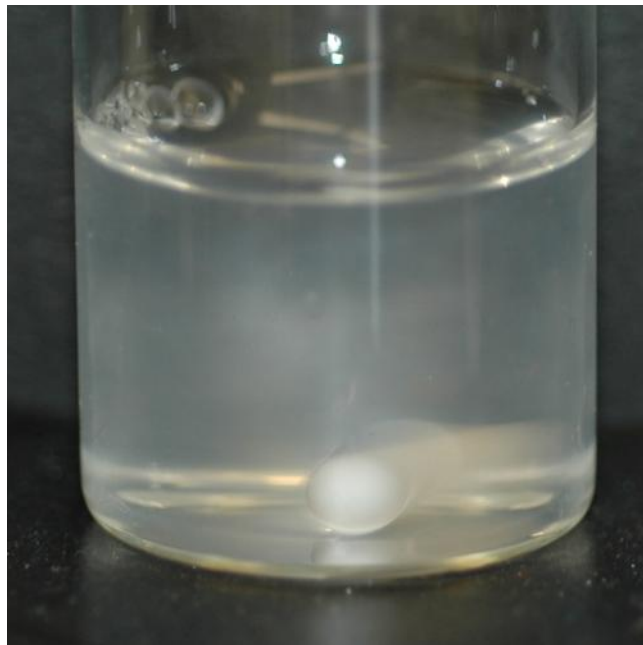
Figure S 5.6: Schlieren texture of the exfoliated nanosheets in suspension.
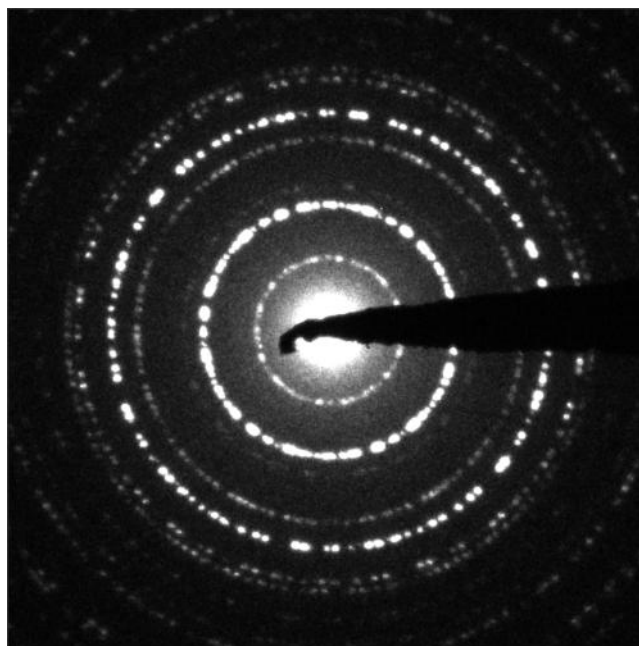
Figure S 5.7: SAED pattern of HSbP$_2$O$_8$ nanosheets. The concentric rings are due to randomly overlapping (e.g. rotated along [001]) nanosheets.

Table S 5.2: Comparison and indexing of *d*-values of SAD and XRD patterns. Note that as the nanosheet has a layer group (*p*$\bar{3}$ (66)) only (*hk*) indices are used for indexing.

HSbP$_2$O$_8$ nanosheets		
Miller indices	*d* value SAD [Å]	*d* value XRD [Å]
(10)	4.16	4.17
(11)	2.43	2.41
(20)	2.09	2.08
(21)	1.58	1.57
(30)	1.40	1.39
(22)	1.21	1.20
(31)	1.16	1.16

Table S 5.3. EDX data of the nanosheet pellet at two measured points.

	Sb Atom%	P Atom%	O Atom%	Calc. Formula
Theo. values	7.7	15.4	76.9	$HSbP_2O_8 \cdot 2\ H_2O$
Exp. values (I)	7.7	15.1	77.3	$HSbP_{1.96}O_{10.04}$
Exp. values (II)	7.2	14.6	78.2	$HSbP_{2.02}O_{10.86}$
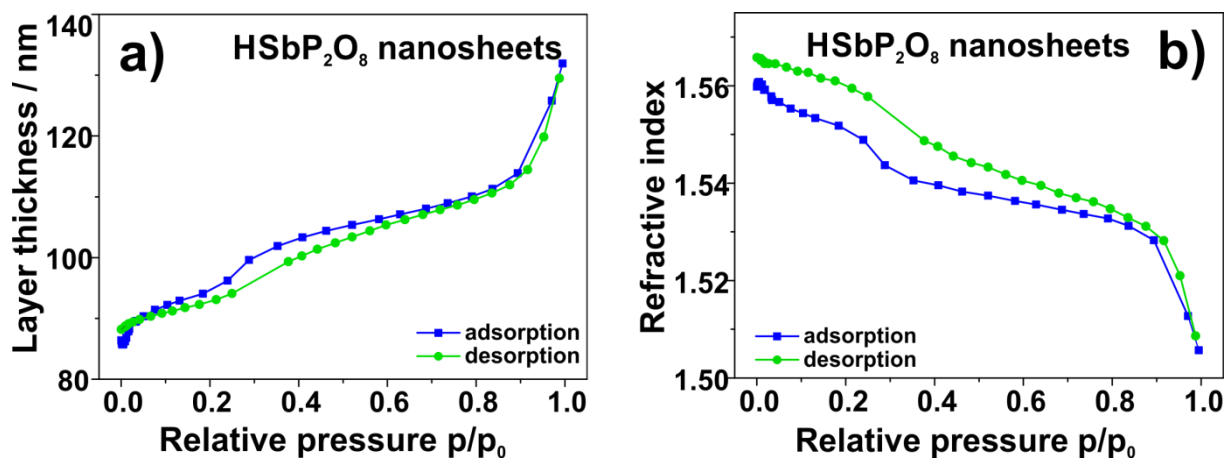
Figure S 5.8: Optical isotherms of a thin film of $HSbP_2O_8$ nanosheets measured by ellipsometric porosimetry. a) Layer thickness and b) RI (at 623 nm) change of a $HSbP_2O_8$ nanosheet thin film measured at different relative pressures of water vapor.
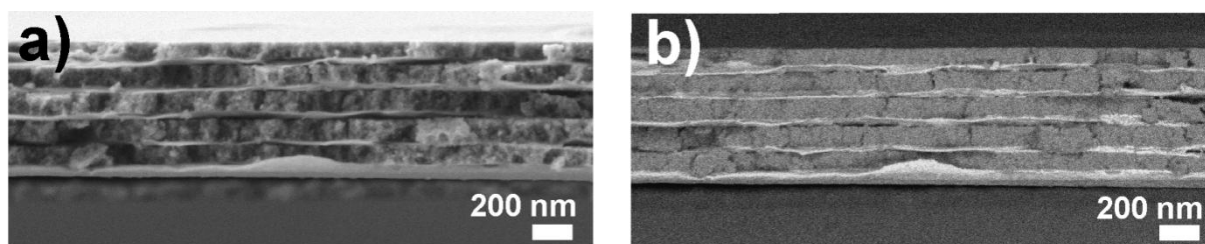
Figure S 5.9: a) In-lens and b) backscattered SEM cross-section images of a $HSbP_2O_8$ nanosheet/TiO_2 NP BS comprised of 11 layers showing the two different materials and the different morphologies.
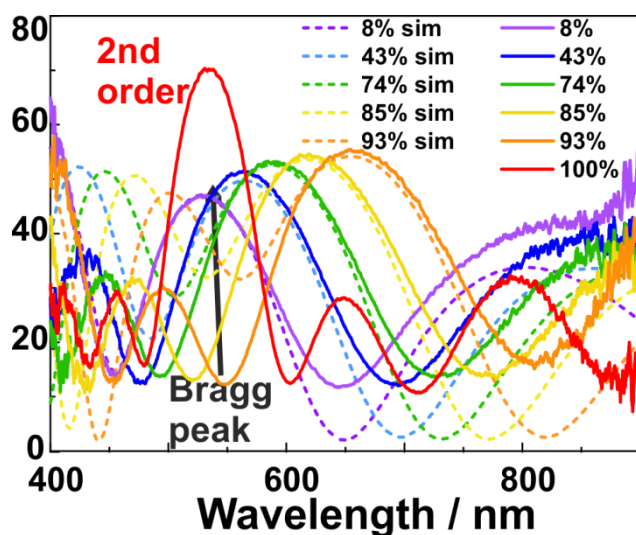
Figure S 5.10: Reflectance spectra and simulated spectra (dashed lines) of the HSbP$_2$O$_8$ nanosheet/TiO$_2$ NP BS taken at different RH values.
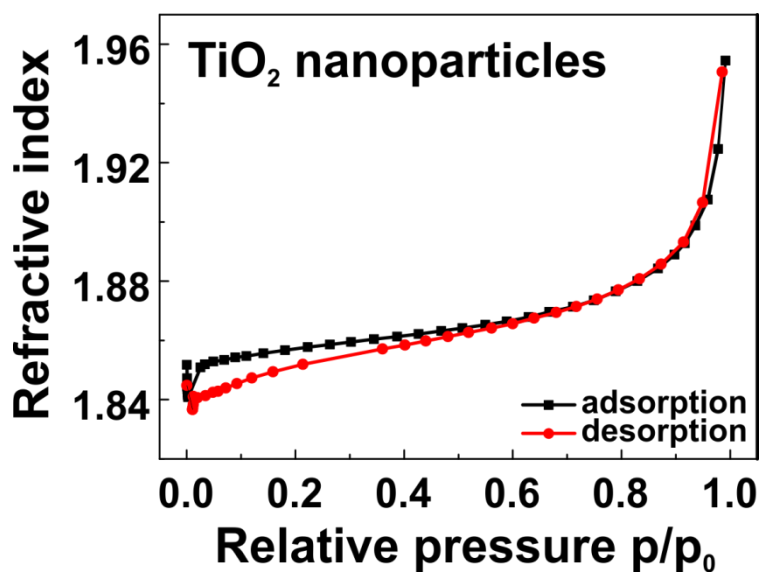
Figure S 5.11: Optical isotherm of the TiO$_2$ NP monolayer monitoring the RI changes (at 623 nm) upon increasing the relative pressure of water vapor measured by ellipsometric porosimetry.

Table S 5.4: Refractive indices and monolayer thicknesses for the TiO_2/$HSbP_2O_8$ Bragg stack used for the Matlab simulations at different relative humidity values. The layer thickness changes for the Bragg stack at different RH values were calculated from the ellipsometry measurements (Figure S 4.8a) for the actual thicknesses of the Bragg stack.

RH	TiO_2		$HSbP_2O_8$	
	Layer thickness	RI	Layer thickness	RI
8%	58 nm	1.840	78 nm	1.560
43%	58 nm	1.870	91 nm	1.539
74%	58 nm	1.93	97 nm	1.533
85%	60 nm	1.934	103 nm	1.525
93%	61 nm	1.940	115 nm	1.520
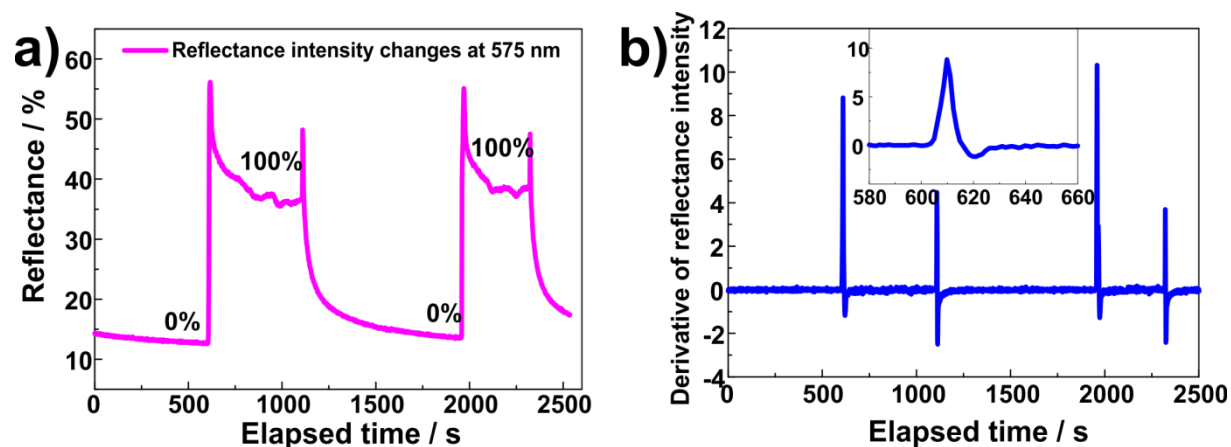
Figure S 5.12: Time-dependent optical response of the $HSbP_2O_8$ nanosheet/TiO_2 NP BS showing a) the reflectance intensity changes at 575 nm and b) the derivative of the reflectance intensity changes. Note that the oscillations after analyte exposure are due to oscillations of the vapor dosing setup. Inset: Magnification of the derivative curve of the time-dependent reflectance intensity changes between 580 and 660 s.
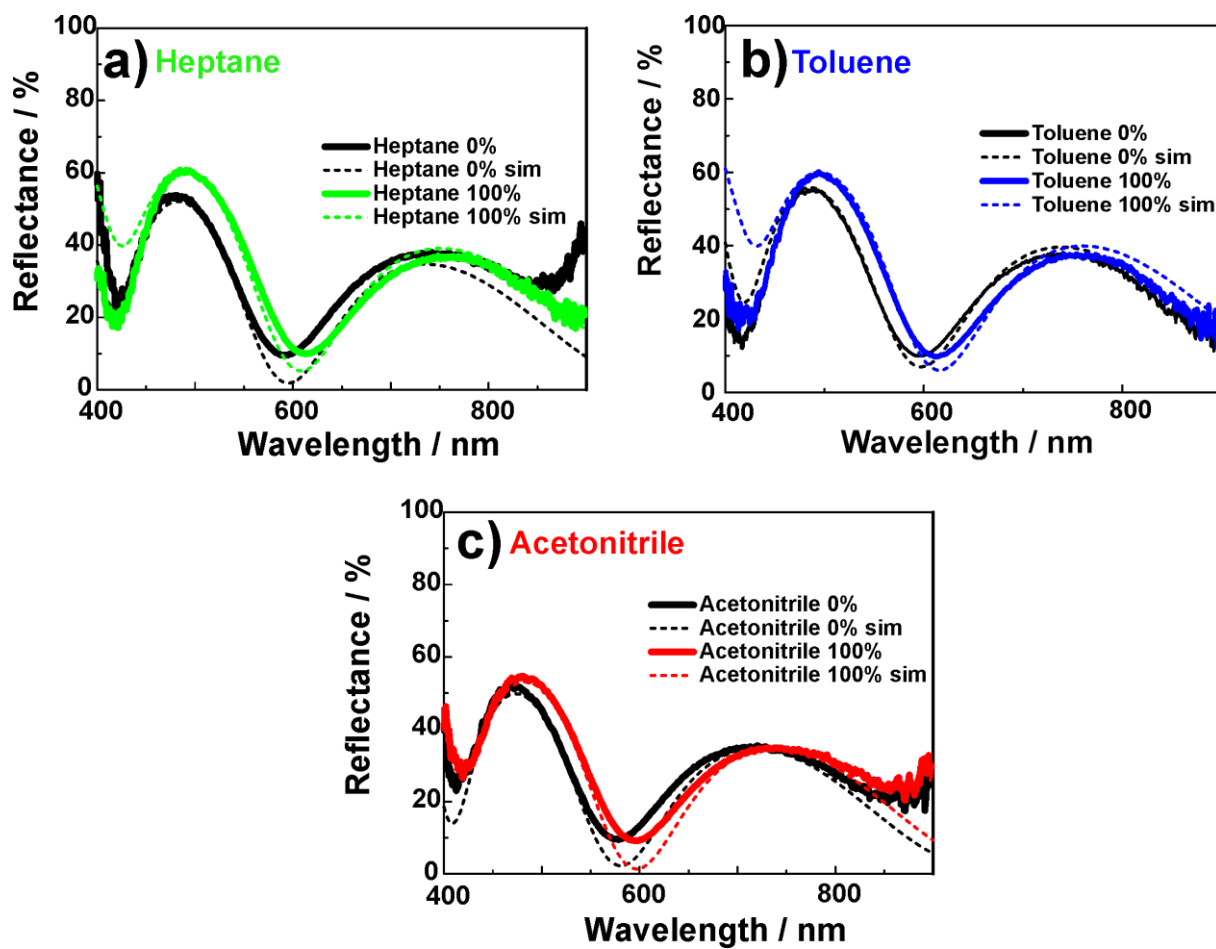
Figure S 5.13: Reflectance spectra and simulated spectra (dashed lines) of the $HSbP_2O_8$ nanosheet/TiO_2 NP BS containing 7 layers, demonstrating the stop band shifts upon adsorption of the non-polar and polar, non-protic solvent vapors: a) heptane, b) toluene, c) acetonitrile.
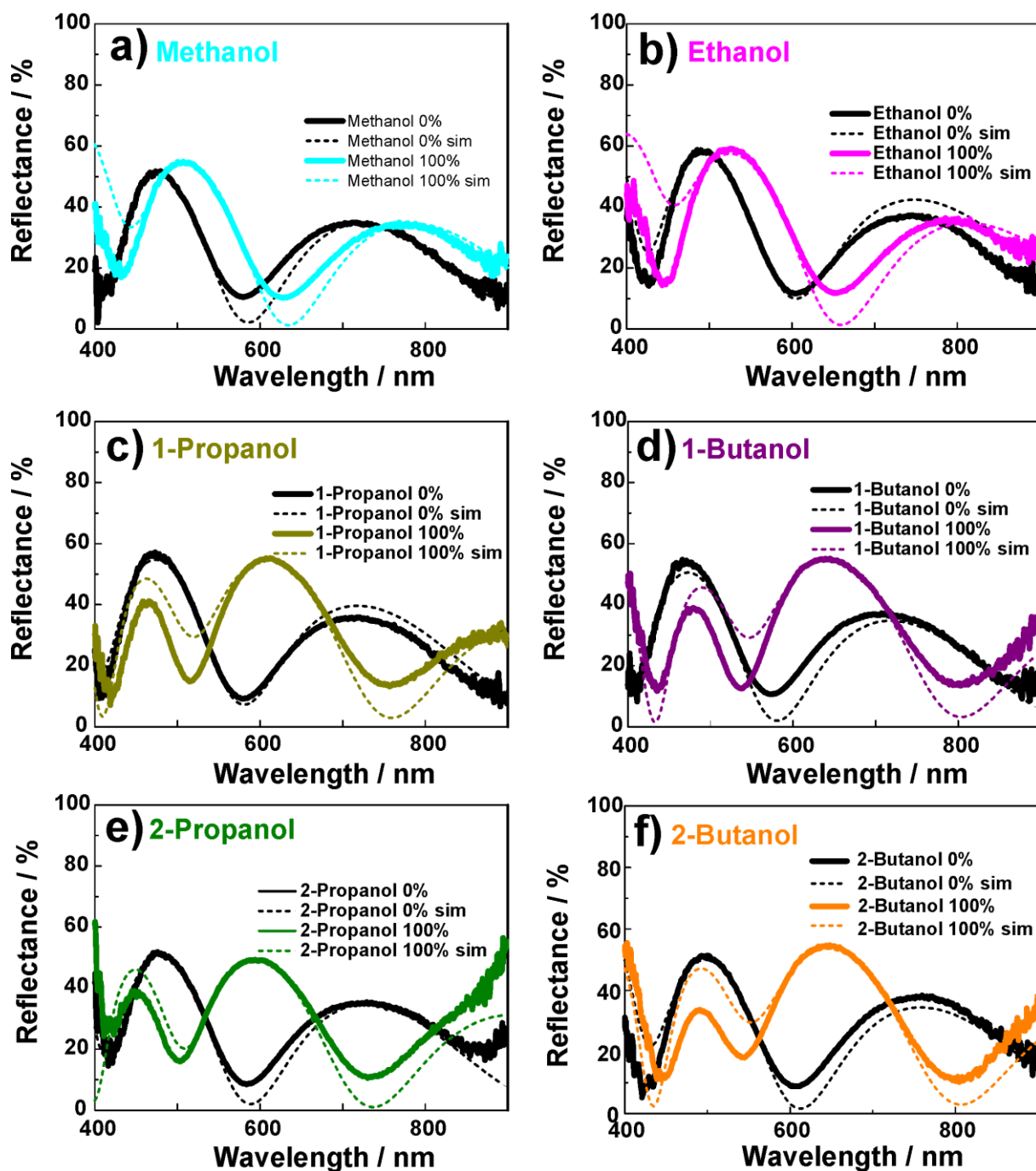
Figure S 5.14: Reflectance spectra and simulated spectra (dashed lines) of the $HSbP_2O_8$ nanosheet/TiO_2 NP BS containing 7 layers, demonstrating the stop band shifts upon adsorption of the polar solvent vapors: a) methanol, b) ethanol, c) 1-propanol, d) 1-butanol, e) 2-propanol, f) 2-butanol.
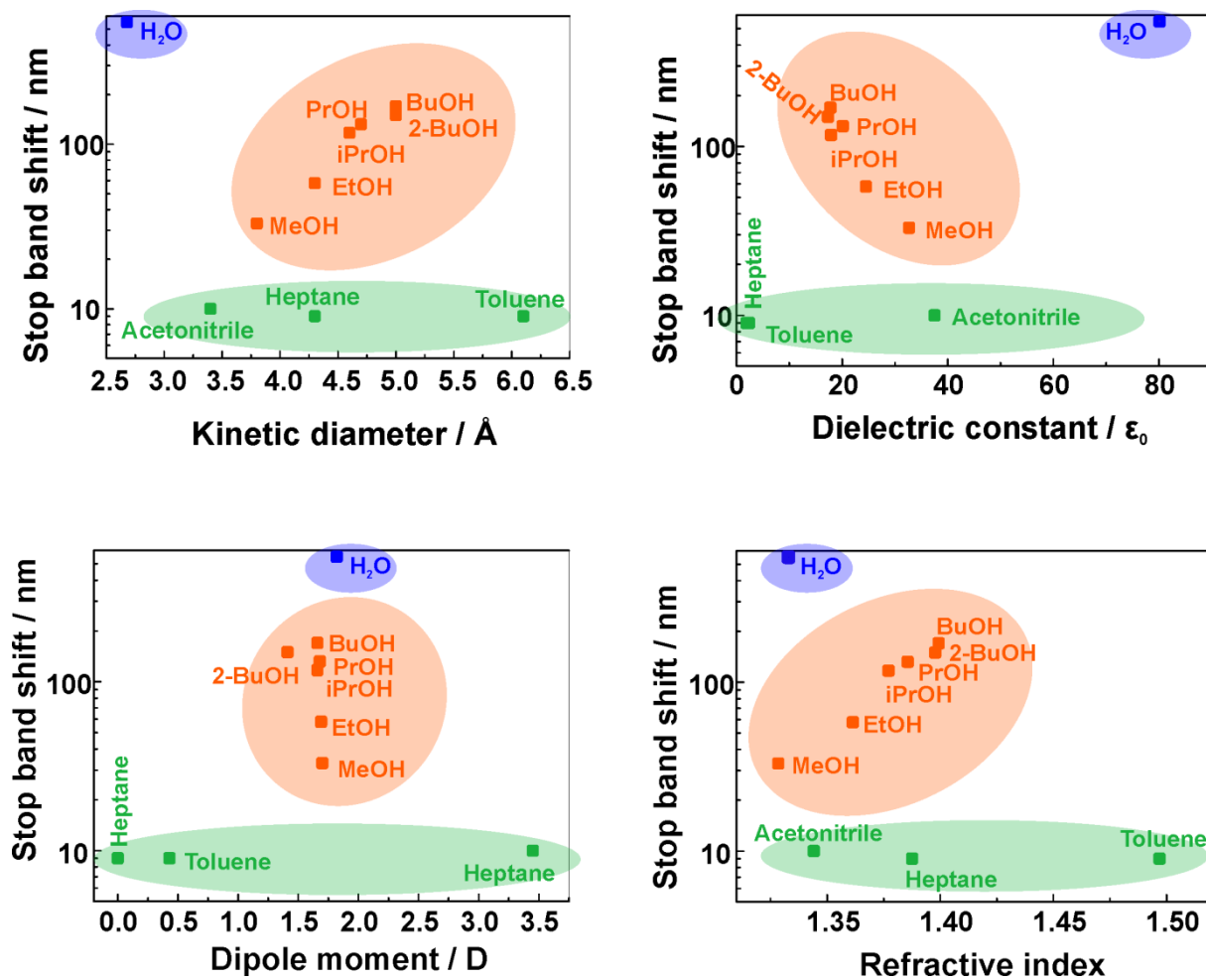
Figure S 5.15: Kinetic diameter, dielectric constant, dipole moment and refractive index of the analyte molecules plotted against the stop band shift.
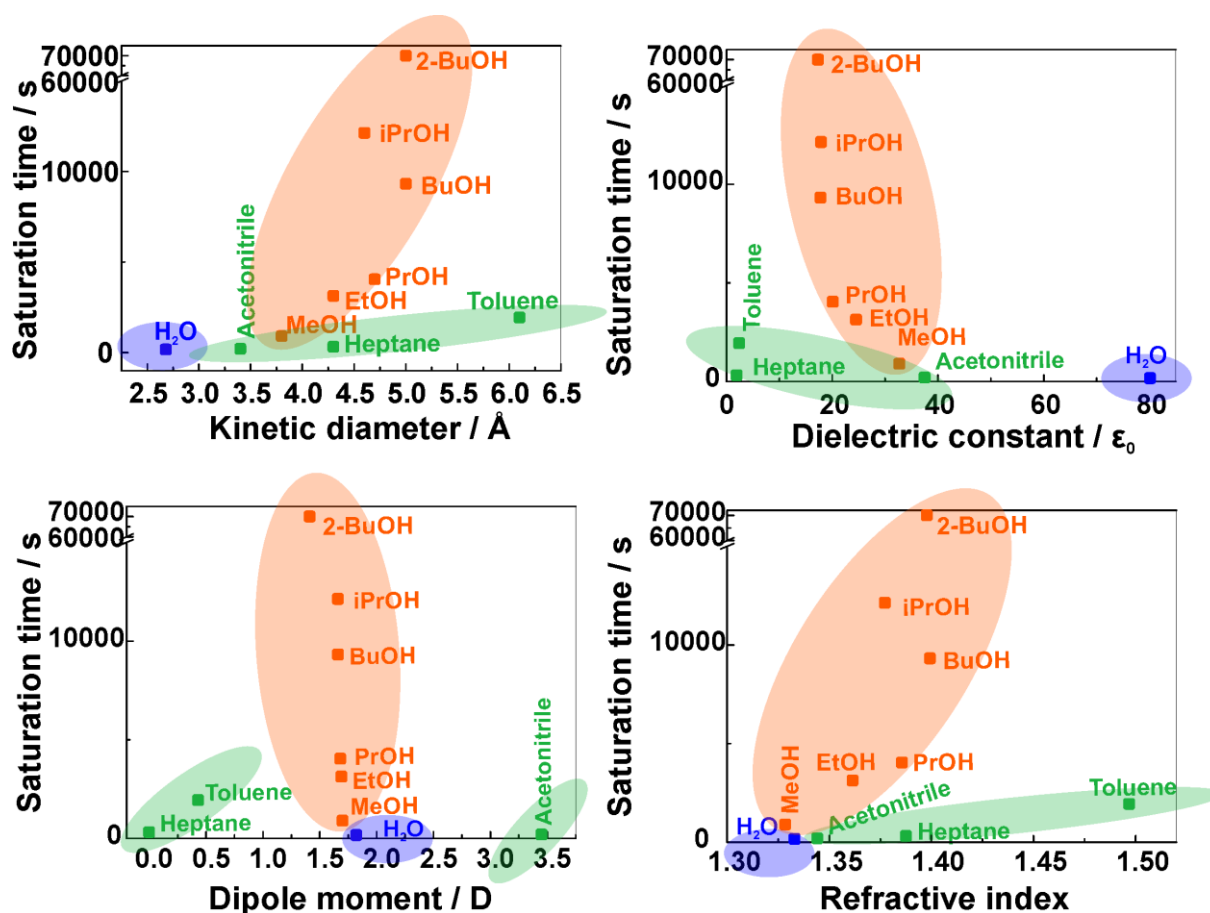
Figure S 5.16: Kinetic diameter, dielectric constant, dipole moment and refractive index of the analyte molecules plotted against the saturation time.
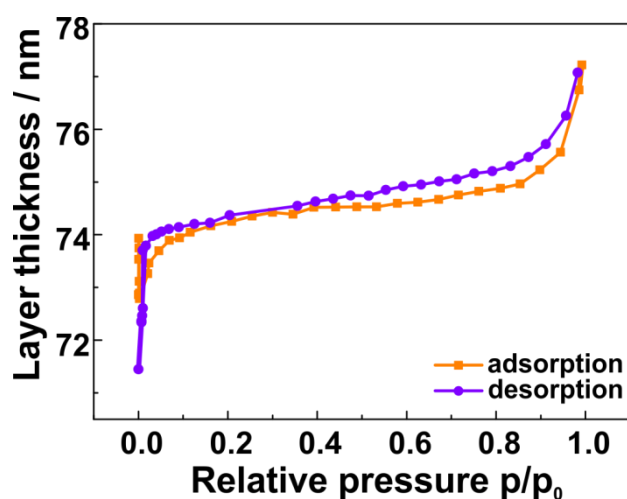

Figure S 5.17: Layer thickness change of a $HSbP_2O_8$ nanosheet thin film measured at different relative pressures of ethanol vapor by ellipsometric porosimetry.

Table S 5.5. Stop band shifts and saturation times of the $HSbP_2O_8$ nanosheet/TiO_2 nanoparticle Bragg stack to different analytes.[10-12]

Analyte	Stop band shift (nm)	Saturation time (s)	RI	Dielectric constant (ε_0)	Dipole moment (D)	Kinetic diameter (Å)
Water	550	166	1.3330	80.1	1.82	2.68
Acetonitrile	10	201	1.3441	37.5	3.45	3.4
Heptane	9	317	1.3876	1.92	0	4.3
Toluene	9	1937	1.4969	2.38	0.43	6.1
Methanol	33	897	1.3284	32.7	1.7	3.8
Ethanol	58	3130	1.3614	24.5	1.69	4.3
1-Propanol	132	4043	1.3856	20.1	1.68	4.7
2-Propanol	120	12140	1.3772	17.9	1.66	4.6
1-Butanol	170	9320	1.3993	17.8	1.66	5.0
2-Butanol	150	~70000	1.3978	17.3	1.41	5.0

Table S 5.6. Refractive indices and monolayer thicknesses for the TiO_2/$HSbP_2O_8$ Bragg stack used for the Matlab simulations for different analytes. The layer thicknesses and refractive indices at 100% analyte relative pressures were fitted to the measured reflectance spectra. Note that for experimental reasons, a different sample was used for the 2-butanol measurements, which is the reason for slightly different TiO_2 NP layer thicknesses.

| Analyte	Relative pressure	TiO₂ Layer thickness	RI	HSbP₂O₈ Layer thickness	RI
Acetonitrile	0%	55 nm	1.880	65 nm	1.540
	100%	55 nm	1.980	65 nm	1.540
Heptane	0%	55 nm	1.920	67 nm	1.537
	100%	55 nm	1.990	67 nm	1.537
Toluene	0%	56 nm	1.900	67 nm	1.537
	100%	56 nm	1.990	67 nm	1.537
Methanol	0%	56 nm	1.880	65 nm	1.540
	100%	56 nm	1.980	72 nm	1.530
Ethanol	0%	57 nm	1.880	67 nm	1.540
	100%	57 nm	1.980	78 nm	1.530
1-Propanol	0%	55 nm	1.880	65 nm	1.540
	100%	55 nm	1.980	108 nm	1.530
1-Butanol	0%	55 nm	1.900	64 nm	1.540
	100%	55 nm	1.960	119 nm	1.530
2-Propanol	0%	55 nm	1.900	66 nm	1.540
	100%	55 nm	1.970	104 nm	1.530
2-Butanol	0%	60 nm	1.900	65 nm	1.540
	100%	60 nm	1.960	114 nm	1.530
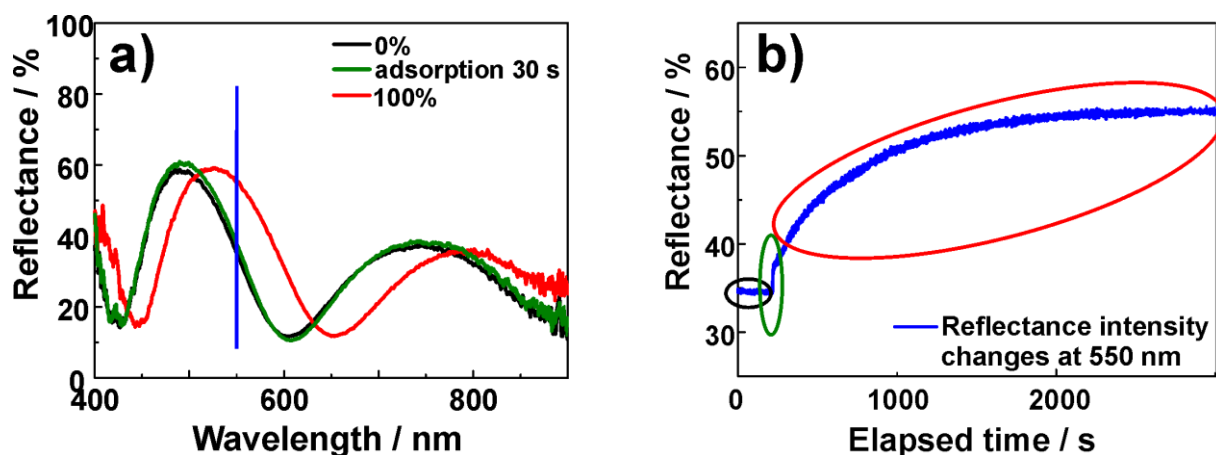
Figure S 5.18: Time-dependent changes of the TiO$_2$/HSbP$_2$O$_8$ Bragg stack upon ethanol adsorption. a) Reflectance spectra at 0% ethanol vapor pressure (black), after 30 s adsorption (green), and at 100% ethanol relative pressure (red), the blue line indicates at which wavelength the intensity changes were reported in b. b) Time dependent reflectance intensity changes of the spectra from a) at 550 nm. Hereby the different ranges are marked with different colors. Black is the intensity at 0% ethanol relative vapor pressure, green is the evolution in the first 6 s of the adsorption. Here, we attribute this initial fast intensity increase to the pore filling of the TiO$_2$ NP layer. The area marked with red indicates the saturation time of the Bragg stack.

REFERENCES

[1]   Y. Piffard, S. Oyetola, S. Courant, A. Lachgar, *J. Solid State Chem.* **1985**, *60*, 209-213.

[2]   B. V. Lotsch, F. Scotognella, K. Moeller, T. Bein, G. A. Ozin, *SPIE Proc. Vol. 7713*, **2010**, 7713V.

[3]   Z. Hu, C.-a. Tao, F. Wang, X. Zou, J. Wang, *J. Mater. Chem. C* **2015**, *3*, 211-216.

[4]   K. Ufer, G. Roth, R. Kleeberg, H. Stanjek, R. Dohrmann, J. Bergmann, *Z. Kristallogr.* **2004**, *219*, 519-527.

[5]   X. Wang, J. Li, R. D. Hart, A. van Riessen, R. McDonald, *J. Appl. Crystallogr.* **2011**, *44*, 902-910.

[6]   P. W. Winston, D. H. Bates, *Ecology* **1960**, *41*, 232-237.

[7]   L. Greenspan, *J. Res. Nat. Bur. Stand.* **1977**, *81A*, 89-96.

[8]   Bronkhorst-High-Tech*,* www.fluidat.com, accessed: 08/2015.

[9]   M. C. Fuertes, S. Colodrero, G. Lozano, A. R. González-Elipe, D. Grosso, C. Boissière, C. Sánchez, G. J. d. A. A. Soler-Illia, H. Míguez, *J. Phys. Chem. C* **2008**, *112*, 3157-3163.

[10]   H. Wu, Q. Gong, D. H. Olson, J. Li, *Chem. Rev.* **2012**, *112*, 836-868.

[11]   T. Borjigin, F. Sun, J. Zhang, K. Cai, H. Ren, G. Zhu, *Chem. Commun.* **2012**, *48*, 7613-7615.

[12]   W. M. Haynes, D. R. Lide, *CRC handbook of chemistry and physics : a ready-reference book of chemical and physical dat*, 92 ed., CRC Press, Boca Raton, **2011**.

10.3 SUPPORTING INFORMATION FOR CHAPTER 6

Lithium tin sulfide – a high-refractive-index 2D material for humidity-responsive Photonic Crystals

Katalin Szendrei-Temesi, Olalla Sanchez-Sobrado, Sophia Betzler, Katharina M. Durner, Tanja Holzmann, Bettina V. Lotsch*
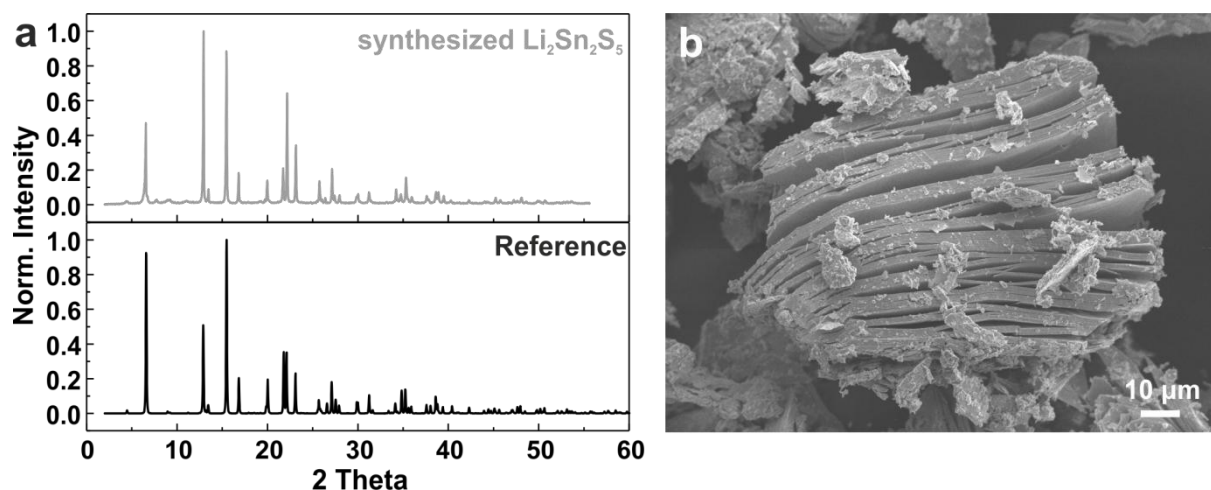

Figure S 6.1: Structural properties of $Li_2Sn_2S_5$. a) Powder diffraction pattern with normalized intensities of the as-synthesized $Li_2Sn_2S_5$ and a reference compound from the literature.[1] The successful synthesis of the $Li_2Sn_2S_5$ was confirmed by powder diffraction analysis, the powder pattern of the as-synthesized product shows good agreement with the reference pattern from the literature. b) Scanning electron microscope (SEM) secondary electron image of a $Li_2Sn_2S_5$ crystal showing the layered structure, which after short contact with ambient moisture exfoliates.

Table S 6.1: Elemental composition of the as-synthesized $Li_2Sn_2S_5$ observed by inductively coupled plasma (ICP) analysis. The good agreement between the measured and the expected values confirm the composition of the as-synthesized compound.

Element	Li	Sn	S
Amount (mmol/g)	4.12 ± 0.05	4.11 ± 0.05	10.88 ± 0.22
Expected	4	4	10

Table S 6.2: Elemental composition of the as-synthesized $Li_2Sn_2S_5$ observed by energy dispersive x-ray (EDX) analysis.

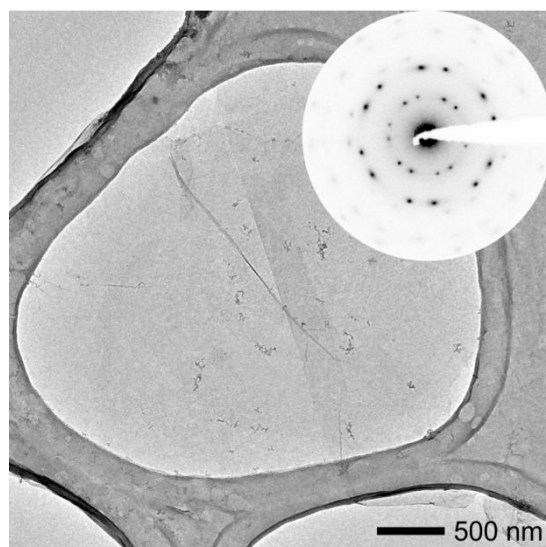| Element	S	Sn
Amount atom%	37.85 ± 7.35	16.84 ± 3.35
Expected	40	16

Figure S 6.2: Transmission electron microscope (TEM) image and the corresponding selected area diffraction (SEAD) pattern showing two single LTS nanosheets lying on top of each other in a turbostratically disordered fashion.
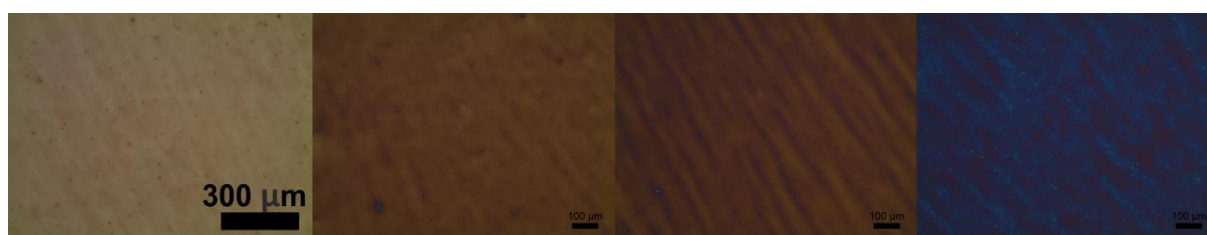

Figure S 6.3: Optical microscope images showing different interference colors of the LTS nanosheet thin films, indicating different thicknesses. The thin films were fabricated at different spin-coating speeds, from left to the right with 5000 rpm, 4000 rpm, 3000 rpm and 4000 rpm (double spin-coated), respectively.
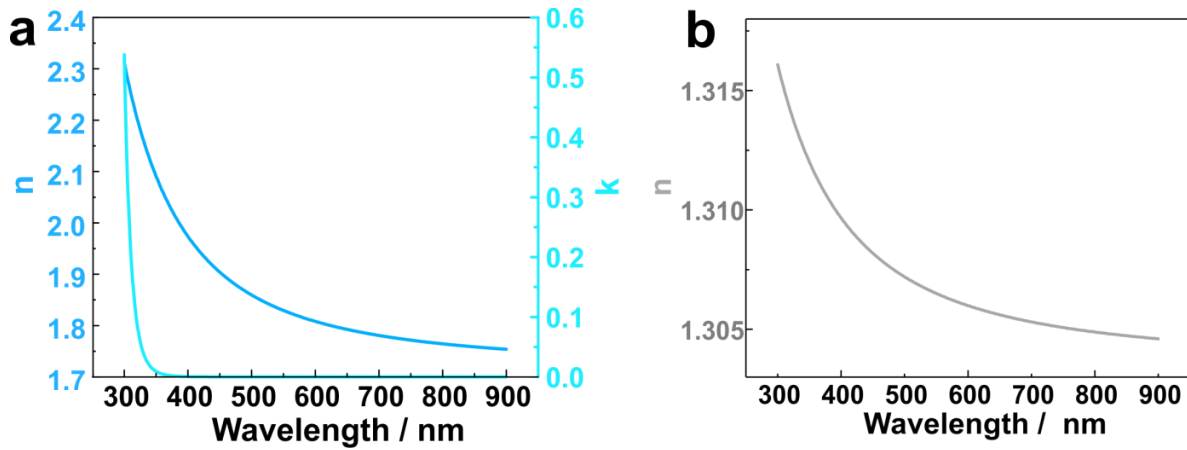
Figure S 6.4: Optical properties of the used TiO_2 and SiO_2 thin films measured by spectroscopic ellipsometry. a) Wavelength dependent RI (*n*) and extinction coefficient (*k*) of the TiO_2 nanoparticle based thin film; b) wavelength dependent RI of the SiO_2 nanoparticle based thin film. The extinction coefficient of the SiO_2 nanoparticle film is negligibly low in the entire spectral range and is therefore not shown.
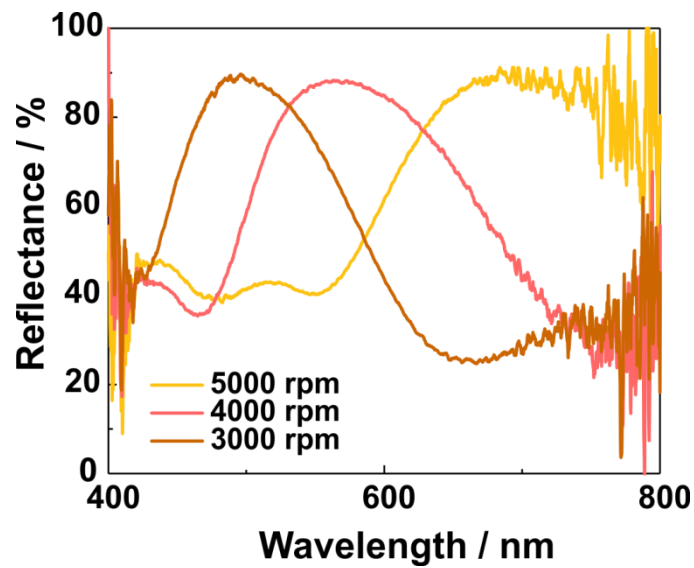

Figure S 6.5: Reflectance spectra of SiO_2 nanoparticles and LTS nanosheet based BSs consisting of seven layers. We observe a slight increase in the reflectance intensity compared to the BS with only five layers, but the defect concentration increases, which is visible by the increased scattering of the structure, seen by the increased background.
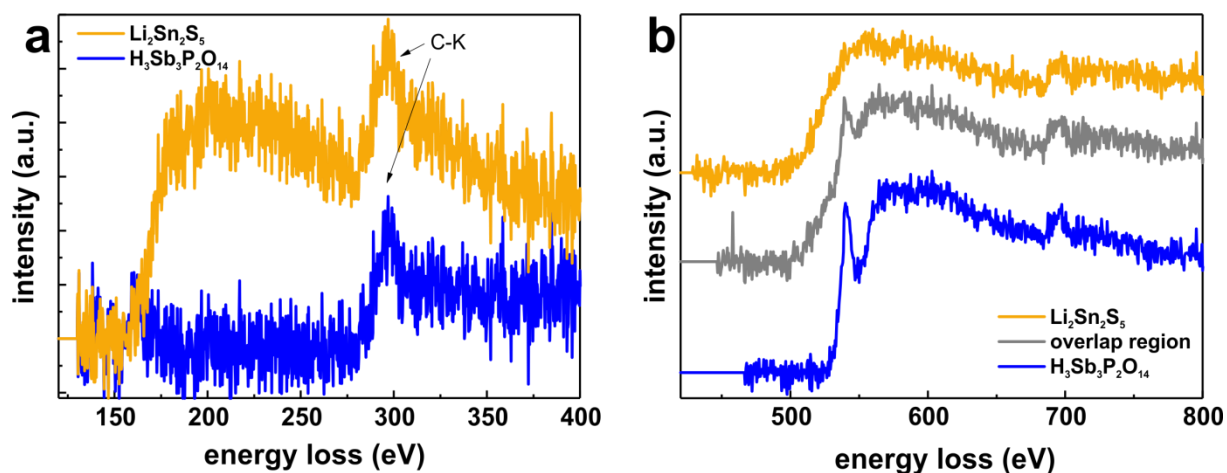
Figure S 6.6: Electron energy loss spectra (EELS) for two different measured energy ranges: a) 100-400 eV and b) 420-800 eV, showing the characteristic edges for the two different nanosheet materials and the overlap region. The S-$L_{2,3}$ edge appears in the spectral region of 150 to 250 eV and is only visible for LTS nanosheets. Both materials show small C-K edges which result from carbon contamination during the measurement. The sawthooth shaped Sn-$M_{4,5}$ edge is clearly visible in the spectrum of LTS for an energy loss of 450-700 eV, while the spectrum of $H_3Sb_3P_2O_{14}$ exhibits a sharp line overlapping the sawthooth shape of the Sb-$M_{4,5}$ edge. This feature most likely results from the superimposed O-K edge. For both materials an additional feature appears for energy losses above 700 eV. This minor feature cannot be identified unequivocally and most likely originates from a contamination introduced by the FIB sample preparation.
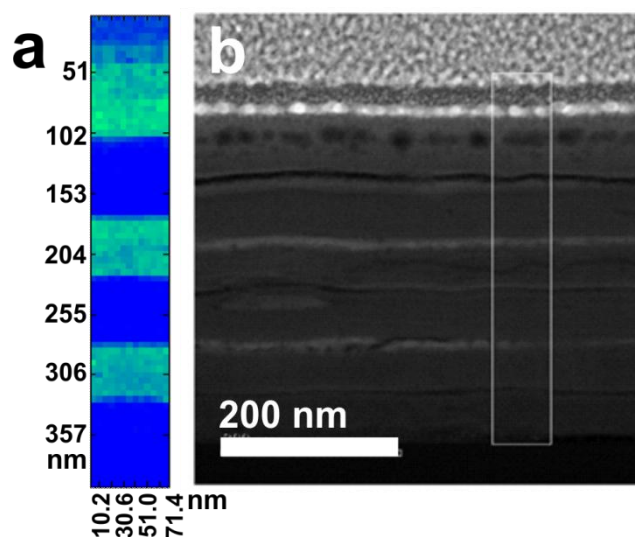

Figure S 6.7: a) Electron energy loss (EEL) map displaying the integrated intensity of the S-$L_{2,3}$ edge. b) The investigated sample area is highlighted in the scanning transmission electron microscope (STEM) image. A pixel size of 5.1 nm was used during the spectrum image acquisition.

For the element mapping for the Sn-M$_{4,5}$ O-K and Sb-M$_{4,5}$ edges (Figure 6.6 d-g), due to the beam sensitivity of the materials, the scanning pixel size (applying subpixel scanning) had to be increased to 8 nm in order to prevent the degradation of the material by the electron beam while keeping sufficient signal intensity for the spectral region of 370-1394 eV (dispersion 0.5 eV/channel). This limits the spatial resolution of the maps and causes an overlap region where the elemental edges of both materials appear in the acquired spectra at the interface of the two materials (indicated by gray color in Figure 6.6f).

According to Figure 6.6d and 6.6g, the layer thicknesses within the photonic architecture are homogenous; only the upper layer containing LTS appears to be thicker, which can be attributed to the TEM sample preparation in the focused ion beam (FIB). Prior to the cutting process, a Pt layer is deposited onto the sample to prevent the implantation of gallium ions used for the cutting. Thus, Ga and Pt integration cause the thickening of the upper layer. Note that the layer thicknesses were also confirmed by spectroscopic ellipsometry measurements at ambient conditions (Figure S 6.8 and Table S 6.3).
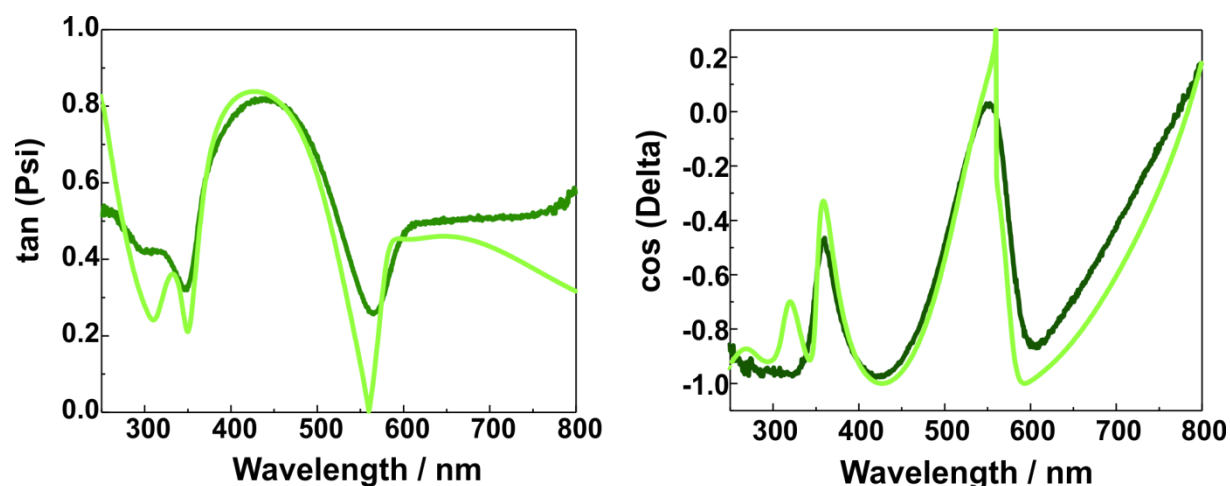

Figure S 6.8: Fittings of the spectroscopic ellipsometry data using the periodic model for the all-nanosheet BS. The dark green lines are the measured data and the light green lines the fitted ones.
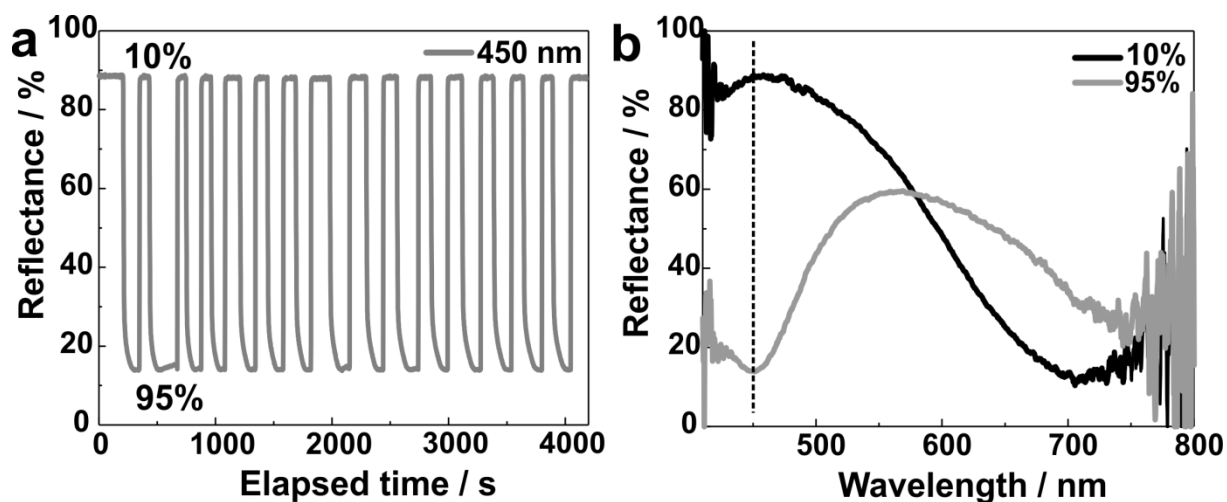
Figure S 6.9: Cycling behavior of the SiO$_2$ / LTS nanosheet based Bragg stack. The cycling was performed by alternatingly applying 11% and 93% relative pressure of water vapor. The spectral changes were detected by recording the reflectance intensity at 450 nm. This wavelength was carefully chosen to monitor the changes at the blue stopband edge, which are measurable for the humidity range between 10-93% RH. Please note that due to the stopband shift, a decrease of the reflectance intensity refers to an increase in the relative humidity, as marked in b).

Figure S 6.10: Cycling behavior of the H$_3$Sb$_3$P$_2$O$_{14}$ / LTS nanosheet based Bragg stack. The cycling was performed by applying 11% and 93% relative pressure of water vapor. The spectral changes were detected by recording the reflectance intensity at 550 nm. This wavelength was carefully chosen to monitor the changes at the red stopband edge, which are measurable for the humidity range between 10-93% RH. Please note that due to the stopband shift, a decrease of the reflectance intensity refers to a decrease in the relative humidity, as marked in b).
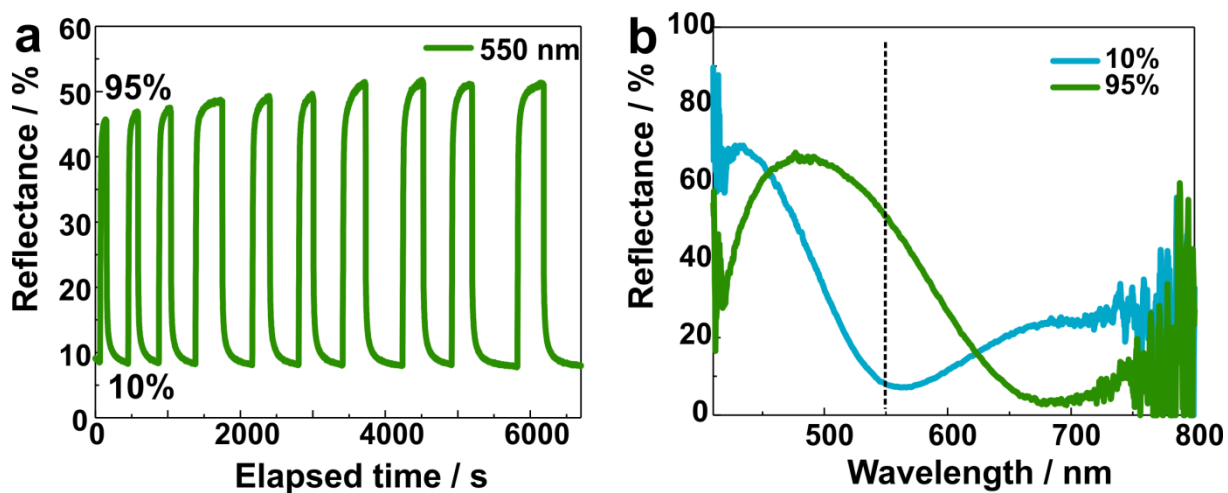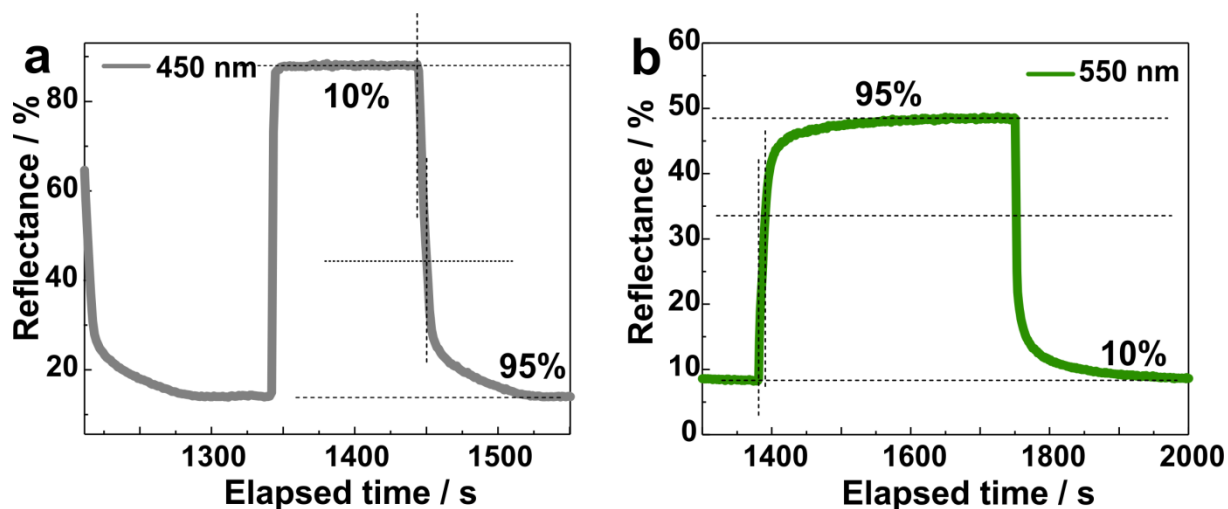
Figure S 6.11: Time dependent reflectance intensity changes at 450 nm and 550 nm, respectively, of a) the SiO$_2$ and b) the H$_3$Sb$_3$P$_2$O$_{14}$ based LTS Bragg stacks. The plots show an excerpt of the time plots shown in S 6.9 and 6.10 in order to demonstrate the calculation of the response times (τ$_{63}$).
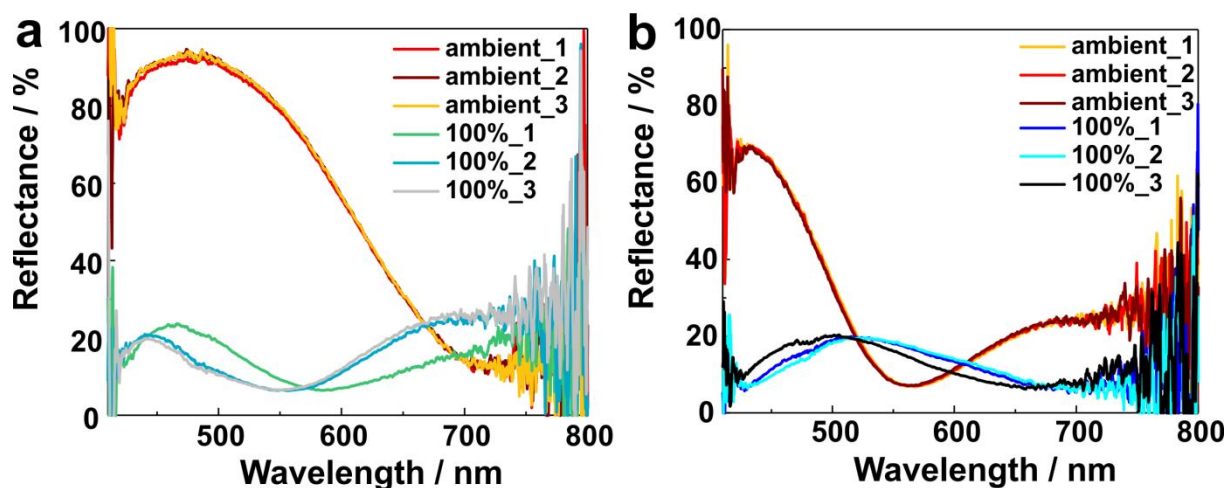

Figure S 6.12: Reflectance spectra of the a) SiO$_2$ / LTS and b) H$_3$Sb$_3$P$_2$O$_{14}$ / LTS based Bragg stack showing the stable cycling behavior between 100% RH and ambient (30% RH) conditions. The features of the reflectance spectra at 100% RH arise from Fabry-Perot oscillations, since at 100% RH the RI contrast cancels out and the structure appears transparent.

Table S 6.3: Fitted layer thicknesses and refractive indices for the two different layer materials measured by spectroscopic ellipsometry using the periodic model for 3 double layers.

Layer material	LTS	H$_3$Sb$_3$P$_2$O$_{14}$
Thickness	44 nm	64 nm
Refractive index (at 633 nm)	2.65	1.56

Table S 6.4: Layer thicknesses and RIs for the differently fabricated TiO_2 nanoparticle / LTS nanosheet BSs calculated by fitting the measured reflectance using the transfer matrix method using the Matlab code described in ref. 2. For the RI of the LTS nanosheets, we used the wavelength dependent RI measured by ellipsometry.

Rotation speed	Material	Layer thickness	Refractive index
3000 rpm	LTS	68 nm	From ellipsometry
	TiO_2	80 nm	1.75
4000 rpm	LTS	60 nm	From ellipsometry
	TiO_2	64 nm	1.75
5000 rpm	LTS	53 nm	From ellipsometry
	TiO_2	55 nm	1.78

Table S 6.5: Layer thicknesses and RIs for the differently fabricated SiO_2 nanoparticle / LTS nanosheet BSs calculated by fitting the measured reflectance using the transfer matrix method using the Matlab code described in ref 2. For RI of the LTS nanosheets, we used the wavelength dependent RI measured by ellipsometry.

Rotation speed	Material	Layer thickness	Refractive index
3000 rpm	LTS	85 nm	From ellipsometry
	SiO_2	163 nm	1.40
4000 rpm	LTS	90 nm	From ellipsometry
	SiO_2	100 nm	1.40
5000 rpm	LTS	85 nm	From ellipsometry
	SiO_2	90 nm	1.40

– *Appendix* –

Table S 6.6: Layer thicknesses and RIs for the differently fabricated $H_3Sb_3P_2O_{14}$ nanosheet / LTS nanosheet BSs calculated by fitting the measured reflectance using the transfer matrix method using the Matlab code described in ref. 2. For the RI of the LTS nanosheets, we used the wavelength dependent RI measured by ellipsometry.

Rotation speed	Material	Layer thickness	Refractive index
3000 rpm	LTS	89 nm	From ellipsometry
	$H_3Sb_3P_2O_{14}$	92 nm	1.65
4000 rpm	LTS	79 nm	From ellipsometry
	$H_3Sb_3P_2O_{14}$	82 nm	1.58
5000 rpm	LTS	63 nm	From ellipsometry
	$H_3Sb_3P_2O_{14}$	65 nm	1.60

Table S 6.7: Layer thicknesses and RIs for the SiO_2 nanoparticle / LTS nanosheet BS at different RH values calculated by fitting the measured reflectance using the transfer matrix method using the Matlab code described in ref. 2. For the RI of the LTS nanosheets at 11% RH, we used the wavelength dependent RI measured by ellipsometry.

Relative humidity	Material	Layer thickness	Refractive index
11%	LTS	86 nm	From ellipsometry
	SiO_2	88 nm	1.32
32%	LTS	90 nm	1.87
	SiO_2	88 nm	1.35
52%	LTS	95 nm	1.82
	SiO_2	88 nm	1.40
74%	LTS	100 nm	1.83
	SiO_2	88 nm	1.45
93%	LTS	110 nm	1.80
	SiO_2	88 nm	1.51

– Appendix –

Table S 6.8: Layer thicknesses and refractive indices for the $H_3Sb_3P_2O_{14}$ nanosheet / LTS nanosheet BS at different RH values calculated by fitting the measured reflectance using the transfer matrix method using the Matlab code described in ref. 2. For the RI of the LTS nanosheets at 11% RH, we used the wavelength dependent RI measured by ellipsometry.

Relative humidity	Material	Layer thickness	Refractive index
11%	LTS	55 nm	From ellipsometry
	$H_3Sb_3P_2O_{14}$	66 nm	1.60
43%	LTS	65 nm	1.90
	$H_3Sb_3P_2O_{14}$	85 nm	1.56
74%	LTS	74 nm	1.82
	$H_3Sb_3P_2O_{14}$	97 nm	1.55
93%	LTS	82 nm	1.78
	$H_3Sb_3P_2O_{14}$	106 nm	1.52

REFERENCES

[1] A. Kuhn, T. Holzmann, J. Nuss, B. V. Lotsch, *J. Mater. Chem. A* **2014**, *2*, 6100-6106.

[2] M. C. Fuertes, S. Colodrero, G. Lozano, A. R. González-Elipe, D. Grosso, C. Boissière, C. Sánchez, G. J. d. A. A. Soler-Illia, H. Míguez, *J. Phys. Chem. C* **2008**, *112*, 3157-3163.

10.4 SUPPORTING INFORMATION FOR CHAPTER 7

Fluorescent Humidity Sensors Based on Photonic Resonators

Katalin Szendrei,[§] Alberto Jiménez-Solano,[§] Gabriel Lozano, Bettina V. Lotsch, Hernán Míguez
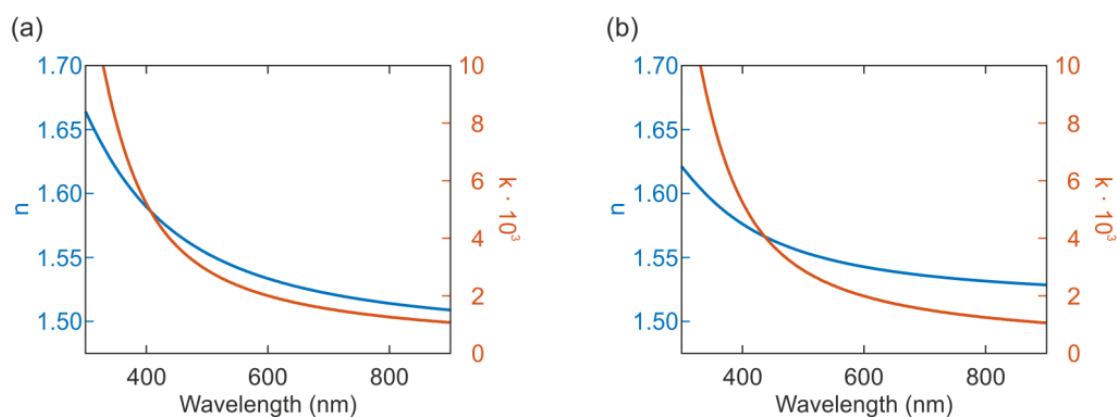
[§] These authors contributed equally to this work

Figure S 7.1: (a-b) Spectral dependence of the real (blue) and imaginary part (red) of the complex refractive index of $H_3Sb_2P_2O_{14}$ nanosheet thin film at 0% relative humidity (RH) (a) and 75% RH (b). The Cauchy-Lorentz parameters according to the ellipsometry fittings are the following. Cauchy parameters: B = 0.01617 μm^2, C = 0 μm^4, D = 0, E = 0 μm^2, F = 0 μm^4; Lorentz parameters: f = 0.02605, E_0 = 6.76658 eV, Γ = 3.7984 eV, ε_{inf} = 0.
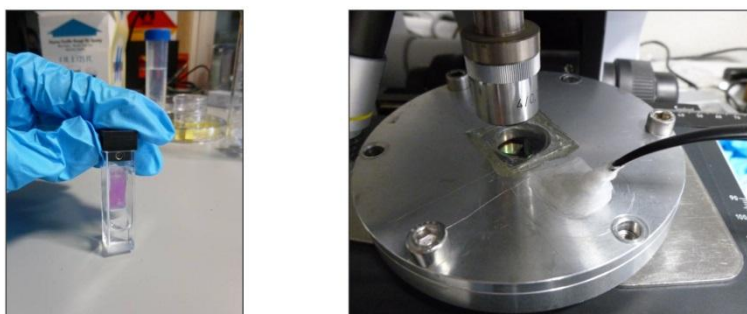

Figure S 7.2: Measurement chambers. Left panel shows the system we employ to perform PL measurements. Sample was fixed to the lid of a quartz cuvette and placed above ca. 1 mL saturated salt solution in order to control the humidity in the closed cuvette. Right panel shows the closed chamber used for reflectance measurements. Sample was placed into a stainless steel chamber with an integrated humidity sensor, and defined the relative humidity with saturated salt solutions.
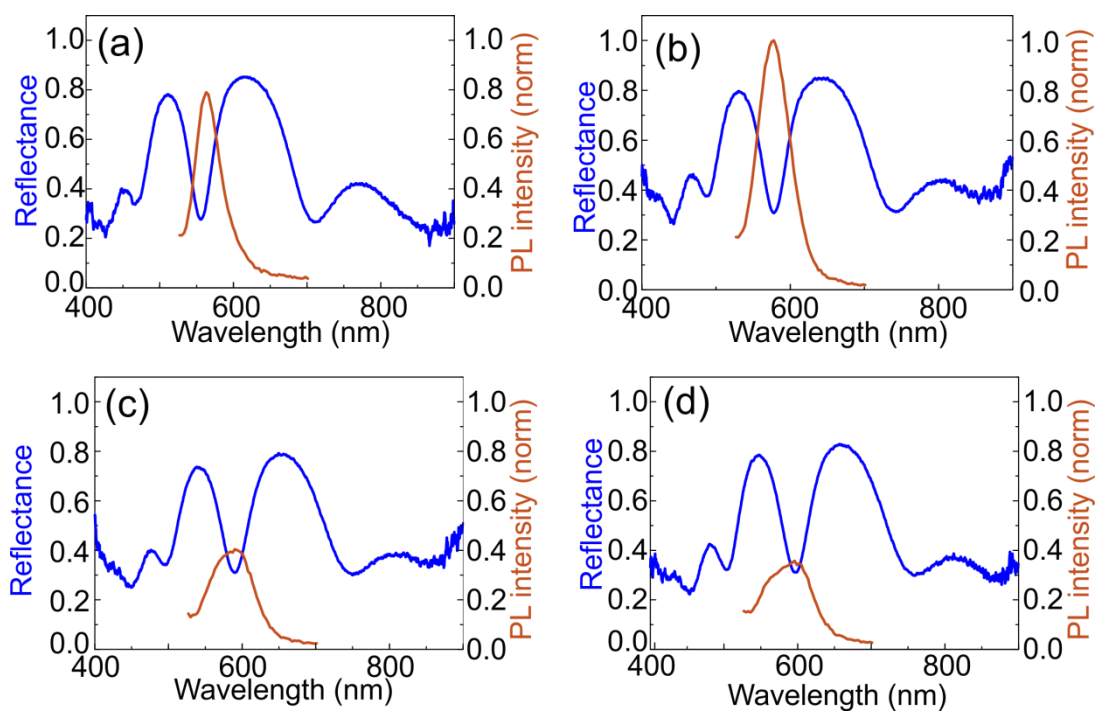
Figure S 7.3: Reflectance spectra and (normalized) photoluminescence spectra of the turn-off sample plotted together at a) 32% RH, b) 74% RH, c) 80% RH and d) 90% RH. The plots demonstrate well the good agreement of the spectral position of the photoluminescence maximum and the photonic coupling mode.

Figure S 7.4: Reflectance spectra and (normalized) photoluminescence spectra of the turn-on sample plotted together at a) 32% RH, b) 74% RH, c) 80% RH and d) 90% RH. The plots demonstrate well the good agreement of the spectral position of the photoluminescence maximum and the photonic coupling mode.
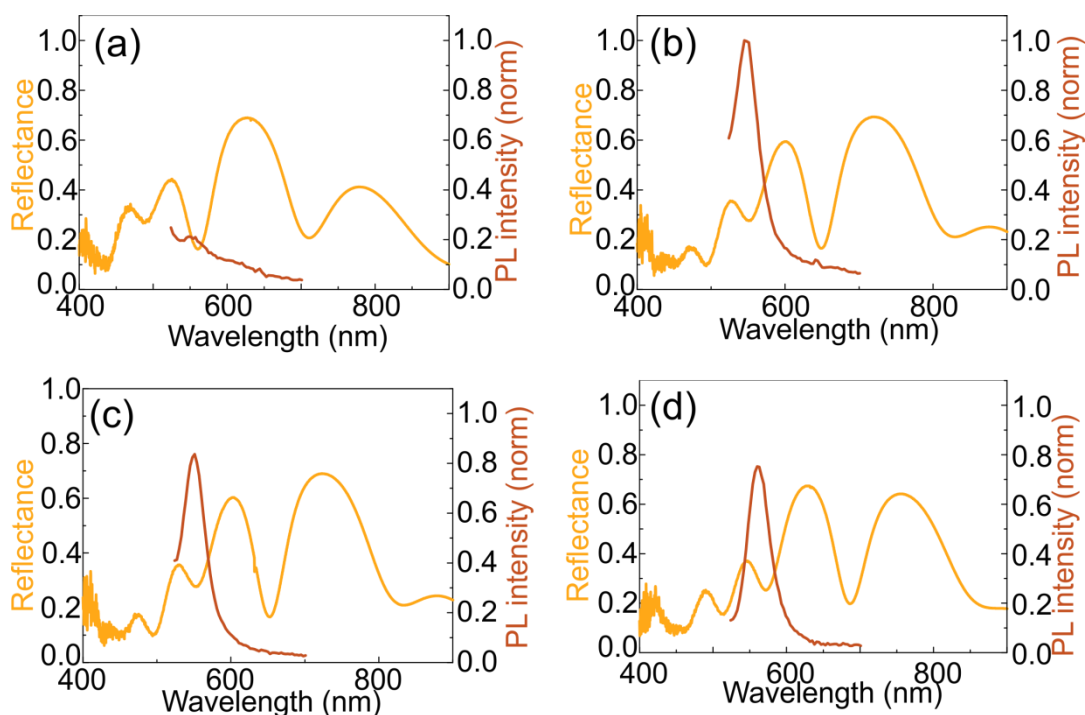
10.5 SUPPORTING INFORMATION FOR CHAPTER 8

Tracking Vertical Molecular Diffusion Into 1-dimensional Photonic Crystals

Katalin Szendrei-Temesi,[§] Alberto Jiménez-Solano,[§] Bettina V. Lotsch

[§] These authors contributed equally to this work

EXPERIMENTAL SECTION

1DPC Fabrication

Multilayered structures consisting of alternate $H_3Sb_3P_2O_{14}$ nanosheets and TiO_2 thin films were fabricated following the spin-coating process previously described.[1] $H_3Sb_3P_2O_{14}$ nanosheets and TiO_2 nanoparticles were synthesized according to the literature.[1-3] In total, we deposited 11 layers, as first and last layer served TiO_2. All 1DPCs were designed to exhibit the reflectance maximum in the blue spectral range ($\approx 450\,nm$), that the entire intercalation process for all amines in study is detectable in the visible spectral range.

Diffusion Experiments

All amines, which were intercalated into the layered structures, were diluted to 1 M with ethanol in order to ensure a similar evaporation rate and to keep the experimental conditions similar. 1 mL of the amine solution was filled into a glass Petri dish with a volume of 20 cm³. Secondly, a 1 mm thick acrylic glass plate with a round opening of 2 mm diameter was placed on top of the Petri dish (Figure 1d). This acrylic glass plate serves as a lid of the chamber and the hole helps to spatially limit the space, where the amine solution can evaporate from the chamber. The 1DPC was directly placed on top of the acrylic glass and the optical measurements were carried out directly above the hole, while the 1DPC was exposed directly to the amine vapor. The spectra were collected at normal incident from a 1 mm spot with an spectrophotometer (Ocean Optics, USB2000+) attached to a microscope (Leica, DM2500). With a smaller observation area compared to the diffusion hole, it could be ensured that the whole sample area under study was exposed to the amine vapour equally. This measurement set-up is summarized in Figure 1d. For all three amine intercalation experiments, different areas of the same sample were used in order to minimize the structural fabrication deviations between different samples.

Structural Characterization

The sample morphology was studied with a FE-SEM (Zeiss, Merlin) working at 1.5 kV collecting both secondary and back scattered electrons.

Theoretical Modelling

Sample design and optical response fittings were carried out with a self-made code based on a combination of the transfer matrix method (TMM),[4, 5] to calculate the reflectance, and a genetic algorithm (GA),[6,7] to search the right fittings parameters (layer thicknesses and refractive index). For every amine in study the whole set of optical responses was fitted at the same time giving the same weight to every spectrum. Refractive index of TiO$_2$ bulk is taken from the literature.[8] The porous layers are modeled by Bruggeman[9] model:

$$\frac{\epsilon_{\text{bulk}}(\lambda) - \epsilon(\lambda)}{\epsilon_{\text{bulk}}(\lambda) + 2\epsilon(\lambda)} ff_{\text{bulk}} + \frac{\epsilon_{\text{air/etOH}}(\lambda) - \epsilon(\lambda)}{\epsilon_{\text{air/etOH}}(\lambda) + 2\epsilon(\lambda)} ff_{\text{air/etOH}} = 0$$

Refractive index of 'dense layers' of NSs are dispersive in l modeled by the Cauchy[10] with absorption empirical law:

$$n(\lambda) = A_1 + \frac{A_2 \cdot 10^4}{\lambda^2} + \frac{A_3 \cdot 10^9}{\lambda^4}$$

$$k(\lambda) = B_1 \cdot 10^{-5} + \frac{B_2 \cdot 10^4}{\lambda^2} + \frac{B_3 \cdot 10^9}{\lambda^4}$$

The refractive indices of the NS layers change with time are calculated by the volumetric average[9] model:

$$\epsilon^t(\lambda) = \epsilon_{\text{NSs}}(\lambda) \cdot ff_{\text{NSs}}^t + \epsilon_{\text{air/etOH}} \cdot ff_{\text{air/etOH}}^t$$

Optical response of the sample in study at different starting points

Reflectance spectra from the sample in study before (t=0$_{ambient}$) and after exposure to the ethanol-amine mixture (t=0$_{EtOH}$) for all three system are shown. Here, it can be seen a reflectance peak shift, Δλ ≈ 40 nm, accompanied with a reflectance intensity increase, ΔR ≈ 10%. The experimental and the theoretical curves show a similar behaviour for all three systems, which indicates that the filling of the multilayer with ethanol is comparable for all three systems.

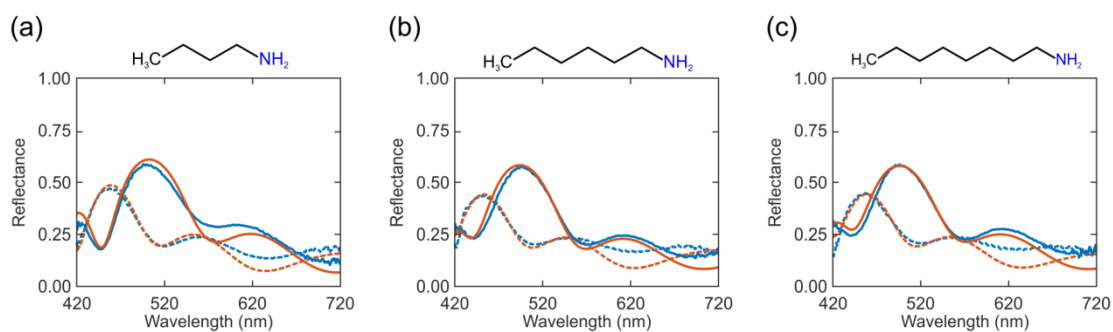
Figure S 8.1: Experimental (blue) and theoretical (red) reflectance spectra of the 1DPCs before (t=0$_{ambient}$, dashed lines and after (t=0$_{EtOH}$, solid lines the infiltration with ethanol for the measurement with a) C2, b) C4 and c) C8.

Optical response of the sample in study at different time slots

Reflectance spectra from the sample in study after exposure to the ethanol-amine mixture (t>0$_{EtOH}$) for all three system are shown. Here, it can be seen the good agreement between the experimental and the theoretical model employed in this work.

Figure S 8.2: (a-g) Experimental (blue) and theoretical (red) reflectance spectra of the 1DPCs at different time points at the beginning (t=0$_{EtOH}$) and during (t>0$_{EtOH}$) the butylamine (C4) intercalation procedure. (h) Multilayer layout for the 1DPC with the individual initial and final layer thicknesses.

Figure S 8.3: (a-g) Experimental (blue) and theoretical (red) reflectance spectra of the 1DPCs at different time points at the beginning (t=0$_{EtOH}$) and during (t>0$_{EtOH}$) the hexylamine (C6) intercalation procedure. (h) Multilayer layout for the 1DPC with the individual initial and final layer thicknesses.
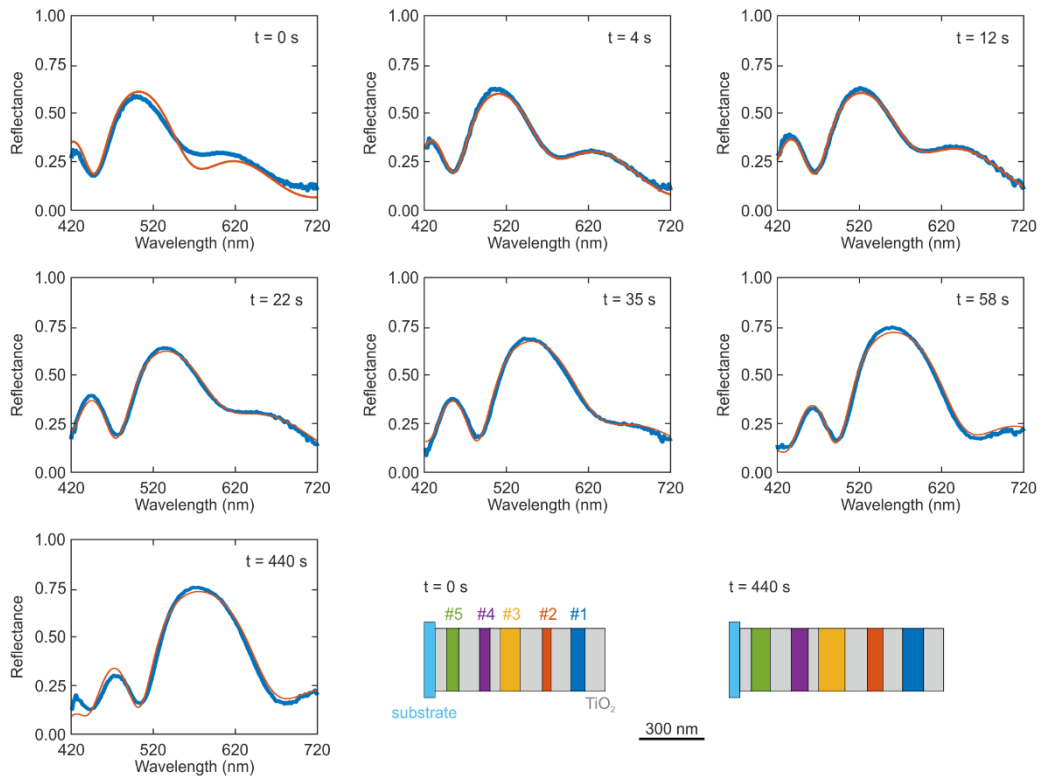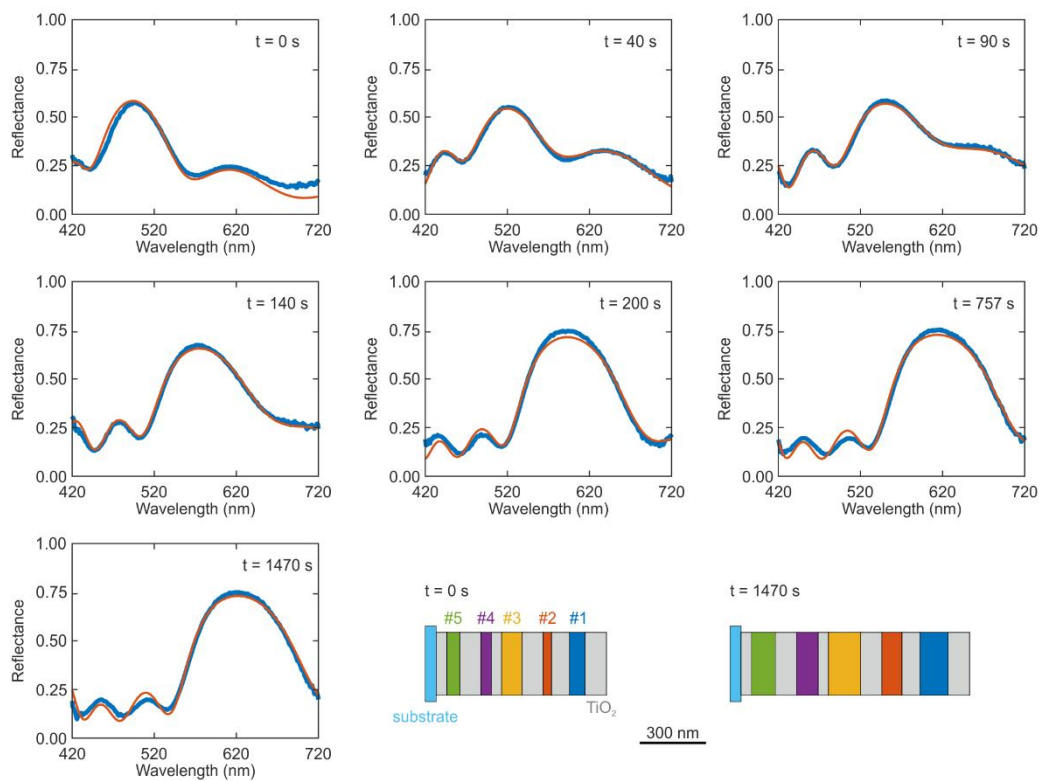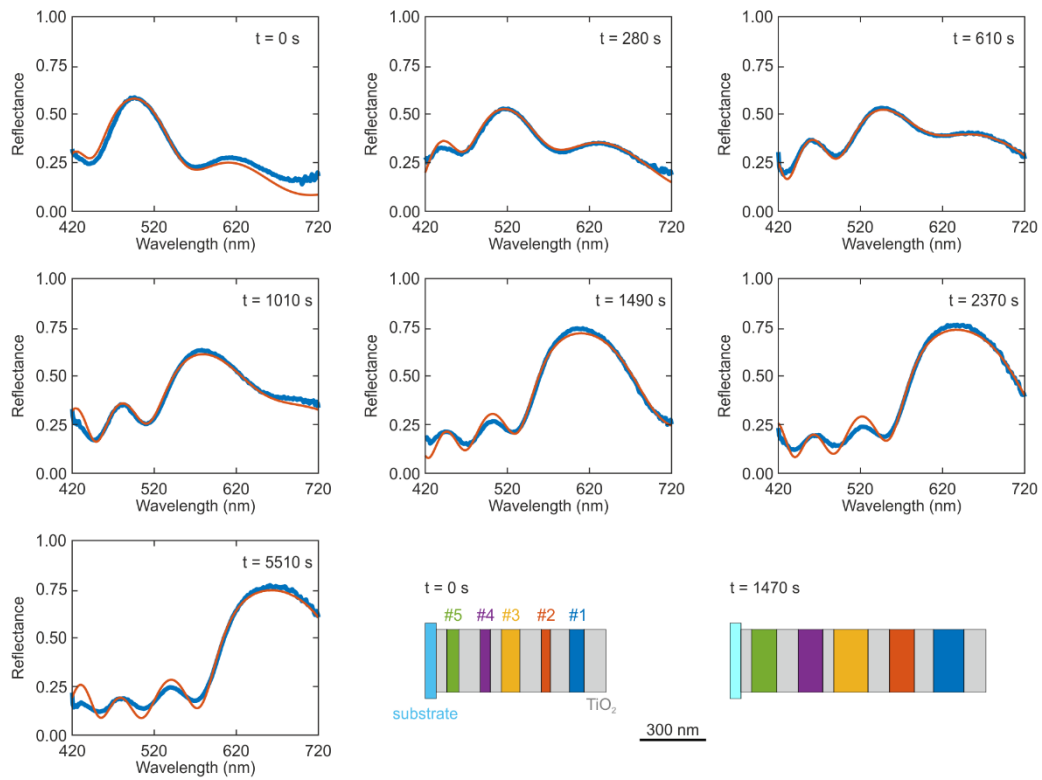
Figure S 8.4: (a-g) Experimental (blue) and theoretical (red) reflectance spectra of the 1DPCs at different time points at the beginning (t=0$_{EtOH}$) and during (t>0$_{EtOH}$) the octylamine (C8) intercalation procedure. (h) Multilayer layout for the 1DPC with the individual initial and final layer thicknesses.

– Appendix –

Table S 8.1: Summary of the individual layer thickness increases and total diffusion times of the three investigated systems at two different diffusion times. Time 1 corresponds to the time, where the individual layers reach a 'common thickness, and Time 2 means the total diffusion time, which is needed to reach the saturation.

Analyte	Butylamine (C4)	Hexylamine (C6)	Octylamine (C8)
Time 1	1.2 s	6 min	30 min
Individual layer thickness swelling	27 nm	#1: 52 nm #2: 47 nm #3: 47 nm #4: 44 nm #5: 43 nm	#1: 57 nm #2: 55 nm #3: 54 nm #4: 48 nm #5: 43 nm
Time 2	7.4 s	24 min	92 min
Individual layer thickness swelling	31 nm	#1: 57 nm #2: 54 nm #3: 54 nm #4: 51 nm #5: 49 nm	#1: 72 nm #2: 71 nm #3: 71 nm #4: 65 nm #5: 60 nm

REFERENCES

[1]   K. Szendrei, P. Ganter, O. Sánchez-Sobrado, R. Eger, A. Kuhn, B. V. Lotsch, *Adv. Mater.* **2015**, *27*, 6341-6348.

[2]   Y. Piffard, A. Verbaere, A. Lachgar, S. Deniard-Courant, M. Tournoux, *Rev. Chim. Miner.* **1986**, *23*, 766-775.

[3]   Y. Li, M. E. Calvo, H. Míguez, *Adv. Opt. Mater.* **2016**, *4*, 464-471.

[4]   P. Yeh, *John Wiley & Sons, New York* **1988**.

[5]   E. Hecht, *Optics*, Addison-Wesley, Reading, Mass., **2002**.

[6]   J. H. Holland, *Adaptation in Natural and Artificial Systems: An Introductory Analysis with Applications to Biology, Control and Artificial Intelligence*, MIT Press, **1992**.

[7]   D. E. Goldberg, *Genetic Algorithms in Search, Optimization and Machine Learning*, Addison-Wesley Longman Publishing Co., Inc., **1989**.

[8]   A. Jiménez-Solano, M. Anaya, M. E. Calvo, M. Alcon-Camas, C. Alcañiz, E. Guillén, N. Martínez, M. Gallas, T. Preussner, R. Escobar-Galindo, H. Míguez, *Adv. Opt. Mater.* **2017**, 1600833.

[9]   N. Nagy, Deak, A., Horvölgyi, Z., Fried, M., Agod, A., Barsony, I., *Langmuir* **2006**, *26*, 8416-8423.

[10]   F. A. Jenkins, H. E. White, *Fundamentals of optics*, 3d ed., McGraw-Hill, New York,, **1957**.

10.6 LIST OF PUBLICATIONS

PUBLISHED AS A PART OF THIS THESIS

1. **Touchless optical finger motion tracking based on 2D nanosheets with giant moisture responsiveness,** K. Szendrei*, P. Ganter*, O. Sánchez-Sobrado, R. Eger, A. Kuhn, B.V. Lotsch, *Adv. Mater.* **2015**, *27*, 341-6348.

2. **Towards the nanosheet-based photonic nose: Vapor recognition and trace water sensing with antimony phosphate thin film devices**, P. Ganter*, K. Szendrei*, B.V. Lotsch, *Adv. Mater.* **2016**, *28*, 7436–7442., *Inside front cover image.*

3. **Selectivity, cycling stability and temperature dependence of touchless finger motion tracking devices based on 1D photonic crystal**, K. Szendrei, P. Ganter, B.V. Lotsch, *Proc. SPIE* 9885, **2016**, Photonic Crystal Materials and Devices XII, 98850Z.

4. **Fluorescent photonic humidity sensors,** K. Szendrei*, A. Jiménez-Solano*, G. Lozano, B. V. Lotsch, H. Miguez, *Adv. Optical Mater*., **2017**, *5*, 1700663.

5. **Lithium tin sulfide – a high-refractive-index 2D material for humidity-responsive Photonic Crystals,** K. Szendrei-Temesi, O. Sanchez-Sobrado, S. B. Betzler, K. M. Durner, T. Holzmann, B. V. Lotsch, *Adv. Func. Mater.*, **2018**, *28*, 1705740., *Back cover image.*

6. **Tracking vertical molecular diffusion into 1-dimensional Photonic Crystals**, K. Szendrei-Temesi*, A. Jiménez-Solano*, B. V. Lotsch, **2018**, *to be submitted*.

PATENTS

Gas and vapor sensing devices based on 2D nanosheet materials, K. Szendrei, P. Ganter, O. Sanchez-Sobrado, A. Kuhn, B. V Lotsch, European Patent PCT/EP2015/07787, **2015**.
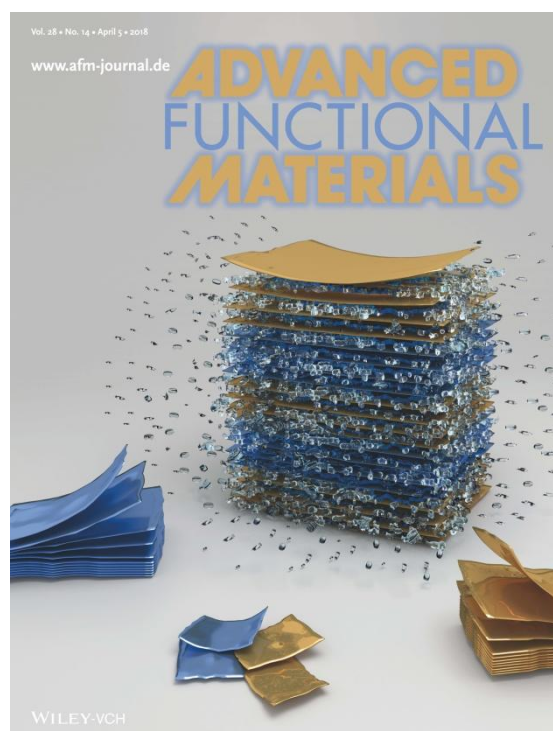
– Appendix –
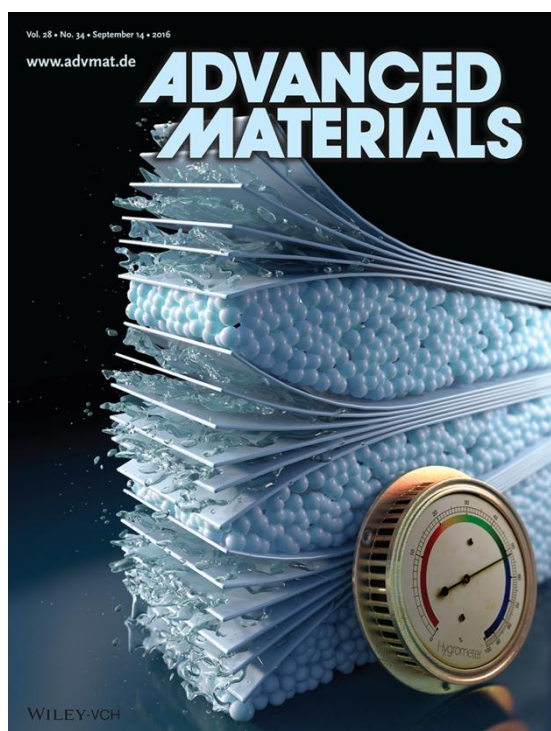
COVER IMAGES

Inside cover image

Adv. Mater. **2016**, *28*, 7436–7442.,

Image Courtesy: Christoph Hohmann, NIM

Backcover image

Adv. Func. Mater. **2018**, *28*, 1705740.

Image Courtesy: Katalin Szendrei-Temesi

PUBLISHED NOT AS A PART OF THIS THESIS

1. **Metal-organic framework based photonic crystal sensors: Improving selectivity by a post-synthetic modification approach**, A. von Mankowski, K. Szendrei-Temesi, C. Koschnick, B. V. Lotsch, *Nanoscale Horizons*, **2018**, DOI: 10.1039/C7NH00209B.

2. **1D photonic defect structures based on colloidal porous frameworks: Reverse pore engineering and vapor sorption,** A. Ranft, I. Pavlichenko, K. Szendrei, P.M. Zehetmaier, Y. Hu, A. von Mankowski, B.V. Lotsch, *Microporous & Mesoporous Mater.* **2015**, *216*, 216–224.

3. **Bringing one-dimensional photonic crystals to a new light: An electrophotonic platform for chemical mass transport visualisation and cell monitoring,** I. Pavlichenko, E. Broda, Y. Fukuda, K. Szendrei, A.K. Hatz, G. Scarpa, P. Lugli, C. Bräuchle, B.V. Lotsch, *Mater. Horiz.* **2015**, *2*, 299–308.

4. **Highly stable and biocompatible gold nanorod–DNA conjugates as NIR probes for ultrafast sequence-selective DNA melting,** V.Baumann, P. Johan, F. Röttgermann, F. Haase, K.

Szendrei, P. Dey, K. Lyons, R. Wyrwich, M. Gräßel, J. Stehr, L. Ullerich, F. Bürsgens, J. Rodríguez-Fernández, *RSC Adv.*, **2016**, *6*,103724.

5. **Use of electronic cigarettes (e-cigarettes) impairs indoor air quality and increases FeNO levels of e-cigarette consumers,** W. Schober, K. Szendrei, W. Matzen, H. Osiander-Fuchs, D. Heitmann, T. Schettgen, R. A. Jörres, H. Fromme, *Int. Journal of Hygiene and Environmental Health*, **2014**, *217*, *6*, 628-637.

10.7 CONTRIBUTIONS TO CONFERENCES

ORAL PRESENTATIONS

April 17-21, 2017 Phoenix, USA	**MRS Spring Meeting** K. Szendrei, P. Ganter, B. V. Lotsch *Touchless finger motion tracking with humidity sensitive 1D Photonic Crystals* **Silver Graduate Student Award**
Februar 25, 2017 Harvard University, Boston, USA	**Boston Photonics Centennial Conference** K. Szendrei, P. Ganter, B. V. Lotsch *1D Photonic Crystals with ultrahigh humidity sensitivity*
April 4-7, 2016 Brussels, Belgium	**SPIE Photonics Europe** K. Szendrei, P. Ganter, B. V. Lotsch *Testing the selectivity, cycling stabilty and the temperature dependency of touchless finger motion tracking devices based on 1D photonic crystals* **Best Student Paper Award**
March 6-11, 2016 Regensburg, Germany	**DPG Spring Meeting** K. Szendrei, P. Ganter, B. V. Lotsch *Touchless finger motion tracking with humidity sensitive 1D Photonic Crystals*

– Appendix –

POSTER PRESENTATIONS

July 31-August 2, 2017 Hirschberg, Germany	**NIM Summer retreat** K. Szendrei, O. Sanchez-Sobrado, S. Betzler, K. M. Durner, B. V. Lotsch, *Reflective and responsive – Li$_2$Sn$_2$S$_5$ based 1D Photonic Crystals for novel optical properties* **Best Poster Award**
July 27-29, 2016 Herrsching	**NIM Summer retreat** K. Szendrei, P. Ganter, B. V. Lotsch *Touchless finger motion tracking with humidity sensitive 1D Photonic Crystals* **Best poster award**
May 27-29, 2015 City University of Hong Kong	**CFP/NIM Workshop on Functional Photonics and Nanosystems** K. Szendrei, P. Ganter, O. Sanchez-Sobrado, R. Eger, A. Kuhn, B. V. Lotsch *2D nanosheet-based 1D Photonic Crystals with giant humidity responsiveness*
Nov 2015 Max Planck Institute Stuttgart	**Scientific Advisory Board Meeting** of the Max Planck Institute for Solid State Research K. Szendrei, P. Ganter, O. Sanchez-Sobrado, R. Eger, A. Kuhn, B. V. Lotsch *2D nanosheet-based 1D Photonic Crystals with giant humidity responsiveness*
August 19-22, 2013 UCL London, UK	**INASCON** (International Nanoscience Conference) **2013** K. Szendrei, I. Pavlichenko, B. V. Lotsch *Towards miniature sensing platform: 1D Photonic Crystals in vapor and solvent sensing applications* **Best poster award**

10.8 CURRICULUM VITAE

EDUCATION

10/2014-Present	**Max Planck Institute for Solid State Research and Ludwig-Maximilians Universität, Munich** **Group of Prof. Dr. Bettina V. Lotsch** PhD student Research topic: 1D Photonic Crystals based on 2D nanosheet materials for optical vapor sensing applications Graduate School: Nanoinitiative Munich (NIM), student board member, 2017
10/2012-09/2014	**Ludwig-Maximilians Universität, Munich** Master of Sciences in Chemistry **Master thesis** – MPI for Solid State research, Group of Prof. Dr. Bettina Lotsch 1D Photonic Crystals based on 2D Nanosheet Materials as Optical Humidity Sensors for Touchless Positioning Interfaces
10/2009-09/2012	**Ludwig-Maximilians Universität, Munich** Bachelor of Sciences in Chemistry and Biochemistry **Bachelor thesis** – LMU Munich, Group of Prof. Dr. Thomas Bein Fluorocarbon surfactant mediated synthesis of mesoporous silica particles and the influence of synthesis parameters
09/2004-06/2009	**Kossuth Lajos Gimnázium, Budapest** High school Bilingual Abitur

Awards and Scholarships

04/2017	Silver Graduate Student Award of the Material Research Society
04/2017	CeNS travel award
04/2016	Best Student Paper award of SPIE Photonics Europe
09-10/2015	Nanoinitiative Munich, Student Research Visit Award
10/2015	CeNS Publication Award
07/2016 and 08/2017	Best Poster award at the Summer Retreat of the Nanoinitiative Muich
08/2013	Best Poster Award at the INASCON Conference in London
06/2013	Lindau Nobel Laureate Meeting, Participation as a DAAD Scholarship holder
2009-2014	DAAD Scholarship for international high school students

„Look up at the stars and not down at your feet. Try to make sense of what you see, and wonder about what makes the universe exist. Be curious."

Stephen Hawking